



Héctor Eduardo Goicoechea Manuel

**Cosserat rods and their application to
drill-string dynamics**

Tese de Doutorado

Thesis presented to the Programa de Pós-graduação em Engenharia Mecânica, do Departamento de Engenharia Mecânica da PUC-Rio in partial fulfillment of the requirements for the degree of Doutor em Engenharia Mecânica.

Advisor : Dr. Roberta de Queiroz Lima
Co-advisor: Dr. Fernando Salvador Buezas

Rio de Janeiro
April 2023



Héctor Eduardo Goicoechea Manuel

**Cosserat rods and their application to
drill-string dynamics**

Thesis presented to the Programa de Pós-graduação em Engenharia Mecânica da PUC-Rio in partial fulfillment of the requirements for the degree of Doutor em Engenharia Mecânica. Approved by the Examination Committee:

Dr. Roberta de Queiroz Lima

Advisor

Departamento de Engenharia Mecânica – PUC-Rio

Dr. Fernando Salvador Buezas

Co-advisor

Department of Physics - UNS

Prof. Fernando Alves Rochinha

Universidade Federal do Rio de Janeiro - UFRJ

Prof. Marcelo Tulio Piovan

Universidad Tecnológica Nacional - UTN

Prof. Mariano Febbo

Universidad Nacional del Sur - UNS

Prof. Rubens Sampaio Filho

Departamento de Engenharia Mecânica – PUC-Rio

Rio de Janeiro, April 19, 2023

All rights reserved.

Héctor Eduardo Goicoechea Manuel

Civil Engineer by the Universidad Nacional del Sur, Bahía Blanca, Argentina.

Bibliographic data

Goicoechea Manuel, Héctor Eduardo

Cosserat rods and their application to drill-string dynamics / Héctor Eduardo Goicoechea Manuel; advisor: Roberta de Queiroz Lima; Co-advisor: Fernando Salvador Buezas. – 2023.

195 f: il. color. ; 30 cm

Tese (doutorado) - Pontifícia Universidade Católica do Rio de Janeiro, Departamento de Engenharia Mecânica, 2023.

Inclui bibliografia

1. Engenharia Mecânica – Teses. 2. Dinâmica de colunas de perfuração. 3. Contato em poços de geometria curva. 4. Dinâmica de corte na rocha. 5. Equação de advecção. 6. Oscilações torcionais. I. de Queiroz Lima, Roberta. II. Buezas, Fernando Salvador. III. Pontifícia Universidade Católica do Rio de Janeiro. Departamento de Engenharia Mecânica. IV. Título.

CDD: 621

To my parents, for their support
and encouragement.

Acknowledgments

I would like start by thanking my current advisors, Fernando Buezas and Roberta Lima, for their guidance and contributions that helped make possible this thesis. I am also grateful for the guidance provided by Prof. Marta Rosales, now retired from teaching, who helped me initiate into the world of research as a pre-graduate student and then, together with Fernando, directed my first years as a Ph.D student. I would also like to say that it has been a true pleasure working with her. Last but not least, I am grateful for having met Prof. Rubens Sampaio, who made my stay at PUC-Rio possible and invited me to take part of his research group in the Laboratory of Vibrations, where I met Roberta. The talks and discussions with Rubens often gave new ideas on ways to improve and continue my research. Also, all the conversations on random topics like economy, politics and leisure activities were always interesting. I am grateful to my parents, that have supported me in this quest, both by lending an ear and economically, when it was required. Finally, I would like to thank my colleagues and friends, from both Argentina and Brasil, for all the discussions, the help, and the little things that make our daily life more entertaining.

This study was financed in part by the Coordenação de Aperfeiçoamento de Pessoal de Nível Superior – Brasil (CAPES) – Finance Code 001, and by the Consejo Nacional de Investigaciones Científicas y Técnicas (CONICET) - Argentina.

Abstract

Goicoechea Manuel, Héctor Eduardo; de Queiroz Lima, Roberta (Advisor); Buezas, Fernando Salvador (Co-Advisor). **Cosserat rods and their application to drill-string dynamics**. Rio de Janeiro, 2023. 195p. Tese de Doutorado – Departamento de Engenharia Mecânica, Pontifícia Universidade Católica do Rio de Janeiro.

In this thesis, the theory of Cosserat rods is applied to the dynamics of drill-strings. The main objective is to evaluate the behaviour of these strings when they move within curved wells. To achieve this goal, a deterministic structural model is constructed, where the drill-pipes and the bottom hole assembly are taken as a Cosserat rod. Next, a strategy to deal with the lateral contact in curved well configurations is developed. After that, the free boundary problem is assessed: while drilling, the boundary changes due to cutting, modifying the position of the soil and, consequently, changing the bit-rock interaction forces. For this reason, a bit-rock model that can account for the cutting dynamics is adopted, in which an extra advection equation is solved together with the equations of motion of the Cosserat rod. Next, application cases are provided. First, some effects included in the model are tested in isolation, such as the lateral friction, the lateral contact, and the cutting. After that, they are all combined. In the first analysis, an off-bottom string is simulated, i.e. without contact at the bit. This allows testing the formulation associated with the lateral contact. Also, the calibration of the lateral friction parameters is made. Following that, the strategy to account for the cutting at the bit is implemented in a low-dimensional 2-DOF model, and in a semi-discrete model with a continuous wave equation for the torsional dynamics. The results show that the use of continuous approaches is more appropriate than low-dimensional models. Especially when long columns are considered, and when there is interest in understanding not only the behaviour at the bit but also along drill-pipes. This finding is reinforced by another application where the cutting dynamics are combined with the Cosserat rod formulation. Again, similar observations from a qualitative point of view are found. Overall, the differences in the results between the lumped low-dimensional models and the continuous Cosserat rod justify the development and application of the Cosserat approach to drilling structures. Finally, an introductory stochastic analysis concerning the variability of the rock is presented as an introduction to a future line of research, where stochasticity is included.

Keywords

Drill-string dynamics; Contact in curved boreholes; Bit-rock cutting dynamics; Advection equation; Torsional oscillations; Stick-slip vibrations.

Resumo

Goicoechea Manuel, Héctor Eduardo; de Queiroz Lima, Roberta; Buezas, Fernando Salvador. **Estruturas unidimensionais de Cosserat aplicadas à dinâmica de colunas de perfuração.** Rio de Janeiro, 2023. 195p. Tese de Doutorado – Departamento de Engenharia Mecânica, Pontifícia Universidade Católica do Rio de Janeiro.

Nesta tese, a teoria das hastes de Cosserat é revisitada e aplicada à dinâmica de coluna de perfuração. O objetivo é estudar o comportamento dessas estruturas dentro de poços de petróleo curvos. Para atingir este objetivo, um modelo estrutural determinístico é construído onde as tubos de perfuração (*drill-pipes*) e o conjunto de fundo (*bottom hole assembly*) são considerados como uma estrutura unidimensional de Cosserat. Em seguida, é desenvolvida uma estratégia para tratar o contato lateral em poços com configuração curvilínea. Depois disso, o problema de contorno livre é tratado mediante uma estratégia que considera como a condição de borda evolui à medida que a estrutura de perfuração avança. Isto é feito mediante uma formulação de interação broca-rocha que deve considerar a dinâmica de corte. Para isso, uma equação extra, de advecção, é resolvida junto com as equações de movimento de Cosserat. Em seguida, alguns casos de aplicação são apresentados. Numa primeira instância, alguns elementos do problema são avaliados separadamente. Seguidamente, eles são integrados e analisados de forma conjunta. Por exemplo, primeiramente uma coluna de perfuração sem contato de fundo (*off-bottom*) é simulada, ou seja, sem contato broca-rocha, para estudar o comportamento e a implementação da estratégia para o contato lateral. Aqui também são calibrados alguns dos parâmetros do modelo de atrito. Em seguida, a estratégia para contabilizar o corte na rocha é implementada em um modelo 2-DOF de baixa dimensão e em um semi-discreto onde a dinâmica de torção é modelada como uma equação de onda. Os resultados mostram que o uso de abordagens contínuas resulta mais apropriado que aquelas onde se utilizam modelos de baixa dimensão, particularmente quando são consideradas colunas longas, e quando há interesse em analisar não apenas o comportamento da broca, mas também o comportamento do sistema mecânico ao longo dos tubos de perfuração. Isso é reforçado por outro exemplo onde a dinâmica de corte é combinada com a formulação de Cosserat. Observações semelhantes do ponto de vista qualitativo são encontradas. Resumindo os resultados obtidos, as diferenças nas previsões dadas pelos modelos de baixa dimensão e o de unidimensional de Cosserat justificam o desenvolvimento e aplicação da abordagem com esta formulação em estruturas de perfuração. Finalmente, a

modo de introduzir outro aspecto importante em colunas de perfuração e que pode ser uma linha de pesquisa para continuar o trabalho, a variabilidades presente em elementos como rocha, inclui-se um caso de aplicação considerando um poço horizontal e um campo estocástico de atrito.

Palavras-chave

Dinâmica de colunas de perfuração; Contato em poços de geometria curva; Dinâmica de corte na rocha; Equação de advecção; Oscilações torcionais.

Resumen

Goicoechea Manuel, Héctor Eduardo; de Queiroz Lima, Roberta (Orientador); Buezas, Fernando Salvador (Orientador). **Estructuras unidimensionales de Cosserat aplicadas a la dinámica de columnas de perforación**. Rio de Janeiro, 2023. 195p. Tesis de Doctorado – Departamento de Engenharia Mecânica, Pontifícia Universidade Católica do Rio de Janeiro.

En esta tesis, la teoría de Cosserat para elementos unidimensionales es revisitada y aplicada a la simulación de columnas de perforación. El objetivo es estudiar el comportamiento de estas estructuras en pozos de geometría curva. Para alcanzar este objetivo se construye un modelo determinístico. En este modelo, los caños de perforación (*drill-pipes*) y el conjunto de fondo (*bottom hole assembly*) son modelados como una estructura unidimensional de Cosserat. Seguidamente, una estrategia para tratar con el contacto lateral en pozos curvos es desarrollada. Luego, el problema de frontera libre es estudiado: durante la perforación, la condición de borde cambia debido al cambio del perfil altimétrico del terreno, alterando su posición y consecuentemente las fuerzas asociadas a la interacción broca-roca. Por esta razón, se decide utilizar un modelo de interacción broca-roca que tiene en cuenta la dinámica del corte. En este abordaje una ecuación extra, la ecuación de advección, es resuelta en forma acoplada con las ecuaciones del movimiento de la estructura de Cosserat. Algunos ejemplos de aplicación son presentados. En una primera instancia, algunos de los elementos del problema son estudiados en forma aislada. Luego combinados en un modelo completo. Por ejemplo, el caso de una columna sin contacto de fondo (*off-bottom*) es tratado para evaluar el comportamiento y la implementación de la estrategia mencionada para detectar el contacto lateral. Además, se efectúa la calibración de alguno de los parámetros relacionados con la fricción lateral. Luego, la estrategia para considerar el corte en la punta es implementada en un modelo de 2-DOF, y en otro semi-discreto donde se considera un modelo de ecuación de onda para la dinámica torsional. Los resultados muestran que el uso de formulaciones continuas es más apropiado que aquellas formulaciones donde se utilizan modelos de dimensiones reducidas, particularmente cuando se estudia columnas largas donde el interés se centra en entender no solo el comportamiento de la broca sino también a lo largo de la tubería. Este resultado es reforzado por otro caso de aplicación en donde se combina la dinámica de corte con un modelo de Cosserat. Observaciones similares son vistas en el comportamiento cualitativo de la solución. En resumen, las diferencias observadas en los diferentes ejemplos de aplicación entre los modelos de dimensiones reducidas y el modelo continuo de Cosserat

justifican el desarrollo y la aplicación de la teoría de Cosserat a estructuras de perforación. Finalmente, dado que uno de los objetivos planteados también es considerar la variabilidad en algunos elementos como ser las propiedades de la roca, un caso de aplicación considerando un pozo horizontal es mostrado.

Palabras clave

Dinámica de columnas de perforación; Dinámica de corte de la roca; Ecuación de advección; Vibraciones torsionales; Vibraciones stick-slip.

Table of contents

1	Introduction	22
1.1	Aims	29
1.2	Outline and contributions	29
2	The theory of Cosserat Rods	32
2.1	The kinematic hypotheses	34
2.1.1	The deformation tensor	36
2.1.2	The velocity field	36
2.1.3	The angular velocity in terms of quaternion components	37
2.1.4	The acceleration field	39
2.2	The equations of motion	40
2.2.1	The kinetic energy	40
2.2.2	Analysis of a rod segment	42
2.2.3	The linear momentum balance	43
2.2.4	The angular momentum balance	44
2.3	The constitutive relations	45
2.3.1	Notation	46
2.3.2	The constitutive relations for a linear elastic material	47
2.3.2.1	Revisiting the kinematic hypotheses	47
2.3.2.2	The 3-D Constitutive for a linear elastic orthotropic material	48
2.3.2.3	Step 1: The displacement gradient measure of deformation tensor	49
2.3.2.4	Step 2: The right Cauchy-Green tensor	52
2.3.2.5	Step 3: The Green-St. Venant strain tensor	52
2.3.2.6	Step 4: Finding the in-plane deformation functions	52
2.3.2.7	Step 5: Integrating the traction associated with the second Piola stress tensor	53
2.4	Linear isotropic elastic materials	55
2.5	Linear Kelvin-Voigt material	55
2.6	Summary of the equations	56
3	The sources of non-linearity in Cosserat rods	58
3.1	Geometric non-linearity in Continuum Mechanics	58
3.2	Geometric non-linearity in the Cosserat theory of rods	59
3.3	The importance of the non-linear terms	61
4	Simulating an off-bottom drill-string in a curved well	64
4.1	Description of the problem	64
4.2	The drill-string model	67
4.2.1	Rotary speed control	67
4.2.2	The contact model for an arbitrary borehole geometry	69
4.2.3	The friction model	71
4.2.4	The distributed forces in the equations of motion	72
4.3	Comparison and calibration of the friction model	72
4.3.1	Qualitative analysis	74

4.3.2	Friction model calibration	76
4.4	Simulations concerning a curved borehole	77
4.5	Final comments concerning this chapter	82
5	Modelling the dynamics of the cutting	83
5.1	Description of the problem	84
5.2	The drill-string models	85
5.2.1	Model M1 and M2: the axial dynamics	86
5.2.2	Model M1: The torsional dynamics	87
5.2.3	Model M2: The torsional dynamics	87
5.3	The bit-rock interaction model	87
5.3.1	The proposed interaction model	89
5.3.2	The cutting process	93
5.3.2.1	The delay approach	93
5.3.2.2	The advection approach	94
5.4	The nominal solution: a special non-oscillatory case	95
5.4.1	The nominal case for model M1	96
5.4.2	The nominal case for model M2	96
5.5	Simulations	97
5.5.1	Parameters	99
5.5.2	Convergence analysis	100
5.5.3	Simulation V1: A benchmark test	101
5.5.4	Simulation V2: The model M1 as a limiting case of M2	104
5.5.5	Simulation C1 (with $\beta = 0.3$)	108
5.5.6	Simulation C2 (with $\beta = 1.3$)	112
5.5.7	Simulation C3 for an imposed variable angular speed	115
5.6	More aspects about the results	117
5.7	Final comments concerning this chapter	118
6	Simulating drill-string via a Cosserat model with cutting	120
6.1	Description of the problem	121
6.2	The drill-string models	122
6.2.1	Models M1 and M2	122
6.2.2	Model M3	123
6.3	Simulations	125
6.3.1	Parameters	126
6.3.2	Convergence analysis for M3	127
6.3.3	Simulation V1: a verification of model M3	128
6.3.4	Simulations C1: assessing the influence of damping in the response	132
6.3.4.1	Simulation with damping $c_d = 10^{-2}$	135
6.3.4.2	Simulation with damping $c_d = 10^{-3}$	136
6.3.4.3	Simulation with damping $c_d = 10^{-4}$	138
6.3.4.4	Simulation with damping $c_d = 10^{-5}$	140
6.3.5	Comparing the responses with those produced by models M1 and M2	140
6.3.5.1	Simulation with damping $c_d = 10^{-5}$	140
6.3.5.2	Simulation with damping $c_d = 10^{-4}$	141
6.3.5.3	Measuring the performance of the drilling process	144
6.3.5.4	Some remarks concerning the three models	145

6.3.6	Simulation C2: considering a non-straight borehole	146
6.4	Final comments of this chapter.	150
7	Simulating a horizontal well with stochastic friction	153
7.1	Description of the problem	153
7.2	The deterministic model	154
7.3	The stochastic model	157
7.4	Results	157
7.4.1	The deterministic case	157
7.4.2	Stochastic results	159
7.5	Final comments concerning this chapter	160
8	Final considerations	162
8.1	Summary	162
8.2	Contributions	164
8.3	Future work	166
	Bibliography	167
A	Appendix to Chapter 2	177
A.1	Quaternions as a tool to parametrise rotations in space	177
A.1.1	Demonstration	180
B	Appendix to Chapter 4	184
B.1	Benchmarks and model verifications	184
B.1.1	A pendulum under the action of gravity	184
B.1.2	A spin-Up manoeuvre	185
B.1.3	A beam under pure bending	186
B.1.4	A drill-string model for a straight vertical borehole	187
B.1.4.1	Rotary speed control	187
B.1.4.2	Contact model	188
B.1.4.3	Friction model	188
B.1.5	Initial Conditions	189
B.1.5.1	Solution	189
C	Appendix to Chapter 6	191
C.1	Geometrical interpretation of the equation for the cutting process	191
C.2	Non-dimensional parameters	192
D	The weak form	194

List of figures

Figure 1.1	Evolution of the oil consumption	22
Figure 1.2	Layout of a drilling rig	23
Figure 2.1	Cosserat rods: flowchart for the derivation of the formulation	33
Figure 2.2	Kinematic hypotheses	34
Figure 2.3	Equilibrium of a rod segment	42
Figure 2.4	Steps to derive a constitutive relation	47
Figure 3.1	Sketch of a horizontal beam	61
Figure 3.2	Application to a beam with an applied force at the tip.	62
Figure 3.3	Application to a beam with an applied force at the tip: results predicted by different models.	63
Figure 4.1	Sketch of the proposed drill-string model.	68
Figure 4.2	The contact model.	70
Figure 4.3	Schematic representation of the variation of the coefficient of friction	71
Figure 4.4	Geometry of well A.	73
Figure 4.5	Distributed torque proposed by [29] vs drill-string length.	74
Figure 4.6	Soil penetration vs drill-string length.	75
Figure 4.7	Soil penetration vs drill-string length. Comparison between models.	76
Figure 4.8	Soil penetration vs drill-string length considering different values of the soil elastic constant.	77
Figure 4.9	Comparison between the Cosserat rod (CR) model using the proposed friction law and the CR model using the friction as proposed in [29]. Angular speed ω_3 vs time a soil constant $k_s = 10^6 \text{N/m}^2$, friction constant $\mu_s = 0.30$, mesh with 200 elements. (a) Duration of the simulation $t = 100$ s; (b) Zoom for $t = 0$ s to $t = 20$ s; (c) Zoom for $t = 80$ s to $t = 100$ s.	79
Figure 4.10	Frequency spectrum comparison between the Cosserat rod (CR) model (black line) and the model in [29](red line). A mesh of $N = 200$ elements is employed.	79
Figure 4.11	Drill-string configurations at different times (CR Model). The centreline of the rod is shown (black line), as well as section orientation through the field of the director $d_1(s_R)$ (red vectors), which is fixed to the cross-section at all times. (a) For $t = 1$ s; (a) For $t = 50$ s; (a) For $t = 77.5$ s.	80
Figure 4.12	Internal forces and moments (CR Model) acting on the rod at $t = 77.5$ s. (a) Bending moment m_1 in Nm; (b) bending moment m_2 in Nm; (c) torsion m_3 in Nm; (d) shear force n_1 in N; (e) shear force n_2 in N; and (f) tensile force n_3 in N.	81

- Figure 5.1 Representation of the models employed. In this figure, special attention is given to the structural aspects of the formulation. Model M1 considers 1-DOF for the axial dynamics and 1-DOF for the torsional dynamics. Model M2 employs the same formulation for the axial dynamics, but a continuous approach for the torsional one. To the right side of the figure, a sketch of a cutter blade is shown. This is used in the definition of the bit-rock interaction model, in section 5.3, where a zoomed version of this part of the sketch is shown, along with a detailed description. The force \mathbf{W} and the torque \mathbf{T} are related to the traction vectors $\mathbf{f}_{f,i}$ and $\mathbf{f}_{c,i}$ via integration over the contact areas. 86
- Figure 5.2 A single cutter i is depicted. The traction vectors $\mathbf{f}_{f,i}$ and $\mathbf{f}_{c,i}$, acting on the wearflat and the cutting blade, respectively, are drawn. These vectors are defined in terms of the functions $\sigma(\omega_b, v_b)$, that defines the contact pressure at the wearflat, and $\epsilon(\omega_b)$, an intrinsic specific energy of the rock. The parameter ζ defines the inclination of the cutting force, μ is the coefficient of friction, l_i is the wearflat length, and d_i is the instantaneous depth of cut. 90
- Figure 5.3 (a) The functional form of $\sigma(\sigma^*(\omega_b), v_b)$ is plotted for a fixed value of σ^* . (b) The form of $\sigma^*(\omega_b)$ is depicted. σ_1 and σ_2 are two parameters associated with the rock contact strength. (c) The form of $\epsilon(\omega_b)$. ϵ_1 is a parameter called the rock intrinsic specific energy. c_1 , c_2 and c_3 are some small regularisation constants. 91
- Figure 5.4 Distribution of the cutting blades in a symmetrical arrangement (example with $n = 6$ blades). a is the radius of the bit, which here coincides with the depth of each cutter so that $a_i = a$, \mathbf{r}_i is a vector that goes from the centre of the bit to the point of application of the resultant forces at each blade. 91
- Figure 5.5 General simulation workflow employed. 98
- Figure 5.6 Convergence analysis. Error percentage in the angular position vs. the sum of elements in used to mesh x_1 and x_2 . 100
- Figure 5.7 Simulation V1. Results obtained for the simulation V1, with model M1. $\omega_b(t)$ is the angular speed, expressed as a function of time t . 103
- Figure 5.8 Simulation V1. Results obtained for the simulation V1, with model M1. $\hat{\omega}_b(\tau)$ is the non-dimensional angular speed as a function of the non-dimensional time parameter τ . 104
- Figure 5.9 Simulation V1. Zoom of the results obtained in the simulation V1, with model M1, for $\tau \in [97.70, 123.2]$. $\hat{\omega}_b(\tau)$ is the non-dimensional angular speed as a function of the non-dimensional time parameter $\tau = t$. 104
- Figure 5.10 Simulation V2. Angular speed at the bit $\omega_b(t)$, (a) for model M2 with $\alpha = 1.00$; (b) model M2 with $\alpha = 0.80$; (c) model M2 with $\alpha = 0.40$; (d) Model M1. 106

Figure 5.11 Simulation V2. FFT of the angular speed at the bit $\omega_b(t)$. Frequency range: 0 to 20Hz. The last 20 s of simulations were used to construct the FRF.	107
Figure 5.12 Simulation V2. Zoom of the FFT of the angular speed at the bit $\omega_b(t)$. Frequency range 0 to 2Hz. The last 20 s of simulations were used to construct the FFT.	107
Figure 5.13 Simulation C1. Angular speed at the bit $\omega_b(t)$ for the cases C1-A and C1-B (models M1 and M2, respectively). The nominal angular bit speed is shown in a dashed line.	109
Figure 5.14 Simulation C1. Angular speed at the bit $\omega_b(t)$ for the cases C1-A and C1-B (models M1 and M2, respectively). Zoom for $t \in [0\text{s}, 10\text{s}]$. The nominal angular bit speed is shown in a dashed line.	109
Figure 5.15 Simulation C1. FFT of the angular speed at the bit $\omega_b(t)$.	110
Figure 5.16 Simulation C1. Axial position of the bit $U(t)$ for the cases C1-A and C1-B (models M1 and M2, respectively). The nominal axial position is shown in a dashed line.	110
Figure 5.17 Simulation C1. Axial speed at the bit $v_b(t)$, for the cases C1-A and C1-B (models M1 and M2, respectively). (a) For $t \in [0, 1]$ and (b) (a) For $t \in [40.5, 45]$.	111
Figure 5.18 Simulation C1. Torques at the bit T for the cases C1-A and C1-B (models M1 and M2, respectively).	111
Figure 5.19 Simulation C2. Angular speed at the bit $\omega_b(t)$ for the cases C2-A and C2-B (models M1 and M2, respectively). The nominal angular bit speed is shown in a dashed line.	112
Figure 5.20 Simulation C2. Angular speed at the bit $\omega_b(t)$, for the cases C2-A and C2-B (models M1 and M2, respectively). Zoom for $t \in [0, 10]\text{s}$. The nominal angular bit speed is shown in a dashed line.	113
Figure 5.21 Simulation C2. FFT of the angular speed at the bit ($\omega_b(t)$).	113
Figure 5.22 Simulation C2. Axial position $U(t)$ at the bit, for the cases C2-A and C2-B (models M1 and M2, respectively). The nominal bit position is shown in a dashed line.	114
Figure 5.23 Simulation C2. Angular speed at the bit ($v_b(t)$), for the cases C2-A and C2-B (models M1 and M2, respectively). The nominal axial bit speed is shown in a dashed line.	114
Figure 5.24 Simulation C1. Torques at the bit T for the cases C1-A and C1-B (models M1 and M2, respectively).	115
Figure 5.25 Simulation C3. Imposed angular speed at the top, for the cases C3-A and C3-B.	116
Figure 5.26 Simulation C3. Angular speed at the bit $\omega(t)$ for the cases C3-A and C3-B (models M1 and M2, respectively). The imposed angular speed (boundary condition at the top) is shown in a dashed line.	116

Figure 5.27 Simulation C3. Angular speed at the bit $\omega_b(t)$ for the cases C3-A and C3-B (models M1 and M2, respectively). Zoom for $t \in [65s, 75s]$. The imposed angular speed (boundary condition at the top) is shown in a dashed line. The arrows indicate where backward rotation is taking place.	117
Figure 5.28 Simulation C3. FFT of the angular speed at the bit $\omega_b(t)$.	117
Figure 6.1 Sketch of the models M1, M2 and M3.	123
Figure 6.2 Convergence analysis. Error Ξ vs. the total number of elements in each spatial domain N_1^i . In the simulation $c_d = 10^{-4}$ was used.	127
Figure 6.3 Model M3. Angular and axial speed vs. time.	129
Figure 6.4 FFT of the angular and axial speed at the bit.	130
Figure 6.5 Angular speed at the bit for different values of the damping coefficient c_d , where (a) $c_d = 10^{-2}$; (b) $c_d = 10^{-3}$; (c) $c_d = 10^{-4}$; (d) $c_d = 10^{-5}$	133
Figure 6.6 Torques at the bit T for (a) model M1; (b) Model M2; (c) model M3 with $c_d = 10^{-2}$; (d) model M3 with $c_d = 10^{-3}$; (e) model M3 with $c_d = 10^{-4}$; and (c) model M3 with $c_d = 10^{-5}$. The mean value is indicated, for each case, with dashed blue line.	134
Figure 6.7 (a) Angular speed at the bit for $c_d = 10^{-2}$; FFT of the previous signal for (b) slice S_1 ; (c) slice S_2 ; (d) slice S_3 .	135
Figure 6.8 (a) Angular speed at the bit for $c_d = 10^{-3}$; FFT of the previous signal for (b) slice S_1 ; (c) slice S_2 ; (d) slice S_3 .	137
Figure 6.9 (a) Angular speed at the bit for $c_d = 10^{-4}$; FFT of the previous signal for (b) slice S_1 ; (c) slice S_2 ; (d) slice S_3 .	138
Figure 6.10 (a) Angular speed at the bit for $c_d = 10^{-5}$; FFT of the previous signal for (b) slice S_1 ; (c) slice S_2 ; (d) slice S_3 .	139
Figure 6.11 FFT of the angular speed at the bit obtained with models M1 and M2. $\alpha = 1$ was used.	141
Figure 6.12 FFT of the angular speed at the bit obtained with models M1, M2, and M3 with damping $c_d = 10^{-5}$. $\alpha = 1$ was used.	142
Figure 6.13 FFT of the angular speed at the bit obtained with models M1, M2, and M3 with damping $c_d = 10^{-4}$. $\alpha = 1$ was used.	143
Figure 6.14 Drilling performance. (a) Depicts the bit displacement δ_{c_d} for each damping case c_d ; (b) depicts the bit displacement difference Δ_{c_d} calculated as the bit displacement δ_{c_d} (where each case follows the colouring indicated in the legend of the figure), subtracted by δ_R corresponding to the case with $c_d = 10^{-2}$.	144
Figure 6.15 Well geometry considered in simulation C2.	146
Figure 6.16 Position of the centreline of the string in the xz plane at (a) $t = 1000$ s; (b) $t = 5000$ s; $t = 10000$ s.	147
Figure 6.17 Well geometry considered in simulation C2.	148
Figure 6.18 Comparison of the dynamics of the curved and straight boreholes. a) shows angular speed in the longitudinal direction; and b) the axial speed in the longitudinal direction.	149
Figure 6.19 Mechanical power produced by the top-drive rotary system.	149

Figure 7.1	Sketch of the drill-string model employed. In the graphic, \mathbf{f}_{sta} stands for the force transmitted by the pipes before the simulated segment of drill-string, \mathbf{f}_c is the normal force, the friction force is given by \mathbf{f}_{fric} , and the self-weight is \mathbf{f}_g . D_{ext} and D_{int} are the internal and external diameters of the cross-section.	155
Figure 7.2	Results for the deterministic problem. Comparison of the displacements and velocities at the bit, which are directly linked to the performance of the drilling process. Case A corresponds to the hypothesis that contact occurs due to the deflection and contact of the beam. Case B considers contact on the whole length of the beam, with the hypothesis that the distributed normal force equals the self-weight of the structure. (a), (b) and (c) show the displacement of the bit in the direction of the z-axis δ_z , while (d) shows the velocity v_z at the bit.	158
Figure 7.3	Soil penetration function f_{sp} [m].	159
Figure 7.4	Some realisations from the Monte-Carlo simulations.(a) Displacement of the bit. (b) Speed of the bit.	160
Figure 7.5	Results for the stochastic problem with the stochastic approach. (a) Convergence graph for the standard deviation of the power ratio. (b) PDF for the power ratio.	161
Figure A.1	A representation of the directors of the rotating frame with respect a the fixed frame of reference, employed to form the rotation matrix \mathbf{Q} .	177
Figure A.2	Correspondence vector - quaternion, and vice versa.	179
Figure A.3	Multiplication diagram.	179
Figure A.4	Representation of the effect of the application of the operator L_q to some vector \mathbf{v} .	183
Figure B.1	Example B.1.1. Initial configuration for the pendulum, with its respective geometrical and material properties.	184
Figure B.2	Example B.1.1. (a) Cosserat rod (CR) model centerline position at different times. Intervals $\Delta t = 0.1s$ are considered. (b) Model comparison. The results obtained with the models SM1 and SM2 from Reference [42] vs the CR model are shown.	185
Figure B.3	Example B.1.2. Initial configuration for the cantilever beam with its respective geometrical and material properties.	186
Figure B.4	Example B.1.2. Spin-up manoeuvre. Comparison of the δ values obtained by the Cosserat rod (CR) model and the works of [42] and [97]. The model from S is that of Reference [97], model B is that of [42], and the CR model stands for the Cosserat approach herein presented.	186
Figure B.5	Example B.1.3. Sketch of the bending beam problem with its geometrical and material properties.	187
Figure B.6	Example B.1.3. Distance between the beam ends (δ) vs. applied bending moment (M).	187

Figure B.7 Comparison between the Cosserat rod (CR) model and that presented in [20]. Angular speed ω_z at the top vs time. The target speed for the PI-controller is represented by a dashed line. The model used by Sampaio et al. is that of [21]. 190

Figure B.8 Comparison between the Cosserat rod (CR) model and that presented in [20]. Angular speed ω_z at the bit vs time. The target speed for the PI-controller is represented by a dashed line. The model used by Sampaio et al. is that of [21]. 190

Figure C.1 Schematic example of the behaviour of the advection equation to model the cutting process. (a-c) depict an off-bottom case, at times t_0 , $t_1 > t_0$, and $t_2 > t_1$, respectively. (d-e) show an example of a normal drilling condition. The red arrow depicts the direction in which the advection equation translates the soil profile with a speed ω . 191

List of tables

Table 2.1	Index notation convention to represent \mathbb{C}_{ijkl} , E_{kl} into the reduced Voigt notation form \mathbb{C}_{pq} , E_q .	49
Table 4.1	Basic geometrical and material parameters for the drill-string, based on the values presented in [20].	68
Table 4.2	Adopted parameters for the PI controller based on the values presented in [20].	69
Table 4.3	Basic geometrical and material parameters for the drill-string, based on the values presented in [20].	78
Table 5.1	List of parameters employed in the simulations. (*) Indicates that the parameter changes for the simulation V2, (**) indicates that it changes for simulation C3 and (***) that it changes for simulation C2 and C3. The modified magnitudes are detailed within the corresponding study case. The parameter α is used to vary the characteristic propagation speed of the wave equation in V2.	102
Table 5.2	Simulation V2. List of frequency content in the FFT, for varying values of α , ordered by amplitude (A). Only amplitudes greater than 0.50 are shown. In blue, the evolution of the amplitude content close to the first natural frequency is shown. In green, the main frequency for $\alpha = 1.00$ is shown, as well as for $\alpha = 0.80$. For the latter, the second amplitude is highlighted in orange.	108
Table 6.1	List of parameters employed in the simulations. (*) indicates that the parameter changes for some of the simulations. (**) indicates that the parameter is only used in model M3. This table is an adaptation from [74].	131
Table 7.1	Material and geometric properties used in the modelling of the horizontal drill-string.	155
Table B.1	Adopted parameter values for the PI controller, based on the values presented in [20].	188
Table B.2	Parameters for the friction model presented in [20].	189

1

Introduction

Despite the known negative effects of the usage of petrol and its associated emissions, the consumption of oil and gas has increased continuously over the last years, with a brief exception during the COVID-19 pandemic period, as illustrated in Fig. 1.1. More than half of the world's total supply of energy is provided by fuels derived from petroleum [1]. Moreover, oil-based fuels continue to be the main source of energy for transportation worldwide: oil demand for road transportation is responsible for more than 50% of the total oil consumption amongst the whole sectors, including aviation, railway, waterways and international maritime transport [2]. In this scenario, oil consumption will remain an important source of energy for the coming years, what justifies the need for further development of the tools employed in the extraction process.

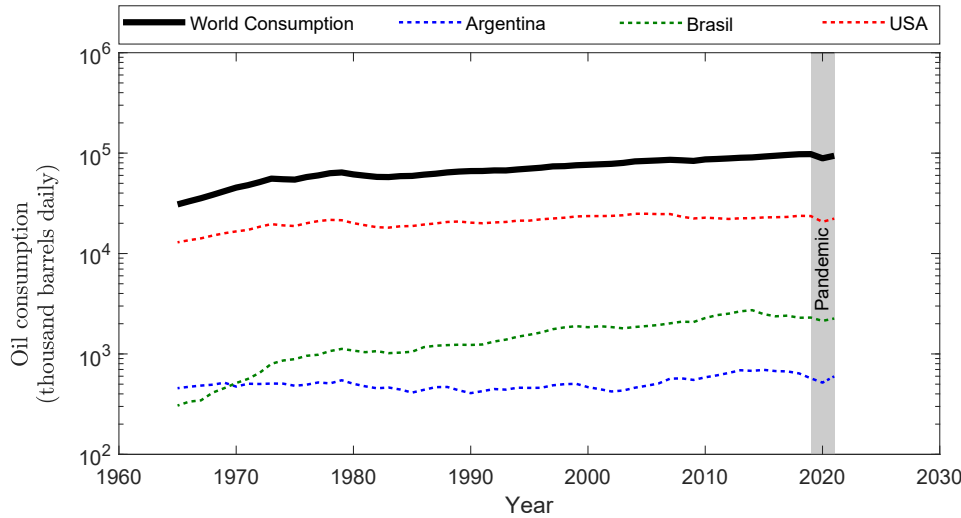


Figure 1.1: Oil consumption from 1965 to 2021, according to the statistical review of world energy [3].

The increasing demand for oil extraction has led to advancements in the technologies employed to build oil wells. An overview of the evolution in drilling technologies is provided in [4]. Additionally, due to directional drilling, the shape of oil wells has also evolved over the years. In this context, understanding the dynamics of drill-strings in complex borehole geometries is crucial to improve their performance and to extend the life cycle of the tools

involved. But before discussing the details of the state of the art concerning the modelling of drill-strings, a brief description of the basic parts of the machinery employed in the drilling process, namely, the drilling rig, is presented.

A sketch of a drilling rig is shown in Figure 1.2. For the description, the rig is divided into two main sections: the top-drive, which contains the devices employed to generate motion in the system, as well as to lift the drilling tools; and the drill-string, which includes the elements that will dig into the ground to perform the drilling operation.

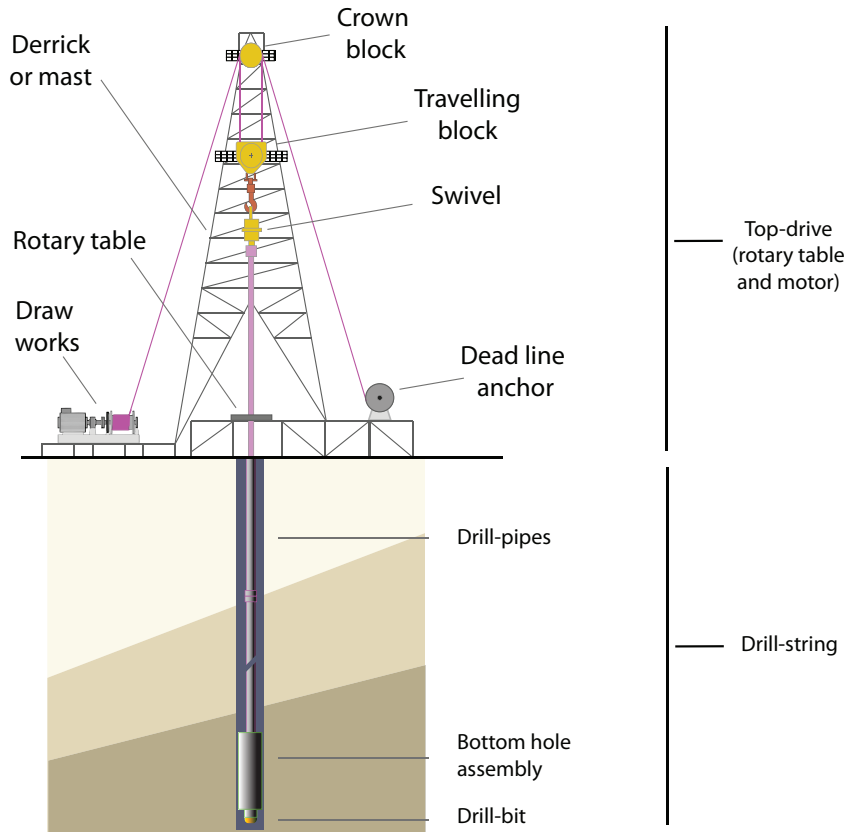


Figure 1.2: Schematic layout of a drilling rig and its components.

The drill-string is the centre of interest in this thesis. It is no more than a slender column in the drilling assembly that has the function of conducting the forces and torques required to drive the drill-bit, as well as to carry the drilling fluids within the oil well. The main elements that form a drill-string are: the drill-pipes; the bottom hole assembly (BHA); and the bit itself. The main function of the drill-pipes, from a structural point of view, is to transmit the power from the motor at the top to the lower elements. The BHA is located between the drill-pipes and the drill-bit, and also transmits movement. It consists of a set of drill-collars, which are heavy thick-walled tubes. Along with the drill-pipes, the drill-collars provide the weight-on-bit (WOB) required for the drilling process. Also, the BHA often contains devices employed in the

control of the inclination and direction of the bit, such as measurement while drilling tools and stabilisers.

As already mentioned, in recent years an evolution in the shape of oil wells has been observed, accompanied by technological progress. At an early stage, oil wells were devised to reach a target that was directly below their surface location and, therefore, vertical geometries were sought. Later on, to gain efficiency and reduce costs, directional drilling gained importance. The first record of a directional oil well dates from the 1930s [4]. It was deliberately drilled to produce oil from beneath shallow coastal waters. For this task, a drilling rig located on the shore at Huntington Beach, California, was used. Since then, up-to-date techniques have allowed directional drilling of wells where the drill's horizontal reach exceeds the true vertical depth. This way, the total depth barrier of 10 km [5] was surpassed, as with the case of the Chayvo Well Z-44 and Z-45, Russia, where a total depth of 12,376 m and a horizontal reach of 11,371 m was achieved.

Given the previous context, the need for models capable of capturing the dynamics of drill-strings under large displacements and rotations is apparent. However, many related literature consider either low-dimensional lumped models or straight beam or shaft formulations to study these complex structures. In addition, when those formulations are used, the attention is usually given to the dynamics of the BHA and, in doing so, the dynamics of the drill-pipes could be oversimplified or neglected. The Ph.D. thesis of [6] raised the attention towards this matter, given the lack of models specifically designed to simulate the drill-string as a whole, including the drill-pipes. The author points out that the drill-pipes involve approximately 90% of the total length and 80% of the total mass of the drill-string, they are slanderer than the BHA, and the gap between the structure and the soil is three times bigger than that of the BHA, what suggests that their dynamics could play an important role in understanding the underlying phenomena behind drill-string vibrations.

To begin with, a broad survey of the drill-string vibration modelling literature is presented in [7]. The state-of-the-art of the models used to predict axial, torsional and bending vibrations (uncoupled and coupled), boundary condition assumptions, model formulation, and applications to vibration mitigation are reviewed. Also, modern techniques, such as deviated drilling, are discussed.

Within the universe of models for drill-strings found in the literature, lumped models are amongst the simplest approaches, and they usually require less computational effort to obtain numerical approximations than that needed by continuous formulations. This is why they tend to be used in applications

such as control, where real-time integration of the equations is required.

Among the articles concerning low-dimensional lumped formulations, reference [8] reports a study on the dynamics of actively controlled drill-strings, making use of a lumped parameter representation which considers coupling of torsional and bending vibrations. The stick-slip oscillations problem is addressed. A similar strategy is employed in [9], taking into account the fact that the drill-string length increases as the drilling operation progresses. Reference [10] uses a 2-DOF model (one axial and one torsional) for the design of a linear quadratic regulator to control torsional vibrations. This model is also used in [11] to study the dynamic response of drill-strings and to define where critical unwanted behaviour of the system occurs, focusing on the stick-slip and bit-bounce phenomena. A lumped parameter formulation is also used in [12] to tackle the torsional vibrations and instabilities of a drill-string including a nonlinear velocity-dependent friction torque representing the bit-rock interaction. Recently, this discrete approach was employed to study the axial motion of a drill-string in a curved borehole in [13].

The aforementioned studies present the common feature that contact and friction at the bit are modelled following a velocity-dependent relation. These velocity-dependent models try to mathematically capture a phenomenon called velocity weakening, which is a behaviour characterised by a torque that decreases when the rotation speed increases. To do this, they state a direct relation between the velocity and the torques involved. The outcome of such models is that, for their consistency, they imply the existence of velocity-dependent rock properties. On top of that, some authors pointed out these rate-dependent properties as the cause for the torsional oscillatory phenomena and the stick-slip observed in field measurements, while others like [14], discuss the nature of this weakening effect as being a consequence of the dynamics of the cutting rather than the cause, a path that provides an entirely different path towards the genesis of stick-slip vibrations. Among other publications that consider low-dimensional models with this different strategy towards the bit-rock interaction formulation, [14] presents a 2-DOF model to study the cause of drill-string stick-slip vibrations considering a theoretical blunt polycrystalline diamond compact (PDC) cutter; [15] employs a lumped parameter axial-torsional model combined with the Galerkin projection method developed by [16] to avoid dealing with differential-delay equations (DDEs); [17] assesses the linear stability and non-linear dynamics of drill-strings with non-uniformly distributed blades by using a 2-DOF model with a delay in the equations to take into account the cutting of the rock; [18] takes a 6-DOF approach (where 2-DOF are associated to the torsional behaviour) to study the non-

linear dynamics of a drill-string in a horizontal well that has a drill-pipe length of 1000 m, and a bottom hole assembly length of 200 m; lastly, in [19] a 2-DOF approach is used to construct a stability map, extending the bit-rock interaction model of [14] to account for a realistic cutter layout. In these studies, instead of taking a velocity-dependent relation that includes a velocity-weakening effect, a velocity-independent interaction law that accounts for the dynamics of the cutting is used. This choice is justified by studies concerning controlled single-cutter experiments, where weakening effects were not observed, suggesting that the weakening properties of the rock are actually unrealistic. Additionally, to construct and calibrate the rate-dependent models, data measurements from stick-slip cycles is required, rendering the velocity-dependent formulations a non-predictive approach. In contrast, the advantage of the velocity-independent formulation is that it is predictive and it does not require well measurements to construct the model.

In addition to the previous observations, another common feature is found among all the previously lumped low-dimensional models: most of them assume that 1-DOF or 2-DOF are sufficient to accurately predict the torsional dynamics of a column that is of at least some hundred meters long. The drawback of these models is that, given the low number of DOF, they are limited in the amount of information that can be captured. In other words, the vibration modes that can be excited are restricted by the arbitrary selection of the number of DOF.

Continuous models do not suffer from the same limitations as discrete models, but computing an approximation requires more computational effort in terms of time, memory and space occupied. Some research based on continuous models includes [20–23], where a bar and a shaft formulation are used to simulate the dynamics of a drill-string; [24] employs a similar bar-shaft representation to build stability maps; [25] constructs a geometrically non-linear drill-string model based on the Bernoulli-Euler hypotheses, capable of simulating the axial, torsional and flexural dynamics. In [26], a distributed axial-torsional approach is utilised. The authors show “how multiple axial modes are excited or attenuated, depending on the bit rotation rate” and suggest that “a lumped drill-string approximation is insufficient for the general case”, with regard to the behaviour observed in the axial dynamics.

The more complex case of directional arbitrary configurations of boreholes is a recent subject of interest. A review article dealing with directional wells and other special trajectory drilling technologies can be found in [27], where two evaluation methods, theoretical and through measurement, are compared systematically. Typical vibration measurement tools are discussed. The

control technologies to improve the rate of penetration, control the borehole trajectory, find the source of seismic while drilling and reduce the friction with the drill-string, are also treated.

Among the research dealing with arbitrary boreholes, reference [28] addresses a horizontal configuration considering axial displacements only. References [29, 30] deal with a three-region borehole geometry (vertical, curved and inclined, although a vertical shaft model is assumed). The Coulomb friction is added as a distributed source term to analyse the effect of the borehole inclination on the torsional vibrations along the drill-string. [31] analyses the dynamics of a drill-string with elastic wall contact in an arbitrary geometry 3-D well with a beam theory. The contact interaction between the drill-string and the wall is introduced through a set of elastic stops and then, the nonlinear dynamics is analysed with finite elements of six degrees of freedom (three translations and three rotations). The behaviour of a drill-string is analysed in [32] by presenting an example of a flexible shaft that rotates inside of a rigid tube which is assumed to be an arbitrary space curve. In this case, the shaft is considered a nonlinear elastic Cosserat rod. By hypothesis, the position vectors of the non-straight tube and the rod are taken as equals. No friction is considered, nor stretching or shear effects. The boundary value problem for the quasi-static rotation is reduced to nonlinear ordinary differential equations which are solved using the shooting method. The rotation behaviour, the resultant forces and torques in the rod, as well as the contact reaction of the inner surface of the tube, are determined and the differences between the static and dynamic solutions are shown. Lastly, [6] uses a Cosserat rod approach based on the modified Cosserat rod element (MCRE) of [33], but the model is not exploited by analysing curved borehole configurations.

Due to the diversity of treatments mentioned so far, it is unclear how well all these models, some lumped, some continuous, perform at representing drill-strings in a more general case, for example, where curved boreholes are considered or when the dynamics couple with other phenomena such as helical buckling. In addition, many of the models are not comprehensive. They may disregard the dynamics in some of the directions, consider continuous contact with the soil, or assume that the shape of the drill-string coincides exactly with that of the borehole, among other simplifications. On top of that, it has been discussed so far that low-dimensional models could be insufficient to capture all the aspects of the dynamics of drill-string in certain scenarios.

To overcome the aforementioned limitations, the thesis of [6] aimed at developing a comprehensive model to study the dynamics of a drill-string with various complexities, by using a Cosserat rod approach. The thesis

was developed in collaboration with researchers from the Centre for Applied Dynamics Research at the University of Aberdeen. In the study, attention was paid to the modelling of the drill-pipes section. The implementation of the Cosserat rod in [6] is based on the Modified Cosserat Rod Element (MCRE) approach described by [33, 34]. Nevertheless, it is indicated in [35], another researcher from the same group at Aberdeen, that the approach presented in [6, 33, 34], based on the MCRE, is unsuitable for modelling systems that involve large displacements. It is important to point out that this observation is only valid for the particular implementation of the Cosserat rod through MCRE, which is not a general conclusion applicable to the theory of Cosserat rods itself nor to other different implementations. For this reason, [35] introduces a model based on the 3D elasticity theory. After that, to the knowledge of the author of this thesis, the authors of [6, 35] and their group have not continued the line of research considering a Cosserat formulation, leaving the same niche that motivated [6] and the present thesis yet to be explored.

In the present thesis, it will be shown that the complexity of borehole configurations and of the drill-string dynamics can be handled by a rod theory such as the Cosserat rod approach. The Cosserat theory of rods analyses the dynamics of a deformable directed curve that has an associated moving frame attached at each point of that curve. The frame, composed of a set of three directors, is used to define section orientation. This 1-D theory of rods was originally formulated by the Cosserat brothers [36]. A detailed and systematical description of the formulation can be found in classical texts such as [37, 38], and it is revisited in this thesis in a complete and accessible way. It will also be shown that the theory can appropriately handle the dynamics of a drill-string under large displacements in a 3-D well geometry.

In brief, there are many complexities related to the geometry, dynamics, contact, the regimes in which drill-strings operate, and there exist many ways to construct physical models for drill-strings. The research herein conducted is aimed at justifying that the Cosserat rod approach, altogether with suitable contact and friction models, can successfully deal with axial, lateral and torsional dynamics in the most general condition, which is under large displacements and rotations, and where different phenomena may couple. Also, it will be shown that through the use of a continuous Cosserat rod formulation, aspects of the dynamics that are not detected in lumped low-dimensional models can be captured. These aspects can completely change the general behaviour of the predictions obtained. Thus, they justify the development of such continuous approaches, like the one presented herein based on the Cosserat rod

formulation.

1.1

Aims

The main objective of the thesis is to study the dynamics involved in the drilling process of oil wells in curved well geometries, that is, not only restricted to the cases of vertical, inclined or horizontal configurations. To achieve this goal, the following main items are considered:

- The development of a deterministic computational model for the dynamics of a drill-string based on the theory of Cosserat rods;
- The development of a formulation that accounts for contact and friction along the length of the string;
- The use of a bit-rock interaction formulation that can also account for the free boundary problem. That is, for the moving boundary condition due to the change in the profile of the soil.
- The improvement and adaptation of a contact and friction relation at the bit that depends on the dynamics of the cutting. For this task, an alternative formulation based on the advection equation is used. This way, the introduction of delays in the differential equations is avoided;
- The development of strategies to validate and compare the results presented in this thesis with those obtained with other models found in the literature, where possible.

1.2

Outline and contributions

A quick literature review on the subject of drill-string modelling is provided in Chapter 1. The aims of the thesis along with its outline and the main contributions of each chapter are stated.

Chapter 2 includes a definition of the Cosserat rod formulation that will be used for the main model of this thesis. The required kinematic hypotheses, the equations of motion and the constitutive relations are stated. Moreover, the chapter includes contributions in the field of the constitutive relations, where a methodology to derive the equations from known 3-D constitutives is presented. This methodology has been developed in the context of piezoelectric materials in [39], a congress publication made by the author of the present thesis, and it was adapted for the present use.

A brief analysis of the sources of non-linearities in the context of Cosserat rods is given in Chapter 3, along with a simple application example.

Chapter 4 studies the dynamics of an off-bottom drill-string, that is, without contact at the bit, with a Cosserat rod model. The contents of this chapter have been published in [40]. The drill-string moves within a curved well. The main contributions include the implementation of the Cosserat model to account for the dynamics in an arbitrary borehole; the inclusion of an algorithm to detect when and where contact and friction occur, as well as the magnitudes of the forces involved; the calibration of the a priori unknown friction parameters with the results of [30]; the verification of the present results with those of [30], being the latter validated against field measurements. On top of that, some interesting results are included in Appendix B, where a set of benchmarks for the current implementation of the Cosserat model are presented. These benchmarks and other examples yielded excellent agreement with known solutions.

Chapter 5 extends the cutting model of [14] to account for other operation regimes. On top of that, it also extends the use of an advection approach to avoid introducing delays in the differential equation, a step that is necessary to calculate the depth-of-cut used in the bit-rock interaction relations. For the structural model, a continuous shaft representation, formulated as a classical wave equation, is employed. The major contributions of this chapter are: the use of a new bit-rock interaction relation that does not restrict backward rotation of the bit nor bit-bounce, and that is dependent on the dynamics of the cutting blade, such as the depth-of-cut; the use of an advection equation to avoid dealing with a system of delay-differential equations in the simulation of the cutting process; the extension of the advection approach treated in the previous works of [15, 68] to allow rotation in both directions; the combination of the previous items with a distributed approach for the torsional dynamics, with a formulation based on the known wave equation; the inclusion of the 2-DOF model as a limiting case of the continuous model; and the findings of this study that support the hypothesis that lumped low-dimensional models could be unable to capture all the aspects of the dynamics of a drill-string.

In Chapter 6 the work of the previous chapter is continued. This time, a Cosserat rod model with internal damping is used. For this task, a Kelvin-Voigt material is considered. The results are compared with those of the previous chapter. The objective is to evaluate the differences in the response, both in the time and the frequency domain, with other lumped or semi-continuous models. The major contributions of this chapter are associated with the combination of the use of a Cosserat rod model; the addition of internal damping through the use of a Kelvin-Voigt constitutive; the inclusion of the 2-DOF model of the previous chapter as a limiting case of the new

Cosserat model, following a similar strategy to that of the previous chapter; a comparison between the three models, the 2-DOF, the semi-continuous and the Cosserat approach, where possible, for one of the scenarios included in the previous chapter, showing that a low dimensional model cannot capture all the aspects of the dynamics reproduced by this continuous approach. The results obtained reassure the findings of the previous chapter, showing that a lumped low-dimensional representation is actually insufficient to address the study of the dynamics of a drill-string.

Chapter 7 briefly introduces another important aspect that has not been yet dealt with in this thesis: the consideration of the uncertainties present in some of the parameters involved. Particularly, those associated with the soil, which is an intrinsically non-homogeneous and variable material. Therefore, an application example related to this topic is presented. The problem of drill-string dynamics is tackled from a stochastic perspective by revisiting [28]. A Cosserat rod model is used, focusing on the axial and flexural dynamics of the system, and taking the friction as a stochastic field.

Finally, in Chapter 8 general conclusions for the studies that were conducted in this thesis are stated, along with ideas for improvement and future research.

In many scientific disciplines including civil, mechanical engineering, physics, biology and computer animation, very slender structures are common. They can be present as structural elements in the form of columns, beams, shafts and cables [21, 41–48]; in computer games where rods, hair or nets need to be simulated [49]; in medical applications, such as DNA strand modelling [50] and in medical tools colonoscopes [51], just to name a few of their many applications. The modelling of such structures can be performed by employing different theories, each with its own advantages and limitations.

Historically, dimensionally reduced theories were available before a three-dimensional framework was fully developed. For example, the Bernoulli-Euler beam theory dates from the 18th century. Since then, other refined approaches, like the Timoshenko-Ehrenfest and Levinson beam theories [52], have emerged to extend the limits of the validity of the classical beam theory and improve their results.

It was not until the late 1940s that great modern mechaniscian such as Noll, Truesdell and Coleman presented an ordered and rigorous formal structure of the theoretical work developed by physicists of the 19th century like Piola, Cauchy, Kirchoff, among others, providing rational context to continuum mechanics, which is understood as the rigorous mathematical framework to treat problems involving large deformation of 3D bodies.

Whereas the theory of continuum mechanics provides a formal way of treating the dynamics of 3D bodies, in many cases, the associated computational cost may justify the use of a simpler dimensionally reduced approach. This is the case of very slender structures, like the drill-strings which are the object of study of this thesis.

In this chapter, the equations associated with the Cosserat theory for rods will be stated. The Cosserat rod theory is based on a one-dimensional representation of a 3D body by means of a special mathematical structure composed of a characteristic curve and a field of directors used to define the orientation of the cross-sections. The derivation procedure is based, in part, on the texts of [37] and [38]. The theory that will be developed can deal with large displacements and rotations of the rod's characteristic curve and cross-sections,

with the condition that strain measures remain small.

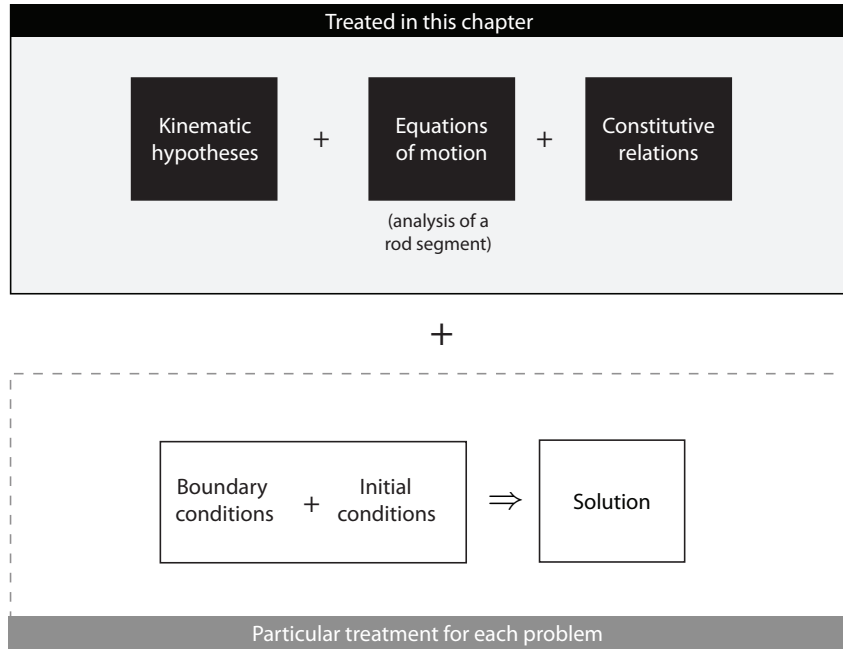


Figure 2.1: Flowchart for the derivation of the Cosserat rod theory.

A scheme representing the derivation procedure to obtain the equations of the theory of Cosserat rods is shown in Fig. 2.1, involving three steps that are treated in detail in the subsequent sections. First, the kinematic hypotheses are stated in Section 2.1. The position field is described in terms of the kinematic hypotheses and an expression for the velocity and acceleration field is deduced. Second, in Section 2.2, a rod segment is analysed and the equations of motions are obtained. Third, in Section 2.3, the constitutive relations are defined to give meaning to the internal efforts that appear in the equations of motion, by linking them with the kinematic hypotheses. All these, together with some boundary and initial conditions, fully define any mechanical problem to be treated by means of the Cosserat rod approach.

Some of the contributions of this chapter include: 1) the combination of the Cosserat rod approach with a quaternion representation for the rotations; 2) the use of the proposal of [53] to avoid enforcing the quaternion unit-constraint, and thus avoiding a differential-algebraic set of equations; 3) the description of a procedure to derive the constitutive relations used in this thesis from a known 3-D constitutive.

2.1

The kinematic hypotheses

The kinematic hypotheses, or kinematic assumptions, are the set of conditions that describe the allowed movement of a body in space. They are introduced to simplify the problem, by reducing the number of variables that need to be evaluated, or by reducing the problem's dimension. In the present context, they will be utilised to study the dynamics of a general slender 3-D body by means of a 1-D formulation, known as the theory of Cosserat rods.

A Cosserat rod is a mathematical representation of a slender body where a special mathematical structure is used. This structure is composed of a curve, \mathcal{L} , and a set of local axes that change along \mathcal{L} , namely \mathbf{d}_i . These two elements are used to define the current position of any point of a body in space.

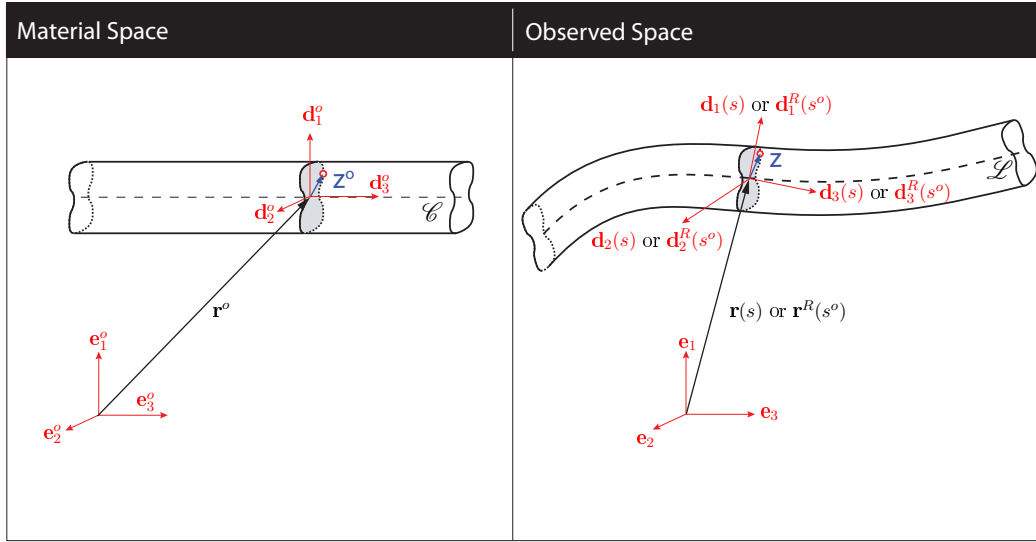


Figure 2.2: Description of the body configuration in the material and observed space.

Alike the theory of continuum mechanics, two vector spaces are used to describe the motion. This is illustrated in Fig 2.2. One of them is called the “material space” or “reference space”, where the reference configuration lives. The other is the “observed space”, where the current (deformed) body exists. In the reference space, the reference configuration is also described by means of a characteristic curve \mathcal{C} and a set of local axis \mathbf{d}_i^o that change along \mathcal{C} . Moreover, the set of points that lie in the perpendicular plane to the tangent of \mathcal{C} define a cross-section, such as the one painted in grey in the figure.

The Cosserat theory of rods is based on the hypotheses that cross-sections remain plane during the deformation, and that cross-sections behave as rigid

bodies. However, in this thesis, the hypothesis that cross-sections behave as rigid bodies will not be adopted everywhere. For example, it will be relaxed when dealing with constitutive relations to avoid some incongruities that would otherwise appear. More information about this topic will be given in Chapter 2.3, and can also be found in [39].

By construction, a set of local axes fixed to the plane of the cross-section will be considered, allowing to capture section orientation in space. These local axes also receive the name of directors. In this way, the position of any 3-D body is fully defined by stating the position of the points that belong to the curve \mathcal{C} , and the orientation of the cross-sections.

Let \mathcal{B} be the reference configuration of a body in the material space, and let \mathbf{e}_i^o define a base for such space. The points the body occupies in the reference space are called material points, \mathbf{x}^o .

In continuum mechanics, a motion of \mathcal{B} is a smooth function χ that assigns a point in the observed space to each material point at a given time. That is, the current configuration is described by a mapping $\mathbf{x} = \chi(\mathbf{x}^o, t)$ from the reference space to the observed space.

Let \mathcal{B} be the reference configuration of a body in the material space, and let \mathbf{e}_i^o define a base for such space. Also, consider a straight reference configuration such that $\mathbf{d}_i^o = \mathbf{e}_i^o$. The points the body occupies in the reference space are called material points, and they can be mathematically expressed as

$$\mathbf{x}^o = \mathbf{r}^o(s^o) + \mathbf{z}^o = \zeta_1^o \mathbf{e}_1^o + \zeta_2^o \mathbf{e}_2^o + s^o \mathbf{e}_3^o, \text{ with } \mathbf{z}^o = \zeta_1^o \mathbf{e}_1^o + \zeta_2^o \mathbf{e}_2^o. \quad (2-1)$$

This expression shows that the reference configuration is described in terms of the position of the points that belong to the parametric curve $\mathcal{C}(s^o)$, given by \mathbf{r}^o , and a vector field \mathbf{z}^o that lies in the cross-section associated at each s^o of \mathcal{C} .

Considering the kinematics of Cosserat rods, the mapping representing the current configuration is

$$\mathbf{x} = \mathbf{r}(s) + \mathbf{z}(s), \quad (2-2)$$

where $\mathbf{r}(s)$ defines the position of the curve \mathcal{L} and \mathbf{z} is a vector field that portrays the distribution of points around in the cross-section at s of \mathcal{L} . The parameter s represents the current arc length of the rod.

The position can also be described in terms of material components as

$$\mathbf{x}^R = \mathbf{r}^R(s^o) + \mathbf{Q}^R(s^o) \mathbf{G}^{RR}(\zeta_1^o, \zeta_2^o, s^o) \mathbf{z}^o, \quad (2-3)$$

with

$$\mathbf{G}^{RR}(\zeta_1^o, \zeta_2^o, s^o) = \begin{bmatrix} 1 + \gamma_1(\zeta_1^o, \zeta_2^o, s^o) & 0 & 0 \\ 0 & 1 + \gamma_2(\zeta_1^o, \zeta_2^o, s^o) & 0 \\ 0 & 0 & 1 \end{bmatrix}, \quad (2-4)$$

where \mathbf{r}^R is the current position of the material point s^o of \mathcal{L} , \mathbf{Q}^R is a rotation matrix associated with the directors of the moving frame, thus also to section orientation, and \mathbf{z}^o is a field that describes the set of points that lie within the cross-sections at s^o . Note that, consistently with the notation introduced, \mathbf{x} and \mathbf{x}^R represent the same fields, although different parametrisations are adopted.

In the previous expression, a tensor \mathbf{G}^{RR} was added to account for possible in-plane deformations. This is not part of the classical treatment of the theory of Cosserat rods and it will be used only to derive the constitutive relations in Chapter 2.3. Nevertheless, in the classical approach to the theory of Cosserat rods, it is assumed that cross-sections behave as rigid bodies. Then, $\mathbf{G}^{RR} = \mathbf{1}$, where $\mathbf{1}$ is an identity matrix, leading to

$$\mathbf{x}^R = \mathbf{r}^R + \mathbf{Q}^R \mathbf{z}^o. \quad (2-5)$$

2.1.1

The deformation tensor

In a classical book for continuum mechanics, such as [54], the deformation gradient is defined as

$$\mathbf{F} = \frac{\partial \mathbf{x}}{\partial \mathbf{x}^o} = \frac{\partial \chi_i}{\partial \mathbf{x}_j^o}. \quad (2-6)$$

In the present context, given the choice of (2-1) for the current configuration, it is true that this tensor can be obtained in terms of the parametrisation variables $\mathbf{S} = (\zeta_1, \zeta_2, s^o)$ as

$$\mathbf{F} = \frac{\partial \mathbf{x}}{\partial \mathbf{x}^o} = \frac{\partial x_i}{\partial \mathbf{S}_j^o}. \quad (2-7)$$

2.1.2

The velocity field

An expression for the velocity field is obtained by calculating the time derivative of (2-5)

$$\dot{\mathbf{x}}^R = \dot{\mathbf{r}}^R + \dot{\mathbf{Q}}^R \mathbf{z}^o, \quad (2-8)$$

and, given the rigid behaviour of the sections, with the aid of $\mathbf{z} = \mathbf{Q}^R \mathbf{z}^o$, it is true that

$$\dot{\mathbf{x}}^R = \dot{\mathbf{r}}^R + \dot{\mathbf{Q}}^R (\mathbf{Q}^R)^T \mathbf{z}. \quad (2-9)$$

The product $\dot{\mathbf{Q}}^R (\mathbf{Q}^R)^T$ is a skew-symmetric matrix. Therefore it admits a representation in terms of an axial vector $\boldsymbol{\omega}(s)$ that belongs to the observed space, or equivalently $\boldsymbol{\omega}^R(s^o)$ if the reference arc-length is used for the parametrisation. Thus, the angular velocity in the observed space reads

$$\dot{\mathbf{x}}^R = \dot{\mathbf{r}}^R + \boldsymbol{\omega}^R \times \mathbf{z}^R \text{ or } \dot{\mathbf{x}} = \dot{\mathbf{r}} + \boldsymbol{\omega} \times \mathbf{z} \quad (2-10)$$

2.1.3

The angular velocity in terms of quaternion components

It can be demonstrated that only a minimum of three independent quantities are needed to specify the orientation of a rigid body. Unfortunately, any three-parameter representation in the special orthogonal group $SO(3)$, such as an Euler angle rotation sequence, has at least one singularity [55]. Moreover, it is mentioned in [56] that “the Euler angles are difficult to use in numerical computation because of the large number of trigonometric functions involved, and the four-parameter representations are much better adapted for use on computers”. For these reasons, there are occasions where it is desired to use a set of variables that contain more than just the minimum number of quantities to describe a rotation. In this work, to overcome these limitations, section orientation and angular velocities will be stated in terms of quaternion components. This mathematical tool was originally developed by Hamilton in an attempt to extend complex numbers to higher spatial dimensions [57].

Let $\mathbf{u}_q, \mathbf{v}_q$ be pure imaginary unit quaternions, and let \mathbf{q} be another unit quaternion with components $\mathbf{q} = \{q_a, q_b, q_c, q_d\}$ that satisfy the following definitions:

$$\mathbf{u}_q = u_x \mathbf{e}_1 + u_y \mathbf{e}_2 + u_z \mathbf{e}_3, \quad (2-11)$$

$$\mathbf{v}_q = v_x \mathbf{e}_1 + v_y \mathbf{e}_2 + v_z \mathbf{e}_3, \quad (2-12)$$

$$\mathbf{i} = \begin{bmatrix} 0 & -1 \\ 1 & 0 \end{bmatrix}, \mathbf{j} = \begin{bmatrix} 0 & -i \\ -i & 0 \end{bmatrix}, \mathbf{k} = \begin{bmatrix} i & 0 \\ 0 & -i \end{bmatrix}, \quad (2-13)$$

$$\mathbf{q} = \cos\left(\frac{\theta}{2}\right) + \mathbf{u}_q \sin\left(\frac{\theta}{2}\right) \quad (2-14)$$

$$= q_a + q_b \mathbf{i} + q_c \mathbf{j} + q_d \mathbf{k}.$$

The transformation $L_q(\mathbf{v}_q)$ rotates \mathbf{v}_q in a counter-clockwise angle θ over the axis defined by \mathbf{u}_q , in accordance with

$$L_q(\mathbf{v}_q) = \mathbf{q}\mathbf{v}_q\bar{\mathbf{q}}. \quad (2-15)$$

Moreover, this can be written in matrix form as

$$L_q(\mathbf{v}_q) = \mathbf{Q}\mathbf{v}_q, \quad (2-16)$$

with

$$L_q(v) = \begin{bmatrix} d_{1x} & d_{2x} & d_{3x} \\ d_{1y} & d_{2y} & d_{3y} \\ d_{1z} & d_{2z} & d_{3z} \end{bmatrix} \begin{pmatrix} v_{qx} \\ v_{qy} \\ v_{qz} \end{pmatrix}. \quad (2-17)$$

Then, if the reference configuration is chosen so that the directors \mathbf{d}_i^o coincide with \mathbf{e}_i , the following relations hold.

$$L_q(\mathbf{v}_q) = \begin{bmatrix} q_a^2 + q_b^2 - q_c^2 - q_d^2 & 2(q_b q_c - q_a q_d) & 2(q_a q_c + q_b q_d) \\ 2(q_a q_d + q_b q_c) & q_a^2 - q_b^2 + q_c^2 - q_d^2 & 2(q_c q_d - q_a q_b) \\ 2(q_b q_d - q_a q_c) & 2(q_a q_b + q_c q_d) & q_a^2 - q_b^2 - q_c^2 + q_d^2 \end{bmatrix} \begin{pmatrix} v_{qx} \\ v_{qy} \\ v_{qz} \end{pmatrix} \quad (2-18)$$

$$q_a^2 + q_b^2 + q_c^2 + q_d^2 = 1. \quad (2-19)$$

A definition of the directors in the current configuration is given in terms of quaternion components in (2-18). Those components need to fulfil the relation (2-19), which imposes a constraint that guarantees that the quaternion is unitary.

As already stated, an expression to determine the angular velocity $\boldsymbol{\omega}$ is required to fully determine its relation with the quaternion representation adopted for the rotations. This can be done by proposing an equation of the form of the Frenet-Serret formulas, as

$$\frac{\partial \mathbf{d}_i}{\partial t} = \boldsymbol{\omega} \times \mathbf{d}_i. \quad (2-20)$$

In (2-20), $\boldsymbol{\omega}$ is a Darboux vector that describes a change in the orientation of the directors. An explicit form of vector $\boldsymbol{\omega}$ is obtained below

$$\begin{aligned} \mathbf{d}_i \times \frac{\partial \mathbf{d}_i}{\partial t} &= \mathbf{d}_i \times (\boldsymbol{\omega} \times \mathbf{d}_i) \\ &= \boldsymbol{\omega}(\mathbf{d}_i \cdot \mathbf{d}_i) - \mathbf{d}_i(\mathbf{d}_i \cdot \boldsymbol{\omega}) \\ &= \boldsymbol{\omega} - \omega_i \mathbf{d}_i \end{aligned} \quad (2-21)$$

$$\begin{aligned} \sum_{i=1}^3 \mathbf{d}_i \times \frac{\partial \mathbf{d}_i}{\partial t} &= 3\boldsymbol{\omega} - \sum_{i=1}^3 \omega_i \mathbf{d}_i \\ &= 2\boldsymbol{\omega} \end{aligned} \quad (2-22)$$

$$\boldsymbol{\omega} = \frac{1}{2} \sum_{i=1}^3 \mathbf{d}_i \times \frac{\partial \mathbf{d}_i}{\partial t} \quad (2-23)$$

if expressed in terms of the arc-length s , and analogously, in terms of s^o it reads

$$\boldsymbol{\omega}^R = \frac{1}{2} \sum_{i=1}^3 \mathbf{d}_i^R \times \frac{\partial \mathbf{d}_i^R}{\partial t}. \quad (2-24)$$

Then, the vector components of (2-23), expressed in the observed space, can be written in its material form as

$$\boldsymbol{\omega}^{RR} = (\mathbf{Q}^R)^T \boldsymbol{\omega}^R. \quad (2-25)$$

The equation (2-25) together with (2-19) can be used to formulate the Cosserat rod problem, but it would require considering a differential-algebraic set of equations. Instead, an alternative approach is given in [53], where a formulation that does not need the enforcement of the unity constraint is used. The authors of [53] propose to use the equation

$$\dot{\mathbf{q}} = \frac{1}{2} \boldsymbol{\Omega} \mathbf{q} + c \mathbf{q}_m \quad (2-26)$$

with

$$\boldsymbol{\Omega} = \begin{bmatrix} 0 & -\omega_1 & -\omega_2 & -\omega_3 \\ \omega_1 & 0 & \omega_3 & -\omega_2 \\ \omega_2 & -\omega_3 & 0 & \omega_1 \\ \omega_3 & \omega_2 & -\omega_1 & 0 \end{bmatrix} \quad (2-27)$$

to update the quaternions from a minimum set of angular velocities, which in the present context also means keeping track of section orientation. In the previous expressions, $c \mathbf{q}_m$ is a correction factor so that $\|\mathbf{q}\| \neq 0$. In fact, this is taken herein as $\mathbf{q}_m = \max_x(\mathbf{q})$, recalling that $\mathbf{q} = \mathbf{q}(s, t)$. In this context, \max_x is the spatial maximum at a given fixed time t .

2.1.4

The acceleration field

Now, an expression for the acceleration is sought. To find such equation, the time derivative of (2-10) is calculated. Keeping in mind that

$$\mathbf{z} = \mathbf{Q}^R \mathbf{z}^o, \quad \dot{\mathbf{z}} = \boldsymbol{\omega} \times \mathbf{z}, \quad (2-28)$$

then, the expression in the observed space reads

$$\begin{aligned} \ddot{\mathbf{x}} &= \ddot{\mathbf{r}} + \dot{\boldsymbol{\omega}} \times \mathbf{z} + \boldsymbol{\omega} \times \dot{\mathbf{z}} \\ &= \ddot{\mathbf{r}} + \dot{\boldsymbol{\omega}} \times \mathbf{z} + \boldsymbol{\omega} \times (\boldsymbol{\omega} \times \mathbf{z}), \end{aligned} \quad (2-29)$$

or

$$\ddot{\mathbf{x}}^R = \ddot{\mathbf{r}}^R + \dot{\boldsymbol{\omega}}^R \times \mathbf{z}^R + \boldsymbol{\omega}^R \times (\boldsymbol{\omega}^R \times \mathbf{z}^R), \quad (2-30)$$

using s or s^o as the parametrisation parameter, respectively.

2.2

The equations of motion

With the aim of finding the equations of motion associated with a Cosserat rod, first, an expression for the kinetic energy is obtained. After that, the previous expression is used as a means to calculate the linear and angular momenta.

2.2.1

The kinetic energy

An expression for the kinetic energy of a portion of a rod is sought. The time derivative of this energy gives an expression for the inertial terms in the linear and angular momenta.

Let ρ , ρ^R be the density of the body in its current configuration and in the reference configuration, respectively. Then, their relationship is given by the equation of conservation of mass. Calling $J = \det(F)$, and with the help of $dV = JdV^R$, the conservation reads

$$\int \rho(\mathbf{x}) dV = \int \rho^R(\mathbf{x}^o) dV^R, \quad \text{with } \rho^R = \rho J. \quad (2-31)$$

In the current context, due to the particular choice of the reference configuration that was adopted, $dV^R = d\zeta_1 d\zeta_2 ds^o$. Also, $\mathbf{x}^o = \zeta_1 \mathbf{e}_1^o + \zeta_2 \mathbf{e}_2^o + s^o \mathbf{e}_3^o$. These two expressions allow to solve the volume integrals in the reference space.

Next, the kinetic energy K is written in terms of the kinetic energy density \mathcal{K} as follows

$$K = \int \mathcal{K} dV = \int \frac{1}{2} \rho \dot{\mathbf{x}} \cdot \dot{\mathbf{x}} dV. \quad (2-32)$$

The results from (2-10) are used in the previous equation. Let $\dot{\mathbf{r}} = \dot{\mathbf{r}}(s)$, $\dot{\mathbf{r}}^R = \dot{\mathbf{r}}^R(s^o)$, $\dot{\boldsymbol{\omega}} = \dot{\boldsymbol{\omega}}(s)$, $\dot{\boldsymbol{\omega}}^R = \dot{\boldsymbol{\omega}}^R(s^o)$, then

$$K(s) = \int \frac{1}{2} \rho \left(\dot{\mathbf{r}} \cdot \dot{\mathbf{r}} + 2\dot{\mathbf{r}} \cdot (\boldsymbol{\omega} \times \mathbf{z}) + (\boldsymbol{\omega} \times \mathbf{z}) \cdot (\boldsymbol{\omega} \times \mathbf{z}) \right) dV, \quad (2-33)$$

or in terms of the reference parameter s^o ,

$$K^R(s^o) = \int \frac{1}{2} \left(\dot{\mathbf{r}}^R \cdot \dot{\mathbf{r}}^R + 2\dot{\mathbf{r}}^R \cdot (\boldsymbol{\omega}^R \times \mathbf{z}^R) + (\boldsymbol{\omega}^R \times \mathbf{z}^R) \cdot (\boldsymbol{\omega}^R \times \mathbf{z}^R) \right) \rho^R dV^R. \quad (2-34)$$

The vectors in the previous integrals still belong to the observed space. Therefore, they maintain their original orientation, what makes the integration more difficult. To overcome this, a pullback of the form

$$(\mathbf{Q}^R)^T(\cdot)^R = (\cdot)^{RR} \quad (2-35)$$

can be considered. Also, a specific notation is used for the pullback of \mathbf{z}^R , which reads $(\mathbf{Q}^R)^T \mathbf{z}^R = \mathbf{z}^o$, leading to a vector that is aligned to the plane of integration \mathbf{e}_1^o , \mathbf{e}_2^o , what simplifies the integrals. With these changes, the kinetic energy reads

$$K^R(s^o) = \int \frac{1}{2} \left(\mathbf{Q}^R \dot{\mathbf{r}}^{RR} \cdot \mathbf{Q}^R \dot{\mathbf{r}}^{RR} + 2 \mathbf{Q}^R \dot{\mathbf{r}}^{RR} \cdot (\mathbf{Q}^R \boldsymbol{\omega}^{RR} \times \mathbf{Q}^R \mathbf{z}^o) + \right. \\ \left. (\mathbf{Q}^R \boldsymbol{\omega}^{RR} \times \mathbf{Q}^R \mathbf{z}^o) \cdot (\mathbf{Q}^R \boldsymbol{\omega}^{RR} \times \mathbf{Q}^R \mathbf{z}^o) \right) \rho^R dV^R \quad (2-36)$$

which simplifies to

$$K^R(s^o) = \int \frac{1}{2} \left(\dot{\mathbf{r}}^{RR} \cdot \dot{\mathbf{r}}^{RR} + 2 \dot{\mathbf{r}}^{RR} \cdot (\boldsymbol{\omega}^{RR} \times \mathbf{z}^o) + \right. \\ \left. (\boldsymbol{\omega}^{RR} \times \mathbf{z}^o) \cdot (\boldsymbol{\omega}^{RR} \times \mathbf{z}^o) \right) \rho^R dV^R \quad (2-37)$$

Now, remembering that the assumption that sections behave as rigid bodies is commonly employed in the derivation of the Cosserat rod theory, the kinetic energy K in terms of the kinetic density per unit length κ reads

$$K^R(s^o) = \int \kappa^R(s^o) ds^o, \quad (2-38)$$

with

$$\kappa^R(s^o) = \frac{1}{2} \rho^R A^o \dot{\mathbf{r}}^{RR} \cdot \dot{\mathbf{r}}^{RR} + \dot{\mathbf{r}}^{RR} \cdot \int \rho^R (-\mathbf{z}^o \times \boldsymbol{\omega}^{RR}) d\zeta_1 d\zeta_2 + \\ \frac{1}{2} \int \rho^R (\boldsymbol{\omega}^{RR} \times \mathbf{z}^o) \cdot (\boldsymbol{\omega}^{RR} \times \mathbf{z}^o) d\zeta_1 d\zeta_2. \quad (2-39)$$

In a more compact form, the previous expression can be written as

$$\kappa^R(s^o) = \frac{1}{2} \rho^R A^o (\dot{\mathbf{r}}^{RR})^2 + \dot{\mathbf{r}}^{RR} \cdot \boldsymbol{\Theta}_1^{RR} \boldsymbol{\omega}^{RR} + \frac{1}{2} \boldsymbol{\omega}^{RR} \cdot \boldsymbol{\Theta}_2^{RR} \boldsymbol{\omega}^{RR}, \quad (2-40)$$

all expressed in terms of pullback quantities, with

$$\boldsymbol{\Theta}_1^{RR} = \int \rho^R (-\mathbf{z}^o \times) d\zeta_1 d\zeta_2 \quad (2-41)$$

which contains the first moment of mass of the cross-section, and

$$\boldsymbol{\Theta}_2^{RR} = \int \rho^R (\mathbf{z}^o \cdot \mathbf{z}^o) \mathbf{I} - \rho^o (\mathbf{z}^o \otimes \mathbf{z}^o) d\zeta_1 d\zeta_2 \quad (2-42)$$

which is a tensor that contains the second moments of mass of the cross-section.

The formulation can be further simplified if \mathcal{C} passes through the centre of mass at each cross-section and if principal axes of inertia are used. This way Θ_1^{RR} vanishes and Θ_2^{RR} becomes diagonal.

Equivalently, through the transformation (2-35), it is possible to rewrite the kinetic energy density per unit length in terms of observed quantities as

$$\kappa^R(s^o) = \frac{1}{2}\rho^R A^o (\dot{\mathbf{r}}^R)^2 + \dot{\mathbf{r}}^R \cdot \Theta_1^R \boldsymbol{\omega}^R + \frac{1}{2}\boldsymbol{\omega}^R \cdot \Theta_2^R \boldsymbol{\omega}^R, \quad (2-43)$$

where the relations to transform the previous expressions from the reference space to the observed space, or vice-versa, are given by

$$\Theta_1^R = \mathbf{Q}^R \Theta_1^{RR} (\mathbf{Q}^R)^T \text{ and } \Theta_2^R = \mathbf{Q}^R \Theta_2^{RR} (\mathbf{Q}^R)^T. \quad (2-44)$$

2.2.2

Analysis of a rod segment

To state the equations of motion, namely the linear momentum balance and the angular momentum balance, a rod segment is studied in accordance with Fig. 2.3. As illustrated, applied and distributed forces and torques are considered.

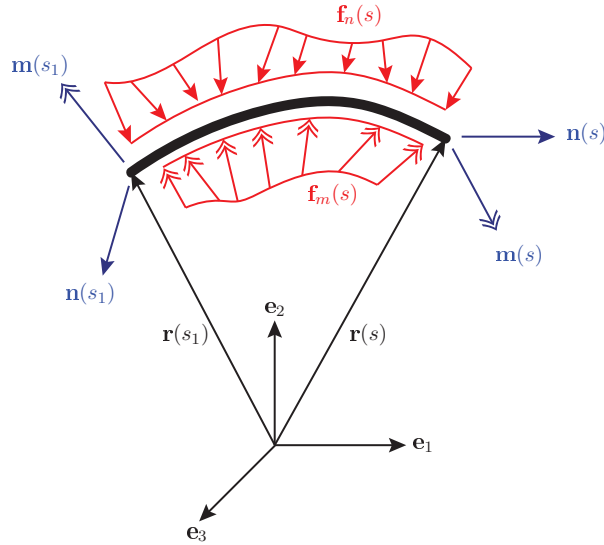


Figure 2.3: Equilibrium of a rod segment. Vectors \mathbf{n} , \mathbf{m} represent applied forces and torques; \mathbf{f}_n , \mathbf{f}_m are distributed forces and torques, respectively.

Hereunder, the following nomenclature will be used: $(\cdot) = (\cdot)(s)$ is any function of s , $(\cdot)^R = (\cdot)^R(s^o)$ is any function of s^o , $(\cdot)' = \frac{\partial(\cdot)}{\partial s^o}$ a derivative in the reference parameter; ρ is the current mass density, ρ^o the reference mass density; E is the elastic Young modulus, G the shear modulus; A , I_{ii} are the cross-sectional area and associated moments of inertia. Finally, \mathbf{n} , \mathbf{m} are applied loads and moments; \mathbf{f}_n , \mathbf{f}_m are distributed forces and torques.

As already stated, the expression for the kinetic energy is given by

$$K(s^o) = \int \kappa(s^o) ds^o, \quad (2-38, \text{ revisited})$$

$$\kappa(s^o) = \frac{1}{2} \rho^R A^R (\dot{\mathbf{r}}^R)^2 + \dot{\mathbf{r}}^R \cdot \boldsymbol{\Theta}_1^R \boldsymbol{\omega}^R + \frac{1}{2} \boldsymbol{\omega}^R \cdot \boldsymbol{\Theta}_2^R \boldsymbol{\omega}^R. \quad (2-40, \text{ revisited})$$

2.2.3

The linear momentum balance

Let $\boldsymbol{\kappa}_1 = \frac{\partial \kappa(s)}{\partial \dot{\mathbf{r}}}$ and $\boldsymbol{\kappa}_1^R = \frac{\partial \kappa(s^o)}{\partial \dot{\mathbf{r}}^R}$. Then, the linear momentum reads

$$\mathbf{p} = \int_{s_1}^s \boldsymbol{\kappa}_1 ds, \quad (2-45)$$

or considering the reference arc length s^o

$$\mathbf{p}^R = \int_{s_1^o}^{s^o} \boldsymbol{\kappa}_1^R ds^o, \quad (2-46)$$

with

$$\boldsymbol{\kappa}_1^R = \rho^R A^R \dot{\mathbf{r}}^R + \boldsymbol{\Theta}_1^R \boldsymbol{\omega}^R. \quad (2-47)$$

The moving coordinate system \mathbf{d}_i^R is chosen so that it passes through the centre of mass at each section. Thus, $\boldsymbol{\Theta}_1^R$ vanishes.

Let $\mathbf{f}_n = \mathbf{f}_n(s)$ and $\mathbf{f}_n^R = \lambda \mathbf{f}_n(s(s^o))$ be distributed forces through the length of the rod, where $\lambda = \frac{ds}{ds^o}$, and $J \approx 1$ is the determinant of the deformation tensor. Considering that $\lambda \approx J \approx 1$, due to the small strain assumption, then

$$\frac{d\mathbf{p}}{dt} = \int_{s_1}^s \mathbf{f}_n ds + \mathbf{n} \Big|_{s_1}^s \quad \text{or} \quad \frac{d\mathbf{p}^R}{dt} = \int_{s_1^o}^{s^o} \mathbf{f}_n^R ds^o + \mathbf{n}^R \Big|_{s_1^o}^{s^o}. \quad (2-48)$$

Employing (2-47), the previous expression reads

$$\frac{d}{dt} \int_{s_1^o}^{s^o} \rho^R A^R \dot{\mathbf{r}}^R ds^o = \int_{s_1^o}^{s^o} \mathbf{f}_n^R ds^o + \mathbf{n}^R \Big|_{s_1^o}^{s^o} \quad (2-49)$$

or

$$\frac{d}{dt} \int_{s_{1R}}^{s_R} \rho^R A^R \dot{\mathbf{r}}^R ds^o = \int_{s_1^o}^{s^o} \mathbf{f}_n^R ds^o + \int_{s_1^o}^{s^o} \frac{d}{ds^o} (\mathbf{n}^R) ds^o \quad (2-50)$$

which, by application of the fundamental lemma of the calculus of variations, leads to the strong form of the linear momentum balance equation:

$$\frac{d}{ds^o} (\mathbf{n}^R) + \mathbf{f}_n^R = \frac{d}{dt} (\rho^R A^R \dot{\mathbf{r}}^R). \quad (2-51)$$

2.2.4

The angular momentum balance

To obtain the second equation of motion, let

$$\boldsymbol{\kappa}_2 = \frac{\partial \kappa(s)}{\partial \boldsymbol{\omega}} = (\boldsymbol{\Theta}_1)^T \dot{\mathbf{r}} + \boldsymbol{\Theta}_2 \boldsymbol{\omega}, \quad (2-52)$$

or

$$\boldsymbol{\kappa}_2^R = \frac{\partial \kappa(s^o)^R}{\partial \boldsymbol{\omega}} = (\boldsymbol{\Theta}_1^R)^T \dot{\mathbf{r}}^R + \boldsymbol{\Theta}_2^R \boldsymbol{\omega}^R, \quad (2-53)$$

where $(\cdot)^T$ denotes a matrix transpose.

The angular momentum, as shown in [38], is given by

$$\mathbf{l} = \int_{s_1}^s \left(\mathbf{r}(s) - \mathbf{r}(s_1) \right) \times \boldsymbol{\kappa}_1 + \boldsymbol{\kappa}_2 \, ds, \quad (2-54)$$

or

$$\mathbf{l}^R = \int_{s_1^o}^{s^o} \left(\mathbf{r}^R(s) - \mathbf{r}^R(s_1^o) \right) \times \boldsymbol{\kappa}_1^R + \boldsymbol{\kappa}_2^R \, ds^o. \quad (2-55)$$

As aforementioned, if \mathcal{C} passes through the centre of mass of each cross-section, and if principal axes of inertia are used, then

$$\boldsymbol{\kappa}_1^R = \rho^R A^R \dot{\mathbf{r}}^R, \text{ and } \boldsymbol{\kappa}_2^R = \boldsymbol{\Theta}_2^R \boldsymbol{\omega}^R. \quad (2-56)$$

The equation of motion associated with the angular momentum balance is given, in material coordinates, by

$$\frac{d\mathbf{l}^R}{dt} = \left(\mathbf{r}^R(s^o) - \mathbf{r}^R(s_1^o) \right) \times \mathbf{n}^R \Big|_{s_1^o}^{s^o} + \mathbf{m}^R \Big|_{s_1^o}^{s^o} + \int_{s_1^o}^{s^o} \left(\left(\mathbf{r}^R(s^o) - \mathbf{r}^R(s_1^o) \right) \times \mathbf{f}_n^R + \mathbf{f}_m^R \right) ds^o \quad (2-57)$$

$$\begin{aligned} \frac{d\mathbf{l}^R}{dt} &= \int_{s_1^o}^{s^o} \frac{d}{ds^o} \left(\left(\mathbf{r}^R(s^o) - \mathbf{r}^R(s_1^o) \right) \times \mathbf{n}^R \right) ds^o + \int_{s_1^o}^{s^o} \frac{d}{ds^o} (\mathbf{m}^R) ds^o \\ &\quad + \int_{s_1^o}^{s^o} \left(\left(\mathbf{r}^R(s^o) - \mathbf{r}^R(s_1^o) \right) \times \mathbf{f}_n^R + \mathbf{f}_m^R \right) ds^o \end{aligned} \quad (2-58)$$

which, by application of the fundamental lemma of the calculus of variations, gives

$$\begin{aligned} \frac{d}{dt} \left(\left(\mathbf{r}^R(s^o) - \mathbf{r}^R(s_1^o) \right) \times \boldsymbol{\kappa}_1^R + \boldsymbol{\kappa}_2^R \right) &= \\ \left(\mathbf{r}^R(s^o) - \mathbf{r}^R(s_1^o) \right) \times \left(\frac{d}{ds^o} (\mathbf{n}^R) + \mathbf{f}_n^R \right) &+ \frac{d}{ds^o} (\mathbf{r}^R) \times \mathbf{n}^R + \frac{d}{ds^o} (\mathbf{m}^R) + \mathbf{f}_m^R \end{aligned} \quad (2-59)$$

which, rearranging terms, reads as

$$\begin{aligned} \frac{d}{dt} \left(\boldsymbol{\kappa}_2^R \right) &= \left(\mathbf{r}^R(s^o) - \mathbf{r}^R(s_1^o) \right) \times \left(\frac{d}{ds^o} (\mathbf{n}^R) + \mathbf{f}_n^R - \boldsymbol{\kappa}_1^R \right) \\ &\quad + \frac{d}{ds^o} (\mathbf{r}^R) \times \mathbf{n}^R + \frac{d}{ds^o} (\mathbf{m}^R) + \mathbf{f}_m^R. \end{aligned} \quad (2-60)$$

In the previous expression, the first term of the right side includes the linear momentum balance. Therefore, it vanishes. Finally, the angular momentum balance reads

$$\frac{d}{ds^o} (\mathbf{r}^R) \times \mathbf{n}^R + \frac{d}{ds^o} (\mathbf{m}^R) + \mathbf{f}_m^R = \frac{d}{dt} \left(\boldsymbol{\kappa}_2^R \right). \quad (2-61)$$

If principal axes of inertia are considered, and if \mathcal{C} passes through the centre of mass of each cross-section, $\boldsymbol{\kappa}_2^R$ simplifies to

$$\boldsymbol{\kappa}_2^R = \mathbf{Q}^R \boldsymbol{\Theta}_2^{RR} (\mathbf{Q}^R)^T \boldsymbol{\omega}^R, \quad \text{with } \boldsymbol{\Theta}_2^{RR} = \begin{bmatrix} I_{11}^{RR} & 0 & 0 \\ 0 & I_{22}^{RR} & 0 \\ 0 & 0 & I_{33}^{RR} \end{bmatrix}, \quad (2-62)$$

where the vector $\boldsymbol{\omega}^R$ represents the angular velocity vector of the cross-sections.

A comprehensive definition of the Cosserat model requires the selection of a constitutive relation for the material in use. This way, the kinematic variables and their derivatives, which define the strain, are linked to the generalised forces that appear in the equations of motion. In the context of this thesis, the next section is devoted to this matter.

2.3

The constitutive relations

In what follows, a mechanism to state the constitutive relations for a Cosserat rod is provided. In most beam and rod theories, it is common to assume rigid cross-sections. Also, it is frequent to make some hypotheses with regard to the stresses, which eventually are incompatible with the previous rigid assumption, leading to inconsistencies from the point of view of the 3D theory of continuum mechanics.

One of the personal interests of the author of this thesis is to connect 1-D theories that come from an engineering background with the concepts of 3-D continuum mechanics. From this point of view, the consistent derivation of the constitutive relation for a Cosserat rod from a known 3D relation satisfies that personal concern. On top of that, it provides a means to state the constitutive relations for materials that, up to the author's knowledge, have not been used in models with the framework of the theory of Cosserat rods. More specifically, the procedure detailed in this chapter was developed in [39] to obtain the

constitutive relations for piezoelectric materials, with the aim of exploring their use as a tool to dampen structures. Up to the author's knowledge, those results concerning piezoelectrics are novel, although they will not be included in this thesis given that these materials will not be used in the models herein described. Nevertheless, the procedure is included for the sake of completeness with regard to the elements that are required to state a problem with the theory of Cosserat rods.

The constitutive relations of a linear orthotropic elastic material are obtained, with an isotropic material being a particular case. After that, the constitutive relations of a Kelvin-Voigt material are stated, given that they will be used in some of the models of this thesis. The equations for the latter are taken from [58].

2.3.1 Notation

Two different vector spaces will be used to describe the motion of a body. For this reason, a notation to help clarify whether an expression is associated with one or another space will be defined first. Also, some concepts from continuum mechanics will be used without giving much detail of their derivation or proofs, which is why the author suggests reading the book [54] as complementary material to this chapter, in case further insight is needed.

As it is usual in the continuum mechanics framework, two different vector spaces are introduced: the material (lagrangian) space where the reference configuration is defined, and the observed (eulerian) space where the current configuration lives. This was illustrated in Fig. 2.2. The mathematical objects (scalars, fields, tensors) that will help build the desired formulation can belong to any of the spaces, or combine elements of both. Therefore, to differentiate one from another, the following nomenclature is used:

- $(\cdot)^R$ explicitly indicates a mixed object that combines elements from both the observed and material spaces. For example, the traction associated with the first Piola tensor is of this kind: it relates the direction and magnitude of the current traction in relation to a reference area vector.
- $(\cdot)^{RR}$ explicitly indicates a pullback to the material space of an object that is originally defined in the observed space. It represents a pure material object.
- $(\cdot)^o$ is used for a material object (that is not a pullback).

2.3.2

The constitutive relations for a linear elastic material

The derivation process and the steps involved in the derivation of the constitutive laws from a known 3D constitutive are presented in Fig. 2.4. This process can be applied to the theory of Cosserat rods as well as to any other beam theory by considering an appropriate set of kinematic hypotheses.

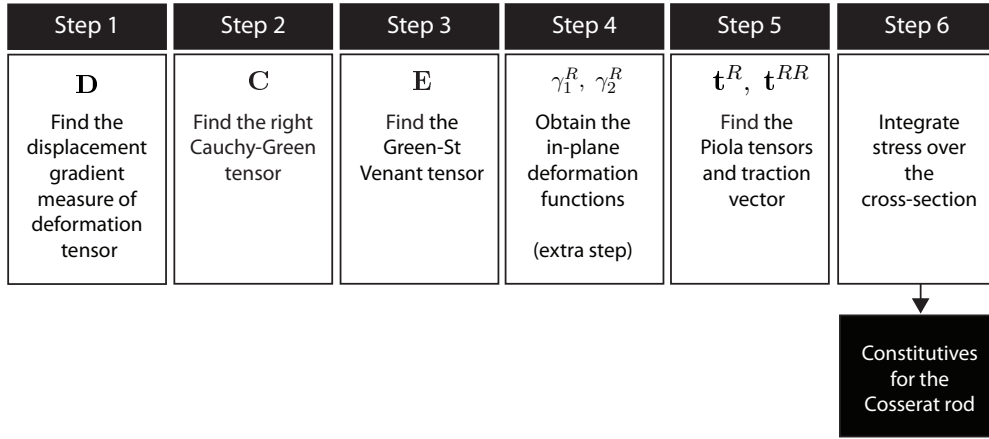


Figure 2.4: Description of the required steps to find a constitutive relation for 1-D rod type theories.

2.3.2.1

Revisiting the kinematic hypotheses

In Section 2.1, the kinematic assumptions for the Cosserat rod were discussed. A general expression describing the motion of the body was given by

$$\mathbf{x}^R = \mathbf{r}^R(s^o) + \mathbf{Q}^R(s^o) \mathbf{G}^{RR}(\zeta_1^o, \zeta_2^o, s^o) \mathbf{z}^o, \quad (2-3, \text{ revisited})$$

with

$$\mathbf{G}^{RR}(\zeta_1^o, \zeta_2^o, s^o) = \begin{bmatrix} 1 + \gamma_1(\zeta_1^o, \zeta_2^o, s^o) & 0 & 0 \\ 0 & 1 + \gamma_2(\zeta_1^o, \zeta_2^o, s^o) & 0 \\ 0 & 0 & 1 \end{bmatrix}. \quad (2-4, \text{ revisited})$$

In the previous equation, a tensor \mathbf{G}^{RR} was added to account for in-plane deformation. On the one hand, it is common to assume that cross-sections do not deform in beam-like theories, and the typical formulation of the theory of Cosserat rods is no exception in this matter. On the other hand, beam formulations also assume that any normal stress perpendicular to the

main direction (the longitudinal axis) is exactly zero. The first assumption is compatible with perfectly compressible materials only, i.e. a Poisson coefficient $\nu = 0$, otherwise one cannot enforce both zero strains and stresses in the non-longitudinal directions. Although typically not much importance is given to this lack of coherence, there are some contexts where it plays an important role. For example, when non-isotropic materials are used, the elasticity constants need to be modified to obtain meaningful physical results, as shown in [39, 59]. For this reason, the introduction of \mathbf{G}^{RR} is essential to obtaining consistent constitutive equations. It will be shown that the resulting mathematical expressions are alike to those of inconsistent formulations considering rigid cross-sections, with an ad-hoc correction where modified elastic coefficients are utilised instead of the original ones.

In continuum mechanics, different measures of stresses can be stated. The most important ones are the Cauchy stress, the First and Second Piola stress tensors, \mathbf{T} , \mathbf{T}^R and \mathbf{T}^{RR} , respectively. The Cauchy stress relates the current tractions with an area in the current (observed) configuration, the First Piola stress links current tractions with an undeformed reference area, and the Second Piola stress relates a pullback traction in the reference space with a reference area. Recalling that the deformation gradient \mathbf{F} and its determinant J , are given by

$$\mathbf{F} = \nabla \mathbf{x}, \quad (\mathbf{F})_{ij} = \frac{\partial \mathbf{x}_i}{\partial \mathbf{x}_j^0}, \quad J = \det(\mathbf{F}), \quad (2-63)$$

and the transformation rules that rely on the previous tensors, read

$$\mathbf{T}^R = \mathbf{F} \mathbf{T}^{RR}, \quad \mathbf{T} = J^{-1} \mathbf{F}^T \mathbf{T}^R. \quad (2-64)$$

A typical constitutive for a linear elastic material is defined in terms of the Second Piola tensor and the Green-St.Venant strain tensor, where the linear part of $\mathbf{C} = \mathbf{F}^T \mathbf{F}$, the right Cauchy-Green tensor, is used to obtain the Green-St.Venant strain tensor, calculated as $\mathbf{E} = \frac{1}{2}(\mathbf{C} - \mathbf{I})$, where \mathbf{I} is the identity matrix.

2.3.2.2

The 3-D Constitutive for a linear elastic orthotropic material

The constitutive law for a linear elastic material can be expressed as

$$\mathbf{T}^{RR} = \mathbb{C} : \mathbf{E}, \quad (2-65)$$

where \mathbb{C} is an elastic fourth-order tensor. Considering the symmetries of \mathbb{C} , this expression can be expressed in matrix form using the compact Voigt notation. Taking $\tilde{\mathbb{C}}_{ijkl} \rightarrow \mathbb{C}_{pq}$, that is, the sub-indices ij and kl are transformed into pq

following Table 2.1.

Regular notation $(\cdot)_{ij}$ or $(\cdot)_{kl}$	Voigt notation $(\cdot)_p$ or $(\cdot)_q$
$(\cdot)_{11}$	$(\cdot)_1$
$(\cdot)_{22}$	$(\cdot)_2$
$(\cdot)_{33}$	$(\cdot)_3$
$(\cdot)_{23}$ or $(\cdot)_{31}$	$(\cdot)_4$
$(\cdot)_{13}$ or $(\cdot)_{31}$	$(\cdot)_5$
$(\cdot)_{12}$ or $(\cdot)_{21}$	$(\cdot)_6$

Table 2.1: Index notation convention to represent \mathbb{C}_{ijkl} , E_{kl} into the reduced Voigt notation form \mathbb{C}_{pq} , E_q .

The general form of (2-64) for an orthotropic material reads

$$\begin{bmatrix} (\mathbf{T}^{RR})_{11} \\ (\mathbf{T}^{RR})_{22} \\ (\mathbf{T}^{RR})_{33} \\ (\mathbf{T}^{RR})_{23} \\ (\mathbf{T}^{RR})_{13} \\ (\mathbf{T}^{RR})_{12} \end{bmatrix} = \begin{bmatrix} \mathbb{C}_{11} & \mathbb{C}_{12} & \mathbb{C}_{13} & 0 & 0 & 0 \\ \mathbb{C}_{21} & \mathbb{C}_{22} & \mathbb{C}_{23} & 0 & 0 & 0 \\ \mathbb{C}_{31} & \mathbb{C}_{32} & \mathbb{C}_{33} & 0 & 0 & 0 \\ 0 & 0 & 0 & \mathbb{C}_{44} & 0 & 0 \\ 0 & 0 & 0 & 0 & \mathbb{C}_{55} & 0 \\ 0 & 0 & 0 & 0 & 0 & \mathbb{C}_{66} \end{bmatrix} \begin{bmatrix} (\mathbf{E})_{11} \\ (\mathbf{E})_{22} \\ (\mathbf{E})_{33} \\ 2(\mathbf{E})_{23} \\ 2(\mathbf{E})_{13} \\ 2(\mathbf{E})_{12} \end{bmatrix} \quad (2-66)$$

where $(\mathbf{T}^{RR})_{ij}$ are the components of the second Piola stress tensor, $(\mathbf{E}^{RR})_{ij}$ the components of the Green-St. Venant strain tensor, both in regular notation, and \mathbb{C}_{pq} are the components of the elastic tensor in Voigt notation. In the previous, due to the symmetry of an orthotropic material, $\mathbb{C}_{12} = \mathbb{C}_{21}$ and $\mathbb{C}_{13} = \mathbb{C}_{31}$.

2.3.2.3

Step 1: The displacement gradient measure of deformation tensor

Following [60], the introduction of a tensor \mathbf{D} , named the displacement gradient measure of deformation, provides a useful way to express the deformation gradient and to state the hypothesis of small strains by a comparison in the material space between the position gradient before and after the deformation.

The displacement gradient measure of deformation is defined as

$$\mathbf{D} = (\mathbf{Q}^R)^T \frac{\partial \mathbf{x}^R}{\partial \mathbf{x}^o} - \frac{\partial \mathbf{x}^o}{\partial \mathbf{x}^o} = (\mathbf{Q}^R)^T \mathbf{F} - \mathbf{I}. \quad (2-67)$$

For the given kinematic assumptions, the tensor \mathbf{D} is expressed in term of column vectors \mathbf{D}_i as $\mathbf{D} = [\mathbf{D}_1, \mathbf{D}_2, \mathbf{D}_3]$, with

$$\mathbf{D}_1 = \left(\gamma_1 \zeta_1^o, \zeta_2^o, s^o \right) + \zeta_1^o \frac{\partial}{\partial \zeta_1^o} \left(\gamma_1 \zeta_1^o, \zeta_2^o, s^o \right) \Big) \mathbf{d}_1^R - \frac{\partial \mathbf{x}^o}{\partial \zeta_1^o}, \quad (2-68)$$

$$\mathbf{D}_2 = \left(\gamma_2 (\zeta_1^o, \zeta_2^o, s^o) + \zeta_2^o \frac{\partial}{\partial \zeta_1^o} \left(\gamma_2 (\zeta_1^o, \zeta_2^o, s^o) \right) \right) \mathbf{d}_2^R - \frac{\partial \mathbf{x}^o}{\partial \zeta_2^o}, \quad (2-69)$$

$$\mathbf{D}_3 = \left(\mathbf{Q}^R \right)^T \left(\frac{\partial \mathbf{r}^R}{\partial s^o} + \frac{\partial \mathbf{Q}^R}{\partial s^o} \mathbf{G}^{RR} \mathbf{z}^o + \mathbf{Q}^R \frac{\partial \mathbf{G}^{RR}}{\partial s^o} \mathbf{z}^o \right) - \frac{\partial \mathbf{x}^o}{\partial s^R}. \quad (2-70)$$

The rate of change of the directors that form the local moving frame with respect to the arc length can be described mathematically by an analogous expression to the one employed in the Frenet-Serret description from differential geometry, as shown in [40, 61], where

$$\frac{\partial \mathbf{d}_i^R}{\partial s^o} = \mathbf{u}^R \times \mathbf{d}_i^R, \quad \frac{\partial \mathbf{Q}^R}{\partial s^o} = \mathbf{u}^R \times \mathbf{Q}^R. \quad (2-71)$$

Now, utilising the properties that any skew-symmetric tensor can be expressed as some cross-product $(\mathbf{u}_\times)_{ij} = \epsilon_{ikj} u_k$ and that a skew-symmetric matrix satisfies $(\mathbf{u}_\times)^T = -(\mathbf{u}_\times)$, it can be shown that $(\mathbf{Q}^R)^T (\mathbf{u}_\times^R) \mathbf{Q}^R$ is also skew-symmetric and it admits a representation of the form

$$(\mathbf{Q}^R)^T (\mathbf{u}_\times^R) \mathbf{Q}^R = (\mathbf{u}_\times^{RR}). \quad (2-72)$$

To prove this, the cross-product property $(\mathbf{M}\mathbf{a}) \times (\mathbf{M}\mathbf{b}) = \det(\mathbf{M}) \mathbf{M}^{-T} (\mathbf{a} \times \mathbf{b})$ is used. Considering the case where \mathbf{M} is orthogonal, then

$$(\mathbf{M}^T \mathbf{a}) \times \mathbf{b} = (\mathbf{M}^T \mathbf{a}) \times (\mathbf{M}^T \mathbf{M} \mathbf{b}) = \mathbf{M}^T (\mathbf{a} \times \mathbf{M} \mathbf{b}) = \mathbf{M}^T \mathbf{a}_\times \mathbf{M} \mathbf{b}. \quad (2-73)$$

Taking $\mathbf{M} = \mathbf{Q}^R$, $\mathbf{a} = \mathbf{u}^R$, and \mathbf{b} an arbitrary vector, by comparison of (2-73) and (2-72), it holds that

$$\mathbf{u}^{RR} = (\mathbf{Q}^R)^T \mathbf{u}^R, \quad \mathbf{u}_\times^{RR} = (\mathbf{Q}^R)^T \mathbf{u}_\times^R \mathbf{Q}^R, \quad (2-74)$$

where \mathbf{u}^{RR} is a pullback of \mathbf{u}^R to the material space

Next, strain measures can be defined by introducing \mathbf{v}^R , \mathbf{v}^o , \mathbf{u}^R and \mathbf{u}^o as

$$\mathbf{v}^R = \frac{d\mathbf{r}^R}{ds^o}, \quad \mathbf{v}^o = \frac{d\mathbf{r}^o}{ds^o} = \mathbf{e}_3^o = \mathbf{d}_3^o, \quad (2-75)$$

and

$$\mathbf{u}^R = \frac{1}{2} \sum_{i=1}^3 \mathbf{d}_i^R \times \frac{d}{ds^o} (\mathbf{d}_i^R), \quad \mathbf{u}^o = \frac{1}{2} \sum_{i=1}^3 \mathbf{d}_i^o \times \frac{d}{ds^o} (\mathbf{d}_i^o) = \mathbf{0}, \quad (2-76)$$

recalling that the reference configuration is straight, thus \mathbf{d}_i^o does not vary. In this expression, an analogous procedure to the one leading to (2-23) was

used. Additionally, all these can be transformed from the observed space to the material space according to $(\cdot)^{RR} = (\mathbf{Q}^R)^T(\cdot)^R$.

Now, considering $\mathbf{z}^R = \mathbf{G}^{RR}\mathbf{z}^o$, vector \mathbf{D}_3 is expressed as

$$\begin{aligned}
 \mathbf{D}_3 &= \mathbf{Q}^{RT} \left(\frac{\partial \mathbf{r}^R}{\partial s^o} + \frac{\partial \mathbf{Q}^R}{\partial s^o} \mathbf{G}^{RR} \mathbf{z}^o + \mathbf{Q}^R \frac{\partial \mathbf{G}^{RR}}{\partial s^o} \mathbf{z}^o \right) - \frac{\partial \mathbf{x}^o}{\partial s^o} \\
 &= \mathbf{Q}^{RT} \left(\mathbf{v}^R + \mathbf{u}_\times^R \mathbf{Q}^R \mathbf{G}^{RR} \mathbf{z}^o + \mathbf{Q}^R \frac{\partial \mathbf{G}^{RR}}{\partial s^o} \mathbf{z}^o \right) - \mathbf{d}_3^o \\
 &= \mathbf{Q}^{RT} \mathbf{v}^R - \mathbf{d}_3^o + \mathbf{Q}^{RT} \mathbf{u}_\times^R \mathbf{Q}^R \mathbf{G}^{RR} \mathbf{z}^o + \frac{\partial \mathbf{G}^{RR}}{\partial s^o} \mathbf{z}^o \\
 &= \mathbf{v}^{RR} - \mathbf{d}_3^o + (\mathbf{u}_\times^{RR}) \mathbf{G}^{RR} \mathbf{z}^o + \frac{\partial \mathbf{G}^{RR}}{\partial s^o} \mathbf{z}^o,
 \end{aligned} \tag{2-77}$$

where the term

$$\mathbf{u}^{RR} \times (\mathbf{G}^{RR} \mathbf{z}^o) = \begin{bmatrix} -u_3^{RR} \zeta_2^o (1 + \gamma_2) \\ u_3^{RR} \zeta_1^o (1 + \gamma_1) \\ -u_2^{RR} \zeta_1^o (1 + \gamma_1) + u_1^{RR} \zeta_2^o (1 + \gamma_2) \end{bmatrix}. \tag{2-78}$$

is nonlinear, as \mathbf{G}^{RR} will eventually depend on u^{RR} and v^{RR} . With the aim of obtaining a linear constitutive, the small strain assumption $\mathbf{G}^{RR} \approx \mathbf{I}$ is used. Hence,

$$\mathbf{u}^{RR} \times (\mathbf{G}^{RR} \mathbf{z}^o) \approx \mathbf{u}^{RR} \times \mathbf{z}^o = \begin{bmatrix} -u_3^{RR} \zeta_2^o \\ u_3^{RR} \zeta_1^o \\ -u_2^{RR} \zeta_1^o + u_1^{RR} \zeta_2^o \end{bmatrix}, \tag{2-79}$$

and substituting (2-79) into (2-77) leads to

$$\mathbf{D} = \begin{bmatrix} \gamma_1 + \zeta_1^o \frac{\partial \gamma_1}{\partial \zeta_1^o} & 0 & v_1^{RR} + \zeta_1 \frac{\partial \gamma_1}{\partial \zeta_1^o} - u_3^{RR} \zeta_2^o \\ 0 & \gamma_2 + \zeta_2^o \frac{\partial \gamma_2}{\partial \zeta_2^o} & v_2^{RR} + \zeta_2^o \frac{\partial \gamma_2}{\partial \zeta_2^o} + u_3^{RR} \zeta_1 \\ 0 & 0 & v_3^{RR} - 1 - u_2^{RR} \zeta_1^o + u_1^{RR} \zeta_2^o \end{bmatrix}. \tag{2-80}$$

Finally, it is possible to find an expression for the deformation gradient \mathbf{F} in terms of the rotation matrix \mathbf{Q}^R and \mathbf{D} . Using (2-67) it holds that

$$\mathbf{F} = \mathbf{Q}^R (\mathbf{D} + \mathbf{I}). \tag{2-81}$$

2.3.2.4

Step 2: The right Cauchy-Green tensor

The right Cauchy-Green tensor is defined as $\mathbf{C} = \mathbf{F}^T \mathbf{F}$, and by using (2-81), it can be stated in terms of the displacement gradient measure of deformation as

$$\mathbf{C} = \mathbf{F}^T \mathbf{F} = (\mathbf{D}^T + \mathbf{I}) \mathbf{Q}^T \mathbf{Q} (\mathbf{D} + \mathbf{I}) = \mathbf{D} + \mathbf{D}^T + \mathbf{D}^T \mathbf{D} + \mathbf{I} . \quad (2-82)$$

A small strain hypothesis implies that $\|\mathbf{D}\|_{\mathbb{F}} \rightarrow 0$, where $\|\mathbf{D}\|_{\mathbb{F}} = \sqrt{\mathbf{D} : \mathbf{D}} = \sqrt{\text{tr}(\mathbf{D}^T \mathbf{D})}$ is the Frobenius norm. For a linear theory, only the terms that are of order $\mathcal{O}(\|\mathbf{D}\|_{\mathbb{F}})$ are kept. It should be noted that the third term $\mathbf{D}^T \mathbf{D}$ introduces a quadratic term of order $\mathcal{O}(\|\mathbf{D}\|_{\mathbb{F}}^2)$ and will be considered negligible. Therefore, \mathbf{C} is approximated as

$$\mathbf{C} = \mathbf{F}^T \mathbf{F} \approx \mathbf{D} + \mathbf{D}^T + \mathbf{I} . \quad (2-83)$$

2.3.2.5

Step 3: The Green-St. Venant strain tensor

The Green-St. Venant tensor is used the constitutive relation of (2-65) to relate the tensions with the strains. It can be expressed as

$$\mathbf{E} = \frac{1}{2} (\mathbf{C} - \mathbf{I}) = \frac{1}{2} (\mathbf{D} + \mathbf{D}^T) = \begin{bmatrix} D_{11} & 0 & \frac{1}{2} D_{31} \\ 0 & D_{22} & \frac{1}{2} D_{32} \\ \frac{1}{2} D_{31} & \frac{1}{2} D_{32} & D_{33} \end{bmatrix} . \quad (2-84)$$

2.3.2.6

Step 4: Finding the in-plane deformation functions

So far an expression has been obtained for the Green-St. Venant tensor, where the components depend on derivatives of the kinematic assumptions as well as on the in-plane cross-section deformation functions γ_1 and γ_2 . An expression for these functions in terms of the kinematic assumptions is sought. To do this, first, the usual beam hypothesis that the second Piola tensor satisfies $T_{11}^{RR} = 0$ and $T_{22}^{RR} = 0$ are considered.

The hypothesis that the non-longitudinal normal stresses vanish is expressed as

$$T_{11}^{RR} = \mathbb{C}_{11}(\mathbf{E})_{11} + \mathbb{C}_{12}(\mathbf{E})_{22} + \mathbb{C}_{13}(\mathbf{E})_{33} = 0, \quad (2-85)$$

$$T_{22}^{RR} = \mathbb{C}_{21}E_{11} + \mathbb{C}_{22}E_{22} + \mathbb{C}_{23}E_{33} = 0, \quad (2-86)$$

allowing to state E_{11} and E_{22} as functions of E_{33}

$$E_{11} = \frac{(\mathbb{C}_{12}\mathbb{C}_{23} - \mathbb{C}_{13}\mathbb{C}_{22})}{\Delta} E_{33}, \quad (2-87)$$

$$E_{22} = \frac{(\mathbb{C}_{13}\mathbb{C}_{21} - \mathbb{C}_{11}\mathbb{C}_{23})}{\Delta} E_{33}, \quad (2-88)$$

$$\Delta = \mathbb{C}_{11}\mathbb{C}_{22} - \mathbb{C}_{12}\mathbb{C}_{21}. \quad (2-89)$$

Combining the latter with the expressions for the Green-St. Venant tensor leads to

$$\gamma_1 + \zeta_1^o \frac{\partial \gamma_1}{\partial \zeta_1^o} = \frac{(\mathbb{C}_{12}\mathbb{C}_{23} - \mathbb{C}_{13}\mathbb{C}_{22})}{\Delta} E_{33}, \quad (2-90)$$

$$\gamma_2 + \zeta_2^o \frac{\partial \gamma_2}{\partial \zeta_2^o} = \frac{(\mathbb{C}_{13}\mathbb{C}_{21} - \mathbb{C}_{11}\mathbb{C}_{23})}{\Delta} E_{33}, \quad (2-91)$$

with

$$E_{33} = v_3^{RR} - 1 - u_2^{RR} \zeta_1^o + u_1^{RR} \zeta_2^o, \quad (2-92)$$

where by inspection, the following expressions satisfy (2-90) and (2-91):

$$\gamma_1 = \frac{(\mathbb{C}_{12}\mathbb{C}_{23} - \mathbb{C}_{13}\mathbb{C}_{22})}{\Delta} \left(E_{33} + \frac{u_2^{RR} \zeta_1^o}{2} \right), \quad (2-93)$$

$$\gamma_2 = \frac{(\mathbb{C}_{13}\mathbb{C}_{21} - \mathbb{C}_{11}\mathbb{C}_{23})}{\Delta} \left(E_{33} - \frac{u_1^{RR} \zeta_2^o}{2} \right). \quad (2-94)$$

2.3.2.7

Step 5: Integrating the traction associated with the second Piola stress tensor

Now that the in-plane deformation functions are known, the second Piola tensor reads

$$\mathbf{T}^{RR} = \begin{bmatrix} 0 & 0 & 2 \mathbb{C}_{55} E_{13} \\ 0 & 0 & 2 \mathbb{C}_{44} E_{23} \\ 2 \mathbb{C}_{55} E_{13} & 2 \mathbb{C}_{44} E_{23} & \mathbb{C}_{31} E_{11} + \mathbb{C}_{32} E_{22} + \mathbb{C}_{33} E_{33} \end{bmatrix}, \quad (2-95)$$

and the traction associated is

$$\mathbf{t}^{RR} = \mathbf{T}^{RR} \boldsymbol{\eta}^R = \begin{bmatrix} 2 \mathbb{C}_{55} E_{13} \\ 2 \mathbb{C}_{44} E_{23} \\ \mathbb{C}_{31} E_{11} + \mathbb{C}_{32} E_{22} + \mathbb{C}_{33} E_{33} \end{bmatrix} = \begin{bmatrix} \mathbb{C}_{55} D_{31} \\ \mathbb{C}_{44} D_{32} \\ \tilde{\mathbb{C}}_{33} D_{33} \end{bmatrix}, \quad (2-96)$$

with the following modified coefficient

$$\tilde{\mathbb{C}}_{33} = A_{33} - \frac{A_{32}A_{23}}{A_{22}}, \quad A_{ij} = \mathbb{C}_{ij} - \frac{\mathbb{C}_{i1}\mathbb{C}_{1j}}{\mathbb{C}_{11}}. \quad (2-97)$$

Integrating within the cross-section, with the normal unit vector being $\eta^R = (0, 0, 1)^T$, the constitutive relations for the internal forces in a Cosserat medium are obtained. The resultant associated with the second Piola tensor is

$$\mathbf{n}^{RR} = \int_{A^o} \mathbf{t}^{RR} dA^o = \begin{bmatrix} \int_{A^o} C_{55} \left(v_1^{RR} + \zeta_1 \frac{\partial \gamma_1}{\partial \zeta_1^o} - u_3^{RR} \zeta_2^o \right) dA^o \\ \int_{A^o} C_{44} \left(v_2^{RR} + \zeta_2^o \frac{\partial \gamma_2}{\partial \zeta_2^o} + u_3^{RR} \zeta_1 \right) dA^o \\ \int_{A^o} \tilde{C}_{33} \left(v_3^{RR} - 1 - u_2^{RR} \zeta_1^o + u_1^{RR} \zeta_2^o \right) dA^o \end{bmatrix}. \quad (2-98)$$

In addition, with the hypothesis that the curve \mathcal{L} passes through the neutral axis, that the directors are associated with principal directions, and that the material is homogeneous, this further simplifies to

$$\mathbf{n}^{RR} = \mathbf{K}_n (\mathbf{v}^{RR} - \mathbf{d}_3^o), \quad \text{with } \mathbf{K}_n = \begin{bmatrix} \mathbb{C}_{55} A^o & 0 & 0 \\ 0 & \mathbb{C}_{44} A^o & 0 \\ 0 & 0 & \tilde{\mathbb{C}}_{33} A^o \end{bmatrix}. \quad (2-99)$$

The resultant associated with the first Piola tensor is

$$\mathbf{n}^R = \int_{A^o} \mathbf{t}^R dA^o = \mathbf{Q}^R \int_{A^o} \mathbf{t}^{RR} d\zeta_1 d\zeta_2 = \mathbf{Q}^R \mathbf{n}^{RR}. \quad (2-100)$$

In an analogous manner, the torque produced by the traction can be integrated to obtain an expression for the pullback of the traction

$$\mathbf{m}^{RR} = \int_{A^o} \mathbf{z}^o \times \mathbf{t}^{RR} dA^o, \quad (2-101)$$

$$\mathbf{m}^{RR} = \begin{bmatrix} \int_{A^o} \zeta_2^o \tilde{C}_{33} \left(v_3^{RR} - 1 - u_2^{RR} \zeta_1^o + u_1^{RR} \zeta_2^o \right) dA^o \\ \int_{A^o} -\zeta_1^o \tilde{C}_{33} \left(v_3^{RR} - 1 - u_2^{RR} \zeta_1^o + u_1^{RR} \zeta_2^o \right) dA^o \\ \int_{A^o} \zeta_1^o C_{55} \left(v_1^{RR} + \zeta_1 \frac{\partial \gamma_1}{\partial \zeta_1^o} - u_3^{RR} \zeta_2^o \right) - \zeta_2^o C_{44} \left(v_2^{RR} + \zeta_2^o \frac{\partial \gamma_2}{\partial \zeta_2^o} + u_3^{RR} \zeta_1 \right) dA^o \end{bmatrix} \quad (2-102)$$

Again, if the curve passes through the neutral axis, the directors are associated to principal directions, and the material is homogeneous, this further simplifies to

$$\mathbf{m}^{RR} = \mathbf{K}_m (\mathbf{u}^{RR}), \quad \text{with } \mathbf{K}_m = \begin{bmatrix} J_{11} & 0 & 0 \\ 0 & J_{22} & 0 \\ 0 & 0 & J_{33} \end{bmatrix}, \quad (2-103)$$

where J_{11} and J_{22} are calculated with the corrected coefficient \tilde{C}_{33} .

It can be proved that the traction associated with the first Piola stress is

$$\mathbf{m}^R = \int_{A^o} (\mathbf{Q}^R \mathbf{G}^{RR} \mathbf{z}^o) \times (\mathbf{T}^R \boldsymbol{\eta}^R) dA^o. \quad (2-104)$$

Again, a linear constitutive is obtained by considering the approximation $\mathbf{G}^{RR} = \mathbf{I}$. Using the property of (2-73), it is obtained that

$$\mathbf{m}^R = \int_{A^o} (\mathbf{Q}^R \mathbf{G}^{RR} \mathbf{z}^o) \times (\mathbf{T}^R \boldsymbol{\eta}^R) dA^o = \int_{A^o} \mathbf{Q}^R (\mathbf{z}^o \times (\mathbf{T}^{RR} \boldsymbol{\eta}^R)) dA^o = \mathbf{Q}^R \mathbf{m}^{RR}. \quad (2-105)$$

2.4

Linear isotropic elastic materials

The equations for a linear elastic material are given by (2-98) and (2-102), or (2-99) and (2-103), with the modified coefficient \tilde{C}_{33} given by (2-97) and the transformation rules

$$\mathbf{n}^R = \mathbf{Q}^R \mathbf{n}^{RR}, \quad \mathbf{m}^R = \mathbf{Q}^R \mathbf{m}^{RR}. \quad (2-106)$$

It should be observed that for an isotropic material, the modified parameter is given by $\tilde{C}_{33} = \mu \frac{(3\lambda + 2\mu)}{\lambda + \mu} = E_y$ and $C_{44} = C_{55} = G_y$, where λ , μ are the Lamé constants; E_y and G_y are the Young moduli, leading to

$$\mathbf{n}^{RR} = \mathbf{K}_n (\mathbf{v}^{RR} - \mathbf{v}^o), \quad (2-107)$$

$$\mathbf{m}^{RR} = \mathbf{K}_m (\mathbf{u}^{RR} - \mathbf{u}^o), \quad (2-108)$$

with

$$\mathbf{K}_n = \begin{bmatrix} K_{11} & 0 & 0 \\ 0 & K_{22} & 0 \\ 0 & 0 & K_{33} \end{bmatrix} = \begin{bmatrix} GA & 0 & 0 \\ 0 & GA & 0 \\ 0 & 0 & EA \end{bmatrix}, \quad (2-109)$$

$$\mathbf{K}_m = \begin{bmatrix} J_{11} & 0 & 0 \\ 0 & J_{22} & 0 \\ 0 & 0 & J_{33} \end{bmatrix} = \begin{bmatrix} E I_{11} & 0 & 0 \\ 0 & E I_{22} & 0 \\ 0 & 0 & G (I_{11} + I_{22}) \end{bmatrix}. \quad (2-110)$$

2.5

Linear Kelvin-Voigt material

Hereunder, the constitutive relations for a linear Kelvin-Voigt material are enumerated. These expressions can be used to account for structural damping. The formulation is taken from [58]. The relationship between internal forces and the dependent variables, in material form, reads as

$$\mathbf{n}^{RR} = \mathbf{K}_n(\mathbf{v}^{RR} - \mathbf{v}^o) + \mathbf{K}_{nt}(\dot{\mathbf{v}}^{RR}), \quad (2-111)$$

$$\mathbf{m}^{RR} = \mathbf{K}_m(\mathbf{u}^{RR} - \mathbf{u}^o) + \mathbf{K}_{mt}(\dot{\mathbf{u}}^{RR}), \quad (2-112)$$

and in spacial form, following $(\cdot)^R = \mathbf{Q}^R(\cdot)^{RR}$, as

$$\mathbf{n}^R = \mathbf{K}_n(\mathbf{v}^R - \mathbf{Q}\mathbf{v}^o) + \mathbf{K}_{nt}(\mathbf{Q}\dot{\mathbf{v}}^{RR}), \quad (2-113)$$

$$\mathbf{m}^R = \mathbf{K}_m(\mathbf{u}^R - \mathbf{Q}\mathbf{u}^o) + \mathbf{K}_{mt}(\mathbf{Q}\dot{\mathbf{u}}^{RR}). \quad (2-114)$$

In [58], these matrices are written in terms of the parameters τ_S , τ_B , which are retardation time constants that relate the shear viscosity and the bulk viscosity to the shear and bulk moduli. Also, another parameter τ_E is used. It can be demonstrated that, by taking $\tau_S = \tau_B = \tau_E = c_d$, where c_d is another constant, the previous matrices can be written as

$$\mathbf{K}_{nt} = c_d \mathbf{K}_n, \quad (2-115)$$

and

$$\mathbf{K}_{mt} = c_d \mathbf{K}_m. \quad (2-116)$$

Note that if $c_d = 0$, the model has no viscous damping and it coincides with the formulation of (2-107) and (2-108).

2.6

Summary of the equations

Considering principal axes of inertia, and \mathcal{C} passing through the centre of mass of each cross-section, the equations of motion are given by

$$\frac{d}{ds^o}(\mathbf{n}^R) + \mathbf{f}_n^R = \frac{d}{dt}(\rho^R A^R \dot{\mathbf{r}}^R), \quad (2-51, \text{ revisited})$$

$$\frac{d}{ds^o}(\mathbf{r}^R) \times \mathbf{n}^R + \frac{d}{ds^o}(\mathbf{m}^R) + \mathbf{f}_m^R = \frac{d}{dt}(\boldsymbol{\kappa}_2^R), \quad (2-61, \text{ revisited})$$

$$\dot{\mathbf{q}} = \frac{1}{2} \boldsymbol{\Omega} \mathbf{q} + c \mathbf{q}_m, \quad (2-26, \text{ revisited})$$

with

$$\boldsymbol{\Omega} = \begin{bmatrix} 0 & -\omega_1 & -\omega_2 & -\omega_3 \\ \omega_1 & 0 & \omega_3 & -\omega_2 \\ \omega_2 & -\omega_3 & 0 & \omega_1 \\ \omega_3 & \omega_2 & -\omega_1 & 0 \end{bmatrix}, \quad (2-27, \text{ revisited})$$

and

$$\boldsymbol{\kappa}_2^R = \mathbf{Q}^R \boldsymbol{\Theta}_2^{RR} (\mathbf{Q}^R)^T \boldsymbol{\omega}^R, \quad \text{with } \boldsymbol{\Theta}_2^{RR} = \begin{bmatrix} I_{11}^{RR} & 0 & 0 \\ 0 & I_{22}^{RR} & 0 \\ 0 & 0 & I_{33}^{RR} \end{bmatrix}, \quad (2-62, \text{ revisited})$$

The vector $\boldsymbol{\omega}^R$ that appears in $\boldsymbol{\kappa}_2^R$ in (2-61) represents the angular velocity vector of the cross-sections, and it is not independent from section-orientation. In fact, their relation is given by the extra equation (2-26). The addition of this extra PDE avoids dealing with a DAE problem, where one has to enforce the unitary quaternion constraint.

An expression for the weak form of the previous expression is given in Appendix D.

With all these, the strain measures required for the constitutive relations can be derived from the generalised coordinates. In fact,

$$\mathbf{v}^R = \frac{d\mathbf{r}^R}{ds^o}, \quad \mathbf{v}^o = \frac{d\mathbf{r}^o}{ds^o} = \mathbf{e}_3^o = \mathbf{d}_3^o, \quad (2-75, \text{ revisited})$$

and

$$\mathbf{u}^R = \frac{1}{2} \sum_{i=1}^3 \mathbf{d}_i^R \times \frac{d}{ds^o} (\mathbf{d}_i^R), \quad \mathbf{u}^o = \frac{1}{2} \sum_{i=1}^3 \mathbf{d}_i^o \times \frac{d}{ds^o} (\mathbf{d}_i^o) = \mathbf{0}, \quad (2-76, \text{ revisited})$$

recalling that a straight reference configuration is being considered and that \mathbf{d}_i is calculated in terms of the quaternion components defined by (2-26), where the generalised coordinate is the angular velocity field. The constitutive relations are given by

$$\mathbf{n}^{RR} = \mathbf{K}_n (\mathbf{v}^{RR} - \mathbf{v}^o) + \mathbf{K}_{nt} (\dot{\mathbf{v}}^{RR}), \quad (2-111, \text{ revisited})$$

$$\mathbf{m}^{RR} = \mathbf{K}_m (\mathbf{u}^{RR} - \mathbf{u}^o) + \mathbf{K}_{mt} (\dot{\mathbf{u}}^{RR}). \quad (2-112, \text{ revisited})$$

Finally, the transformation rule from the material to the spatial configuration is given by

$$(\cdot)^R = \mathbf{Q}^R (\cdot)^{RR}, \quad (2-117)$$

and the constitutive relations take the spatial form

$$\mathbf{n}^R = \mathbf{K}_n (\mathbf{v}^R - \mathbf{Q}\mathbf{v}^o) + \mathbf{K}_{nt} (\mathbf{Q}\dot{\mathbf{v}}^{RR}), \quad (2-113, \text{ revisited})$$

$$\mathbf{m}^R = \mathbf{K}_m (\mathbf{u}^R - \mathbf{Q}\mathbf{u}^o) + \mathbf{K}_{mt} (\mathbf{Q}\dot{\mathbf{u}}^{RR}). \quad (2-114, \text{ revisited})$$

3

The sources of non-linearity in Cosserat rods

The aim of this chapter is to hold a brief discussion on what the sources of non-linearity in the theory of Cosserat rods are.

A linear differential equation is a differential equation that is defined by a linear polynomial of the unknown functions and its derivatives. A more formal definition involves demonstrating that it is composed of operators O , that satisfy $O(af_1 + bf_2) = aO(f_1) + bO(f_2)$, as described in Reference [62]. Therefore, a non-linear differential equation is one that does not satisfy the previous condition, i.e. it is not a linear polynomial of the unknown functions and its derivatives.

In continuum mechanics, as well as in reduced order theories such as the theory of Cosserat rods, there are two main sources of non-linearities that may intervene in the governing equations:

- the geometric non-linearity, due to the statement of the equations of motion in a configuration that is not close to the reference,
- the material non-linearity.

For the sake of completeness, it is important to mention that a particular problem may include other sources of non-linearities depending on the nature of the external forces being considered, as well as the boundary conditions (e.g., in the case of intermittent contact).

3.1

Geometric non-linearity in Continuum Mechanics

The inclusion of this chapter aims at clarifying what are the terms that introduce the geometric non-linearity in the context of the Cosserat rods which, like in continuum mechanics, comes from the transformation rules between the Second Piola tensor, the First Piola tensor, and the Cauchy tensor. Also, this chapter is aimed at pinpointing which hypotheses lead to a linear Cosserat theory. It will be shown that two considerations are needed: first, a simplification in the geometrical aspects of the deformations to avoid geometric non-linearities; second, the statement of an intrinsically linear constitutive relation.

The geometric aspect of the non-linearity will be discussed first. The material form of the equation of motion is stated in (2-61) and (2-62). The expression requires a constitutive relation to establish a link between the First Piola tensor and the position field \mathbf{x} .

The analysis is made considering hyper-elastic materials where the constitutive relation is given as a linear expression for the Second Piola tensor. For example, in the case of a linear isotropic elastic material, $\mathbf{T}^{RR} = 2\mu\mathbf{E} + \lambda\text{tr}(\mathbf{E})\mathbf{I}$, where \mathbf{E} is a linearised version of the Green-St.Venant strain tensor in the vicinity of a natural (stress-free) configuration, and $\{\mu, \lambda\}$ are the Lamé constants. Then, given that \mathbf{T}^{RR} is linear, the source of geometric non-linearity can be pinpointed to how this tensor transforms into the First Piola stress tensor, which is required by the equation of motion in its material form.

Considering the transformation relation between the second and first Piola tensors, $\mathbf{T}^R = \mathbf{F}\mathbf{T}^{RR}$, if \mathbf{T}^{RR} were a linear expression on the variables of the problem, the source of non-linearity would undoubtedly be \mathbf{F} , which depends on the current geometric configuration of the body. In order to avoid geometric non-linearities, for any linear expression of \mathbf{T}^{RR} , it is sought that $\mathbf{T}^R = \mathbf{F}\mathbf{T}^{RR}$ remains linear, and the only possible way to attain such condition is to consider $\mathbf{F} \approx \mathbf{I}$. Now, let $\mathbf{x} = \mathbf{X} + \mathbf{u}$, where \mathbf{u} is a displacement from the reference configuration \mathbf{X} , and consequently, $\mathbf{F} = \mathbf{I} + \mathbf{H}$, where $\mathbf{H} = \text{Grad}(\mathbf{u})$. In order to satisfy the previous condition, it is required that $\mathbf{H} \rightarrow 0$, which means that the gradient of the displacement field needs to be small.

Actually, the previous is one of the main hypotheses employed in linear elasticity theory, and its consequence is that $\mathbf{T}^{RR} \approx \mathbf{T}^R \approx \mathbf{T}$, which means that the Second Piola tensor, the First Piola tensor, and the Cauchy tensor, all coincide. Also, it is equivalent to saying that the gradient of the displacements is supposed small (small strain). Note that no particular hypothesis is required with regard to the displacement field itself, which means that a body can undergo large displacements and yet present small strains.

3.2

Geometric non-linearity in the Cosserat theory of rods

Alike continuum mechanics, geometric non-linearity is related to the fact that Newton's laws of motion can be applied, as a general rule, to the current configuration only. To such purpose, the transformation rules for tractions, which are associated with the First and Second Piola tensors and the Cauchy tensor, play an important role. It will be shown that strain and rotations should remain small for the theory to be linear. In other words, it is only

in rare cases that the current and the reference configuration are very close, allowing for Newton's laws to be applied in the reference configuration without introducing much error. And only in such cases, the resulting formulation is linear.

1-D theories describe the configuration \mathbf{x} of the body by considering the position of a centreline \mathbf{r} , and the orientation of the cross-sections. For the latter, some parametrisation of the rotations needs to be used in defining orientation, such as Euler angles or quaternions. Given that no such parametrisation is linear in the parameters employed, this foreshadows the need for small rotations if linearity is sought. In fact, the geometrical non-linearity appears in, at least, two aspects of the statement of the formulation of Cosserat rods: how tractions transform, and the equations of motion themselves.

To begin with, how tractions transform, the constitutive relations (2-113) and (2-114) are originally stated in material form. As known from continuum mechanics, the transformation law for tractions is given by $\mathbf{t}^R = \mathbf{F}\mathbf{t}^{RR}$.

In Chapter 2.3, it was shown that there exists a representation of the form

$$\mathbf{F} = \mathbf{Q}^R(\mathbf{D} + \mathbf{I}), \quad (2-81, \text{ revisited})$$

where \mathbf{Q}^R is a rotation matrix, \mathbf{D} is the so-called measure of deformation tensor, and \mathbf{I} the identity. This description shows that the geometric non-linearity introduced in the transformation from \mathbf{t}^{RR} to \mathbf{t}^R is associated to the non-linear nature of the rotation matrix \mathbf{Q}^R , and the non-linearity introduced by the measure of deformation tensor \mathbf{D} , which is a measure of strain.

The theory of Cosserat rods is based on the hypothesis that sections behave as rigid bodies and that strains are small, while finite rotations are allowed. By hypothesis, compatible with the previous statements, \mathbf{D} is neglected so that $\mathbf{F} = \mathbf{Q}^R$. The consequence is that the transformation rules in the theory of Cosserat rods read, given by (2-117), read

$$\mathbf{n}^R = \mathbf{Q}^R \mathbf{n}^{RR}, \quad (3-1)$$

$$\mathbf{m}^R = \mathbf{Q}^R \mathbf{m}^{RR}. \quad (3-2)$$

Now, analysing the equations of motion, the balance of linear momentum states that

$$\frac{d}{ds^o}(\mathbf{n}^R) + \mathbf{f}_n^R = \frac{d}{dt}(\rho^R A^R \dot{\mathbf{r}}^R), \quad (2-51, \text{ revisited})$$

which is linear if \mathbf{t}^R is also linear. Due to (3-1) and (3-2), it is clear that, in order to retain linearity, small rotations need be considered. On the other hand, the equation corresponding to the angular momentum balance states

$$\frac{d}{ds^o}(\mathbf{r}^R) \times \mathbf{n}^R + \frac{d}{ds^o}(\mathbf{m}^R) + \mathbf{f}_m^R = \frac{d}{dt}(\boldsymbol{\kappa}_2^R), \quad (2-61, \text{revisited})$$

which is non-linear in nature due to the term

$$\frac{d}{ds^o}(\mathbf{r}^R) \times \mathbf{n}^R. \quad (3-3)$$

The internal efforts \mathbf{n}^R also depend on the solution through $\mathbf{v}^R = \frac{d}{ds^o}(\mathbf{r}^R)$, the tangent to the curve, which it is also used to obtain a measure of the strains in the constitutive relations. Thus, the cross product containing \mathbf{v}^R introduces a non-linearity in the equation. Given that \mathbf{n}^R is defined by a constitutive relation that is linear, linearity requires \mathbf{v}^R to be a known field based on the small strain assumption, this is, it cannot depend on the solution. As an illustrative example, the case of a straight beam is considered in what follows, following Fig. 3.1. In this case, the beam has its main length in the direction of a versor \mathbf{e}_3 . Thus, assuming $\mathbf{v}^R = \mathbf{e}_3$ for the cross-product would lead to a linear set of equations that is compatible with the small strain assumptions.

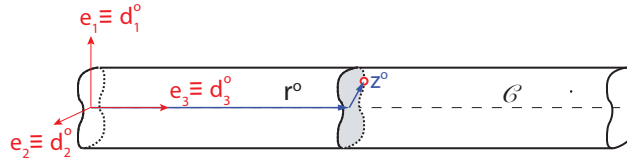


Figure 3.1: Example of a horizontal beam that experiences a dynamic with configurations close to its reference configuration.

3.3

The importance of the non-linear terms

The importance of the non-linear terms is shown with a simple example of a bending beam. For such purpose, the static problem of a horizontal cantilever beam under the influence of a vertical force at the tip is analysed. The displacements at the end of the beam are compared.

The problem is solved by means of five different models:

- CR1: A linear Cosserat rod model. For such purpose, the hypothesis that rotations are small (and in the plane of the paper), and that $\mathbf{v}^R = \mathbf{e}_3$ are considered. The hypothesis that rotations are small means that a Taylor expansion close to the horizontal configuration was used.

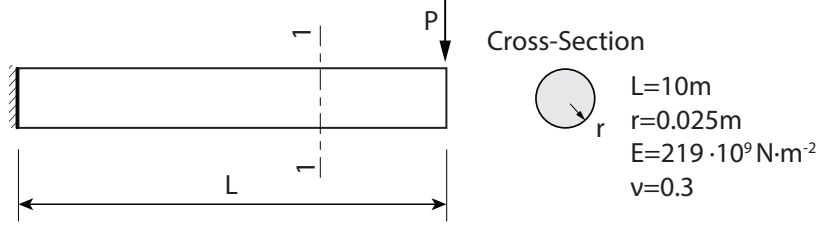


Figure 3.2: Sketch of the problem under analysis, with the geometric and material properties used.

- CR2: A simplified non-linear Cosserat rod model where the hypothesis that rotations are large, and $\mathbf{v}^R = \mathbf{e}_3$ are considered. This means that the term (3-3) does not introduce any extra non-linearity.
- CR3: A non-linear Cosserat rod model where no simplificative hypothesis have been used: rotations are large, and \mathbf{v}^R in the term (3-3) is also a source of non-linearity.
- E1: The model is based on geometrically non-linear 3D elasticity theory.
- E2: The model is based on linear 3D elasticity theory.

For E1, the equation of motion is of the form of $\text{Div}(\mathbf{T}^R) + \mathbf{f}^R = \rho^R \ddot{\mathbf{x}}^R$, where \mathbf{T}^R is the first Piola stress tensor, f is a body force. Also, an isotropic elastic material is considered, with a constitutive relation of the form of $\mathbf{T}^{RR} = 2\mu\mathbf{E} + \lambda\text{tr}(\mathbf{E})\mathbf{1}$, where \mathbf{T}^{RR} is the second Piola stress tensor, related to the first one through $\mathbf{T}^R = \mathbf{F}\mathbf{T}^{RR}$, \mathbf{E} is the Green - St. Venant strain tensor, μ and λ are the Lamé parameters. For E2, a linearised version of the formulation of E1 is used (see [54] for more details on how to obtain a linear elasticity theory).

The vertical displacement at the tip of the beam is compared for the different models, and the results are shown in Fig. 3.3.

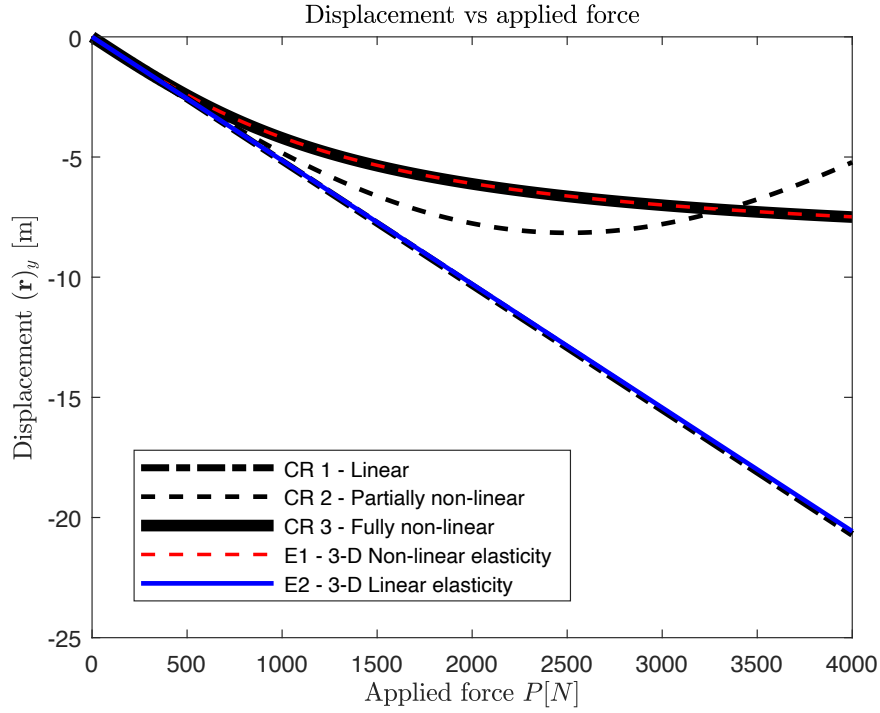


Figure 3.3: Displacement at the tip of the beam, in the y-direction vs. applied force. CR1 is a linearised Cosserat Rod model; CR2 considers non-linear rotation but the non-linear term in the angular momentum balance is simplified to remain linear; CR3 is a fully non-linear Cosserat rod model (with no simplifications); E1 is a geometrical non-linear elasticity model; finally E2 is a linear elasticity model.

It is observed that the results from a linear CR model, and a non-linear CR model differ greatly when large displacements are involved. Moreover, the result for the CR rod coincide with the more complex geometrically non-linear 3D elasticity model, which is considered as the reference for this benchmark.

For the purpose of the comparisons, it is important to highlight that the objective was to provide some observations about the results provided by each models, where the same constitutive and material were used. In this context, all models should give the same results in their range of validity. However, it was not verified that the stresses fall within the acceptable range for a regular steel beam. If that aspect were considered, the domain of the graph might need to be reduced.

4

Simulating an off-bottom drill-string in a curved well

In this chapter, it will be shown that the modelling of a drill-string moving within a borehole of arbitrary shape can be tackled with the Cosserat rod formulation. The equations of motion described in Chapter 2 can account for large displacements of the rod within the 3-D oil well. In particular, the dynamics of a drill-string within the curved borehole for an off-bottom configuration, i.e. without contact at the bit, will be studied.

The main contributions that the author identifies in the study presented in this chapter are: 1) the implementation of the Cosserat model to account for the dynamics in an arbitrary borehole; 2) the inclusion of an algorithm to detect when and where contact and friction occur, as well as the magnitudes of the forces involved; 3) the calibration of the a priori unknown friction parameters, with the results of [29]; 4) the verification of the present results with those of [29], being the latter validated against field measurements.

Some other important aspects of this study include the set of verification tests that were carried out for the current implementation of the Cosserat model, that are included in the Appendix B.1. The benchmarks and other examples calculated with the current implementation of the Cosserat rod yielded excellent agreement with other known solutions in the appendix.

The contents of the study considering the off-bottom case have been published in [40, 63, 64].

4.1

Description of the problem

Directional arbitrary configurations of boreholes have become a subject of recent interest. However, many related literature still use continuous straight beam theories or lumped models to tackle the dynamics of drill-strings. In this context, auxiliary assumptions are employed so that the modelling of the contact within the arbitrary borehole geometry can be simplified or omitted. Additionally, some of those models are not comprehensive, as they do not take into account all possible axial, torsional and flexural motions of the string, among other aspects.

The works [6] and [32] are some of the few studies that tackle drill-string dynamics with Cosserat rod formulations, and they show that there is an opportunity to continue exploring the usability of Cosserat rod models in the context of drill-string dynamics.

The first of these, [6], is a doctoral thesis aimed at using a Cosserat approach to study drill-string dynamics. The implementation of the rod is based on the Modified Cosserat Rod Element (MCRE) formulation described by [33, 34]. Nevertheless, it is indicated in [35] that the approach of [6, 33, 34] based on the MCRE, which is no more than one of the possible ways to implement a Cosserat formulation, is unsuitable for modelling systems that involve large deformations, which is why [35] abandons their Cosserat model implementation to employ another one based on the 3D elasticity theory. After that, to the knowledge of the author of this thesis, the authors of [6, 35] and their group have not continue the line of research considering a Cosserat formulation.

The second work, [32], analyses the behaviour of a drill-string for an application example consisting of a rotating flexible shaft moving within a rigid tube. The tube is assumed to be an arbitrary space curve and the shaft is formulated as a non-linear elastic Cosserat rod. However, the theory is simplified so that the position vectors of the centreline of the non-straight tube and the rod coincide. This way, the problem of intermittent contact with the walls is substituted by a model where contact is present all the time. On top of that, no friction, stretching or shear effects are considered. In the end, the authors of [32] solve a projected version of the Cosserat equations in the direction of the tangent to the borehole, leading to a simpler model than that of a Cosserat rod.

The contact between the drill-string and the borehole wall can be a tricky issue. On the one hand, some studies, like [31], consider contact only at discretisation nodes. Others deal with contact in simpler rectilinear inclined borehole geometries, where the wall can be mathematically described as a cylinder [65]. In the latter case, if a penalisation method is used to determine where contact occurs and the magnitude of the force, the formulation is reduced to verifying whether the current position satisfies some inequality containing the equation of the cylinder.

On the other hand, another approach is given by the so-called soft-string models, like [29, 32], which are also common in the oil industry. Their name stands for the fact that the entire drill-string is assumed to have zero bending stiffness, therefore the shape of drill-string matches that of the well-bore in inclination, azimuth, and curvature. In other words, contact is considered

along the whole length of the structure, all the time. This is also the case of the work that was previously discussed, [32]. Contact is closely related to friction in the dynamics of a confined structure. Being the latter the cause of stick-slip phenomena, the friction model is of great importance. Depending on the actual working regime, drill-strings are subjected to stick-slip vibrations which are characterised by a stick phase where the rotary speed at the bit can be less than half the target speed, followed by a slip phase where the rotary speed can double or triple the target speed. This phenomenon has a strong negative impact on the lifespan of the assembly as it induces alternating stress variations. Many friction models consider a distributed torque proportional to the inclination of the oil-well [29, 66]. As stated in [67], soft-string models mathematically assume continuous contact of the drill-string with the casing or the well-bore. This assumption may not be accurate due to the significantly different outer diameters between the connection (tool joint) and the pipe body. Also, these models are incapable of predicting the actual location of contact along the drill-string, as well as any buckling, given that they neglect the bending stiffness.

The previous commentaries on the works [6, 32] show that by overcoming the disadvantages of the implementation discussed in [6, 33, 34] by [35], and by considering a different approach to modelling the contact, there is yet a huge potentiality for the Cosserat rod models. Especially with the aim of analysing whether intermittent contact, buckling, and other effects play an important role in the dynamics of the string. For this reason, in the present chapter, a study of the dynamics of an off-bottom drill-string that moves within a curved borehole is presented. The model is based on the Cosserat rod formulation described in Chapter 2.

The main contributions of this chapter are: that the known singularities mentioned in [35] regarding [6, 33, 34] are overcome by the choice of a quaternion representation for the rotation, instead of the description used in the MCRE model. Moreover, a strategy to account for the distributed contact and friction along the drill-string is developed. For this task, a parametric description of the borehole shape, which can be any arbitrary curve, is considered. This means that no ad-hoc hypotheses are used in the predictions of the contact and friction phenomena, as it happens with the so-called soft-string models. But the problem becomes more complex as a differential-algebraic (DAE) set of equations needs to be solved. Additionally, a four-parameter friction law that considers the Stribeck effect, *i.e.* a continuity solution for the transition between static and dynamic friction, is chosen.

An approximate solution is obtained by implementing the DAEs, along

with the particular boundary and initial conditions, in the software COMSOL Multiphysics [68]. Results in the time and frequency domains match very well the outcomes of [29], despite the obvious differences of the model. It should be mentioned that the case analysed is that of an “off-bottom start-up” and thus, the axial motion is not the main oscillation. Furthermore, the results of [29] have been validated with field measurements.

The present chapter is organised as follows. First, the proposed drill-string model based on the Cosserat theory of rods is presented. For this task, the set of parameters used in the simulations is enumerated along with the top-drive conditions for which a proportional-integral (PI) controller is used. After that, the contact model formulation for arbitrary borehole geometries is developed. Next, a friction model is stated. The friction model is calibrated with the data in [29]. Following that, an application case considering an off-bottom drill-string moving within a curved well is simulated. The results are compared against those of [29]. Some of the novelties of the result include the variation of the forces and torques predicted by the Cosserat model, which differs from that of [29]. Finally, final commentaries on the study are provided.

4.2

The drill-string model

As already stated, the formulation for the string is based on the Cosserat rod model of Chapter 2. The following components are considered within the model: a lumped mass and inertia located at the top-end of the drill-pipes; a concentrated mass and inertia attached to the lower end of the BHA, to simulate the drill-bit (Fig. 4.1). The BHA is also considered as a Cosserat rod with different geometrical properties than those of the drill-string. The set of parameters employed in the simulations, such as the material and geometrical properties, are given in Table 4.1. A linear elastic isotropic material model is used, which means that there is no internal damping being considered.

4.2.1

Rotary speed control

An optimal drilling operation implies that the drill-string angular speed at the bit, ω , matches the target speed Ω . With this aim, the same approach proposed in the works of [20, 69] is followed.

A control strategy is implemented via a proportional-integral controller (PI-Controller) at the top drive. The response of the PI controller in terms of torque at the top of the drill-string is introduced as a boundary condition at the upper end.

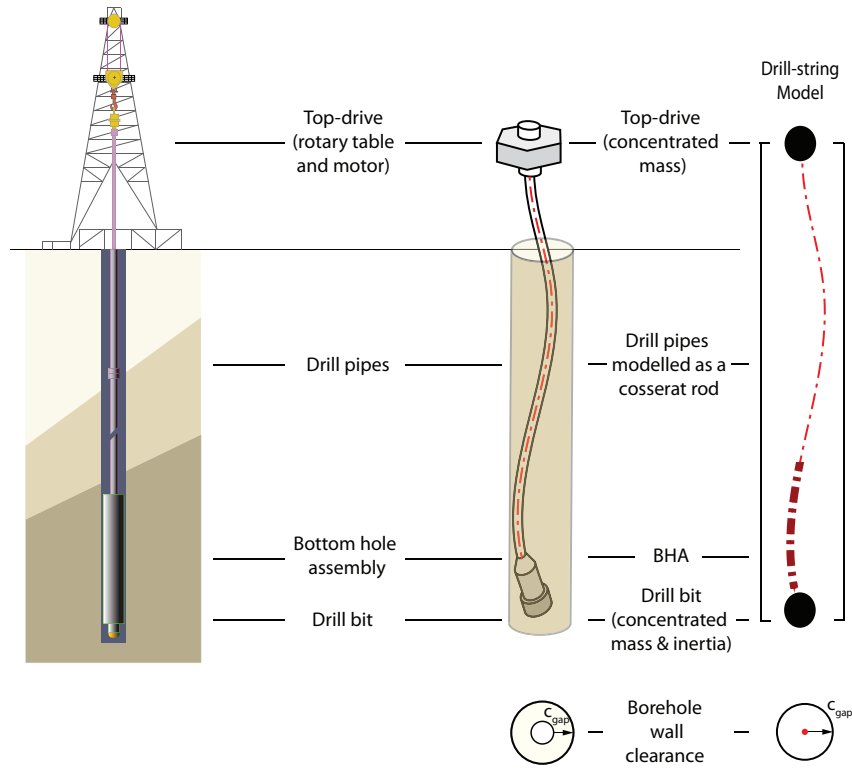


Figure 4.1: Sketch of the proposed drill-string model.

Variable	Symbol	Value	Units
Mesh size	-	200	elements
Mass density	ρ^o	$7.85 \cdot 10^3$	kg m^{-3}
Standard Gravity	g	9.81	m s^{-2}
Elastic modulus	E	$2.10 \cdot 10^{11}$	N m^{-2}
Shear modulus	G	$69 \cdot 10^9$	N m^{-2}
DS + BHA length	L	2500	m
DS & BHA outer radius	r_{ext}	$7.3264 \cdot 10^{-2}$	m
DS & BHA radius	r_{int}	$6.1512 \cdot 10^{-2}$	m
TD rotary inertia	J_{top}	$2.9 \cdot 10^3$	kg m^2
Bit rotary inertia	J_{bit}	none	kg m^2
Bit rotary mass	J_{bit}	none	kg m^2
Borehole-wall clearance	c_{gap}	0.01	m

Table 4.1: Basic geometrical and material parameters for the drill-string, based on the values presented in [20].

$$T_{top} = k_p(\Omega - \omega) + k_i((\Omega \cdot t - \phi)) \quad (4-1)$$

Variable	Symbol	Value	Units
Target Speed	Ω	100	rpm
Proportional constant	k_p	200	N m s rad ⁻¹
Integral constant 1	k_i	100	N m rad ⁻¹

Table 4.2: Adopted parameters for the PI controller based on the values presented in [20].

4.2.2

The contact model for an arbitrary borehole geometry

The simplest case to implement contact with the borehole wall is that of a straight vertical geometry. In such configuration, the borehole can be represented by a cylinder of equation $x^2 + y^2 = c_{gap}^2$, where c_{gap} is the clearance between the outer radius of the drill-string and the borehole wall. Then, detecting whether contact occurs is straightforward: if the coordinates of the position vector are introduced into the previous equation, $r_x^2 + r_y^2 \geq c_{gap}^2$ implies contact with the wall.

When dealing with geometries other than straight, finding a mathematical expression for the borehole wall is not so simple. To model an arbitrary geometry, the authors propose to define the borehole shape by considering a centreline curve and clearance.

As per Fig. 4.2, let \mathcal{J} be the borehole centreline curve defined parametrically by $\mathbf{r}_p(p)$; let A be a point at the drill-string; P be a point at the borehole centreline; $\mathbf{r}_P = \mathbf{r}_p(p = P)$ be the position vector of \mathcal{J} at P ; \mathbf{t}_P be the tangent vector to the borehole centreline at $p = P$; \mathbf{r}_r be a relative position vector from P to A . Note that, so far, the cross-section associated to parameter $p = P$ does not necessarily contain A .

The tangent at the point P and the relative position between P and A are

$$\mathbf{t}_P = \left. \frac{d\mathbf{r}_p}{dp} \right|_{p=P} \quad (4-2)$$

$$\mathbf{r}_r = \mathbf{r} - \mathbf{r}_P. \quad (4-3)$$

Given that the sections of the borehole are normal to the tangent vector \mathbf{t}_c , the contact problem in an arbitrary borehole geometry involves finding the right value for p so that the section at $\mathbf{r}_p(p)$ contains A . Based on geometrical considerations, \mathbf{r}_r , A and P , should all lie within the same plane as shown in Fig. 4.2. Thus, the following algebraic equation, to be solved together with the

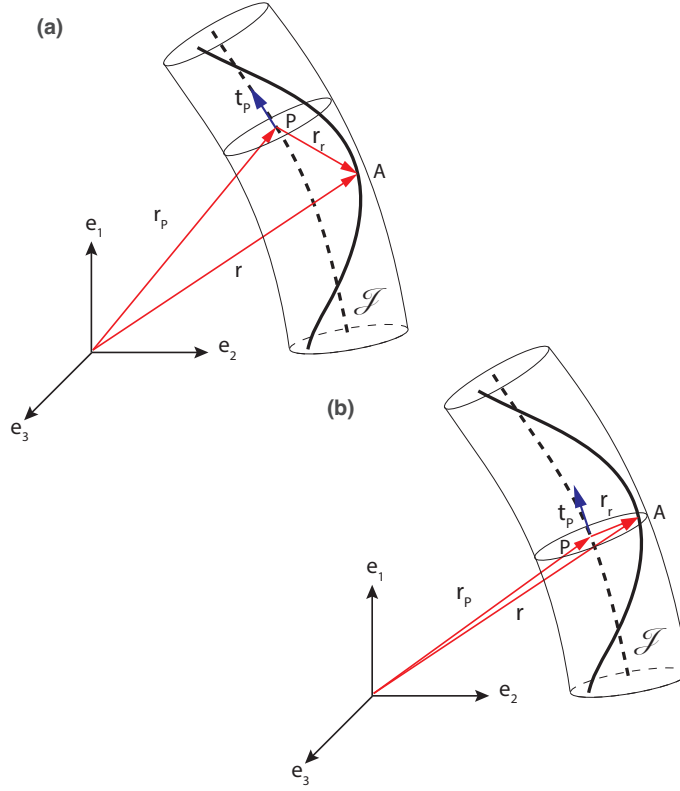


Figure 4.2: The contact model. (a) Sketch of the relative position vector for an arbitrary cross-section. (b) Sketch of the relative position vector for the sought contact condition. In both cases, $\mathbf{r}_p(P)$ is the relative position of the cross-section mass centre at P ; \mathbf{t}_P is both a tangent vector to the borehole centreline and a normal vector to the cross-section; and \mathbf{r}_r is a relative position vector from P to A where A is a contact point between the borehole wall and the drill-string.

equations of motion for the Cosserat rods, is used the position of the borehole at which contact happens:

$$\mathbf{r}_r \cdot \mathbf{t}_p = 0. \quad (4-4)$$

Finally, the contact model is introduced as a distributed force \mathbf{f}_s that depends on the scalar soil penetration function f_{sp} and some elastic constant k_s . The essence of the mathematical formulation is based on the penalty method to solve the Signorini problem [70, 71]. The equations read

$$f_{sp} = \begin{cases} 0 & \text{if } |\mathbf{r}_r| - c_{gap} \leq 0 \\ |\mathbf{r}_r| - c_{gap} & \text{if } |\mathbf{r}_r| - c_{gap} > 0 \end{cases} \quad (4-5)$$

$$\mathbf{f}_s = -k_s f_{sp} \hat{\mathbf{r}}_r. \quad (4-6)$$

4.2.3

The friction model

There exist many different mathematical formulations to characterise friction with the Stribeck effect that is presented as good alternatives to modelling Coulomb friction. For instance, in [69] a friction model that accounts for the Stribeck effect, i.e the transition between static and dynamic friction, is used. Unfortunately, the parameters involved have been calibrated to model bit-rock interaction at the bit, an effect that will not be present in the case under analysis where there is no contact between the bit and the rock. Moreover, a definition of the six parameters required in the aforementioned friction model is not straightforward. For this reason, a formulation based upon four parameters [72], each with a simple physical interpretation, is adopted. The formulation reads

$$k_{fr}(v_c) = \frac{\mu_d v_c \sqrt{(v_c^2 + \epsilon_c/n_c^2)} + 2(\alpha_c/n_c) v_c}{v_c^2 + 1/n_c^2} \quad (4-7)$$

$$\alpha_c = \sqrt{\mu_s(\mu_s - \mu_d)}. \quad (4-8)$$

In this mathematical description, the friction coefficient k_{fr} is a function of the velocity modulus ($v_c = ||\mathbf{v}_c||$) based upon four parameters: the static and dynamic friction coefficients, μ_s and μ_d respectively; a regularisation factor n_c that modifies the stiffness of the regularization; and ϵ_c , a fixed small parameter (e.g. $\epsilon_c = 10^{-4}$).

A schematic representation of the previous equation is given in Fig. 4.3 with the parameters $\mu_s = 0.30$, $\mu_d = 0.15$, $\epsilon_c = 10^{-4}$, $n_c = 5$.

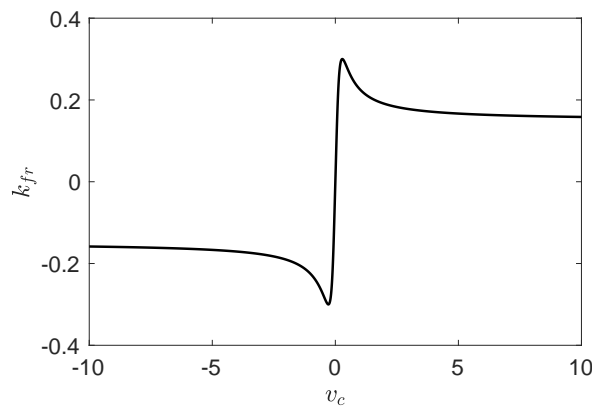


Figure 4.3: Schematic representation of the variation of the coefficient of friction k_{fr} with the velocity v_c

In the drill-string model, contact is assumed to occur at a single point where the drill-string and the borehole wall touch. The magnitude of the

friction force f_{fr} along the drill-string is proportional to the magnitude of the normal force f_s . Therefore, it is also proportional to the friction coefficient k_{fr} which depends, in turn, on the velocity magnitude v_c , at the point where the structure-soil interaction occurs. As for the direction, the frictional force acts in opposition to the velocity vector. Consequently, \mathbf{f}_{fr} takes the form

$$\mathbf{f}_{fr} = -k_{fr}(v_c) k_s f_{sp} \hat{\mathbf{v}}_c, \quad (4-9)$$

and

$$\mathbf{v}_c = \dot{\mathbf{r}} + \boldsymbol{\omega} \times r_{ext} \hat{\mathbf{r}}, \quad (4-10)$$

with \mathbf{v}_c being the velocity vector and $\hat{\mathbf{v}}_c$ a unitary vector.

For this particular approach, the velocity vector is mathematically defined by Eq. (4-10), where r_{ext} represents the external radius of the cross-section.

The frictional torque \mathbf{m}_{fr} is obtained by considering the moment provoked by the frictional force with respect to the origin of the unit vector $\hat{\mathbf{r}}$.

$$\mathbf{m}_{fr} = r_{ext} \hat{\mathbf{r}} \times \mathbf{f}_{fr}. \quad (4-11)$$

If $\dot{\mathbf{r}}$ in (4-10) is neglected, the frictional torque can be simplified into the expression further stated. Note that this condition could belong to the case of an off-bottom drilling start-up where the borehole is hanging and not advancing in depth, if lateral motion is not taken into account.

$$\mathbf{m}_{fr} = -k_{fr}(\omega) k_s r_{ext} f_{sp} \hat{\boldsymbol{\omega}}. \quad (4-12)$$

4.2.4

The distributed forces in the equations of motion

With the previous definitions, the distributed forces in the equations of Chapter 2 take the form

$$\mathbf{f}_n^R = -\rho_0 A g \hat{\mathbf{k}} + \mathbf{f}_{fr}, \quad \mathbf{f}_m^R = \mathbf{m}_{fr}. \quad (4-13)$$

The initial conditions ($t = 0$) are those corresponding to a configuration at rest. The boundary conditions correspond to a structure that is fully hanging from the top, and free at the lower end.

4.3

Comparison and calibration of the friction model

To find a suitable value for the regularised friction parameter k_{fr} , a friction model based on [29, 66] will be compared against a modified version of the frictional torque described by Eq. (4-12). The authors of [29, 66] analyse

the dynamics of a drill-string at an off-bottom start-up condition. With this purpose, they employ a straight vertical beam model to simulate the curved borehole geometry. This is achieved by introducing a frictional torque law that is proportional to the dogleg severity (DLS), i.e. the amount of change in inclination, in degrees, per 30 meters. It is important to note that [29] presents a model that has been successfully validated with field data. Therefore, the magnitudes of the resulting frictional forces should match those found in the field.

The present study is based on the original geometry depicted in Fig. 4.4, where three parts are distinguished: one vertical segment, one curved, and one inclined. The dynamics of a drill-string which is at rest at the beginning of the simulations, with no contact at the bit, are analysed. The maximum static frictional force based on [29] is shown in Fig. 4.5. For the simulation, a dynamic to static ratio $\mu_d/\mu_s = 0.5$ is adopted. The parameters $n_c = 5$ and $e_c = 10^{-4}$ are used. The transition from a static to a dynamic friction torque is regularised following an expression analogous to Eq. (4-7). The properties of the drill-string shown in Table 4.1 are used.

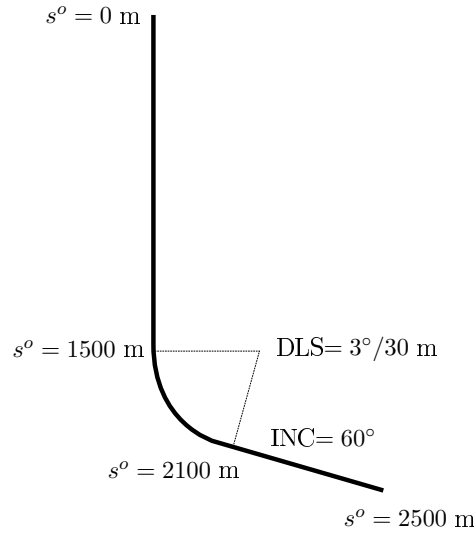


Figure 4.4: Geometry of well A presented in [29]. The well is composed of one vertical segment (1500 m), one curved (600 m) and another inclined (400 m).

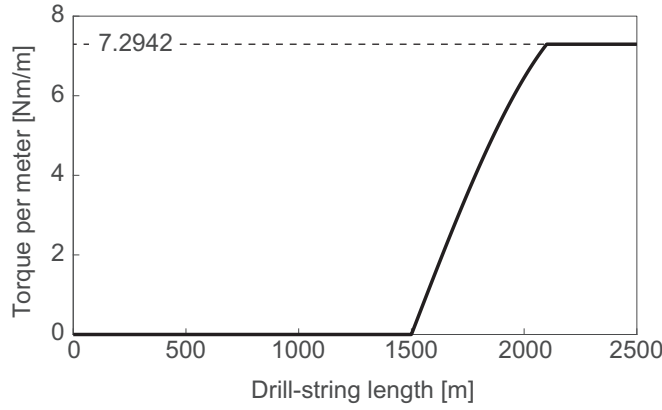


Figure 4.5: Applied distributed torque for the model proposed in [29] vs drill-string length. The Maximum torque under static friction is shown by the dashed line.

4.3.1

Qualitative analysis

A qualitative analysis concerning the shape of a diagram showing the variation of the frictional force along the drill-string is carried out. The solution is compared with that presented in [29]. As aforementioned, the frictional force is proportional to the penetration, thus to verify the similarities among models, their shape is compared.

For this task, the spatial discretisation is made in COMSOL [68], where a mesh composed of 200 Hermite finite elements of order 3 is employed. It is shown in Fig. 4.6 that such density is sufficient to attain convergence, as the solution does not vary significantly. Next, in Fig. 4.7, the friction law described in [29] is compared against the proposed friction model. The curves for different values of the soil elastic constant k_s are depicted. Also, these curves have been scaled so that the magnitude at the bit is unitary.

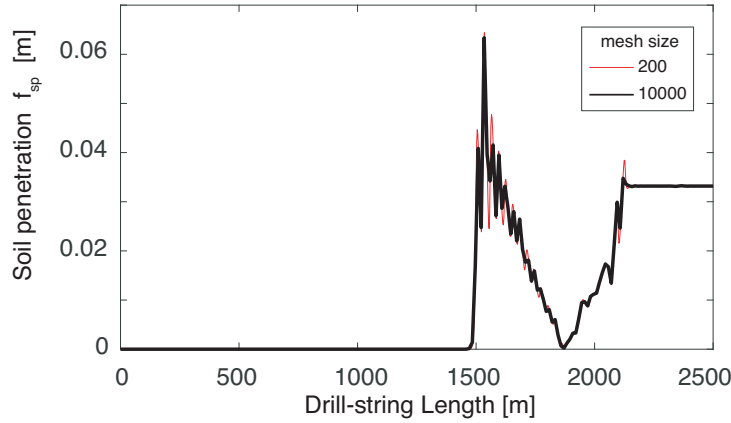


Figure 4.6: Soil penetration vs drill-string length for the Cosserat rod (CR) model. The elastic constant $k_s = 10^7 \text{ N/m}^2$ is used.

It is noted that the presented curves are both constant in the straight inclined part of the drill-string, and only differ in shape on the curved region. For this reason, the friction value at the bit ($s^o = 2500 \text{ m}$) will be used to adjust the proposed friction model. The profile was, with the Cosserat approach, obtained directly from the dynamics, without the need to add any extra hypothesis. In the transition between these two constant parts, different behaviour is observed. While with [29] the graph shows a smooth increasing variation, with the new friction model it shows an increased magnitude on the region where the structure enters into the curved borehole and begins to bend; a small region where the friction goes to a minimum, closer to the end of this transition area, after which it increments against to reach the constant value over assumed in the straight inclined part of the borehole.

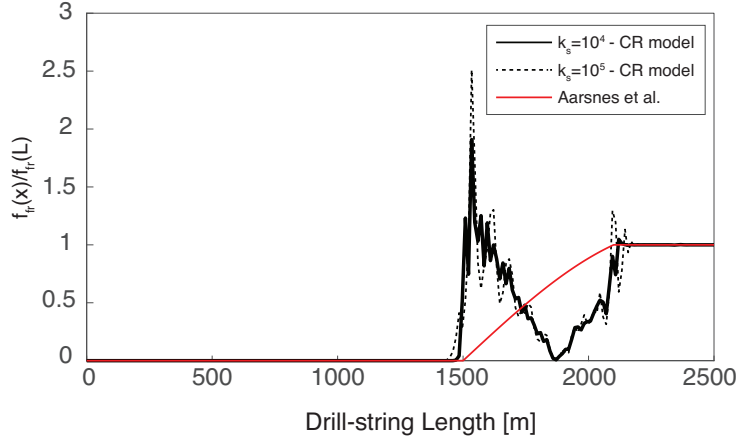


Figure 4.7: Comparison between a Cosserat rod (CR) model with the proposed alternate friction model and a CR model with friction following the proposal of Aasnes et al. in [29]. The relative soil penetration vs drill-string length is shown for the CR model for: $k_s = 10^4$ in solid black line; $k_s = 10^5$ in dashed black line; for the model of Aarsnes et al., [29], in red line. A mesh of $N = 200$ elements is employed.

4.3.2

Friction model calibration

In order to calibrate the required friction parameters that define $k_{fr}(v_c)$, the model provided in [29] is employed as a reference, recalling that it has been validated with field measurements. Therefore, it is safe to assume that the friction torques that were calculated in the reference match those that occur in real working conditions. Then, the parameters for the friction model proposed in Section 4.2.3 are calibrated with the value of the static friction k_{frS} at $s^o = 2500$ m, following an expression derived from (4-12). However, for the calibration $k_{frS} = \mu_S$. This means that, only for calibration purposes, the regularisation in (4-7) and (4-8) is not employed. In this case,

$$\mu_S = \frac{\|\mathbf{m}_{frS}\|}{k_s f_{sp} r_{ext}} \Big|_{s^o=2500 \text{ m}} \quad (4-14)$$

As already stated, in this equation μ_S is the static friction coefficient, $\|\mathbf{m}_{frS}\|$ is the magnitude of the static friction torque, k_s is a soil rigidity constant, r_{ext} the external radius of the associated cross-section, and f_{sp} is the penetration given by the penalty function introduced in (4-5). In [29], a dynamic-to-static friction ratio of 0.5 is also considered.

The values of the soil constant k_s should be chosen based on field measurements. In this case, due to the lack of field data, different values

of k_s are assessed. Then, their corresponding static friction coefficient μ_S is calculated so that the magnitude of the resulting static friction torque $\|\mathbf{m}_{f_{rS}}\|$ matches that employed in [29]. Fig 4.8 shows the magnitudes of f_{sp} for the values of k_s that were tested. It was found that for $10^4 \text{N/m}^2 \leq k_s \leq 10^7 \text{N/m}^2$, the static friction coefficient is $\mu_S = 0.30$.

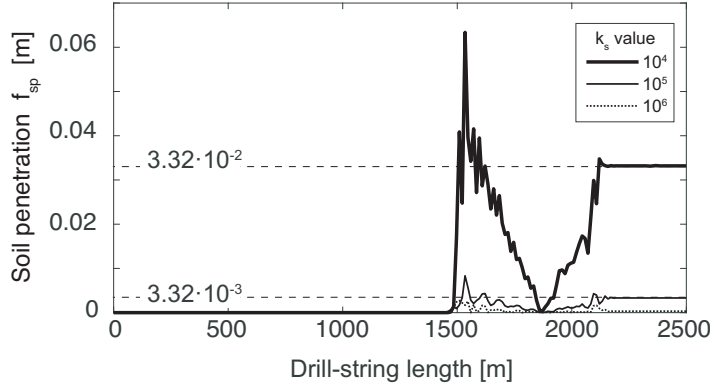


Figure 4.8: Soil penetration vs drill-string length for the Cosserat (CR) model with the proposed alternate friction model. Solutions for different values of the elastic constant k_s are superimposed. A mesh of $N = 200$ elements is employed. For each case, the penetration values at the bit are shown by a dashed line.

4.4

Simulations concerning a curved borehole

A comparison between the present Cosserat rod (CR) model with contact and friction, and a reference (R) model following the soft-string approach presented in [29] is performed. The problem of an off-bottom startup (at rest at $t = 0$ s) in the curved borehole geometry described in Figure 4.4 is analysed. The set of material and geometric properties from Table 4.3 is employed in all simulations. In the R model, the transition between the static and dynamic friction obtained by following [29] is regularised by employing an expression in the form of (4-7), where two of the variables involved are the static and dynamic friction torques calculated via the ad-hoc hypothesis. In the CR model, the additional set of parameters $k_s = 10^6 \text{N/m}^2$, $\mu_S = 0.30$ are used (see Section 4.3.2).

On the one hand, [29] presents an alternative to simulate the dynamics of drill-strings in curved bore-hole geometries where a fictitious straight beam is employed (soft-string model), and the geometry of the curve is taken into account by means of an ad-hoc hypothesis. In this case, the friction force and torque are considered proportional to the dog-leg severity (DLS). The beam is

Table 4.3: Basic geometrical and material parameters for the drill-string, based on the values presented in [20].

Variable	Symbol	Value	Units
Mesh size	-	150	elements
Drill-string mass density	ρ_0	$8.01 \cdot 10^3$	kg m^{-3}
Drill-string length	L	$3.00 \cdot 10^3$	m
Drill-string outer radius	r_{ext}	$6.35 \cdot 10^{-2}$	m
Drill-string inner radius	r_{int}	$5.43 \cdot 10^{-2}$	m
Standard Gravity	g	9.81	m s^{-2}
Young's modulus	E	$2.07 \cdot 10^{11}$	N m^{-2}
Poisson modulus	ν	0.30	-
Shear modulus	G	$7.96 \cdot 10^{10}$	N m^{-2}
Top-drive mass	M_{top}	$5.08 \cdot 10^4$	kg
TD rotary inertia	J_{top}	$5.00 \cdot 10^{02}$	kg m^2
BHA/Bit mass	M_{bit}	$5.00 \cdot 10^{03}$	kg
BHA/Bit rotary inertia	J_{bit}	$3.94 \cdot 10^{02}$	kg m^2
Borehole-wall clearance	c_{gap}	0.01	m

analysed via the classical angle of twist equations (1-D wave equation) for a straight beam, and the results are validated against field measurements.

On the other hand, the present CR model accounts for 3-D displacements in space (translations and rotations), with a contact detection technique that is suitable to simulate arbitrary bore-hole geometries. In this case, the inclusion of the friction effects is apparent: the magnitude is stated proportional to the contact force, which is intrinsic to the dynamics of a drill-string constrained to stay within the bore-hole (see section 4.2.2 and 4.2.3). The results for the simulations are shown in Figs. 4.9, 4.10, 4.11 and 4.12.

Fig. 4.9 shows the response in terms of angular speed w_3 (the component of ω in the longitudinal direction) vs. time is depicted. Even though, in essence, the friction formulation in the CR model differs from that of the R model (see Fig. 4.7), an excellent agreement is observed between the results for the stationary regime in both the time response (Fig. 4.9) and the frequency spectrum (Fig. 4.10). Appreciable differences are only found in the transient response. This shows that, while the approach proposed by [29] leads to a much simpler model, it is adequate for the resolution of this problem in the stationary regime.

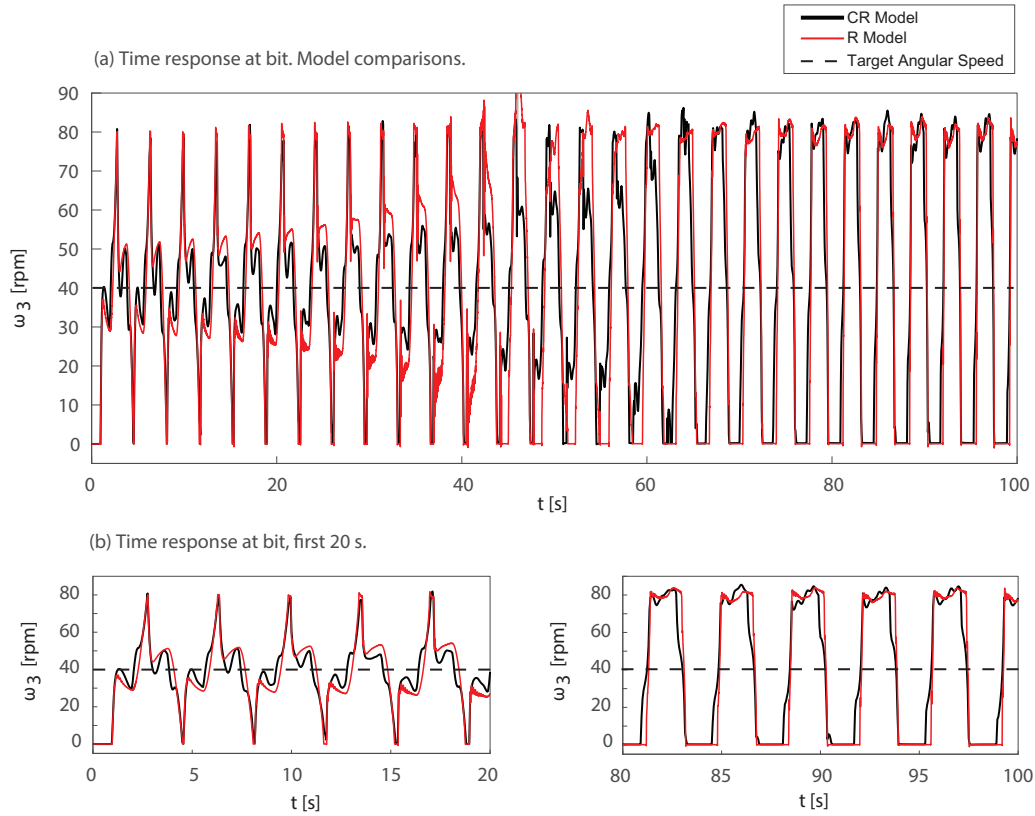


Figure 4.9: Comparison between the Cosserat rod (CR) model using the proposed friction law and the CR model using the friction as proposed in [29]. Angular speed ω_3 vs time a soil constant $k_s = 10^6 \text{ N/m}^2$, friction constant $\mu_s = 0.30$, mesh with 200 elements. (a) Duration of the simulation $t = 100$ s; (b) Zoom for $t = 0$ s to $t = 20$ s; (c) Zoom for $t = 80$ s to $t = 100$ s.

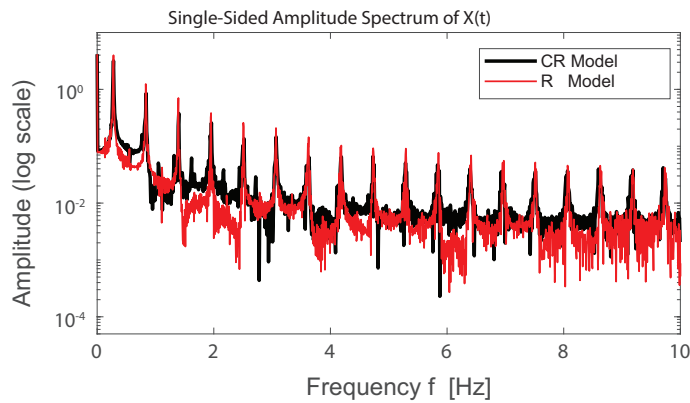


Figure 4.10: Frequency spectrum comparison between the Cosserat rod (CR) model (black line) and the model in [29] (red line). A mesh of $N = 200$ elements is employed.

Next, Fig. 4.11 shows the current configuration at different times. The

centreline of the rod is shown in black, and the section orientation is represented by the orientation of vector \mathbf{d}_1 , which is fixed to the cross-section at each point of the rod. Then, a change in the direction of \mathbf{d}_1 provides a visual representation of the twist along the drill-string length.

Fig. 4.12 depicts all the possible sets of internal forces and moments that act within the rod at time $t = 77.5$ s. The internal forces in the curved zone exhibit irregularities due to the intermittent contact and friction, which is to be expected. It should be noted that the CR model could prove advantageous as an exhaustive tool for the study of the dynamics of the drill-string dynamics, given that bending and shear are not neglected. It is worth mentioning that the analysed example (off-bottom) does not exhibit axial situations which could certainly couple with bending and torsion. In such case, the soft-string model would be insufficient to exhibit the complex oscillations, as well as to account for the buckling effect that may arise due to the WOB loads.

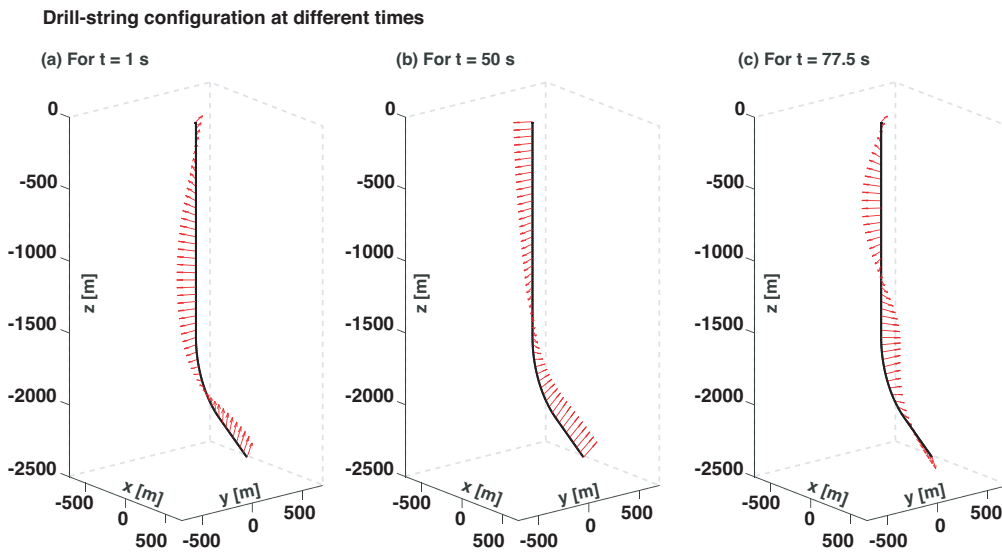
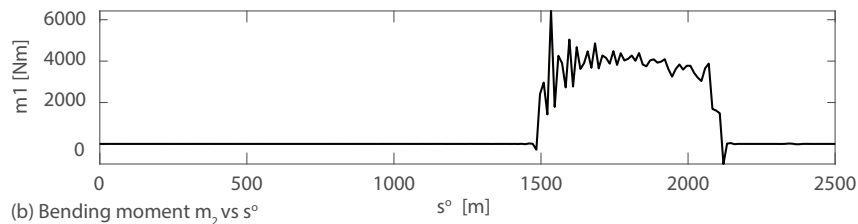


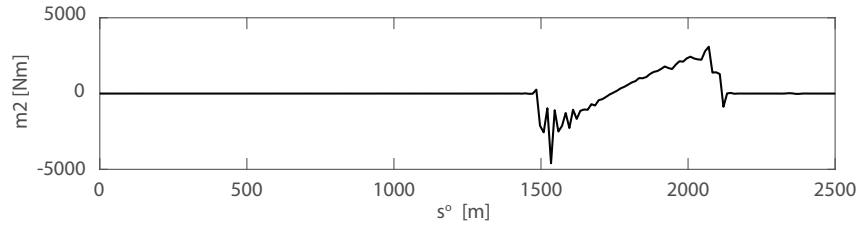
Figure 4.11: Drill-string configurations at different times (CR Model). The centreline of the rod is shown (black line), as well as section orientation through the field of the director $d_1(s_R)$ (red vectors), which is fixed to the cross-section at all times. (a) For $t = 1$ s; (a) For $t = 50$ s; (a) For $t = 77.5$ s.

Internal forces and moments at time $t = 77.5$ s

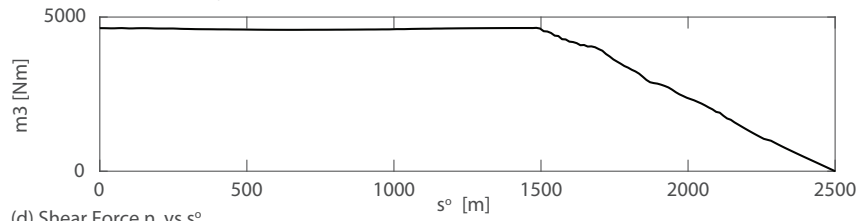
(a) Bending moment m_1 vs s°



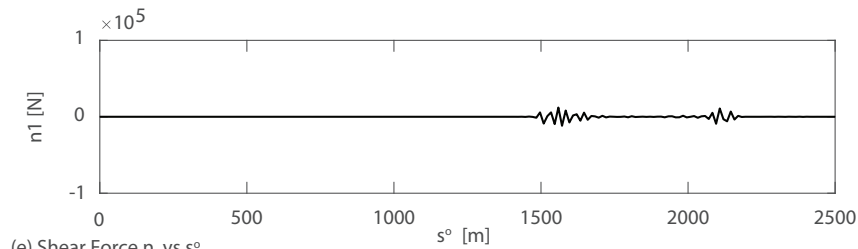
(b) Bending moment m_2 vs s°



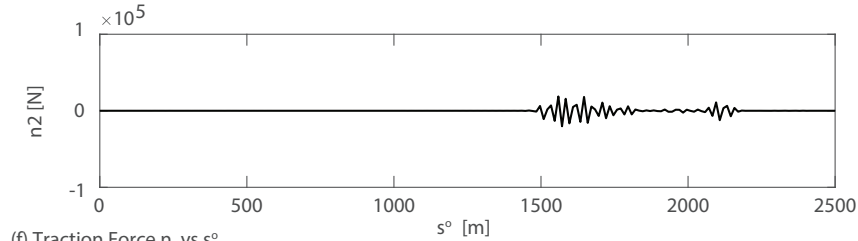
(c) Torsional moment m_3 vs s°



(d) Shear Force n_1 vs s°



(e) Shear Force n_2 vs s°



(f) Traction Force n_3 vs s°

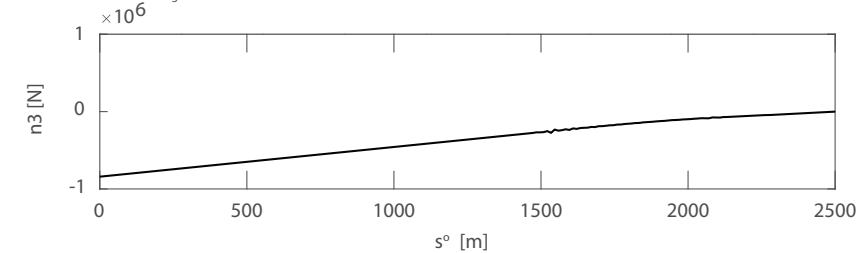


Figure 4.12: Internal forces and moments (CR Model) acting on the rod at $t = 77.5$ s. (a) Bending moment m_1 in Nm; (b) bending moment m_2 in Nm; (c) torsion m_3 in Nm; (d) shear force n_1 in N; (e) shear force n_2 in N; and (f) tensile force n_3 in N.

4.5

Final comments concerning this chapter

In this chapter, the Cosserat rod equations were implemented through their weak form (Appendix D) in COMSOL, a FEM software. First, a contact model for drill-string dynamics in arbitrary borehole geometries was presented. The borehole was successfully introduced in a parametric form, and the contact forces were calculated considering the soil to be fully elastic. Next, the normal force obtained from the previous contact model was used to define a friction model. The latter was calibrated with the wall friction value proposed in [29]. No ad-hoc hypotheses were used in the definition of the friction force, except for contact to occur at only one point at each cross-section. Later, the soft-string model from [29] for curved borehole geometries was compared against the model herein presented. A close agreement was observed for the results obtained in the time and frequency domains for the angular velocities in both models, verifying the applicability of such simplifying hypothesis in the case of study. Therefore, it has been shown that the present Cosserat model can successfully deal with drill-strings constrained in arbitrary borehole geometries. Also, given that the bending and shear are not neglected, it has the advantage of capturing the whole range of the dynamics.

It should be noted that other effects, such as bit-rock interaction during the drilling operation could be easily as a boundary condition at the bit, e.g. by following the approach in [69] or [14], what will be explored in the subsequent chapters. The CR model could prove an advantageous and exhaustive tool for drill-string dynamics, e.g. in a strain (i.e. stress) state analysis as well as service life prediction, given that bending and shear are not neglected. It is worth mentioning that the analysed example (off-bottom) does not exhibit axial situations which can certainly couple with bending and torsion. In such case, the soft-string model would be insufficient to exhibit the complex oscillations, as well as to account for the buckling effect that may arise due to the WOB loads.

Finally, the model was also verified against non-linear problems available in the literature, the results are shown in the Appendix B.1. These other verifications show that the simulations match known results of other problems involving large deformations.

In this chapter, a model to study drill-strings that accounts for the dynamics of the cutting is developed. For now, the Cosserat rod model is abandoned. Instead, a simpler continuous wave equation is considered for the torsional dynamics of the straight shaft, and 1-DOF is used for the axial behaviour.

The major novelties of the study presented in this chapter are: 1) the use of a new bit-rock interaction relation that does not restrict backward rotation of the bit nor bit-bounce, and that is dependent on the dynamics of the cutting blade, such as the depth-of-cut; 2) the use of an advection equation to avoid dealing with a system of delay-differential equations in the simulation of the cutting process; 3) the extension of the advection approach treated in the works of [14, 73] to allow rotation in both directions; 4) the combination of the previous items with a distributed approach for the torsional dynamics, with a formulation based on the known wave equation; 5) the inclusion of the 2-DOF model as a limiting case of the continuous model. For this purpose, a strategy considering an extra parameter α is used. All these aspects lead to a coupled non-linear formulation that can exhibit self-sustained vibrations associated with the regenerative cutting process.

The new model is compared, from a numerical point of view, with an established 2-DOF approach. For this task, five scenarios considering a 1200 m column with different friction parameters and top drive conditions are simulated.

Dissimilar predictions are observed in the simulations with the different approaches, showing a more complex response for the continuum model where higher frequencies are excited as well.

The results indicate that the more sophisticated model could capture other aspects of the dynamics that are neglected in the 2-DOF approach. Nevertheless, the approach herein presented has more value for mathematical comparison purposes, given that the model still retains a 1-DOF axial formulation which is yet unrealistic. Hence, the main use is to provide an interpretation on how to deal with the dynamics of the cutting and to make a first analysis as to how good are low-dimensional models at representing drill-strings.

The analysis is then continued in Chapter 6 where a fully continuous model is adopted.

The contents of this chapter are already published in [74].

5.1

Description of the problem

Deciphering whether a continuous or a discrete approach should be used to capture the dynamics of drill-strings is not evident. In fact, this has been the motivation for this thesis and Chapter 4, where a Cosserat rod model was used to study an off-bottom application case. Both discrete and continuous models can be found in the literature in studies involving experimental set-ups and in research papers that deal with real-scale columns. But only when dealing with experimental test rigs, like [35, 75, 76], it is apparent that a discrete approach can be employed: easily identifiable lumped elements within the mechanical system are present in such cases, and a few degrees of freedom (DOF) suffice to construct an accurate physical model. Unfortunately, this is not equally evident when real-scale drilling systems are studied.

Examples of low dimensional models were discussed in Chapter 1, and include [10, 11, 14–19], among others. The common linking factor of these works is that they assume that 1-DOF or 2-DOFs are sufficient to accurately model the torsional dynamics of a column that is at least some hundred meters long. The drawback of these models is that, given the low number of DOFs, they are limited in the amount of information that can be captured. In other words, the vibration modes that can be excited are restricted by the arbitrary selection of the number of DOFs.

Continuous models, such as [20–26, 40, 77, 78], do not suffer from the earlier limitations of discrete models, but they require more computational effort, in terms of time and memory occupied, to calculate an approximation to the solution.

Due to the diversity of treatments mentioned so far, it is unclear how well all these models perform at representing drill-strings. In this context, the aim of the present research is, first, to construct a continuous model for a 1200 m drill-string that includes the dynamics of the evolution of the oil-well and the soil that is being removed. This objective is aligned with the study performed in [14], where both the dynamics of drill-columns and the free-boundary problem considering the evolution of the soil are tackled. Second, to compare and assess the suitability of both approaches, continuous and discrete. The results of the simulations considering the continuous model are compared with those of the 2-DOF model based on the propositions of [14].

The use of the 2-DOF model of [14], with a 1-DOF torsional pendulum representation of a 1200 m drill-string, implies that a quasi-static assumption is used for the dynamics of the column. With this representation, it is not possible to simulate the travelling waves within the structure, nor to capture any resonance other than that with the fundamental frequency. As a consequence, it is presumed that the 2-DOF model may be unable to accurately capture the rich dynamics that arise in drill-strings, in which case a more sophisticated continuous approach should provide better results. In fact, this presumption is also sustained by the field data measurements published in [79], and the simulations in [80], where it is said that frequencies other than the fundamental one are excited in some stick-slip scenarios.

In the simulations, particular interest is paid to the torsional dynamics of the structure. The simulations are studied in the time domain, and in the frequency domain by performing a Fast Fourier Transform (FFT) of the signal of interest, the angular speed at the bit. In addition, the responses containing the axial speed and the axial position of the bit are also shown and the differences are pointed out.

The present chapter is organised as follows. First, the structural model for the drill-string is presented. Second, a bit-rock interaction model is built based on the definition of an instantaneous depth-of-cut. Third, a methodology to obtain the depth-of-cut that relies in solving the advection equation is introduced. Next, a particular non-oscillatory solution, herein called the nominal case, is studied. After that, the results of five simulation scenarios are analysed to compare the two models. Finally, some conclusions are drawn.

5.2

The drill-string models

Two different models to study the dynamics of a drill-string will be used. A sketch of the two proposals is shown in Fig. 5.1. Each approach is comprised of two aspects: the structural model that is described in this section, and the bit-rock interaction model detailed in Section 5.3. Model M1 follows the established structural 2-DOF approach employed in [14]: it considers 1-DOF for the axial dynamics and 1-DOF for the torsional dynamics, with a lumped mass M , lumped inertia I , spring constant C . Model M2 condenses all the aforementioned novelties of this chapter. It employs a continuous approach for the torsional dynamics, while the formulation for the axial one remains the same 1-DOF strategy. As depicted in Fig. 5.1, two different cross sections are considered, with J_1 and J_2 representing the geometric moment of inertia of the drill-pipes and the bottom hole assembly (BHA), respectively. At the lower

end, a lumped inertia I_2 is also considered. G_1 and G_2 are the shear elastic moduli, ρ_1 and ρ_2 the densities of the material. $\Theta(t)$ is the rotation imposed at the top of the drill.

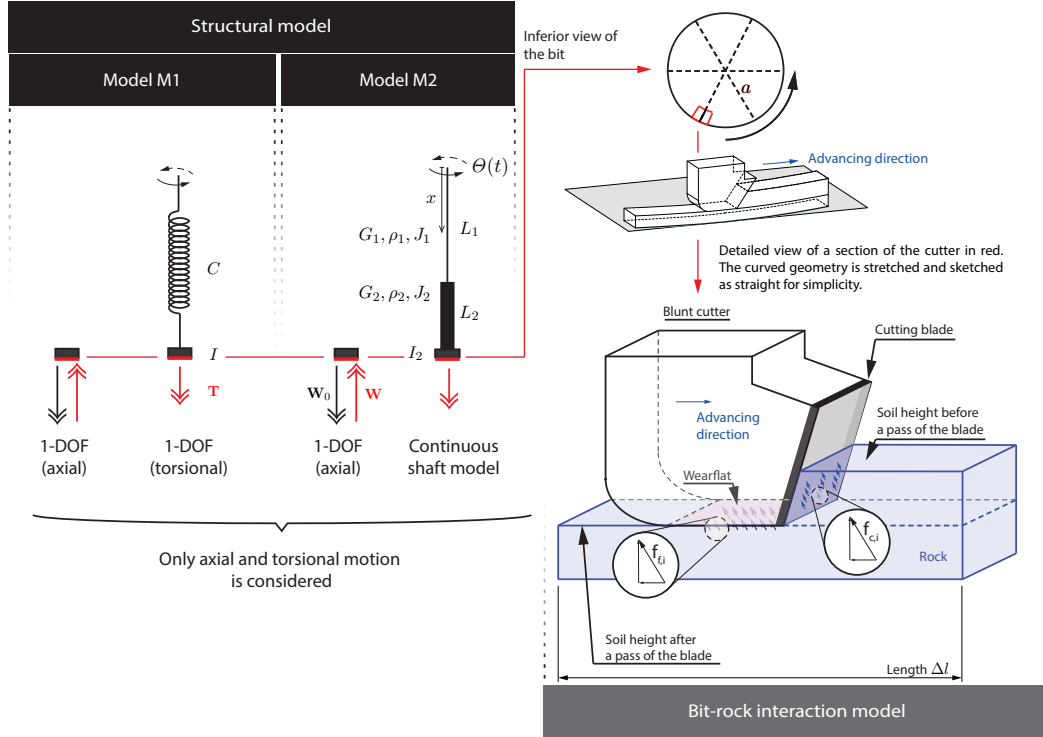


Figure 5.1: Representation of the models employed. In this figure, special attention is given to the structural aspects of the formulation. Model M1 considers 1-DOF for the axial dynamics and 1-DOF for the torsional dynamics. Model M2 employs the same formulation for the axial dynamics, but a continuous approach for the torsional one. To the right side of the figure, a sketch of a cutter blade is shown. This is used in the definition of the bit-rock interaction model, in section 5.3, where a zoomed version of this part of the sketch is shown, along with a detailed description. The force \mathbf{W} and the torque \mathbf{T} are related to the traction vectors $\mathbf{f}_{f,i}$ and $\mathbf{f}_{c,i}$ via integration over the contact areas.

5.2.1

Model M1 and M2: the axial dynamics

In both scenarios, M1 and M2, the axial dynamics are described by

$$M \frac{d^2 U}{dt^2} = W - W_0, \quad (5-1)$$

where M is a lumped mass, U the position of the bit, W_0 a constant representing the difference between the submerged weight and the hook load and W is the modulus of the reaction force \mathbf{W} due to the bit-rock interaction associated to the cutting process (see Section 5.3 for more details).

5.2.2

Model M1: The torsional dynamics

The equation employed to simulate the column in the lumped model (also used in [14]) is given by

$$I \frac{d^2 \Phi}{dt^2} + C(\Phi - \Theta) = T, \quad (5-2)$$

where Φ is the angular displacement of the bit, C is a torsional spring constant that represents the set of drill-pipes, and I is the inertia of the BHA. T is the modulus of the torque-on-bit \mathbf{T} , which is yet to be defined (see Section 5.3 for more details).

5.2.3

Model M2: The torsional dynamics

A continuous uni-dimensional description of the torsional problem is used in model M2. The behaviour of the elastic medium is described by the following wave equation [81, 82] :

$$G_j J_j \frac{\partial^2 \Phi_j}{\partial x_j^2} = \alpha \rho_j J_j \frac{\partial^2 \Phi_j}{\partial t^2}, \text{ with } j = \{1, 2\}, \quad (5-3)$$

with domains $x_1 \in [0, L_1]$, and $x_2 \in [L_1, L_1 + L_2]$, and $\alpha = 1$. The problem is completed by the following boundary conditions:

$$\begin{aligned} \Phi_1(x_1 = 0, t) &= -\Theta(t), \\ \Phi_1(x_1 = L_1, t) &= \Phi_2(x_2 = L_1, t), \\ G_1 J_1 \frac{\partial \Phi_1}{\partial x_1}(x_1 = L_1, t) &= G_2 J_2 \frac{\partial \Phi_2}{\partial x_2}(x_2 = L_1, t), \\ G_2 J_2 \frac{\partial \Phi_2}{\partial x_2}(x_2 = L_1 + L_2, t) &= T - I_2 \frac{\partial^2 \Phi_2}{\partial t^2}(x_2 = L_1 + L_2, t), \end{aligned} \quad (5-4)$$

where $\Phi_j = \Phi_j(x_j, t)$ defines the angular displacement of the column, $\Theta(t)$ is an imposed rotation at the top, T is the modulus the torque-on-bit \mathbf{T} , which is yet to be defined (see Section 5.3), and I_2 stands for a lumped inertia at the lower end.

5.3

The bit-rock interaction model

In the previous section, two dynamic models for simulating drill-strings have been presented, but the contact forces and torques associated with the interaction of the bit with the rock remain to be determined. For this reason,

first, the bit-rock interaction model used in [14] is briefly described and the hypotheses employed are discussed. The authors of the present work find that some improvements over the assumptions employed in the reference can be made. Therefore, second, a new bit-rock interaction model is introduced. The model further explores the ideas employed in [14].

The reference [14] defines a bit-rock interaction relation where two main effects are considered in the cutting process: the forces acting at the cutter blade, and the forces acting at the wear-flat of a blunt polycrystalline diamond compact (PDC) bit. These forces are calculated in terms of four characteristic rock parameters. The bit-rock relations are based on the interpretation of the data in [83], which provide results regarding the performance of a PDC bit obtained from a laboratory drilling test at simulated down-hole conditions. These relations were used in a 2-DOF model with the intention of simulating the dynamics of a drill-string.

Let ω_b stand for the bit angular speed, v_b its axial speed and d_i for the instantaneous depth-of-cut of the cutter “ i ” (a measure of how much soil is being removed). The proposal developed in 2007 by Richard et al. [14] accounts for the following cutting conditions:

- If $d_i > 0$, $\omega_b > 0$ and $v_b > 0$, the driller is operating within the “normal cutting” regime, and both the cutter blade and the wearflat are in contact with the rock. The magnitude of the contact forces reaches their maximum value;
- If $d_i > 0$, $\omega_b > 0$ and $v_b < 0$, the bit is moving up and the wearflat has lost contact with the bit, thus the only interaction occurs at the cutting blade;
- If $d_i > 0$, $\omega_b > 0$ and $v_b = 0$, the system experiences axial stick. This means that, axially, the bit stops. During this period, the contact force at the wearflat takes a value between its maximum and zero;
- If $d_i > 0$, $\omega_b = 0$ the bit is in an absolute stick phase, remaining totally immobile. During this phase the axial speed is exactly $v = 0$;
- $d_i = 0$, $\omega_b > 0$ the bit is in “sliding mode”. It is not penetrating the soil at all, and there are no forces acting on the cutter blade;
- $d_i < 0$, corresponds to the “off-bottom” case where all forces acting on the cutter vanish. This state corresponds to the bit-bouncing condition.

In that model, the forces that intervene are defined in terms of four characteristic constant parameters: the rock contact strength σ , which is the saturated contact pressure on the wearflat; the intrinsic specific energy ϵ , which

is, according to [14, 84], a measure of the amount of energy spent to cut a unit volume of rock during one minute of operation, although it is actually measured in units of work (thus it is not formally an energy which is why some name, like rock cutting strength, would be more suitable); the cutter inclination coefficient ζ ; and the coefficient of friction μ .

The authors of [14] mention that, for the sake of simplicity, it is assumed that “the frictional component of the torque is sufficient to hinder any backward rotation of the bit”, which means that $\omega_b < 0$ cannot occur. This assumption implies that the magnitude of the torque (acting at the wearflat) does not have an upper limit, thus it can take up to an infinite value in order to avoid the bit from rotating backwards, what looks unrealistic. In this work, such behaviour is expected as a result from the dynamics itself rather than an outcome of an imposed assumption.

5.3.1

The proposed interaction model

In what follows a new bit-rock interaction model that can deal with backward rotation is introduced, taking the research conducted in [14] as a reference, but abandoning the hypothesis restricting backward rotation of the bit ($\omega_b < 0$). To such purpose, consider a blunt cutter, such as the one depicted in Fig. 5.2. The contact of the blunt cutter i occurs at: the contact area between the rock and the cutting blade $A_{c,i} = a_i d_i$, where a_i is the width of the cutter blade which coincides with the bit radius and d_i is the instantaneous depth-of-cut; and the contact area between the wearflat and the rock $A_{f,i} = a_i l_i$, where l_i is the wearflat length. The latter is associated with the fact that the cutter is worn, whereas a sharp cutter would not present a wearflat contact area. In the new model, the traction vectors $\mathbf{f}_{c,i}$ and $\mathbf{f}_{f,i}$ acting at the contact regions (cutter and wearflat, respectively) are obtained from the following characteristic variables:

- The rock contact strength function $\sigma = \sigma(\omega_b, v_b)$, defined in terms of two contact strength parameters σ_1 and σ_2 , and the small regularisation constants c_1 and c_2 ;
- The rock intrinsic specific energy function $\epsilon = \epsilon(\omega_b)$, that depends on the intrinsic specific energy parameter ϵ_1 and a regularisation constant c_3 ;
- the cutter inclination coefficient ζ ;
- the coefficient of friction μ .

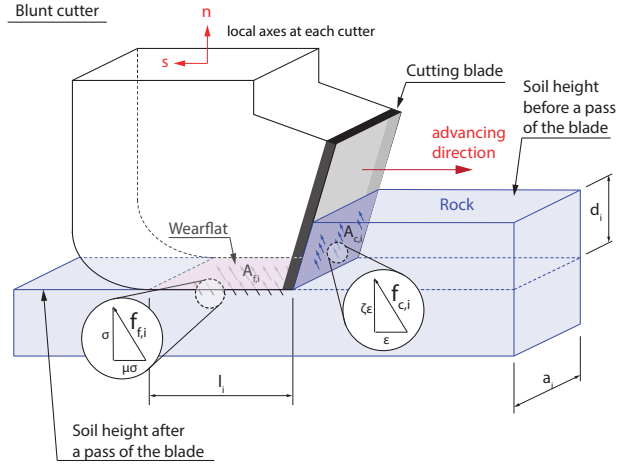


Figure 5.2: A single cutter i is depicted. The traction vectors $\mathbf{f}_{f,i}$ and $\mathbf{f}_{c,i}$, acting on the wearflat and the cutting blade, respectively, are drawn. These vectors are defined in terms of the functions $\sigma(\omega_b, v_b)$, that defines the contact pressure at the wearflat, and $\epsilon(\omega_b)$, an intrinsic specific energy of the rock. The parameter ζ defines the inclination of the cutting force, μ is the coefficient of friction, l_i is the wearflat length, and d_i is the instantaneous depth of cut.

With the definition that ω_b and v_b are the torsional and axial speed of the bit, the expression for the functional form of $\sigma(\omega_b, v_b)$ and $\epsilon(\omega_b)$ is given by:

$$\sigma(\omega_b, v_b) = \begin{cases} 0 & v_b \leq 0 \\ \frac{\sigma^*(\omega_b)}{c_1} v_b & 0 < v_b < c_1 \\ \sigma^*(\omega_b) & v_b \geq c_1 \end{cases} \quad (5-5)$$

with

$$\sigma^*(\omega_b) = \begin{cases} \sigma_2 & \omega_b \leq 0 \\ \sigma_2 + \frac{\sigma_1 - \sigma_2}{c_2} \omega_b & 0 < \omega_b < c_2 \\ \sigma_1 & \omega_b \geq c_2 \end{cases} \quad (5-6)$$

and

$$\epsilon(\omega_b) = \begin{cases} 0 & \omega_b \leq 0 \\ \frac{\epsilon_1}{c_3} \omega_b & 0 \leq \omega_b \leq c_3 \\ \epsilon_1 & \omega_b \geq c_3. \end{cases} \quad (5-7)$$

A sketch showing the shape of $\sigma(\omega_b, v_b)$ and $\epsilon(\omega_b)$ is depicted in Fig. 5.3. The graphs depict a model for the behaviour of the characteristic resistance capacity of the rock when cutting is taking place (for $\omega_b > 0$ and $v_b > 0$), as well as its resistance capacity while contact without cutting occurs (for $\omega_b \leq 0$ and $v_b \leq 0$), and a regularised transition between these two regimes. In what comes next, the previous definitions are used to obtain the resulting forces and

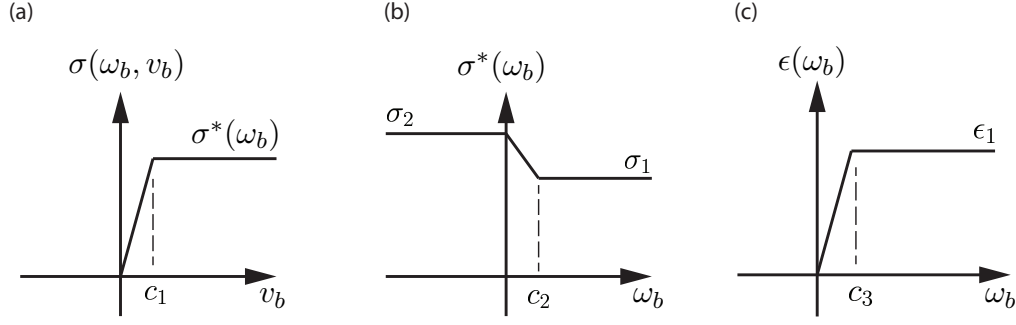


Figure 5.3: (a) The functional form of $\sigma(\sigma^*(\omega_b), v_b)$ is plotted for a fixed value of σ^* . (b) The form of $\sigma^*(\omega_b)$ is depicted. σ_1 and σ_2 are two parameters associated with the rock contact strength. (c) The form of $\epsilon(\omega_b)$. ϵ_1 is a parameter called the rock intrinsic specific energy. c_1 , c_2 and c_3 are some small regularisation constants.

torques that act on the bit. The width of each cutter a_i is considered equal to the radius of the bit, a . In total n_b cutters are employed. First, the resultant acting on the cutter i is obtained in (5-8) and (5-9):

$$\begin{aligned} \mathbf{F}_{c,i} &= \int_{A_{c,i}} \mathbf{f}_{c,i} dA_{c,i} \\ &= \int_{A_{c,i}} \left(\epsilon(\omega_b) \zeta \mathbf{n} + \epsilon(\omega_b) \mathbf{s} \right) dA_{c,i} , \end{aligned} \quad (5-8)$$

$$\begin{aligned} \mathbf{F}_{f,i} &= \int_{A_{f,i}} \mathbf{f}_{f,i} dA_{f,i} \\ &= \int_{A_{f,i}} \left(\sigma(\omega_b, v_b) \mathbf{n} + \sigma(\omega_b, v_b) \mu \mathbf{s} \right) dA_{f,i} , \end{aligned} \quad (5-9)$$

where \mathbf{n} and \mathbf{s} are unit vectors that define a local orthogonal basis at each cutter, indicated in Fig. 5.2, and $i = \{1, \dots, n_b\}$. With the hypothesis that the traction vectors are constant over the contact region, the previous integrals lead to

$$\mathbf{F}_{c,i} = \epsilon(\omega_b) \zeta a_i d_i \mathbf{n} + \epsilon(\omega_b) a_i d_i \mathbf{s}, \quad (5-10)$$

$$\mathbf{F}_{f,i} = \sigma(\omega_b, v_b) a_i l_i \mathbf{n} + \sigma(\omega_b, v_b) \mu a_i l_i \mathbf{s}. \quad (5-11)$$

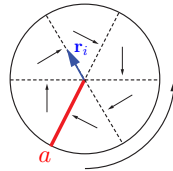


Figure 5.4: Distribution of the cutting blades in a symmetrical arrangement (example with $n = 6$ blades). a is the radius of the bit, which here coincides with the depth of each cutter so that $a_i = a$, \mathbf{r}_i is a vector that goes from the centre of the bit to the point of application of the resultant forces at each blade.

If a regular distribution of blades is considered (as in Fig. 5.4), and if all the blades have the same associated parameters $a_i = a$, $d_i = d$, $l_i = l$, for $i = \{1, \dots, n_b\}$, the total force on the bit is

$$\mathbf{W} = \mathbf{W}_c + \mathbf{W}_f, \quad (5-12)$$

with

$$\mathbf{W}_c = \sum_i \mathbf{F}_{c,i} = \begin{cases} \epsilon(\omega_b) \zeta a d n_b \mathbf{n}, & \text{if } (d \geq 0) \\ 0, & \text{otherwise} \end{cases} \quad (5-13)$$

$$\mathbf{W}_f = \sum_i \mathbf{F}_{f,i} = \begin{cases} \sigma(\omega_b, v_b) a l n_b \mathbf{n}, & \text{if } (d \geq 0) \\ 0, & \text{otherwise} \end{cases} \quad (5-14)$$

where all the components in the direction of \mathbf{s} cancel due to the symmetry. If $d < 0$, the bit is not in contact with the soil, therefore the previous forces vanish.

Now, let \mathbf{r}_i be a vector field that goes from the centre of the bit to the points of application of the distributed contact forces. The torques are obtained in an analogous way via integration:

$$\mathbf{T}_{c,i} = \int_{A_{c,i}} \mathbf{r}_i \times \mathbf{f}_{c,i} dA_{c,i}, \text{ with } i = \{1, \dots, n_b\}, \quad (5-15)$$

$$\mathbf{T}_{f,i} = \int_{A_{f,i}} \mathbf{r}_i \times \mathbf{f}_{f,i} dA_{f,i}, \text{ with } i = \{1, \dots, n_b\}. \quad (5-16)$$

Assuming that the traction vectors do not vary over the contact area, and taking into account the symmetry of the distribution of blades, the non-cancelling terms of the torques are originated from the forces in the direction of \mathbf{s} taking the values

$$\mathbf{T} = \mathbf{T}_c + \mathbf{T}_f, \quad (5-17)$$

$$\mathbf{T}_c = \begin{cases} \frac{1}{2} \frac{a}{\zeta} \mathbf{W}_c, & \text{if } (d \geq 0) \\ 0, & \text{otherwise} \end{cases} \quad (5-18)$$

$$\mathbf{T}_f = \begin{cases} \frac{1}{2} a \mu \gamma \mathbf{W}_f, & \text{if } (d \geq 0) \\ 0, & \text{otherwise} \end{cases} \quad (5-19)$$

with γ being a form coefficient. If $d < 0$, the bit is not in contact with the soil, therefore the previous torques vanish too.

Finally, with all these definitions the bit-rock interaction model is almost complete. The forces and torques have been defined in terms of the instantaneous depth of cut d_i a way to calculate its value is yet missing. This void will be filled in the following section.

5.3.2

The cutting process

In [14, 80] the formulation accounts for the removal of material as the drilling advances: the profile of the soil changes with each pass of the bit, removing soil as the drill rotates. Due to the contact between the drill-string and the borehole, the forces and torques depend on the soil profile, and its shape changes as the drilling rig operates. Thus, a free boundary problem needs to be solved.

5.3.2.1

The delay approach

The authors of the references [14, 80] tackle the free boundary problem by introducing a delay to account for the variation of the position of the soil with respect to time. The idea behind the delay formulation is simple, although its implementation requires some effort. With the delay approach, at the resolution of each time-step, the history of two functions needs to be accessed: that of the angular and the axial position at the bit.

With the sole purpose of explaining the methodology, the delay approach will be explained considering only one cutting blade at the bit. However, the procedure can be generalised in a similar manner to more cutters, although the formulation may require some tweaking.

Let the current time be referred as \hat{t} . At that time, the angular position of the bit is at an angle $\phi_b(\hat{t})$. Also, the bit was at the same angular position in previous turns, at times $t_j = \hat{t} - \tau_j$ such that

$$\phi_b(\hat{t} - \tau_j) = \phi_b(\hat{t}) - j2\pi. \quad (5-20)$$

Then, if the angular position is accessible up to the current time, by solving finding the roots of equations of the form of 5-20 it is possible to obtain the times at which the bit was cutting at the same position. However, this procedure implies finding the roots of a non-linear equation for a number of delays τ_j with $j = 1 \dots N$, so that by evaluating the axial position at these previous delayed times, one can calculate the depth-of-cut from the differences $\Delta_j = u_b(\hat{t}) - u_b(t_j)$. In fact, the depth-of-cut can be calculated as $d = \min(\Delta_j) > 0$.

The previous procedure shows that working with delay-differential equations introduces an extra difficulty: the method is intrusive. The solver has to be specially designed or modified to include the previous calculations. On top of that, the number of delays to be considered is not known beforehand,

therefore the simulation needs to be repeated to verify the accuracy of the depth-of-cut obtained, as discussed in [85].

5.3.2.2

The advection approach

In this work, the extra considerations and difficulties of including delays in the formulation are avoided. The free boundary problem is tackled by introducing an extra advection equation [73], where the main variable $L_s(\eta, t)$ is used to keep track of the soil elevation profile. This methodology allows to tackle both the case with equiangular distributions of blades and non-equiangular distributions (see the extension presented in [85] for more details). The advection equation is solved along with switching boundary conditions.

A periodic boundary condition is used to describe a translation of the solution in the material domain. The dynamics given by the advection equation can be interpreted as looking at the soil from the point of view of an observer that is fixed at the bit. Then, as the observer is fixed at the bit, and the bit is considered at a fixed position of $\eta = 0$ and $\eta = 2\pi$, the observer would watch the soil profile pass below him, or in other words, a translation of the soil profile with the velocity ω_b , which is exactly the behaviour the advection equation described.

The fact that the two endpoints of the domain, $\eta = 0$ and $\eta = 2\pi$, represent the position of the bit is also exploited. It can be used to introduce a discontinuity between the left side and the right side. For instance, the side to the left can be used to keep track of the soil elevation after the pass of the blade, and the right side to keep track of the soil elevation before the pass of the blade. This way, a non-negative difference between the two is the sought depth-of-cut.

As already detailed, if no cutting is taking place, then the boundary conditions are of a periodic type, and the values at $\eta = 0$ and $\eta = 2\pi$ match. However, if cutting is taking place, a geometric boundary condition is used to impose the new soil elevation so that the cutting depth matches the current position of the bit.

The advection equation is stated as

$$\frac{\partial L_s}{\partial t} + \omega_b(t) \frac{\partial L_s}{\partial \eta} = 0, \quad \text{with } \eta \in \left[0, \frac{2\pi}{n_b}\right], \quad (5-21)$$

where n_b is the number of blades. The boundary conditions are:

if $\omega_b \geq 0$,

$$L_s(\eta = 0, t) = \begin{cases} U(t), & L_s(\eta = \frac{2\pi}{n_b}, t) < U(t) \\ L_s(\eta = \frac{2\pi}{n_b}, t), & L_s(\eta = \frac{2\pi}{n_b}, t) \geq U(t) \end{cases} \quad (5-22)$$

and if $\omega < 0$,

$$L_s(\eta = \frac{2\pi}{n_b}, t) = L_s(\eta = 0, t), \quad (5-23)$$

These equations reflect that cutting can only occur if the bit is rotating in the positive direction. In the previous equation, $U(t)$ is the position of the bit.

Finally, at all times the instantaneous depth of cut is given by

$$d_i = \max\left\{L_s\left(\eta = \frac{2\pi}{n_b}, t\right) - L_s(\eta = 0, t), 0\right\}, \quad (5-24)$$

which completes the missing piece to calculate the bit-rock interaction forces and torques. A geometrical interpretation for the equation (5-21) and boundary conditions (5-22) and (5-23) is given in the Appendix C.1.

The advection formulation has the advantage of not being intrusive, thus a regular solver can be used for the numerical integration; it allows the addition of an arbitrary number of blades with just a minor number of adaptations in the boundary conditions and the domain (the boundary conditions should be set as a cascade in a closed loop); it can be used to model a non-equiangular distribution of blades without adding much complexity.

Now, with the bit-rock interaction relations complete, it is possible to provide more details about the sources of the non-linearities within the model, which result from the interaction between the axial and torsional equation of motion with the advection equation. This interaction is a consequence of the contact model employed. On the one hand, the contact forces that appear in the boundary conditions of the axial-torsional model are functions of the current angular and axial speed as well as the current depth-of-penetration d_i . On the other hand, d_i is obtained by solving the advection equation (5-21), which is explicitly coupled with the angular speed of the bit in its definition: the angular speed acts as the parameter that defines the transport speed of the soil profile. In addition, the advection boundary conditions are discontinuous. They depend on the angular speed too, and the axial position of the bit.

5.4

The nominal solution: a special non-oscillatory case

In the case that a constant angular speed is imposed at the top so that $\Theta(t) = \Omega_0 t$, the formulation employed in models M1 and M2 admits a solution that is non-oscillatory (second time derivatives vanish). In what follows, among other properties, the set of initial conditions and boundary conditions that lead

to this non-oscillatory behaviour are found. This solution will be referred to as “the nominal case”.

The following constant parameters associated with the nominal solution will be calculated:

- V_0 a constant axial speed
- \mathbf{T}_0 a torque associated to the bit-rock interaction and T_0 its module
- d_0 a constant instantaneous depth of cut

5.4.1

The nominal case for model M1

The nominal case for model M1 is characterised by the values

$$\Phi_0(t) = \Omega_0 t - \frac{T_0}{C}, \quad (5-25)$$

$$V_0 = \left(W_0 - \sigma_1 a l n_b \right) \frac{\Omega_0}{2\pi \epsilon_1 a \zeta}, \quad (5-26)$$

$$d_0 = V_0 t_{n0} = \frac{V_0 2\pi}{n_b \Omega_0}, \quad (5-27)$$

$$\mathbf{T}_0 = \frac{1}{2} \left(\epsilon_1 d + \mu \gamma \sigma_1 l \right) a^2 n_b \mathbf{n}, \quad (5-28)$$

following the derivation procedure in [14].

5.4.2

The nominal case for model M2

Considering that a non-oscillating behaviour is sought, the second-order time derivatives should vanish. In this case, a solution to (5-3), the equation that governs the torsional dynamics of model M2, with the boundary conditions in (5-4), is given by

$$\Phi_j(x_j, t) = A_j x_j + B_j(t), \quad \text{with } j = \{1, 2\}, \quad (5-29)$$

and

$$\begin{aligned} A_1 &= -\frac{T_0}{G J_1}, \\ A_2 &= -\frac{T_0}{G J_2}, \\ B_1 &= \Omega_0 t, \\ B_2 &= \frac{J_1 L_1 T_0 - J_2 L_2 T_0 + G J_2 J_1 \Omega_0 t}{G J_2 J_1}, \end{aligned} \quad (5-30)$$

where $x_1 \in [0, L_1]$, and $x_2 \in [L_1, L_1 + L_2]$.

It is observed that the angular speed, i.e. the time derivative of (5-29), is constant in the steady-state scenario and coincides with Ω_0 . This means that the time taken for the bit to complete a turn is given by

$$t_0 = \frac{2\pi}{\Omega_0}, \quad (5-31)$$

and the time taken to cover the angle between two successive blades that are evenly separated by a constant angle is

$$t_{n0} = \frac{2\pi}{n_b \Omega_0}. \quad (5-32)$$

Suppose that the driller is operating in the normal cutting regime ($d > 0$, $\omega_b > 0$, $v_b > 0$, with $\sigma = \sigma_1$ and $\epsilon = \epsilon_1$). Then, there exists an axial speed V_0 that, due to the hypothesis of the nominal solution, is constant. The depth of cut at each blade is given by

$$d_0 = V_0 t_{n0} = \frac{V_0 2\pi}{n_b \Omega_0}. \quad (5-33)$$

This expression can be obtained by imagining the depth-of-cut as a solution to a problem with constant delay t_0 (see [14] for more details).

The penetration rate and the torque are calculated from the bit-rock interaction laws. Considering the axial equation (5-1) and vanishing second time derivatives, the following vector equations are obtained:

$$\mathbf{W} = \mathbf{W}_0, \text{ with } \mathbf{W} = \mathbf{W}_c + \mathbf{W}_f. \quad (5-34)$$

Next, recalling that the current drilling conditions are those of the normal drilling case, it holds that $\sigma(\omega, v) = \sigma_1$ and $\epsilon(\omega) = \epsilon_1$. Therefore, by combining these expressions with (5-34), it is true that

$$d_0 = \left(W_0 - \sigma_1 a l n_b \right) \frac{1}{\epsilon_1 a \zeta n_b}. \quad (5-35)$$

The axial speed V_0 is calculated by joining the previous expression with (5-33)

$$V_0 = \frac{d_0}{t_{n0}} = \left(W_0 - \sigma_1 a l n_b \right) \frac{\Omega_0}{2\pi \epsilon_1 a \zeta}, \quad (5-36)$$

and the value for the torque-on-bit \mathbf{T}_0 for the nominal case is given by

$$\mathbf{T}_0 = \frac{1}{2} \left(\epsilon_1 d_0 + \mu \gamma \sigma_1 l \right) a^2 n_b \mathbf{n}. \quad (5-37)$$

Finally, the nominal solution for the advection equation (so that d_0 is a constant) is

$$L_s(\eta, t = 0) = -\frac{d_0 n_b}{2\pi} \eta. \quad (5-38)$$

5.5 Simulations

To begin with, two verification tests (V1 and V2) are carried out. These tests are essential to providing support to the soundness of model M2. After

that, three different simulations scenarios (C1 to C3) are presented. All the simulations are run using COMSOL Multiphysics [68], a simulation software that uses the finite element method (FEM). The simulation workflow is shown in Fig. 5.5. The equations associated with the torsional shaft are entered using the mathematics module of the software, in their weak form. The axial equation is also entered using its mathematics module. The advection formulation is already available in the software's transport module. The latter utilises a Do Carmo and Galeão crosswind diffusion stabilisation so that spurious oscillations are reduced. This way the need for excessively small time steps to maintain the accuracy of the temporal integration is also avoided. All equations are solved in COMSOL with a fully coupled approach, where the backward differentiation formulas (BDF) are used for the numerical integration.

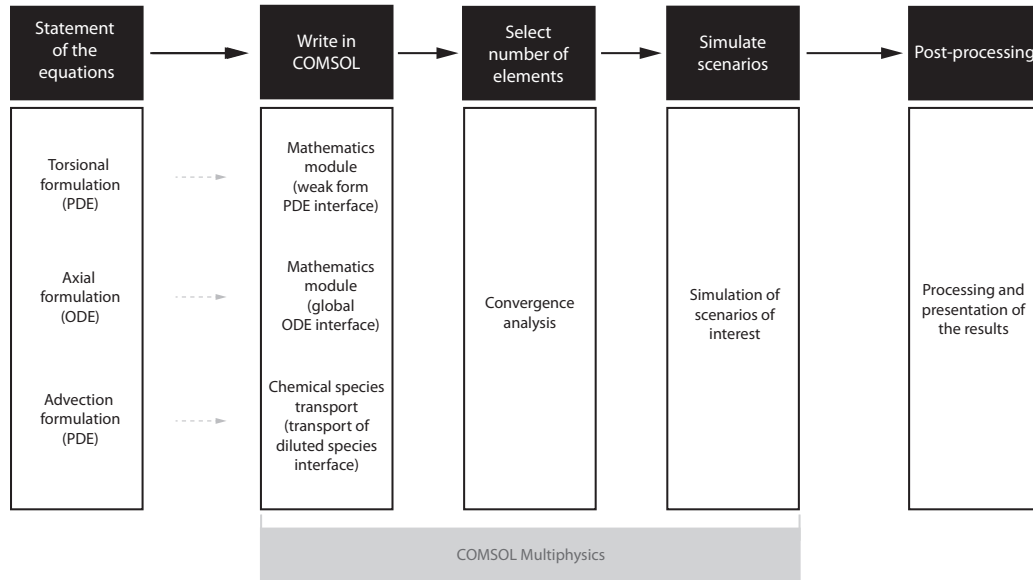


Figure 5.5: General simulation workflow employed.

The purpose of the first verification test (V1) is to check that the M1 model, with the new bit-rock interaction relations, reproduces the results of [14] with fidelity. In contrast with the model in [14], two important differences are presented in the new approach: 1) the new bit-rock interaction relations avoid the need to switch the equations of motions, an approach often used when non-continuous contact models are taken into consideration in low-dimensional formulations (as in [86]); 2) the dynamics of the soil are captured through the advection equation instead of a differential-delayed formulation.

The second verification test (V2) shows that model M1 is a limiting case of model M2 if a quasi-static hypothesis is adopted. This is a first step

into proving that, for the problems tackled within this work, the quasi-static assumption is voided.

Next, the simulation scenarios C1 to C3 consider different possible regimes of operations for a drill-string.

The study in [14] presents detailed results for two sets of non-dimensional parameters, where β , a non-dimensional constant that is related to the friction coefficient, take the values of 0.3 and 1.3, respectively. The cases C1 employ a set of dimensional parameters that are compatible with the non-dimensional parameters used in [14] for $\beta = 0.3$. For this reason, the C1 cases serve two purposes: they work as a benchmark test for the simulations with model M1, and they help to assess whether an appreciable difference in the response is observed if a continuous approach is chosen. The simulations show that self-excited regenerative vibrations appear, as predicted by [14]. More details about the sources of these self-excited vibrations are available in [87], which is an interesting review paper on the subject.

The cases C2-A and C2-B consider a set of dimensional parameters that are compatible with the non-dimensional counterparts of [14] for $\beta = 1.3$, which translates into a variation of the friction coefficient μ . According to the results in [14], this case should experience decaying oscillations. However, the simulations show a different behaviour for the continuous model.

So far, the previous cases considered an initial angular speed that is a small deviation from the nominal solution (see Section 5.4), which is associated with an imposed constant rotation at the top.

Finally, cases C3-A and C3-B depict a new scenario that has not been analysed in [14] where, unlike the previous simulations, the imposed speed at the top is not constant. This condition leads to backward rotation of the bit, a situation that is, by hypothesis, not allowed in [14].

As already mentioned, the results of [14] are all based on some non-dimensional parameters. To facilitate the comparison, the equations describing the transformation from the dimensional parameters to their non-dimensional counterparts employed in the reference are provided in Appendix C.2.

5.5.1 Parameters

A summary of the parameters employed in the simulations is provided in Table 6.1. If a value is altered for a particular simulation, it is indicated with an asterisk, and the details are given within the corresponding simulation section.

Following the recommendation of [14], the corrected inertia I of the BHA for model M1 is calculated as

$$I = \rho \left(\frac{1}{3} L_1 J_1 + L_2 J_2 \right). \quad (5-39)$$

Considering the definitions in [14], the parameters in Table 6.1 characterise the following non-dimensional parameters: system number $\psi = 50$, bit-rock interaction number $\beta = 0.3$, non-dimensional imposed top-drive speed $\omega_0 = 5$, non-dimensional weight-on-bit $\mathcal{W}_0 = 7$, and bluntness number $\lambda = 5$. The previous non-dimensional parameters follow the definitions contained in Appendix C.2.

The number of elements N_1 (Table 6.1) is the sum of elements present in the domains x_1 and x_2 , employed in the discretisation of the torsional wave equation, where quadratic Lagrange elements are used. This number was chosen after the convergence study described below. Additionally, the number of elements N_2 is used in the discretisation of the advection equation, where linear Lagrange elements are used. This number was selected after verifying that the results can capture the dynamics seen in [14].

5.5.2

Convergence analysis

In all the simulations, the FEM is used to discretise the continuous differential equations. The convergence analysis is a fundamental part of the simulations using FEM, as it assures that the spatial error of the simulation is kept below a pre-selected threshold. Also, it illustrates one of the main differences between lumped models and continuous ones: with the first type, the number of DOF is pre-set during the conception of the model itself, while in the latter it is chosen after some criteria is met.

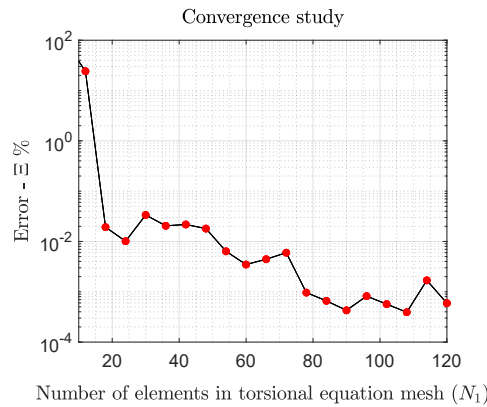


Figure 5.6: Convergence analysis. Error percentage in the angular position vs. the sum of elements in used to mesh x_1 and x_2 .

A convergence analysis is carried out to define the number of elements required to obtain an acceptable approximation for the equations (5-3) with the boundary conditions given by (5-4) that will be used in the present simulations.

A total number of elements N_1^i within the spatial domain $x \in [0, L_p + L_c]$ is considered, with i varying from 12 to 126, in increments of 6 for each iteration of i . The number of elements N_2 , associated with the advection equation, is fixed for this analysis in $N_2 = 64$ elements. The error for the spatial mesh is calculated according to

$$\Xi\% = \frac{\int (\Phi_{N_1^i} - \Phi_{N_1^{i+1}}) dx}{\int \Phi_{N_1^{i+1}} dx} \cdot 100 \Big|_{t=80s} \quad (5-40)$$

where Φ represents the angular position.

The results are depicted in Fig. 6.2 show that a mesh $N_1^i \geq 60$ is sufficient to ensure $\Xi\% \leq 10^{-2}$. For that reason, it was chosen to take $N_1 = 64$ elements.

5.5.3

Simulation V1: A benchmark test

The objective of this particular scenario is to verify that the implementation and modifications herein proposed do not appreciably affect the results, compared to those already published in [14].

The reference [14] employs a lumped 2-DOF approach, with a bit-rock interaction law that is discontinuous. In that study, the model was implemented via a switch in the equations depending on the speed conditions (whether it is a stick or slip phase). On top of that, the evolution of the soil profile was obtained by introducing a set of delays, defining a system of delay-differential equations to be solved.

The model M1 also considers a 2-DOF problem, one axial and one torsional, but employs the new bit-rock interaction law defined by (5-5) and (5-7) (see Section 5.3). With the current approach, the differential-delay set of equations is avoided by replacing the function evaluations at a delayed time with a third PDE equation, the advection equation.

Alike the reference, this scenario models the drill-pipes in a quasi-static condition by means of an equivalent torsional spring, and the BHA as a rigid body.

The parameters employed in this simulation are shown in Table 6.1 (see Section 6.3.1). The initial conditions are:

$$U(t = 0) = 0, \quad (5-41)$$

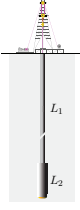
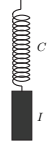
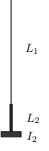
		Real structure	Model M1	Model M2
				
Property	Description			
L_1	Drill-pipe length	1000 m	spring (C)	1000 m
L_2	BHA length	200 m	rigid	200 m
N_1	Number of elements (torsion)	-	-	64
N_2	Number of elements (advection)	-	64	64
I, I_2	Lumped inertia	-	$I = 112.67 \text{ kgm}^2$	$I_2 = 0 \text{ kgm}^2$ (*)
α	Artificial parameter	-	-	1.00 (*)
C	Rigidity parameter	-	469.05 Nm/rad	-
ρ, ρ_1, ρ_2	Density	7800 kg/m ³		
r_{po}	Drill-pipe external radius	63.5 mm		
r_{pi}	Drill-pipe internal radius	54.0 mm		
r_{co}	Collar external radius	76.2 mm		
r_{ci}	Collar internal radius	28.0 mm		
G_1, G_2	Shear modulus	77 GPa		
a	Bit radius	108.0 mm		
l	Drill-bit wearflat length	1.2 mm		
ϵ_1	Rock intrinsic specific energy	0.252 GPa		
σ_1	Rock contact strength	0.252 GPa		
ϵ_2	Rock intrinsic specific energy	0.504 GPa		
σ_2	Rock contact strength	0.504 GPa		
M	Lumped mass	24614.40 kg		
Ω_0	Imposed angular speed	14.42 rad/s (**)		
W_0	Nominal weight-on-bit	45.7 kN		
γ	Drill-bit geometry parameter	1.00		
ζ	Cutter inclination coefficient	0.38		
μ	Coefficient of friction	0.80 (***)		
c_1	Regularisation constant	$1 \cdot 10^{-5}$		
c_2	Regularisation constant	$1 \cdot 10^{-1}$		
c_3	Regularisation constant	$1 \cdot 10^{-3}$		

Table 5.1: List of parameters employed in the simulations. (*) Indicates that the parameter changes for the simulation V2, (**) indicates that it changes for simulation C3 and (***) that it changes for simulation C2 and C3. The modified magnitudes are detailed within the corresponding study case. The parameter α is used to vary the characteristic propagation speed of the wave equation in V2.

$$\left. \frac{dU}{dt} \right|_{t=0} = V_0, \quad (5-42)$$

$$L_s(\eta, t=0) = -\frac{d_0 n_b}{2\pi} \eta, \quad (5-43)$$

with the following conditions for model M1 only

$$\Phi(t=0) = \Phi_0(t=0) = -\frac{T_0}{C}, \quad (5-44)$$

$$\left. \frac{d\Phi}{dt} \right|_{t=0} = \Omega_0 + \Delta\Omega_0, \text{ with } \Delta\Omega_0 = \Omega_0/10; \quad (5-45)$$

and the following conditions for model M2 only

$$\Phi_j(x_j, t=0) = A_j x_j + B_j(t=0), \text{ with } j = \{1, 2\}, \quad (5-46)$$

with A_j and B_j as defined in (5-30),

$$\left. \frac{\partial \Phi_j}{\partial t} \right|_{t=0} = \Omega_0 + \frac{\Delta\Omega_0 x_j}{(L_1 + L_2)}, \text{ with } \Delta\Omega_0 = \Omega_0/10. \quad (5-47)$$

In the previous equations V_0 and Ω_0 are constants associated to the nominal solution (obtained in Section 5.4).

The results for the angular speed $\omega(t)$ at the bit are plotted in Fig. 5.7, while Fig. 5.8 and Fig. 5.9 depict the non-dimensional angular speed at the bit $\hat{\omega}_b(\tau)$, with τ being a non-dimensional time. In the latter graph, the non-dimensional axial speed $\hat{v}_b(\tau)$ is also shown. The conversions from the dimensional to the non-dimensional forms follow the formulas in C.2.

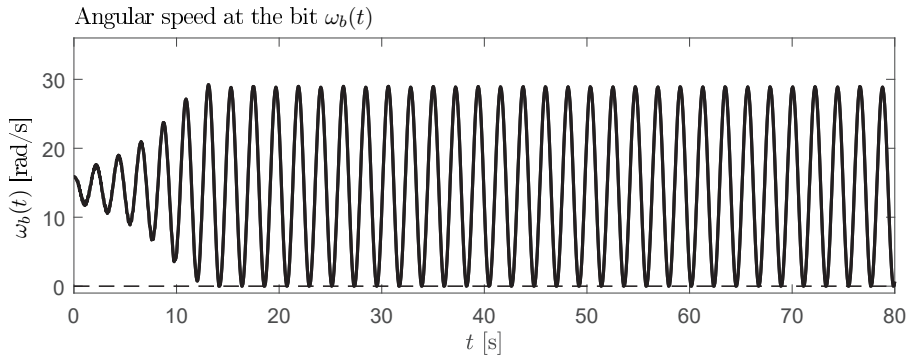


Figure 5.7: Simulation V1. Results obtained for the simulation V1, with model M1. $\omega_b(t)$ is the angular speed, expressed as a function of time t .

The simulations confirm that the non-dimensional results in V1, with the lumped model M1 and the bit-rock interaction laws described in this chapter, match the results of [14] for both the angular and axial speed.

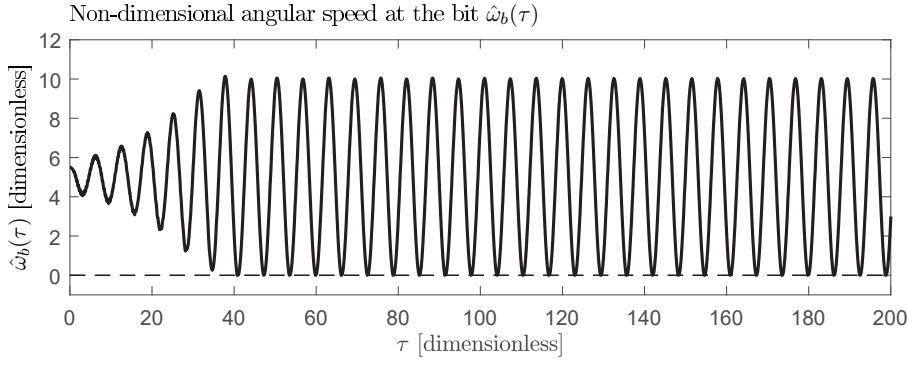


Figure 5.8: Simulation V1. Results obtained for the simulation V1, with model M1. $\hat{\omega}_b(\tau)$ is the non-dimensional angular speed as a function of the non-dimensional time parameter τ .

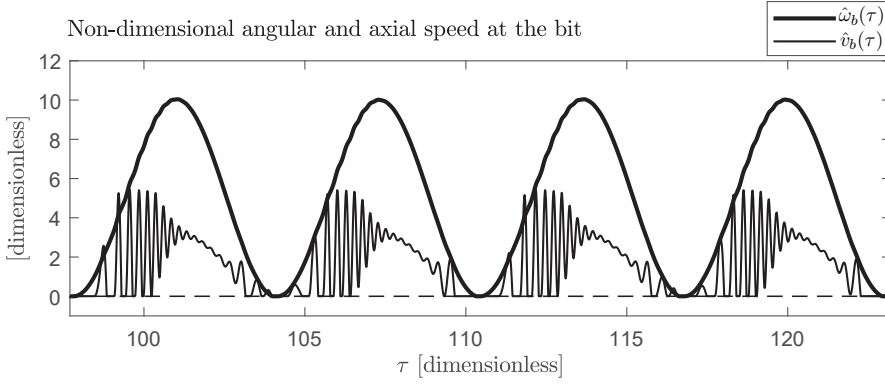


Figure 5.9: Simulation V1. Zoom of the results obtained in the simulation V1, with model M1, for $\tau \in [97.70, 123.2]$. $\hat{\omega}_b(\tau)$ is the non-dimensional angular speed as a function of the non-dimensional time parameter $\tau = t$.

5.5.4

Simulation V2: The model M1 as a limiting case of M2

The aim of this scenario is to perform an extra verification of model M2: it can be proved that model M1 is a limiting case of model M2, if some assumptions are made.

The 2-DOF model defined in [14], M1, considered a quasi-static formulation for the drill-pipes, i.e. the effect of all external excitations acting at one end is transmitted instantly to the other. This assumption allowed the modelling of the drill-pipes as a simple torsional spring with constant C . Also, the flexibility of the BHA was neglected in the calculation of the spring constant.

For model M2 to behave like M1, the set of material and geometric parameters needs to reflect the previous hypotheses. First, the rigidity of the BHA should be negligible, thus $G_2 \rightarrow 0$ needs to be considered. Second, an

artificial parameter α is introduced so that the propagation speed of the wave equation, given by $v_w = \sqrt{G/(\alpha\rho)}$, can be controlled. In fact, a quasi-static problem is equivalent to considering an infinite propagation speed, compatible with taking $\alpha \rightarrow 0$. Additionally, the concentrated inertia, I_2 , in the boundary conditions takes the form

$$I_2 = (1 - \alpha)I. \quad (5-48)$$

This expression permits the transition from a fully distributed inertia, for $\alpha = 1.00$, to a fully concentrated inertia when $\alpha \rightarrow 0$. It is important to remark that only M2 with $\alpha = 1.00$ has a physical meaning. All intermediate values, smaller than the unity, just make sense in helping to understand how the response varies from a lumped quasi-static formulation with concentrated inertia to a continuous approach, and to observe how the main frequency in the signal of the angular speed at the bit changes.

The initial conditions coincide with those employed in the previous simulation, V1.

The aforementioned theoretical result is illustrated by comparing the results associated with model M2 with varying α , and model M1. The parameters used in this simulation are given in Table 6.1 (see Section 6.3.1), except for I_2 which takes the form given in (5-48), and G_2 that is made arbitrarily small. The angular speed at the bit $\omega_b(t)$ is plotted in Fig. 5.10 for (a) $\alpha = 1.00$, (b) $\alpha = 0.80$, (c) $\alpha = 0.40$, (d) model M1.

A quick inspection of the results confirms that the simulation gets closer to that of M1 as α evolves from 1.00 in Fig. 5.10(a) to 0.40 in Fig. 5.10(c). On top of that, it is observed that the behaviour changes substantially between (a) and (e): it is apparent that the frequency content is different. To better analyse these results, Figs. 5.11 and 5.12 show the response in the frequency domain, for $t > 50$ s, after the transient effects vanish. In addition, Table 5.2 shows how some of the frequencies over 0.15 vary along with a change in the parameter α . To such purpose, different colours are used to track the most important frequencies in the signal. In blue, the evolution of the amplitude content close to the first natural frequency is shown. In M1 and M2 with $\alpha = 0.40$, this represents the main component of the signal; for $\alpha = 0.80$ it is the third component; while for $\alpha = 1$ it is negligible. The case where $\alpha = 0.8$ shows two frequencies with almost the same importance in terms of amplitude (coloured green and orange). Finally, the main frequency for $\alpha = 1$ is coloured in green.

According to Fig. 5.11, Fig. 5.12 and Table 5.2, the signal for the angular speed with model M1 contains a main frequency that matches the fundamental

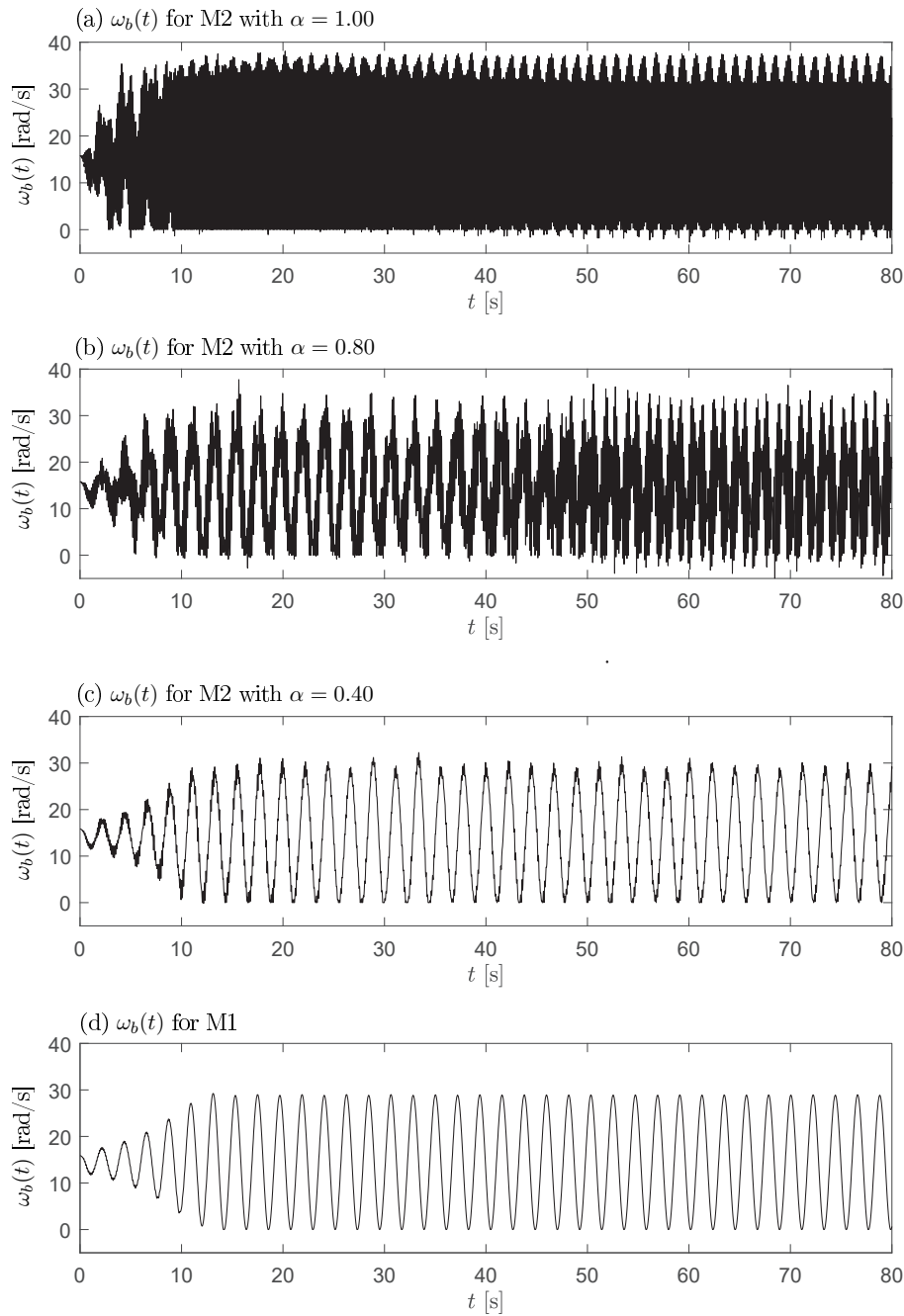


Figure 5.10: Simulation V2. Angular speed at the bit $\omega_b(t)$, (a) for model M2 with $\alpha = 1.00$; (b) model M2 with $\alpha = 0.80$; (c) model M2 with $\alpha = 0.40$; (d) Model M1.

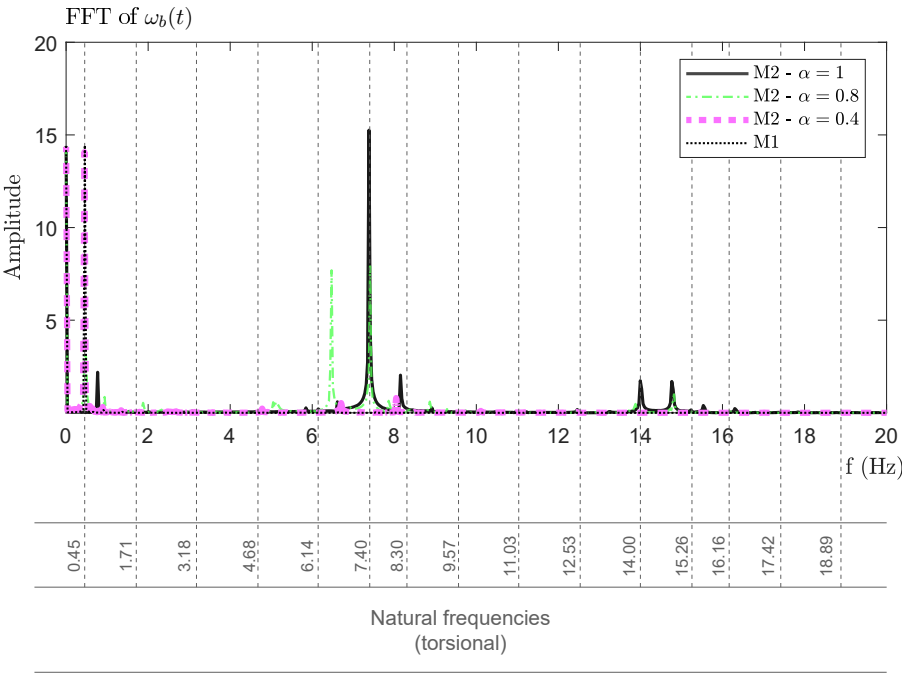


Figure 5.11: Simulation V2. FFT of the angular speed at the bit $\omega_b(t)$. Frequency range: 0 to 20Hz. The last 20 s of simulations were used to construct the FRF.

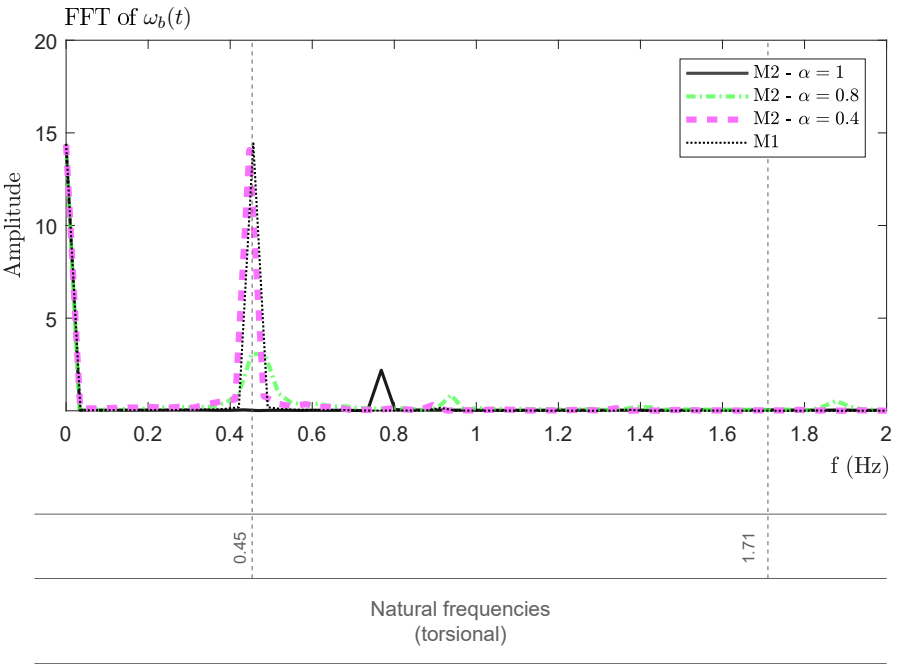


Figure 5.12: Simulation V2. Zoom of the FFT of the angular speed at the bit $\omega_b(t)$. Frequency range 0 to 2Hz. The last 20 s of simulations were used to construct the FFT.

one (0.45 Hz). This is different for model M2, where the main frequency is close to the sixth natural frequency (7.40 Hz), and the amplitudes associated to frequencies close to 0.45 Hz are negligible. This explains the appreciable difference observed with the signals in the time domain.

Through the results herein presented, it has been shown that model M2 provides similar results to model M1 for small values of α , while for $\alpha = 1$ the frequency content differs greatly.

M1		M2, $\alpha = 0.40$		M2, $\alpha = 0.80$		M2, $\alpha = 1.00$	
A	f [Hz]	A	f [Hz]	A	f [Hz]	A	f [Hz]
14.44	0.46	14.07	0.45	7.90	7.41	15.25	7.38
0.16	0.91	0.80	8.05	7.69	6.47	2.19	0.77
-	-	0.53	6.70	3.10	0.45	2.03	8.15
-	-	-	-	1.00	14.82	1.73	14.00
-	-	-	-	0.86	0.94	1.69	14.76
-	-	-	-	0.65	7.86	1.47	29.56
-	-	-	-	0.60	8.87	0.60	6.61
-	-	-	-	0.59	5.11	0.57	22.95
-	-	-	-	0.57	5.05	-	-
-	-	-	-	0.54	1.88	-	-
-	-	-	-	-	-	0.05	0.43

Table 5.2: Simulation V2. List of frequency content in the FFT, for varying values of α , ordered by amplitude (A). Only amplitudes greater than 0.50 are shown. In blue, the evolution of the amplitude content close to the first natural frequency is shown. In green, the main frequency for $\alpha = 1.00$ is shown, as well as for $\alpha = 0.80$. For the latter, the second amplitude is highlighted in orange.

5.5.5

Simulation C1 (with $\beta = 0.3$)

The cases for M1 and M2 with $\alpha = 1$ that were presented in V2, namely C1-A and C1-B, are further analysed. The set of properties described in Table 6.1 (Section 6.3.1) are used in the simulations. The case associated to $\beta = 0.30$ is simulated given that the results are among the few cases described in detail in [14]. The initial conditions coincide with those used in simulations V1 and V2. The simulation times were 1 h 49 min for C1-A and 3 h 56 min for C1-B.

The angular speed at the bit is plotted in Fig. 5.13 for $t \in [0 \text{ s}, 80 \text{ s}]$, and a zoomed graph for $t \in [0 \text{ s}, 10 \text{ s}]$ is shown in Fig. 5.14.

The results show that the initial deviation from the nominal solution leads to self-excited vibrations that do not vanish within the total simulation time, as predicted by [14]. Moreover, the signals corresponding to the angular speed at the bit are considerably different one from another in terms of amplitude and frequency content. Also, for C1-B, some periods of negative speed are observed, which means that backward bit rotation occurs.

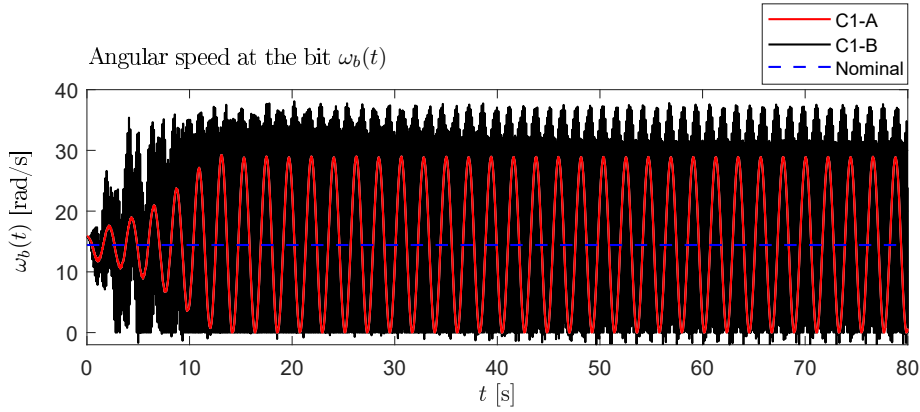


Figure 5.13: Simulation C1. Angular speed at the bit $\omega_b(t)$ for the cases C1-A and C1-B (models M1 and M2, respectively). The nominal angular bit speed is shown in a dashed line.

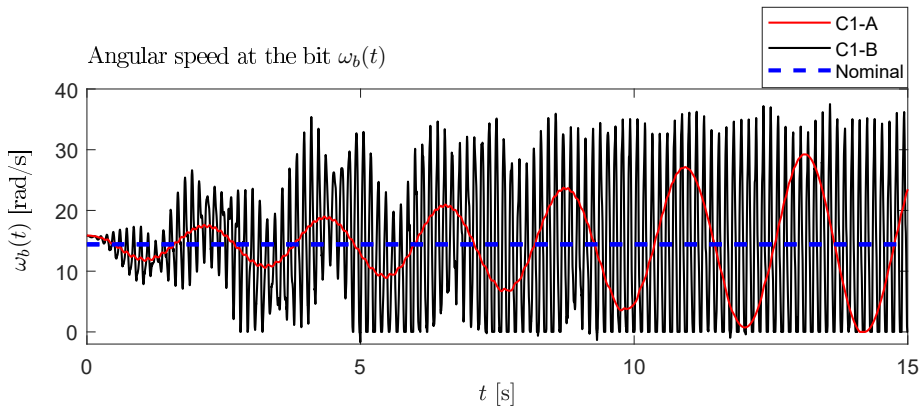


Figure 5.14: Simulation C1. Angular speed at the bit $\omega_b(t)$ for the cases C1-A and C1-B (models M1 and M2, respectively). Zoom for $t \in [0\text{s}, 10\text{s}]$. The nominal angular bit speed is shown in a dashed line.

To gain further insight, the FFT of the angular speed is depicted in Fig. 5.15. Again, the transient effects are neglected by considering the portion of the signal for $t > 50$ s. Also, the natural frequencies associated with the continuous model are illustrated in the figure.

The FFT shows that the main frequency of C1-A (model M1) is close to the fundamental frequency of 0.45 Hz. This changes for C2-B (model M2), where the main frequency is 7.40 Hz, close to the sixth vibration mode. Some other non-negligible frequencies exist in the range between 0.77 Hz to 30 Hz (see Table 5.2 with $\alpha = 1$ for more specific details).

In Fig. 5.16 the axial position at the bit, $U(t)$, is shown along with the nominal position, which corresponds to the unperturbed steady-state solution. Fig. 5.17 depicts the associated axial speed. An interesting result is observed by

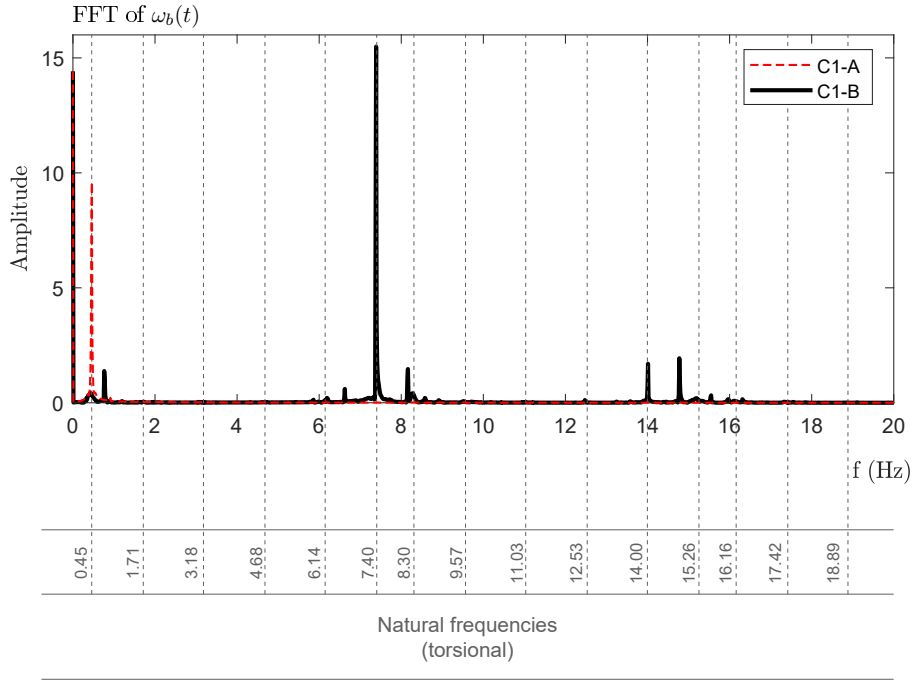


Figure 5.15: Simulation C1. FFT of the angular speed at the bit $\omega_b(t)$.

analysing the behaviour of $U(t)$: both curves are above the nominal response, which implies faster drilling.

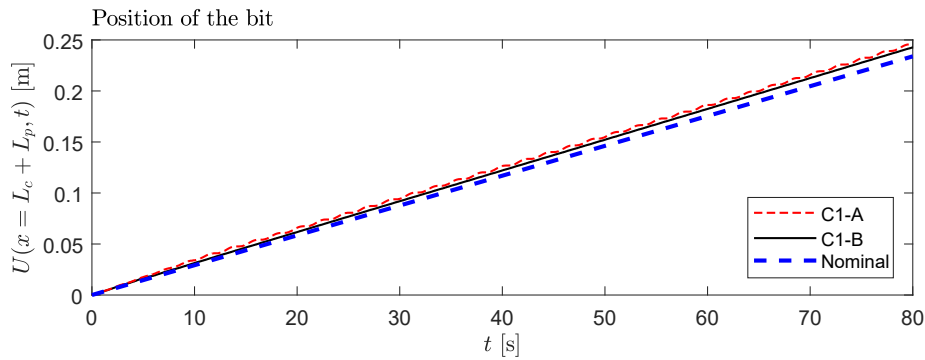


Figure 5.16: Simulation C1. Axial position of the bit $U(t)$ for the cases C1-A and C1-B (models M1 and M2, respectively). The nominal axial position is shown in a dashed line.

On the one hand, the previous graphs show that the system undergoes stick-slip motion for the axial dynamics as well as torsional vibrations. Stick-slip motion is usually linked to a reduction in the efficiency of the drilling tool [10, 88]. On the other hand, vertical oscillations mean that the system's dynamics are similar to those of a percussive driller. Given that the previous simulations demonstrate better performance than the nominal case, in terms

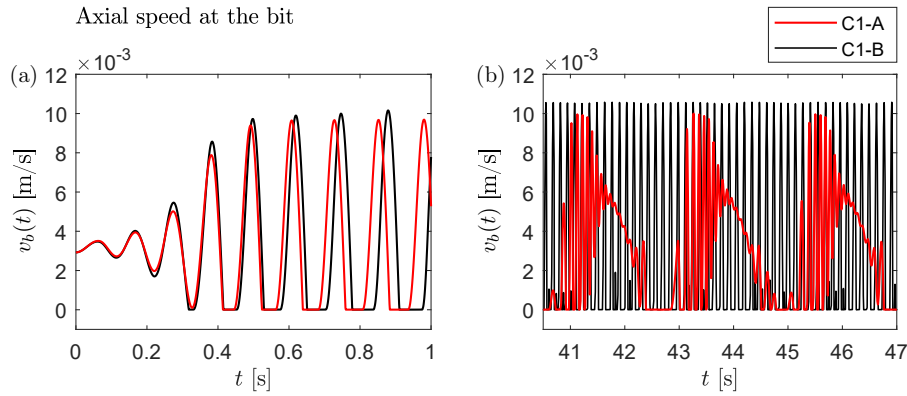


Figure 5.17: Simulation C1. Axial speed at the bit $v_b(t)$, for the cases C1-A and C1-B (models M1 and M2, respectively). (a) For $t \in [0, 1]$ and (b) (a) For $t \in [40.5, 45]$.

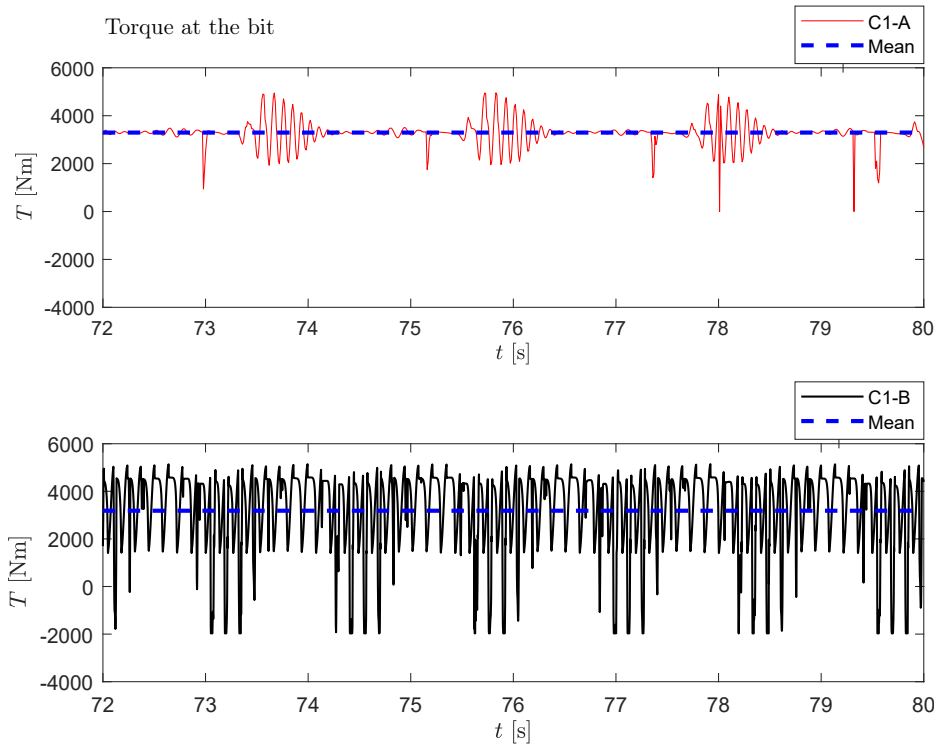


Figure 5.18: Simulation C1. Torques at the bit T for the cases C1-A and C1-B (models M1 and M2, respectively).

of the depth achieved, the authors attribute the performance gain to the percussive (vibro-impact) nature of the dynamics, which is known to improve the penetration rate [89–92].

Finally, Fig. 5.18 depicts the simulated torques for $t \in [72 \text{ s}, 80 \text{ s}]$. These signals also present differences, although the mean values of both signals are similar: 3295 Nm for C1-A and 3184 Nm for C1-B (a 3% difference). Additionally, C1-A does not show any sign change, while C2-B does, exhibiting short periods of backward rotation of the bit.

5.5.6

Simulation C2 (with $\beta = 1.3$)

The set of simulations C2 consider the same set of parameters from Table 6.1, except for the coefficient of friction which now takes a value $\mu = 3.46$. This parameter is chosen so that, for the given geometric, material, and bit-rock interaction properties, the non-dimensional counterparts match those described in detail in [14]. More specifically, they take the values: non-dimensional bit-rock parameter $\beta = 1.3$, system number $\psi = 50$, non-dimensional imposed top-drive speed $\omega_0 = 5$, non-dimensional weight-on-bit $\mathcal{W}_0 = 7$, and bluntness number $\lambda = 5$. For this set of values, [14] predicts a solution with vanishing oscillations. The initial conditions are the same employed for case V1.

The angular speed of the bit is shown in Fig. 5.19, for $t \in [0 \text{ s}, 50 \text{ s}]$, and a zoomed graph for $t \in [0 \text{ s}, 10 \text{ s}]$ is depicted in Fig. 5.20.

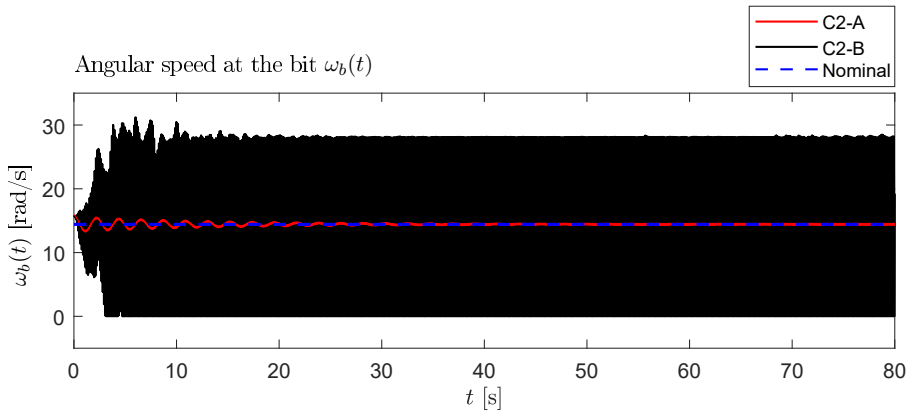


Figure 5.19: Simulation C2. Angular speed at the bit $\omega_b(t)$ for the cases C2-A and C2-B (models M1 and M2, respectively). The nominal angular bit speed is shown in a dashed line.

The analysis of the signals corresponding to the angular speed in Fig. 5.19 and Fig. 5.20 show very different results from a qualitative point of view.

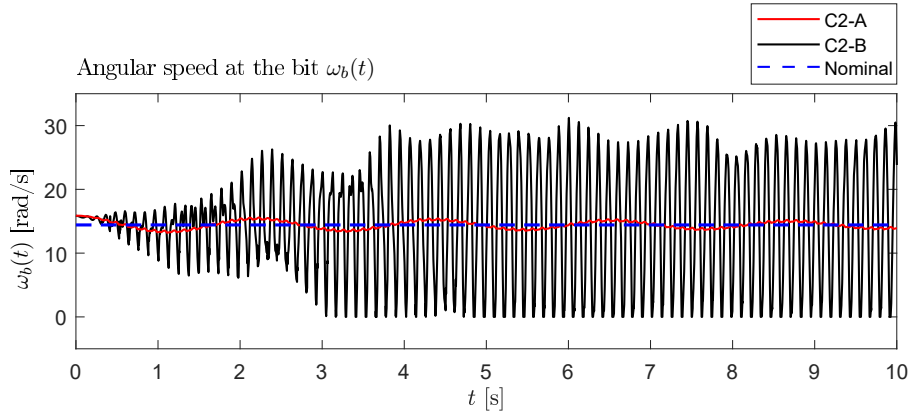


Figure 5.20: Simulation C2. Angular speed at the bit $\omega_b(t)$, for the cases C2-A and C2-B (models M1 and M2, respectively). Zoom for $t \in [0, 10]$ s. The nominal angular bit speed is shown in a dashed line.

At a first glance, it is observed that the frequency content in the signals is different, as well as the general behaviour of the system: C2-A shows decaying oscillations, whereas in C2-B the vibrations do not vanish. In other words, C2-B shows self-excited oscillations while C2-A does not. On top of that, the speed never takes negative values, so no backward rotation is observed.

The FFT of the angular speed is plotted in Fig. 5.21, for $t > 50$ s. For C2-A (model M1), as the oscillation vanishes, most of the amplitude is associated with the zero-frequency, and the most prominent frequency is 8.70 Hz (with an associated amplitude of 0.12). For C2-B (model M2), the main frequency is 8.30 Hz and it coincides with the seventh natural frequency of the structure.

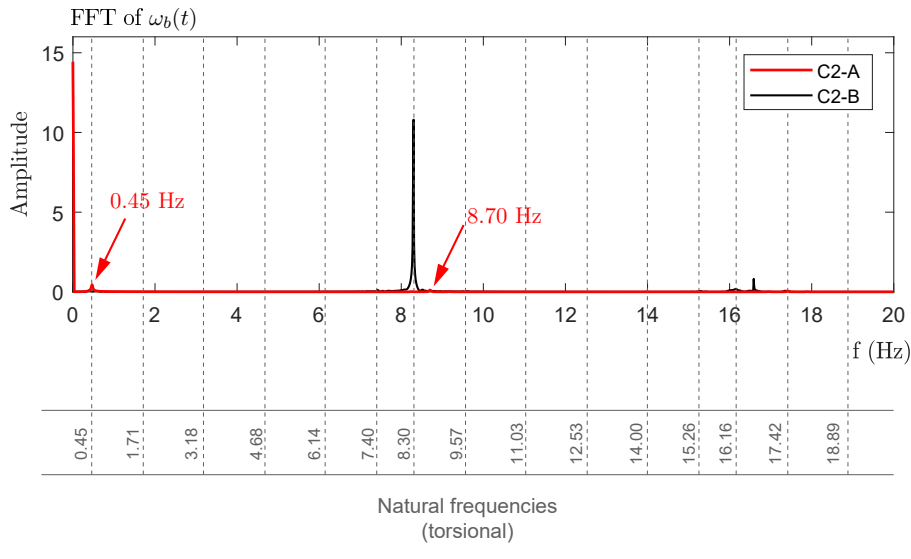


Figure 5.21: Simulation C2. FFT of the angular speed at the bit ($\omega_b(t)$).

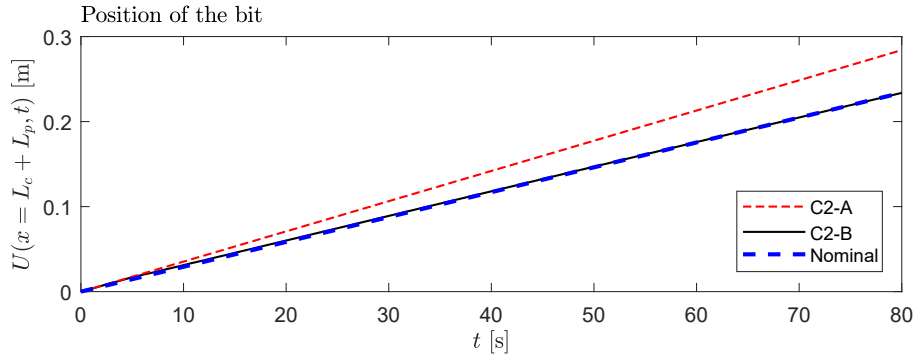


Figure 5.22: Simulation C2. Axial position $U(t)$ at the bit, for the cases C2-A and C2-B (models M1 and M2, respectively). The nominal bit position is shown in a dashed line.

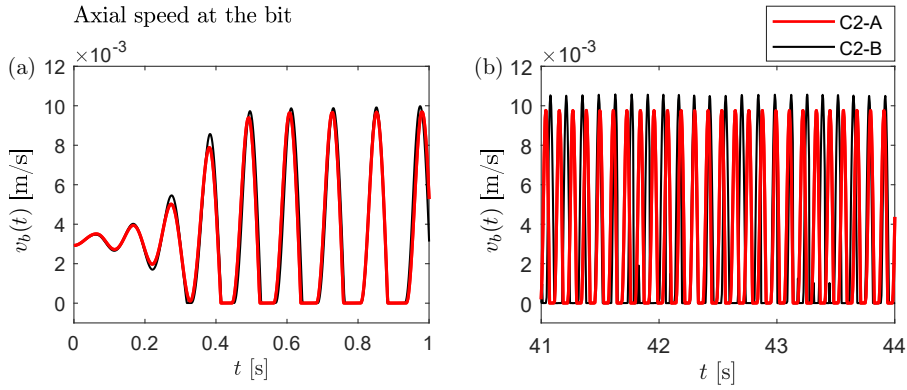


Figure 5.23: Simulation C2. Angular speed at the bit ($v_b(t)$), for the cases C2-A and C2-B (models M1 and M2, respectively). The nominal axial bit speed is shown in a dashed line.

Fig. 5.22 depicts the axial position of the bit, while Fig. 5.23 its respective axial speed. Alike the simulations C1-A and C1-B, axial stick-slip motion is observed. C1-A exhibits an increase in the drilling performance, in terms of the maximum depth achieved when compared with the nominal case. C1-B does not show such an evident increase, although the performance is slightly above the nominal case at all times.

Finally, Fig. 5.24 depicts the simulated torques for $t \in [79 \text{ s}, 80 \text{ s}]$. These signals also present differences, although the mean values of both signals are similar: 7847 Nm for C1-A and 7339 Nm for C1-B (a 6% difference). None of the cases show signs of backward rotations of the bit.

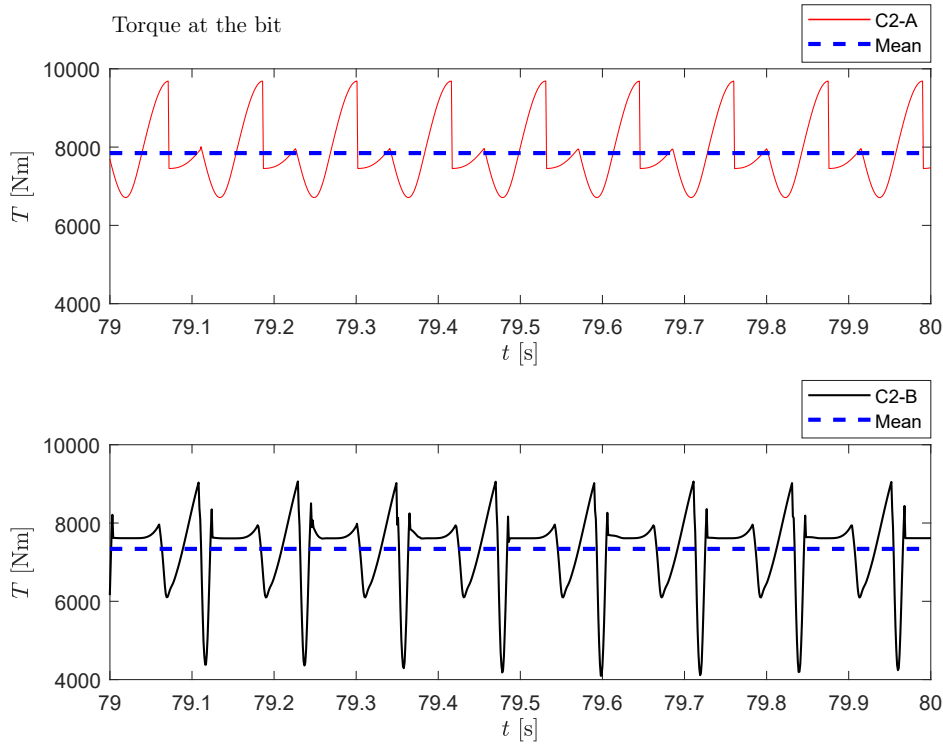


Figure 5.24: Simulation C1. Torques at the bit T for the cases C1-A and C1-B (models M1 and M2, respectively).

5.5.7

Simulation C3 for an imposed variable angular speed

This scenario considers the same set of parameters shown in Table 6.1, except for the friction coefficient which takes the value $\mu = 0.40$. In contrast with V1, V2, C1, and C2, the boundary condition at the top for the torsional dynamics is not defined by an imposed constant angular speed. Instead, it is given by

$$\theta(t) = \begin{cases} \Omega_0 t, & \text{for } t \leq 2 \\ \Omega_0 t + \cos\left(2(t-2)\right) + \frac{1}{5} \cos\left(10(t-2)\right) - \frac{6}{5}, & \text{for } t > 2 \end{cases} \quad (5-49)$$

with $\Omega_0 = 14.42$ rad/s. Its time derivative is plotted in Fig. 5.25. The choice of (5-49) is arbitrary, but the oscillatory behaviour is realistic: in drilling, a torque is applied rather than an imposed angular speed. The magnitude of the torque is usually defined by some control mechanism (e.g. a PID controller), which, in general, cannot completely mitigate vibrations at the top. Thus, vibrations are usually observed.

The oscillatory behaviour of the chosen input has an important effect on the response, as it will be shown by the simulations: the new scenario shows

that backward bit rotation occurs, with both models.

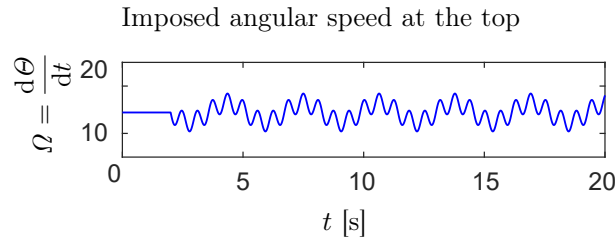


Figure 5.25: Simulation C3. Imposed angular speed at the top, for the cases C3-A and C3-B.

For the initial conditions, the values associated with the nominal solution are adopted. The angular speed of the bit is depicted in Fig. 5.26, for $t \in [0 \text{ s}, 80 \text{ s}]$ and zoomed in Fig. 5.27 $t \in [54 \text{ s}, 68 \text{ s}]$.

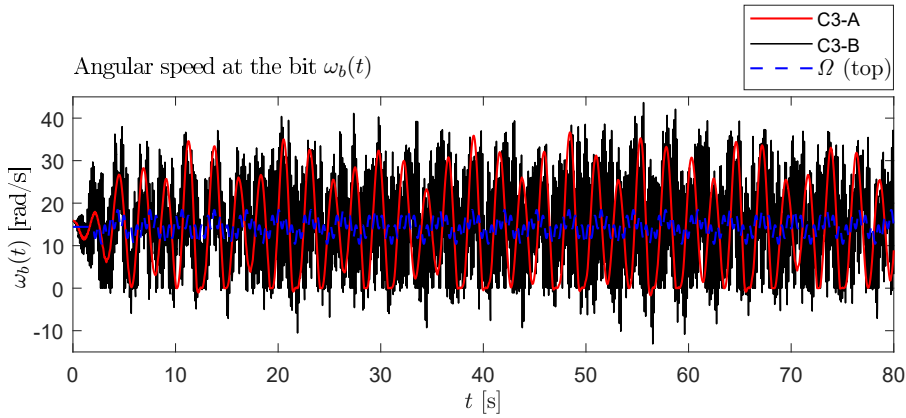


Figure 5.26: Simulation C3. Angular speed at the bit $\omega(t)$ for the cases C3-A and C3-B (models M1 and M2, respectively). The imposed angular speed (boundary condition at the top) is shown in a dashed line.

Alike the previous cases, by simple observation of the signals in the time domain it is perceived that C3-A and C3-B differ in terms of frequency content. Additionally, it is observed that backward rotation of the bit is experienced in both simulations.

The FFT of the angular speed is depicted in Fig. 5.28. The graph shows that the main frequency in C3-A is the fundamental one (0.45 Hz). For C3-B this is close to the sixth frequency (7.40 Hz).

This scenario shows that backward rotation of the bit occurs in both situations, for the set of parameters considered in the simulations.

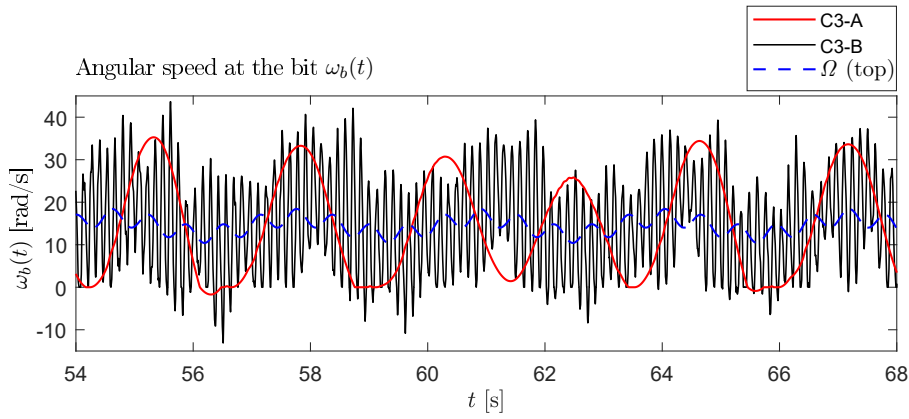


Figure 5.27: Simulation C3. Angular speed at the bit $\omega_b(t)$ for the cases C3-A and C3-B (models M1 and M2, respectively). Zoom for $t \in [65\text{s}, 75\text{s}]$. The imposed angular speed (boundary condition at the top) is shown in a dashed line. The arrows indicate where backward rotation is taking place.

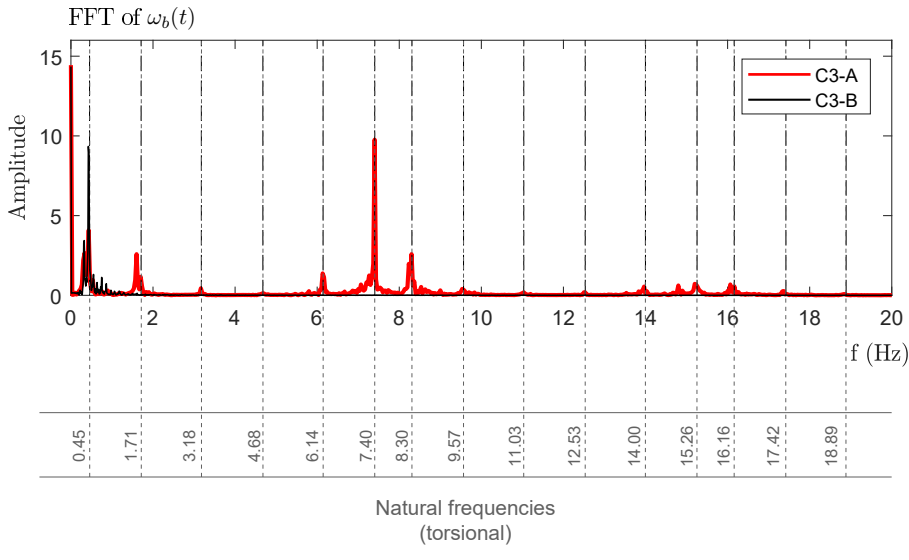


Figure 5.28: Simulation C3. FFT of the angular speed at the bit $\omega_b(t)$.

5.6

More aspects about the results

The simulations V1, including the same structural models but different strategies for the cutting dynamics, showed matching results. After that, the dynamics of two drill-string models, a continuous torsional shaft representation and a lumped one, were compared. In both cases, a 1-DOF-axial model was used. Important discrepancies among the results with the different models were found. The simulations V2 show that the model M1 can be obtained as a limiting case of M2 if the parameters involved are such that the formulation

behaves as a quasi-static problem. The fact that the simulations differ indicates that this hypothesis is not satisfied by the structure under analysis: a 1200 m vertical drill-string. This conclusion is further supported by the three simulations scenarios C1, C2 and C3, where the main vibration frequencies in the angular speed of the bit for model M1 differ from those of M2, as well as the maximum depth achieved. The accuracy of the prediction of the latter is essential to determine the performance of the drilling process.

Cases C2-A and C2-B show diverging behaviour: vanishing vibrations are observed in the first case, whereas self-excited oscillations appear in the latter. However, [80] and [14] state that stick-slip vibrations are generally prohibited for $\beta > 1$, a conclusion that is in direct opposition with the new simulations.

With regard to the magnitudes of the torques involved, in both cases, C1 and C2, discrepancies in the shape of the simulated signals are observed, although the difference is less than 6 % in terms of their mean values. In C1-A short periods of backward rotation of the bit are observed.

Additionally, with case C3 it is also shown that the new model can capture other phenomena such as backward rotation of the bit which, by hypothesis, is not allowed in [14, 80]. The simulations show more pronounced backward rotations in this case where the angular speed at the top is allowed to oscillate.

5.7

Final comments concerning this chapter

The first part of this article contains a discussion regarding modelling strategies for drill-strings, whether lumped or continuous. Part of the novelty of this work lies, from a modelling perspective, in the combination of an advection approach to deal with the cutting dynamics of a drill-string with a new bit-rock interaction model and a continuous torsional shaft formulation. After a search of relevant literature, it was found that the advection approach had not been so far used in combination with a continuous description. The resulting model is reducible to the established 2-DOF approach used in the comparisons. Additionally, another contribution is that the advection formulation was extended to deal with rotations in both directions, for which switching boundary conditions were defined. From the perspective of the results, the differences observed in the comparisons between the previous model and an established 2-DOF approach could indicate that the continuous torsional representation is capturing other aspects of the dynamics that are neglected in the 2-DOF model. For this reason, this work is understood as a step into exploring the hypothesis that the 2-DOF model may not capture the

whole aspects of the dynamics of a full-length column.

The simulations including the same structural models but different strategies for the cutting dynamics showed matching results, confirming that the advection formulation is an effective alternative that can be numerically integrated without the need for special solving strategies, unlike the delayed approach, as pointed out by other existing investigations [73].

On the other hand, the simulations comparing the continuous and the 2-DOF model showed important discrepancies in the results, as expressed in Section 5.6. The main differences observed, which in fact are the main findings of this work, are an indication that more sophisticated models could reproduce other aspects of the dynamics that are neglected in the 2-DOF approach. This hypothesis is also supported by other existing works, such as [26] and partially by [80], given that the simulations predict vibrations at higher frequencies than the fundamental one, which cannot be reproduced with the 2-DOF model. However, the continuous formulation herein employed is conservative, hence the only responsible element taking energy out of the system is the contact at the bit. The fact that no internal damping associated with the structure itself, nor external damping associated with the drilling mud have been considered, may also have an important impact on the responses, and should be studied further.

On top of these findings, the contributions of this work included the definition of a bit-rock interaction law that is also defined for negative speeds. This is an improvement over the bit-rock interaction model of [14, 80], as the new approach allows for backward rotation and bit-bounce. In this aspect, this work continued the discussion on the ideas presented in [14].

In this chapter, a model based on the Cosserat formulation will be used to study the dynamics of a drill-string with a bit-rock interaction model that considers the dynamics of the cutting. With this choice, the analysis can be broadened to account for axial, torsional and lateral motion, and it can be used to simulate curved boreholes with the help of the strategy to detect contact that was developed in Chapter 4.

One of the main objectives of the study is to evaluate the influence of adding an internal source of dissipation for which a Kelvin-Voigt material model is considered. For the task, two application cases are analysed. The first one deals with a vertical borehole, while the second application case is used to illustrate the full potential of the new model to tackle the 3-D lateral, axial, and torsional dynamics in a curved borehole. A comparison among the simulations obtained with the Cosserat model and others from the literature show divergences in the predictions. These results justify the importance of employing continuous approaches to study the dynamics of drill-strings, such as the one adopted herein.

Some of the novelties of the present study reside in the combination of 1) a Cosserat rod model, capable of accounting for all possible motions, axial, torsional and lateral; 2) the inclusion of a strategy to account for the lateral contact in curved wells; 3) the adoption of the bit-rock interaction model presented in 5 and [74]; 4) the addition of internal damping through the use of a Kelvin-Voigt constitutive relation; 5) the inclusion of the 2-DOF model M1 as a limiting case of the new Cosserat model, M3, through the addition of an extra parameter α . A similar strategy to that utilised in [74] adopted, allowing to verify the model in known scenarios; 6) a comparison among the three models, M1, M2 and M3, in the time and the frequency domain, showing that the continuous Cosserat approach provides different predictions than those obtained with the other models. Moreover, the formulation overcomes many of the limitations of the previous models used in [14, 74]. For instance, it does not employ a lumped representation for the axial behaviour like the ones used in Chapter 5 and in [14, 74].

6.1

Description of the problem

In Chapter 5, the dynamics of a vertical drill-string were studied with two different models. On the one hand, model M1 considered 2-DOF, one axial and one torsional, in a similar way to that presented in [14]. On the other hand, model M2 used a continuous torsional formulation and retained the 1-DOF axial description. In that previous study, model M2 was devised so that it contained M1. In this way it was verified that, through the use of a strategy involving a controllable parameter α , in the limit where $\alpha \rightarrow 0$ the results of M2 coincide with those of M1 and [14]. After that, different scenarios were simulated with M2 and compared against those published in the reference [14]. The simulations predicted different outcomes, where other frequencies different from the fundamental one are excited as well. The finding was understood as an indicator that some aspects of the dynamics could be neglected by the choice of a 2-DOF model and, as a consequence, that the low-dimensional lumped model can be insufficient to represent a 1,200 m column. However, the models M1 and M2 suffer from some limitations:

- The axial dynamics were still based on a 1-DOF formulation, a choice that was not justified. In the study of Chapter 5 it was arbitrarily decided to modify the torsional part only, with the aim of evaluating the effect of this change in isolation;
- The torsional formulation employed in M2 is that of a conservative wave equation where the only source of dissipation is the friction force at the bit;
- Other sources of dissipation were not considered. The fact that no internal damping associated with the structure itself nor external damping that could be associated with external effects were included could have some important impact on the responses.

In what follows, a continuation of the study carried out in Chapter 5 and [74] is presented. The dynamics of a drill-string are studied with a Cosserat rod model, namely M3, where the dynamics of the cutting are also taken into account. The objective is to analyse the influence of introducing internal dissipation in the formulation using a continuous model and to compare its predictions with those of the discrete and semi-continuous approaches of the previous chapter. To this purpose, structural damping is introduced by considering a Kelvin-Voigt material.

Two application cases are analysed. The first one deals with a vertical borehole. It includes four simulations that are used to further investigate the

hypothesis that low-dimensional lumped formulations are not able to capture the dynamics of a drill-string and, while doing so, evaluate the effect of the damping in the system's response. The predictions are compared with those given by two other models: a 2-degrees-of-freedom (DOF) formulation (M1), with 1-axial and 1-torsional DOF, and a semi-discrete one (M2), with 1 DOF for the axial dynamics and a continuous torsional formulation. These are the same models that were used in Chapter 5.

Divergences between the predictions are found, associated to the presence of higher frequencies in the signals obtained with the new model, what reassures the hypothesis that the new continuous approach can capture aspects of the dynamics that cannot be modelled with low-dimensional representations. The efficiency of the drilling is also assessed for the previous simulations with the new model. The highest performance was attained in those simulations where only axial oscillations occurred, while a performance drop was seen when those vibrations were accompanied by torsional stick-slip, suggesting that an optimum damping value associated to the best the drilling performance could be found, were damping controllable. Finally, the second application case is used to illustrate the full potential of the new model to tackle the 3-D lateral, axial, and torsional dynamics in a curved borehole.

6.2

The drill-string models

Three drill-string models, namely M1, M2 and M3, will be used. A sketch showing their main components is presented in Fig. 6.1. To the left, the different structural models are depicted. To the right, the main elements used to obtain the bit-rock interaction model are illustrated.

6.2.1

Models M1 and M2

Model M1 has been described in full in Chapter 5. It considers a 1-DOF axial and 1-DOF torsional formulation. The equations of motion are given in (5-1) and (5-2).

Model M2 has been explained in detail in Chapter 5 too. It considers 1-DOF for the axial equation, whereas a continuous wave equation is used for the torsional one. The equations of motion are given in (5-1) and (5-3).

In both cases, the cutting dynamics are analysed following the description given for the bit-rock interaction relations of Section 5.3.1. The previous equations of motion are solved together with the advection formulation in (5-21).

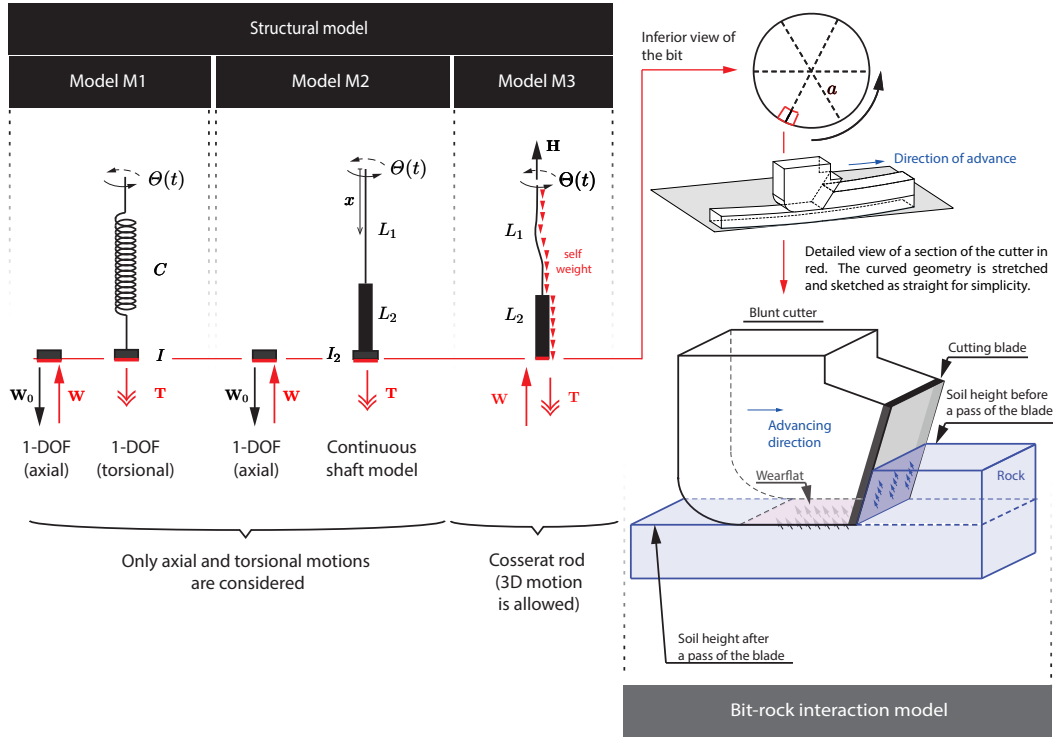


Figure 6.1: Sketch of the models M1, M2 and M3, used in the simulations, and bit model used for the bit-rock interaction relation.

For M1 and M2, the boundary conditions match those given in the previous chapter for scenarios C1-A and C1-B, respectively. With regard to the initial conditions, they are taken as a perturbation from the nominal case, also following the description given in Chapter 5.

6.2.2 Model M3

This new model, M3, is based on the theory of Cosserat rods. It accounts for a continuous formulation for the axial and the torsional dynamics. In comparison with M1 and M2, this formulation allows to capture more aspects of the dynamics. The reason for this is that, unlike the previous approaches, M3 can simulate the axial, torsional, and flexural motion in any direction; it can detect lateral contact with the wall; and, on top of that, a continuous formulation is used for any of the possible dynamics. Additionally, the main contributions of the previous models are retained: the bit-rock interaction relations account for the cutting at the bit, coinciding with that used for M1 and M2; and the approach can be used to study the dynamics in other borehole geometries that are not necessarily vertical or straight.

The equations of motion for M3 are those given in (2-26), (2-51), and

(2-61) of Chapter 2, coupled with the formulation for the dynamics of the cutting described in Chapter 5. This is done through a coupling with the advection equation given in (5-21), with boundary conditions (5-22) and (5-23), plus some initial conditions. The constitutive relations are those of a Kelvin-Voigt material, provided in Section 2.5 of Chapter 2, with c_d being a damping coefficient that will be varied in the simulations.

The distributed forces and torques to be considered are

$$\mathbf{f}_n^R = \rho^o g A(s^o) \mathbf{e}_3, \quad \mathbf{f}_m^R = \mathbf{0}, \quad (6-1)$$

with $A(s^o)$ being the area associated to the cross-section, ρ^o the density of the material and g the gravity constant. Therefore, the only distributed force acting in the length of the string is the self-weight in the longitudinal direction.

The model M3, consisting of a Cosserat rod formulation, admits a non-oscillatory solution for the straight vertical case. This solution is herein referred to as the nominal solution, and it can be found following an analogous procedure to that of Section 5.4.

Also, alike with M1 and M2, the boundary conditions for M3 are taken as those that correspond to the nominal case, as well as the initial conditions, with the exception of the initial angular velocity that includes a perturbation from the nominal state due to the magnitude $\Delta\Omega_0 \neq 0$.

Considering the functions

$$\begin{aligned} \Psi(s^o, t) &= \left(\Omega_0 + \frac{\Delta\Omega_0 s^o}{(L_1 + L_2)} \right) t, \text{ with } \Delta\Omega_0 = \Omega_0/10 \\ h(s^o, t) &= \frac{d}{dt}(\Psi(s^o, t)) \\ f(s^o) &= \begin{cases} \frac{s^o(2H_0 - A_p g \rho^o s^o)}{2A_p E_p}, & \text{if } s^o \leq L_p \\ \frac{s^o(H_0 + A_c L_p g \rho^o - A_p L_p g \rho^o)}{A_c E_c} - \frac{g \rho^o (s^o)^2}{2E_c} \\ - \frac{L_p(2A_p E_p H_0 - 2A_c E_c H_0 - 2A_p^2 E_p L_p g \rho^o)}{2A_c A_p E_c E_p} \\ - \frac{L_p(A_c A_p E_c L_p g \rho^o + A_c A_p E_p L_p g \rho^o)}{2A_c A_p E_c E_p}, & \text{if } s^o > L_p \end{cases} \end{aligned} \quad (6-2)$$

the initial conditions for M3 are

$$\mathbf{r}^R(s^o, t = 0) = \begin{bmatrix} 0 \\ 0 \\ f(s^o) \end{bmatrix} \quad (6-3)$$

$$\boldsymbol{\omega}^R(s^o, t = 0) = \begin{bmatrix} 0 \\ 0 \\ h(s^o, t = 0) \end{bmatrix} \quad (6-4)$$

$$\mathbf{q}^R(s^o, t = 0) = \begin{bmatrix} \cos(\Psi(s^o, t = 0)/2) \\ 0 \\ 0 \\ \sin(\Psi(s^o, t = 0)/2) \end{bmatrix} \quad (6-5)$$

where \mathbf{q}^R is found by using (2-15), with \mathbf{e}_q in the longitudinal direction, taking the quaternion form $\mathbf{e}_q = \{0, 0, 0, 1\}$. The values taken for the previous functions can be easily obtained given that, for the straight configuration, the solution using a Cosserat rod matches that given by a classical straight 1-D linear bar-shaft formulation.

The boundary conditions at the top are

$$\mathbf{r}^R(s^o = 0, t) = \begin{bmatrix} 0 \\ 0 \\ N/A. \end{bmatrix}, \quad \mathbf{n}^R(s^o = 0, t) = \begin{bmatrix} N/A. \\ N/A. \\ H_0 \end{bmatrix}, \quad (6-6)$$

$$\boldsymbol{\omega}^R(s^o = 0, t) = \begin{bmatrix} 0 \\ 0 \\ \frac{d}{dt}\Psi(s^o = 0, t) \end{bmatrix}, \quad (6-7)$$

where N/A indicates that no condition is applied for the corresponding component; H_0 is the hook load at the top, from where the drill-string hangs.

At the bit, they are given by

$$\mathbf{r}^R(s^o = L_1 + L_2, t) = \begin{bmatrix} 0 \\ 0 \\ N/A. \end{bmatrix}, \quad \mathbf{n}^R(s^o = L_1 + L_2, t) = \begin{bmatrix} N/A. \\ N/A. \\ W_c + W_f \end{bmatrix} \quad (6-8)$$

$$\boldsymbol{\omega}^R(s^o = L_1 + L_2, t) = \begin{bmatrix} 0 \\ 0 \\ N/A. \end{bmatrix}, \quad \mathbf{m}^R(s^o = L_1 + L_2, t) = \begin{bmatrix} N/A. \\ N/A. \\ T_c + T_f \end{bmatrix} \quad (6-9)$$

6.3

Simulations

A comparison among the predictions obtained with the Cosserat rod model M3 and those given by M1 and M2 will be made. Four simulations will be carried out focusing on studying a vertical borehole with varying damping

levels. In those simulations, no lateral forces nor other lateral effects will act over the string during the simulations. This choice is made for comparison purposes, given that the other models do not consider lateral displacements. After that, one last simulation concerning a curved borehole will also be included to show the full potential of the Cosserat rod approach.

6.3.1

Parameters

A summary of the parameters employed in the simulations is provided in Table 6.1.

- Following [14], a corrected inertia I for the BHA is used in model M1. The inertia is calculated as

$$I = \rho \left(\frac{1}{3} L_1 J_1 + L_2 J_2 \right). \quad (6-10)$$

- The hook load H_0 is calculated as the difference between the total weight of the column (drill-pipes and BHA) and W_0 .
- Only for model M3, that includes the lateral contact, the parameters $k_s = 10^4$, $\mu_s = 0.3$, $\mu_d = 0.15$, $n_{fr} = 20$, and $\epsilon_{fr} = 10^{-4}$ are adopted, although these parameters will only play a role in the non-vertical drill-string configuration of Section 6.3.6.
- The number of elements N_1 (Table 6.1) is the sum of elements present in the domains x_1 and x_2 .

For M2, the convergence analysis that was used is provided in [74]. With this model, the number of elements refers to the one used in the torsional wave equation, with a discretisation considering quadratic Lagrange elements. For M3, cubic Lagrange shape functions were used. The number of elements is chosen after the convergence study further below. Additionally, the number of elements N_2 is used in the discretisation of the advection equation, where linear Lagrange elements are used. Its value is chosen after verifying that the results can capture the dynamics seen in [14].

6.3.2

Convergence analysis for M3

The finite elements method (FEM) is adopted to spatially discretise all the equations that will be used in the simulations. An appropriate choice of the number of elements in the mesh is fundamental before simulating any problem with a FEM discretisation, as it allows to arbitrarily control the accuracy of the approximation, by choosing an acceptable threshold for some error criteria. This is a characteristic that, by construction, is not present in lumped formulations.

The number of elements is linked to the number of DOFs that are considered in a discretised implementation of a continuous model. Its importance lies in the capacity of the formulation to produce a sufficiently accurate representation of the waves that will be travelling within the structure, an aspect that is among the main differences between the implementation of models based on continuum approaches and lumped ones.

In what follows, this selection is done after a convergence analysis is carried out. For the convergence analysis, a reference problem is solved many times considering a different number of elements. In particular, the case of a vertical borehole with the parameters in Table 6.1 and $c_d = 10^{-4}$ was used. The results are depicted in Fig. 6.2, where a measure of the error, Ξ , is plotted against the total number of elements N_1^i used in the approximations of each of the equations.

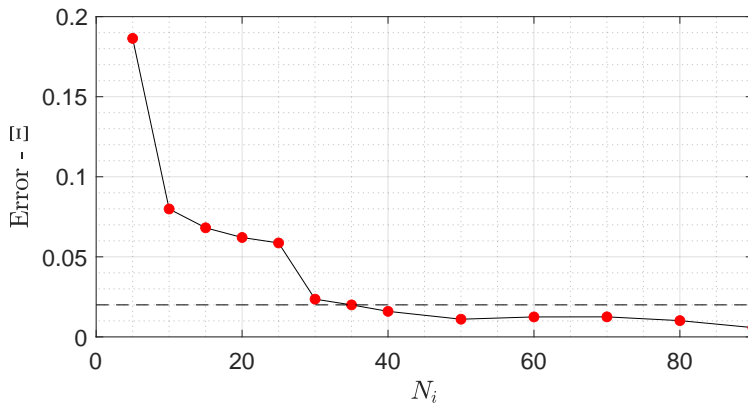


Figure 6.2: Convergence analysis. Error Ξ vs. the total number of elements in each spatial domain N_1^i . In the simulation $c_d = 10^{-4}$ was used.

The error is calculated as

$$\Xi = \frac{\int \left(\omega_{3,N_i} - \omega_{3,N_{300}} \right) dx}{\int \omega_{3,N_{300}} dx} \Big|_{t=80s} \quad (6-11)$$

where ω_3 represents the angular speed in the longitudinal direction (the direction of \mathbf{d}_3^R), and $\omega_{3,N_{300}}$, with 300 elements, is taken as the reference for the comparisons.

The results are depicted in Fig. 6.2 show that a mesh $N_i \geq 40$ is sufficient to ensure the selected threshold $\Xi\% \leq 0.02$. It was chosen to take $N_1 = 64$ elements.

Before moving forward to the actual simulations, it is important to point out that the way the number of DOF, or elements in the mesh, is chosen, is different in continuous models and lumped ones. In the latter type, the number of DOF is preselected upon the model's construction without a theoretical justification. Thus, the only means to check the correctness of the results is through validation. To the authors of this work, such an upfront choice only makes sense when clear lumped elements are present in the system that is to be studied. For instance, if the system contained evident elements with mass and inertia concentrated in a small portion of the system, connected by flexible elements with much smaller mass and inertia, which is not the case of a drill-string. Drill-strings are a typical example of extremely slender long distributed systems.

6.3.3

Simulation V1: a verification of model M3

A first simulation to verify the predictions of model M3 with other known results is run. For this task, it is shown that the Cosserat model M3 can be reduced to the lumped formulation M1 if a quasi-static condition is adopted for the drill-pipes, and if the BHA inertia is concentrated at the end of the string. Thus, a similar strategy to that used in [74] to show that the semi-continuous model M2 can also be reduced to M1 is adopted. The strategy involves adding an additional parameter, α , that modifies the distributed inertia of the drill-pipes and the BHA. When $\alpha = 1$, the inertia is fully distributed over the total length of the system, while in the limit $\alpha \rightarrow 0$ the distributed inertia is negligible, and it is added as a lumped element in the boundary condition at the bit (for more details see [74]). In other words, in the limit where $\alpha \rightarrow 0$, the results for M3 are those of a quasi-static condition and coincide with the predictions given by M1 and M2.

In Fig. 6.3(a) the predictions for the angular speed at the bit, $\omega_b(t)$, are illustrated. Figure 6.3(b) depicts the non-dimensional angular and axial speeds as functions of a non-dimensional time variable τ , in black thick and thin lines, respectively. For this simulation, the parameter $\alpha = 0.05$ was used. To express the angular and axial speed in their non-dimensional form used in the figure,

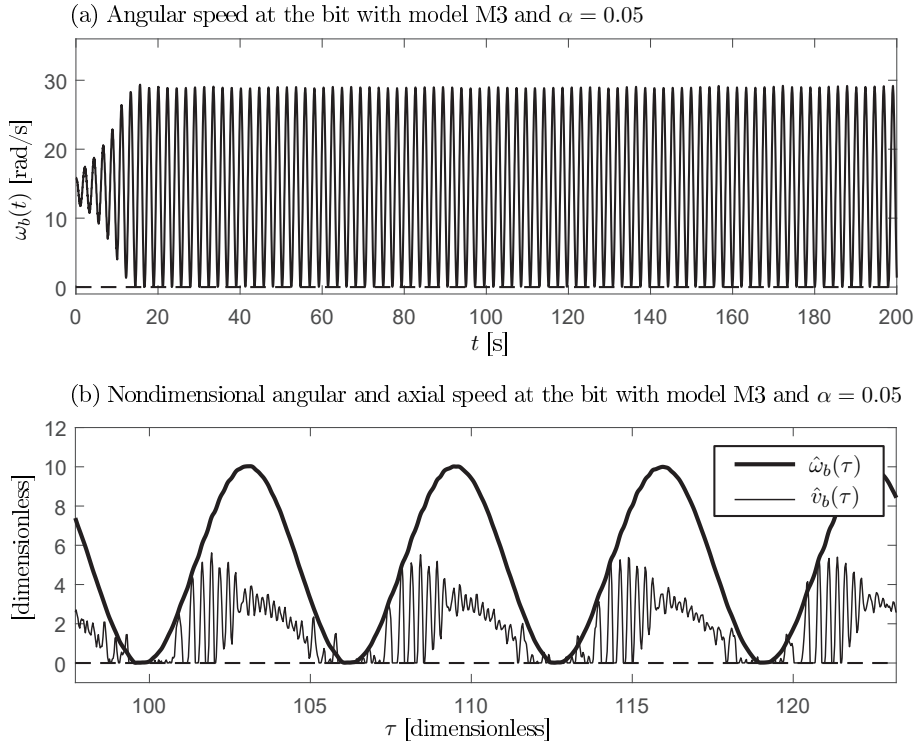


Figure 6.3: Considering model M3 with $\alpha = 0.05$, the graph shows: (a) Angular speed vs. time considering model M3 with $\alpha = 0.05$; (b) Non-dimensional angular and axial speed, $\hat{\omega}_b(\tau)$ and $\hat{v}_b(\tau)$ vs. non-dimensional time τ .

the following definitions were considered: $L^* = 6.383 \cdot 10^{-4}$ m, $t^* = 0.3467$ s, and $\hat{\omega}_b(\tau) = \omega_b(t = \tau t^*)t^*$, $\hat{v}_b(\tau) = v_b(\tau t^*)t^*/L^*$, $\tau = t/t^*$ (see [74] for more details).

The graphs of Fig. 6.3, obtained with the Cosserat rod model, are very similar to those presented in [14], as well as to the ones simulated with M2 for small α in [74].

To analyse these new results in the frequency domain, Fig. 6.4 contains the FFT for both the angular and the axial speed at the bit. The spectrum shows that the same frequencies are excited in all cases, as it was expected due to the similarity of the responses in the time domain.

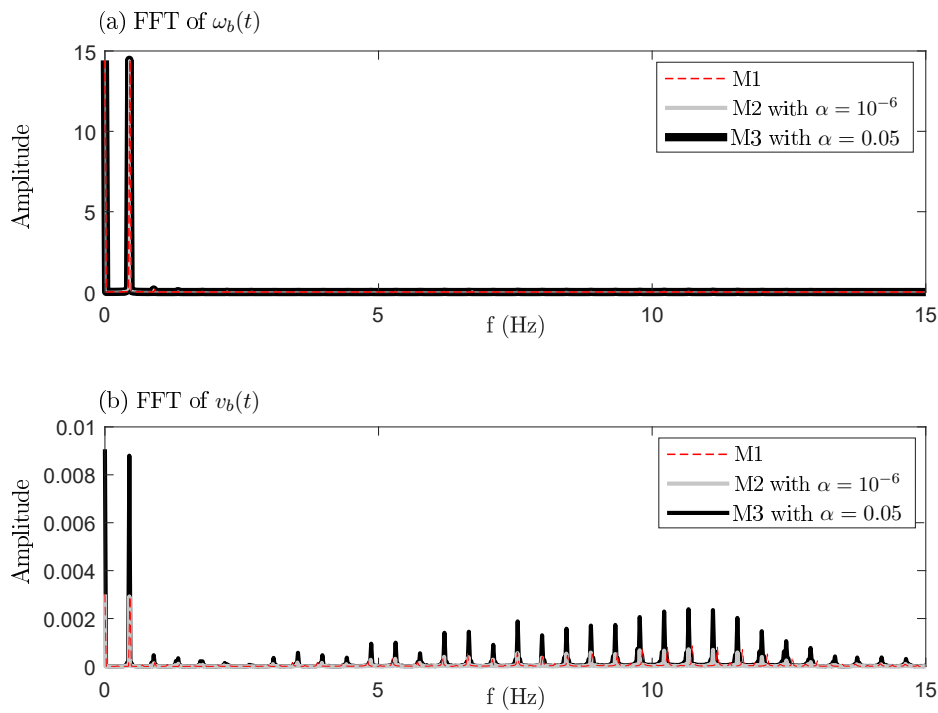


Figure 6.4: FFT for (a) the angular speed at the bit; (b) the and axial speed at the bit. The results obtained with models M1, M2 and M3 are overlaid.


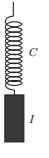
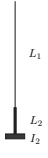
		Real structure	Model M1	Models M2 and M3
				
Property	Description			
L_1	Drill-pipe length	1000 m	spring (C)	1000 m
L_2	BHA length	200 m	rigid	200 m
N_1	Number of elements (torsion)	-	-	64
N_2	Number of elements (advection)	-	64	64
I, I_2	Lumped inertia	-	$I = 112.67 \text{ kgm}^2$	$I_2 = 0 \text{ kgm}^2$ (*)
α	Artificial parameter	-	-	1.00 (*)
H_0	Hook load	-	-	463.93 kN (**)
C	Rigidity parameter	-	469.05 Nm/rad	-
ρ, ρ_1, ρ_2	Density	7800 kg/m ³		
r_{po}	Drill-pipe external radius	63.5 mm		
r_{pi}	Drill-pipe internal radius	54.0 mm		
r_{co}	Collar external radius	76.2 mm		
r_{ci}	Collar internal radius	28.0 mm		
G_1, G_2	Shear modulus	77 GPa		
a	Bit radius	108.0 mm		
l	Drill-bit wearflat length	1.2 mm		
ϵ_1	Rock intrinsic specific energy	0.252 GPa		
σ_1	Rock contact strength	0.252 GPa		
ϵ_2	Rock intrinsic specific energy	0.504 GPa		
σ_2	Rock contact strength	0.504 GPa		
M	Lumped mass	24614.40 kg		
Ω_0	Imposed angular speed	14.42 rad/s (**)		
W_0	Nominal weight-on-bit	45.7 kN		
γ	Drill-bit geometry parameter	1.00		
ζ	Cutter inclination coefficient	0.38		
μ	Coefficient of friction	0.80 (***)		
c_1	Regularisation constant	$1 \cdot 10^{-5}$		
c_2	Regularisation constant	$1 \cdot 10^{-1}$		
c_3	Regularisation constant	$1 \cdot 10^{-3}$		

Table 6.1: List of parameters employed in the simulations. (*) indicates that the parameter changes for some of the simulations. (**) indicates that the parameter is only used in model M3. This table is an adaptation from [74].

6.3.4

Simulations C1: assessing the influence of damping in the response

The Cosserat rod model, M3, will be used in all the simulations presented in this section. The effect of taking different values for the damping coefficient c_d is analysed, considering the cases $c_d = 10^{-2}$, 10^{-3} , 10^{-4} , and 10^{-5} . All the simulations are run for 1000 s, and special attention is paid to the signals of the angular speed at the bit, $\omega_b(t)$, and the axial speed at the bit, $v_b(t)$, in both the time and the frequency domains.

To begin with, the torsional behaviour of the system is analysed through Fig. 6.5. The graph contains a time domain representation of the angular speed at the bit for each of the different damping cases. Three different qualitative behaviours are observed when these cases are compared:

- Vanishing torsional oscillations appear in Fig. 6.5(a) and 6.5(b). These two belong to the cases with $c_d = 10^{-2}$ and $c_d = 10^{-3}$, which correspond to the highest dampings that were used.
- Non-vanishing oscillations are found in Fig. 6.5(c), with $c_d = 10^{-4}$. The response observed for the angular speed is divided into two regions of similar qualitative characteristics, named as R_1 and R_2 in the plot. Three different sub-regions can be also identified within each of the previous: the first sub-region is characterised for presenting a response where low frequencies are dominant; then, another one follows where higher frequencies prevail; and in the last sub-region, a combination of both low and high frequencies is observed. This observations are further justified below where a study in the frequency domain is conducted.
- Torsional stick-slip behaviour: extreme torsional oscillations showing stick-slip oscillations are observed in Fig. 6.5(d), with $c_d = 10^{-5}$.

Through the previous analysis it was noted that the results notably changed as the damping in the system decreased, giving rise to dynamics where higher frequencies appeared throughout the simulated time. To understand why this behaviour occurred, a study in the time and frequency domain will be conducted further below. In that analysis focus will be given to the link between the torsional and the axial dynamics provoked by the coupling produced by the bit-rock interaction model. However, before doing so, a brief comment about the torques involved in this simulations is made as a means to verify the rationality of the results.

The torques associated with the previous cases are depicted in Fig. 6.6, for some portion of the total simulated time. The aim of including a graph

showing their variation is to verify that the involved magnitudes do not differ greatly, in their mean, from the values reported in [14, 74]. The simulations in [74] present a completely developed permanent response after $t = 50$ s, while the total simulation lasts 80 s. This is shorter than the simulated time with M3, which also needs a longer simulated time window for the oscillations to fully develop. For that reason, the comparisons are made using different time windows: $t \in [75; 80]$ s for the prediction of [74], and $t \in [195; 200]$ s for the new cases with different damping coefficients.

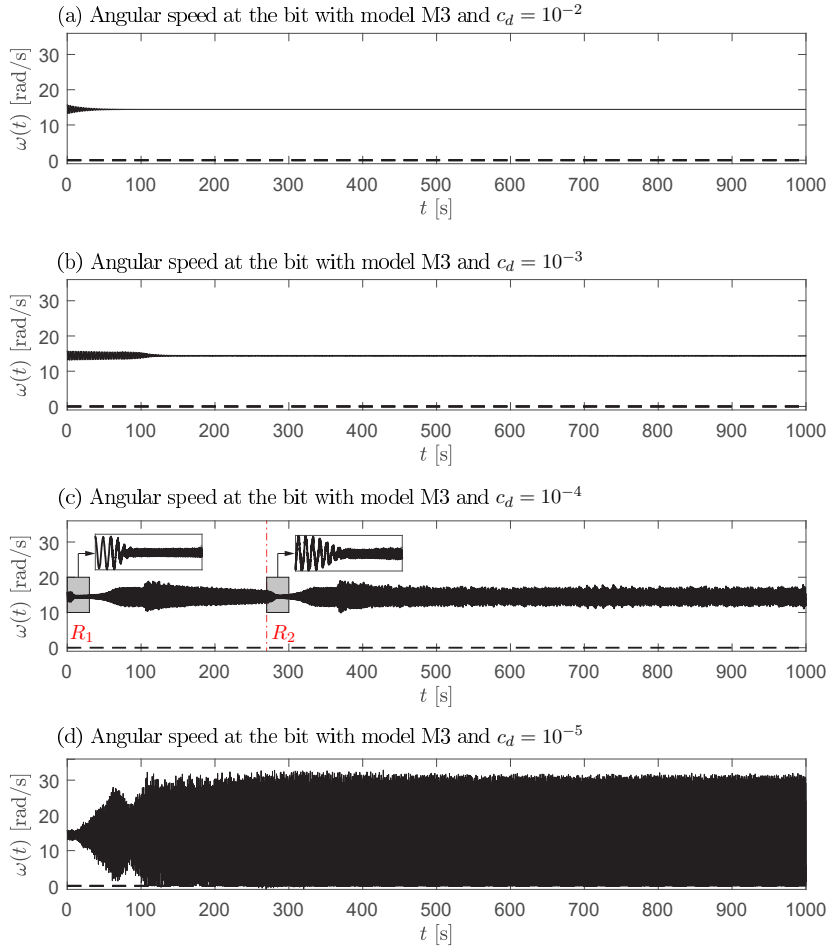


Figure 6.5: Angular speed at the bit for different values of the damping coefficient c_d , where (a) $c_d = 10^{-2}$; (b) $c_d = 10^{-3}$; (c) $c_d = 10^{-4}$; (d) $c_d = 10^{-5}$.

The torques found with the three different models show a difference in their mean value of less than 4% from that obtained with M1. The shape and amplitude are different in all cases, although the variation from the mean is smaller in all the scenarios simulated with M3. For that reason, the new model does not produce very different results in terms of the mean forces and torques that act in the structure.

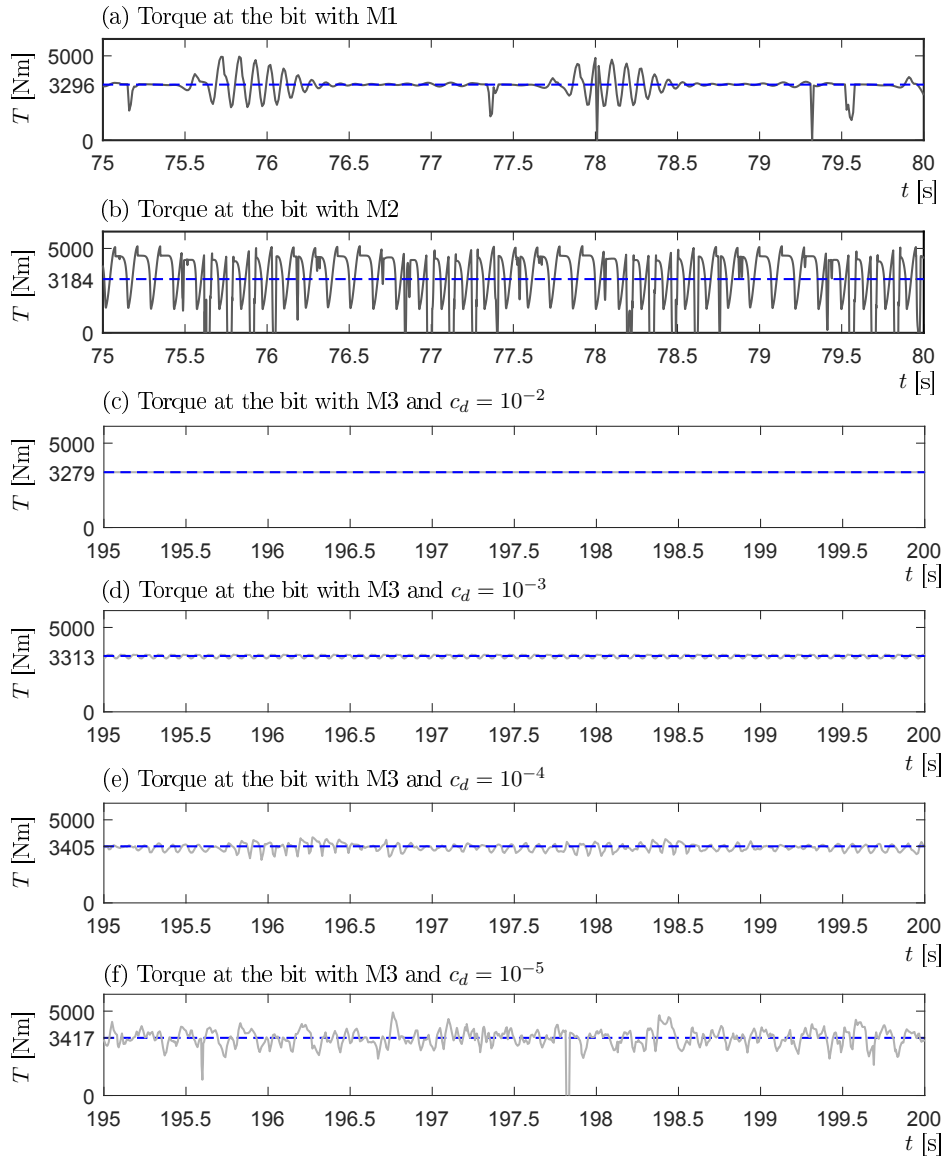


Figure 6.6: Torques at the bit T for (a) model M1; (b) Model M2; (c) model M3 with $c_d = 10^{-2}$; (d) model M3 with $c_d = 10^{-3}$; (e) model M3 with $c_d = 10^{-4}$; and (c) model M3 with $c_d = 10^{-5}$. The mean value is indicated, for each case, with dashed blue line.

Next, the previous signals associated with the torsional behaviour as well as the ones related to the axial speed at the bit will be analysed in more detail in the frequency domain.

Each of the following plots, from Fig. 6.7 to Fig. 6.10 present a similar structure where four subplots are used: in (a) the angular speed at the bit is depicted; in (b) the axial speed at the bit is shown; (c) to (e) give the FFTs associated to different time windows of the angular speed signal; and (f) to (h) depict the FFTs associated to different time windows of the angular speed signal. These windows have been named and coloured in grey for easy

identification in the plots in the time domain. In all cases the first 200 s of simulations are analysed.

6.3.4.1

Simulation with damping $c_d = 10^{-2}$

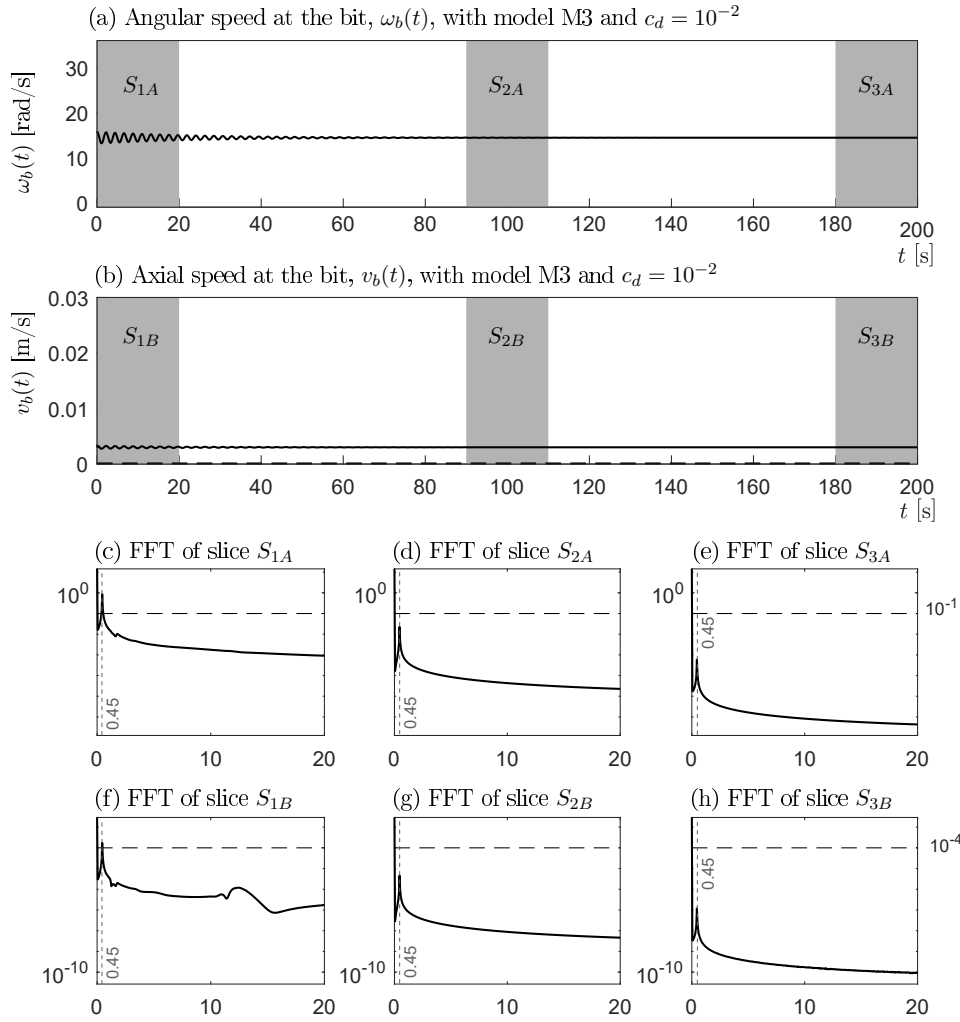


Figure 6.7: (a) Angular speed at the bit for $c_d = 10^{-2}$; FFT of the previous signal for (b) slice S_1 ; (c) slice S_2 ; (d) slice S_3 .

Figure 6.7 depicts the results associated with the damping coefficient $c_d = 10^{-2}$. This case considers the highest damping that was simulated. In this scenario, vanishing oscillations are observed for both the torsional and the axial dynamics at the bit, consistent with the graphs of the temporal domain in Fig. 6.7 (a) and (b). This is also seen in the FFTs in (c) to (e) and (f) to (h), where the only identifiable frequency is the fundamental torsional frequency of 0.45 Hz. As already mentioned, the amplitudes observed in these FFTs decay with time.

6.3.4.2

Simulation with damping $c_d = 10^{-3}$

Figure 6.8 shows the results for a damping coefficient $c_d = 10^{-3}$. Low-frequency vanishing oscillations are observed for the torsional dynamics in the time domain. The axial response shows self-excited oscillations throughout the whole simulation. Due to the coupling in the bit-rock interface, the axial dynamics have a forcing effect on the torsional one. Additionally, these axial oscillations lead to stick-slip behaviour in the axial direction, characterised by phases where the column advances in the longitudinal direction and phases where the axial advance is stopped, while the column can still rotate and drill (removing material at a constant axial bit position, at most, up to the completion of a turn). In this context, the axial stick can occur for, at the most, one turn of the bit, where all the material that was preventing the axial advance of the column will have been removed. Additionally, no torsional stick-slip is observed.

An analysis in the frequency domain allows a better understanding of the underlying behaviour of the response. The FFTs for the torsional and axial behaviour show an evolution in the frequency profiles as time goes by.

The FFT associated with the torsional behaviour in (c), for a time window $t \in [0; 20]$ s shows that the main and only identifiable frequency in the signal is the fundamental torsional one of 0.45 Hz. For the same time window, the FFT of the axial response depicts a secondary frequency of higher amplitude, at around 13 Hz, while the main frequency is still 0.45 Hz.

As time evolves, for $t \in [90; 110]$ s, (d) shows that the fundamental frequency in the torsional response continues to be the main frequency, but now the secondary amplitude at 13.09 Hz can also be distinguished in the torsional signal. In fact, this secondary amplitude is the one driving the axial response due to the regenerative cutting's self-excited oscillations, as shown in (g).

Finally, looking at the time window associated with the end of the simulation for $t \in [180; 200]$ s, in (e) the main frequency in the torsional response is 13.09 Hz. In contrast with the previous time windows, the structure does not vibrate at the fundamental frequency anymore. Again, this secondary frequency of 13.09 Hz is driving the axial behaviour due to the regenerative cutting effect (the repeated cutting of a wavy surface).

The simulation showed how the frequency content is affected as time goes by. It was observed that the structure vibrates at the fundamental frequency at the beginning of the simulation, and with the passing of time, due to the couplings and the different interactions, the response changes to a vibration in

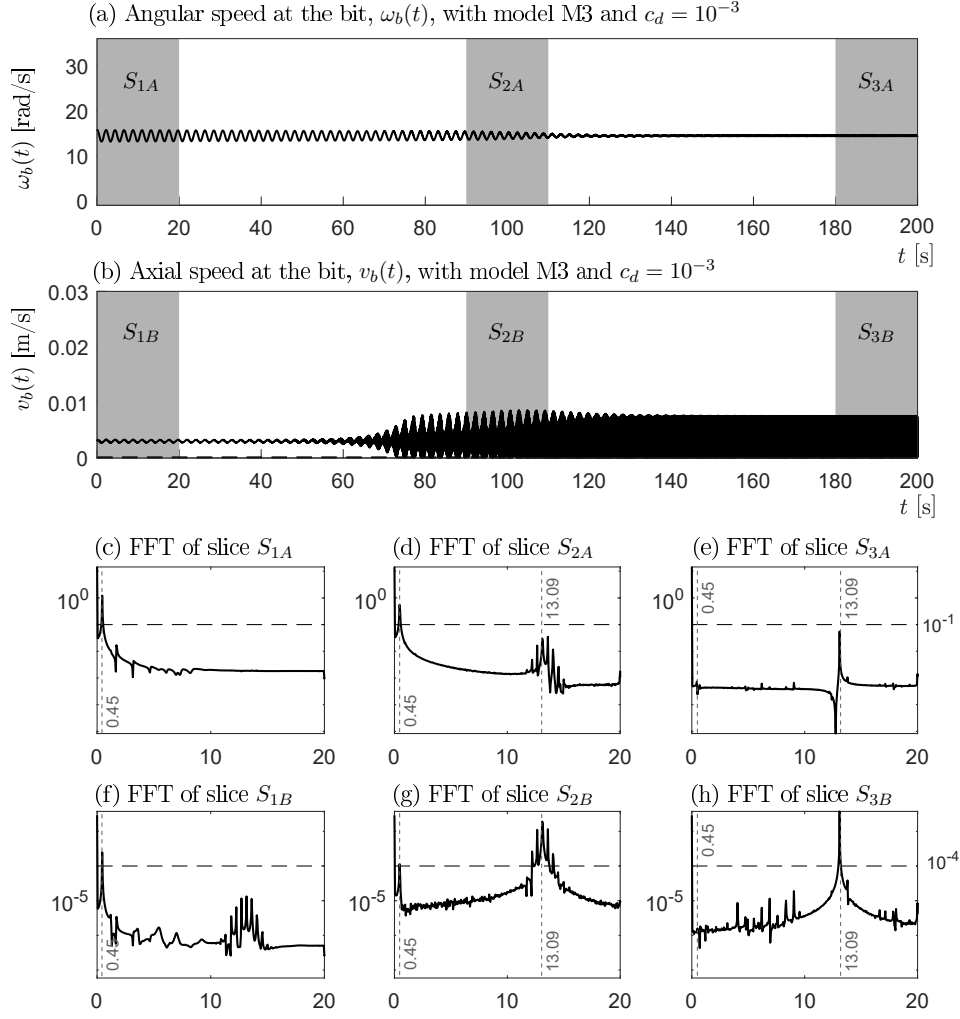


Figure 6.8: (a) Angular speed at the bit for $c_d = 10^{-3}$; FFT of the previous signal for (b) slice S_1 ; (c) slice S_2 ; (d) slice S_3 .

a higher frequency.

The analysis at the different time windows helped to understand the energy exchange between the axial and the torsional dynamics due to the coupling produced by the bit-rock interaction. More importantly, the findings reassure the importance of considering continuous approaches to the modelling of the dynamics of drill-strings, in line with the findings of [74]. In particular, these higher frequency self-excited oscillation that, through the coupling, passes energy to the torsional model, could not have been captured with the 1-DOF axial representation used in M1 and M2. In that matter, M3 presents an advantage over very low-dimensional models which, by construction, are unable to capture the behaviour around the higher frequencies.

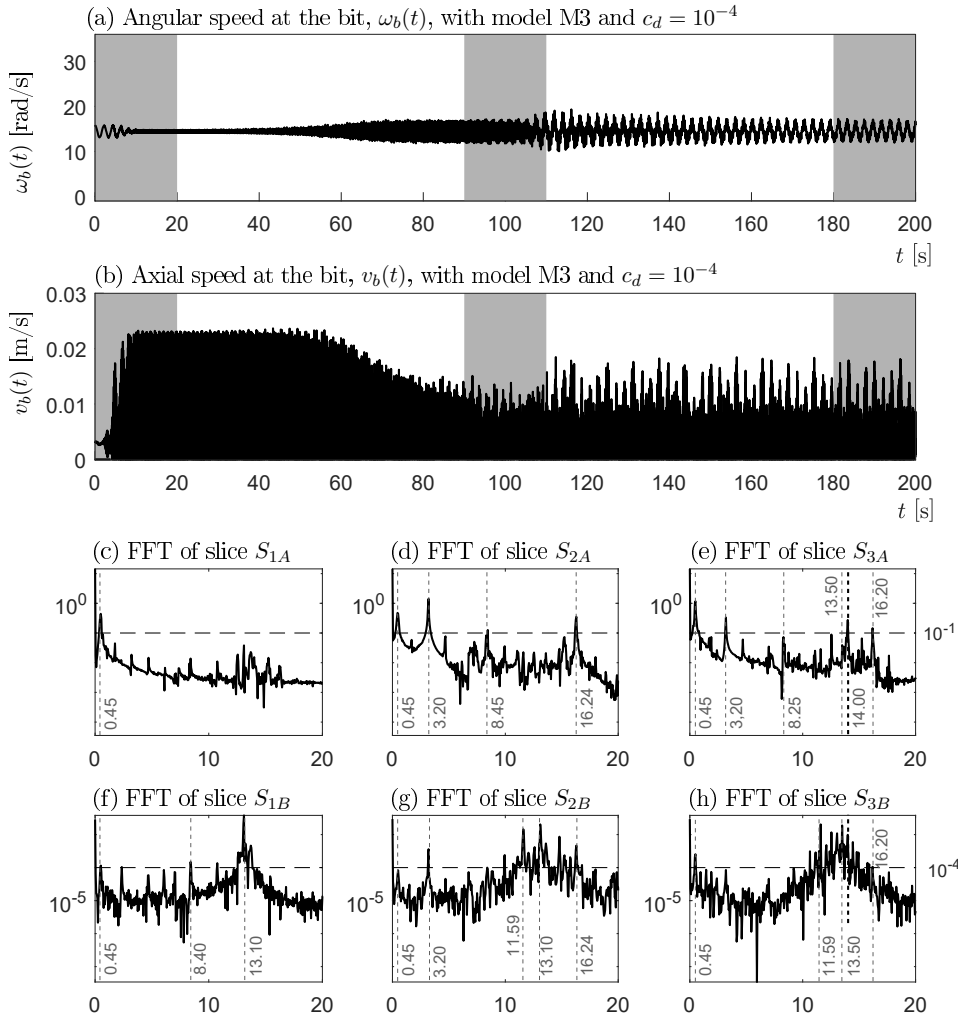


Figure 6.9: (a) Angular speed at the bit for $c_d = 10^{-4}$; FFT of the previous signal for (b) slice S_1 ; (c) slice S_2 ; (d) slice S_3 .

6.3.4.3

Simulation with damping $c_d = 10^{-4}$

Figure 6.9 depicts the predictions for a damping coefficient $c_d = 10^{-4}$. The simulation presents different results from the previous two cases with higher damping coefficients.

In the time domain, the axial dynamics exhibit self-excited oscillations that lead to axial stick-slip. In the torsional response, self-excited oscillations that do not vanish for the simulated time are also observed. The latter shows three distinguishable regions from a qualitative point of view, where different frequency bands drive the response.

Figure 6.9(c) shows that the main frequency in the torsional response considering the time window $t \in [0; 20]$ s is the fundamental one of 0.45 Hz, while in the axial prediction, in (f), a higher frequency of 13.10 Hz is the most

prominent one driving the response. This means that the main frequencies found in the signals at the beginning of the simulation are very different, being the torsional response driven by a low frequency, and the axial response driven by a higher one.

Observing the second time window, $t \in [90; 110]$ s in (g), the situation changes. The frequencies found in the torsional dynamics are 0.45 Hz, 3.20 Hz and 16.24 Hz. The latter, 16.24 Hz, is also in the range of the higher frequencies that drive the axial behaviour.

Finally, the torsional behaviour in (e) for a time window which $t \in [180; 200]$ s, shows that low and high frequencies dominate the torsional predictions. Some of these are 0.45 Hz, 3.20 Hz, 13.50 Hz and 16.20 Hz. The illustration in (h) for the axial response where the band between 11 Hz and 16 Hz is dominant.

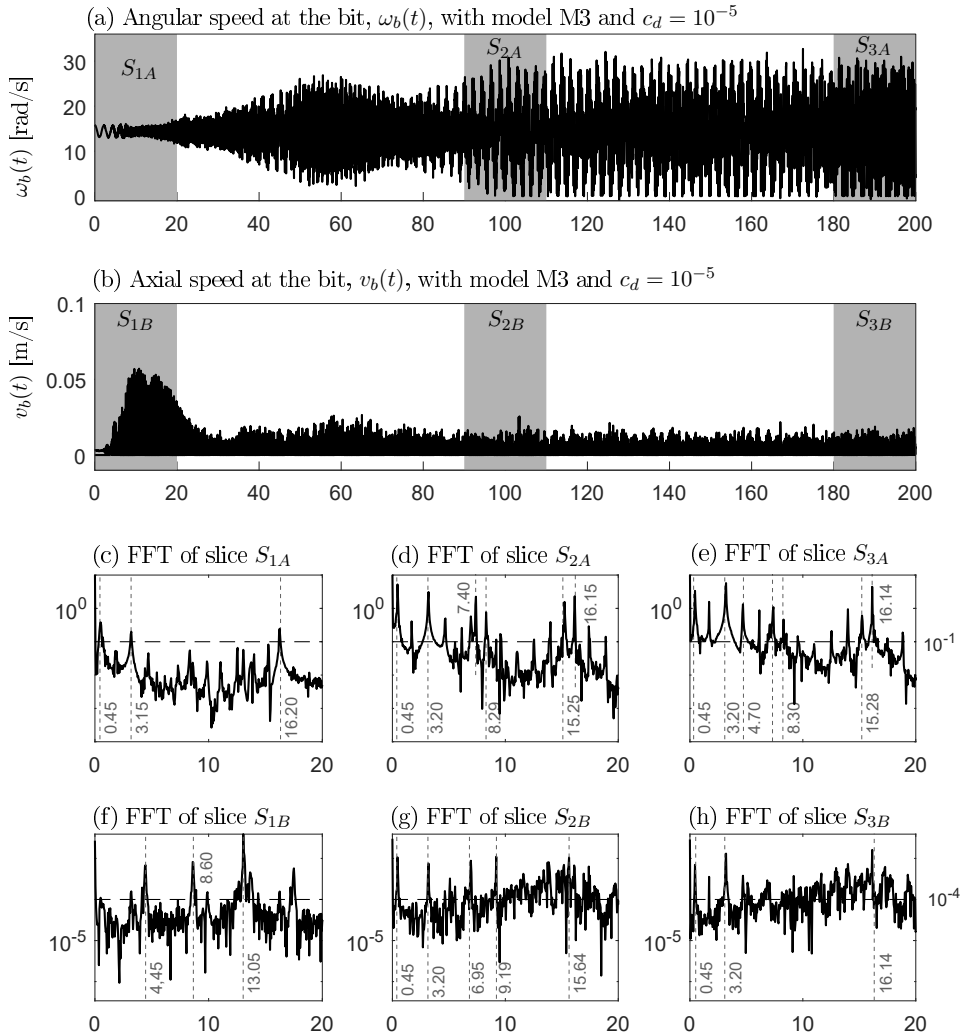


Figure 6.10: (a) Angular speed at the bit for $c_d = 10^{-5}$; FFT of the previous signal for (b) slice S_1 ; (c) slice S_2 ; (d) slice S_3 .

Again, the analysis at the different time windows shows the existing energy exchange between the torsional and the axial dynamics, where the self-excited oscillations due to the regenerative effect provoked axial stick-slip and torsional vibrations.

6.3.4.4

Simulation with damping $c_d = 10^{-5}$

Figure 6.10 illustrates the results for a damping coefficient $c_d = 10^{-5}$. The vibrations lead to stick-slip phenomena in both the torsional and axial dynamics. The FFTs show an evolution of the frequencies with time, where both low and higher frequencies drive the torsional response at all times, and, as with the previous cases, they show an energy exchange between the vibration modes. For instance, from (c) to (e), 0.45 Hz, 3.20 Hz, 15.28 Hz and 16.20 Hz are among the frequencies with the most prominent amplitudes in the FFTs of the torsional response. With the axial ones, a similar situation occurs, where both low and high frequencies are dominant.

As already stated, this case presents a situation where both low and high frequencies are observed in the response in all the time windows, although the higher frequencies are more prominent after the stick-slip vibrations are fully developed, that is, close to the ending of the simulated time, in 6.10(e) and (h).

6.3.5

Comparing the responses with those produced by models M1 and M2

The responses obtained with M3 are compared against those with M1 and M2 in the frequency domain. The corresponding FFTs associated with the models M1 and M2 are depicted in Fig. 6.11, which is included below to facilitate the analysis. The comparisons consider the signals in the time window where $t \in [180; 200]$ s, being $\omega_b(t)$ the angular speed at the bit and $v_b(t)$ the axial speed at the bit.

6.3.5.1

Simulation with damping $c_d = 10^{-5}$

Figure 6.12 shows that the results for $c_d = 10^{-5}$, with M3, present higher frequencies than those observed with M1 and in [14]. This is in line with the findings presented in [74] for the comparison between M2 and M1, where M2 also showed a response involving higher frequencies. Nevertheless, with M2, the most prominent amplitude is linked to 7.40 Hz, which coincides with a torsional natural frequency, while with M3 the most prominent peaks in the FFT are

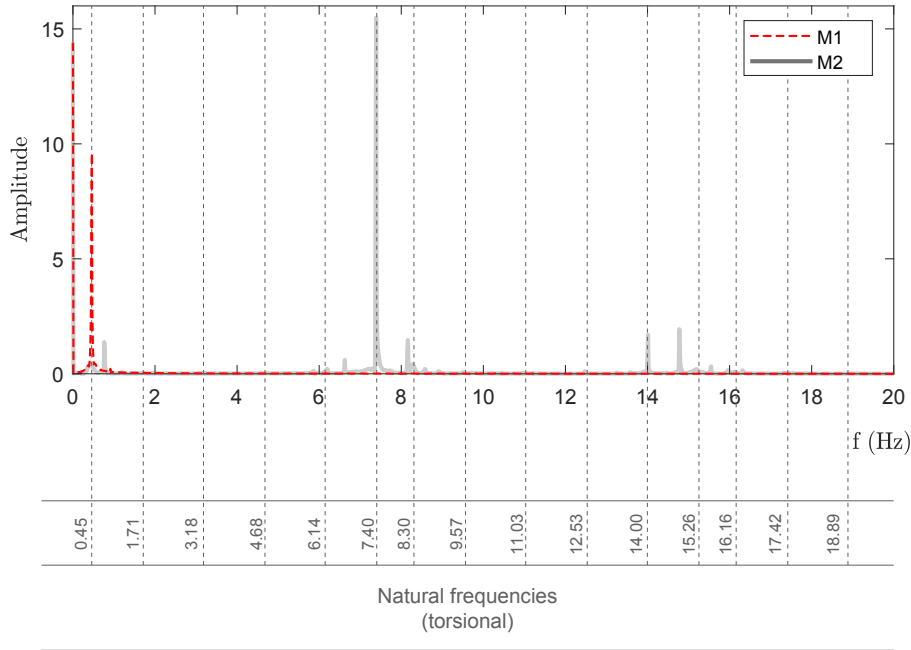


Figure 6.11: FFT of the angular speed at the bit obtained with models M1 and M2. $\alpha = 1$ was used.

0.45 Hz, 3.20 Hz and 16.14 Hz. That is, both lower and higher frequencies appear. The main difference between the two models is that M2 considers a 1-DOF rigid axial approach, thus it is incapable of exciting any axial natural frequency, as opposed to what happens in a continuous model like M3.

6.3.5.2

Simulation with damping $c_d = 10^{-4}$

Figure 6.13 depicts the results for $c_d = 10^{-4}$. This scenario is different from the previous one with the lowest damping. The most prominent frequency found is 0.45 Hz, followed immediately by 3.20 Hz. As it was shown, the case $c_d = 10^{-4}$ did not show self-excited vibrations that lead to a torsional stick-slip motion for the period evaluated, as opposed to the predictions of [14], and the models M1 and M2, where torsional stick-slip is expected. On top of that, these simulations show that other amplitudes apart from the fundamental one are excited even in these scenarios, what indicates that considering only a rigid mode of axial vibration is insufficient to capture all the aspects of the dynamics given by this model. This result reinforces the observations made by [74] as to the importance of the use of a continuous approach.

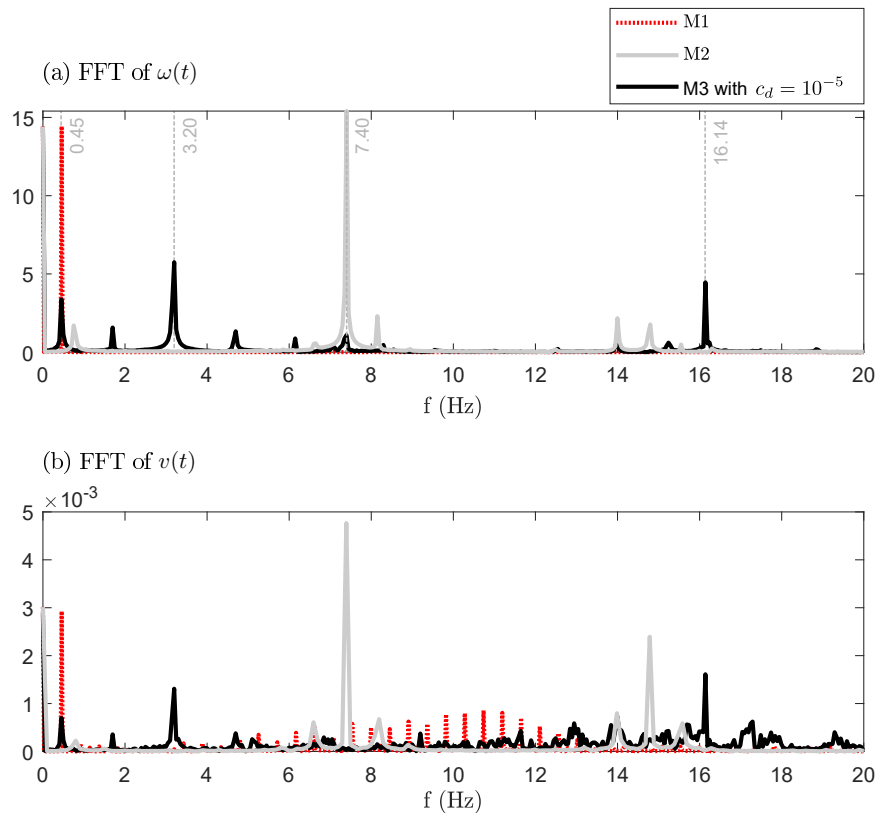


Figure 6.12: FFT of the angular speed at the bit obtained with models M1, M2, and M3 with damping $c_d = 10^{-5}$. $\alpha = 1$ was used.

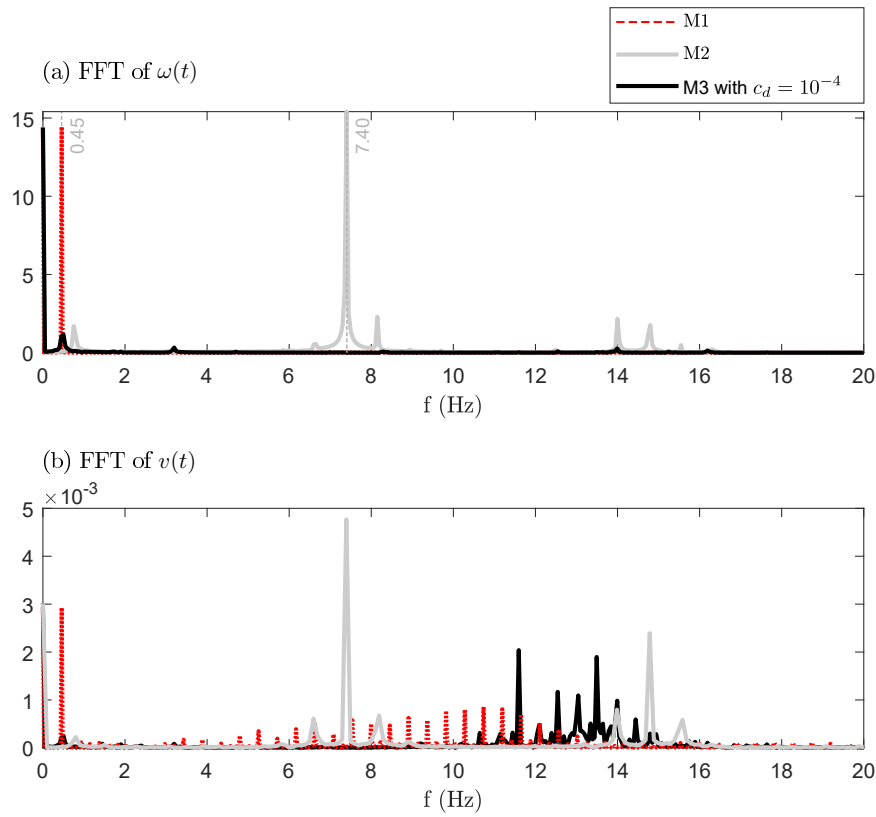


Figure 6.13: FFT of the angular speed at the bit obtained with models M1, M2, and M3 with damping $c_d = 10^{-4}$. $\alpha = 1$ was used.

6.3.5.3

Measuring the performance of the drilling process

To assess the performance of the drilling process, the evolution of the depth reached by the bit is analysed.

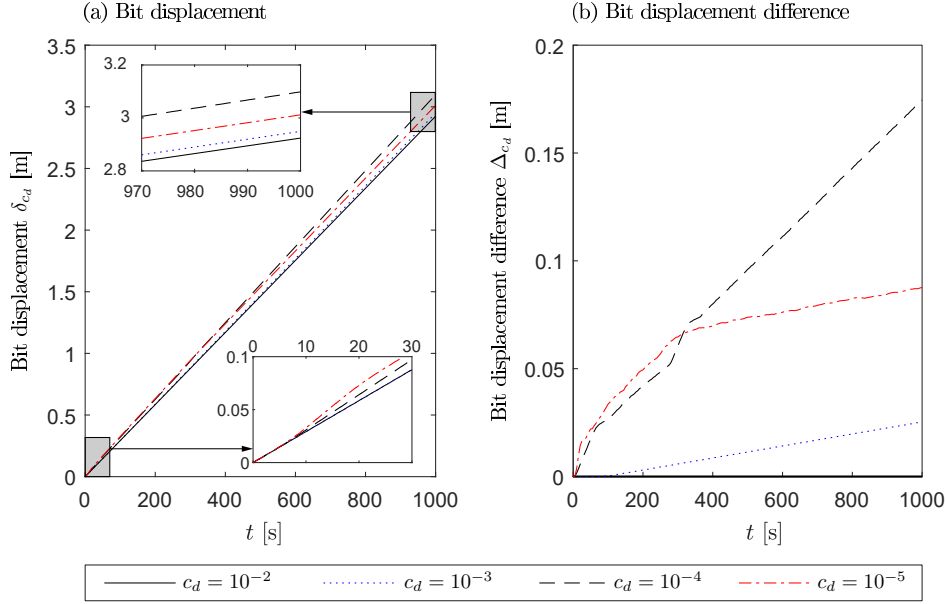


Figure 6.14: Drilling performance. (a) Depicts the bit displacement δ_{c_d} for each damping case c_d ; (b) depicts the bit displacement difference Δ_{c_d} calculated as the bit displacement δ_{c_d} (where each case follows the colouring indicated in the legend of the figure), subtracted by δ_R corresponding to the case with $c_d = 10^{-2}$.

The evolution of the bit depth δ_{c_d} , for each value of damping c_d , is depicted in Fig. 6.14(a). In Fig. 6.14(b) the bit displacement difference Δ_{c_d} is shown. The latter is calculated as $\Delta_{c_d} = \delta_{c_d} - \delta_R$, where δ_i is the bit displacement for the current damping coefficient (following the colouring in the legend) and δ_R is that obtained with $c_d = 10^{-2}$.

Figure 6.14(b) is used to identify what cases present the highest and lowest performances. In the graph:

- The highest damping condition, $c_d = 10^{-2}$, is represented by the horizontal axis ($\Delta_{10^{-2}} = 0$). The fact that all other cases are depicted above this line indicates that this is the simulation with the lowest reach, thus, the poorest performance. Recalling that the case showed quickly decaying torsional and axial oscillations (see Fig. 6.7), this result is, at first, counter-intuitive. The simulation is the closest, at all times, to the nominal solution which is non-oscillatory, and it was expected to be the most efficient case.

- The simulation with $c_d = 10^{-3}$ shows an increased performance in comparison with the previous. The reason for this is that it is characterised by very small torsional oscillations accompanied with axial stick-slip behaviour (see Fig. 6.8).
- The simulation with the highest efficiency is that with $c_d = 10^{-4}$. This corresponds to a case where torsional oscillations exist and they show higher amplitudes than the previous scenarios, but those torsional vibrations do not enter into a stick-slip regime. At the same time, the axial behaviour is characterised by the presence of stick-slip vibrations.
- The simulation with $c_d = 10^{-5}$, the lowest damping, shows a cutting process that is more efficient than with $c_d = 10^{-2}$ and 10^{-3} , but below the performance of $c_d = 10^{-4}$. It is important to recall that this scenario is characterised by both torsional and axial stick-slip.

The previous observations show that the drilling performs better when axial oscillations exist, what makes the system act as a percussive driller. However, performance drop was found when torsional stick-slip occurs. This is expected given that cutting cannot take place when the bit is not rotating.

The findings of this section suggest that, were the damping variable controllable, there exists an optimum level of damping for which the performance is at a maximum.

6.3.5.4

Some remarks concerning the three models

In relation to the axial dynamics, the models of [74], M1, and M2, employ a 1-DOF axial formulation consisting of a free-body subjected to the bit-rock interaction forces. Such models can only account for axial movements compatible with those of a rigid body, that is, no natural axial frequencies can be excited. Therefore, the only axial vibration possible is forced, it is due to the contact and impacts with the soil and the coupling with the torsional dynamics. Then, the self-excited vibrations that are observed in those models must occur on the torsional side, due to the axial-torsional coupling. In contrast, M3 considers a continuous formulation, thus natural axial frequencies can also be excited. The analysis at the different time windows has been useful in understanding the energy exchange between the axial and the torsional dynamics due to the coupling produced by the bit-rock interaction and evaluating how axial vibrations appear. All the results that showed self-excited vibrations reassure the importance of considering a continuous approach to model the dynamics of a drill-string, in particular, to capture this exchange

that can produce axial and torsional vibrations at higher frequencies than those predicted by the aforementioned low-dimensional lumped models.

6.3.6

Simulation C2: considering a non-straight borehole

Up to now, the simulations that were run considered a straight and vertical borehole, with an initial configuration where the string is centred in the borehole. The forces and torques applied were such that the configuration remained centred at all times. Therefore, even though a Cosserat formulation was used, the full potential of the approach with regard to its ability to model non-straight wells was not fully exploited.

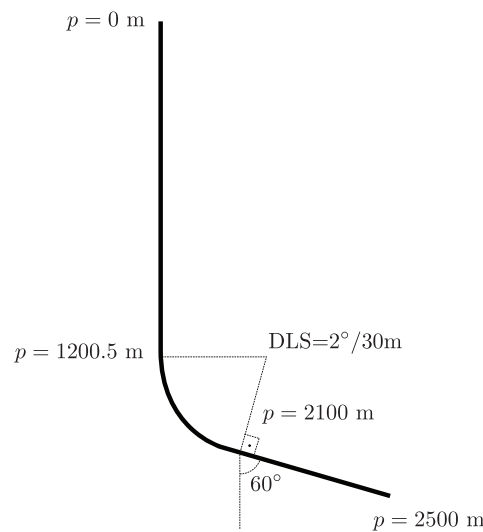


Figure 6.15: Well geometry considered in simulation C2.

The aim of this last simulation is to present a case of a string moving in a curved well, what can only be tackled with the continuous Cosserat model M3. Thus, this application aims at showing other advantages that model M3 presents over the previous two models, apart from those benefits related to using a continuous formulation, discussed in the previous scenario, C1. In this simulation, the drill-string advances into a curved well path provoking lateral contact with the wall, thus forcing the column to change its shape to accommodate to the geometry of the well. Also, when this happens, extra lateral friction affects the system. The well geometry that is considered is given in Fig. 6.15. The set of parameters and initial conditions are those used for the previous simulation considering $c_d = 10^{-2}$, with exception of except for the nominal weight on bit, $W_0 = 68,550 \text{ N}$, and the hook load, $H_0 = 441.08 \text{ kN}$. A total of $t = 10000 \text{ s}$ are simulated.

The position of the centreline of the drill-string is depicted in Fig. 6.16 for 1000, 5000 and 10000 s. The graph illustrates how the drill-string gets curved, following the pre-defined well path, as drilling takes place. Recalling that neither M1 nor M2 consider the lateral dynamics, to exemplify one of the advantages of M3, the bending moments associated with the latter time, $t = 10000$ s, are depicted in Fig. 6.17. All the bending moments present a local change in their values in an area close to the contact region.

The behaviour shown in the previous two figures can only be captured with a model that includes the lateral dynamics, thus the importance of a Cosserat rod formulation that can account for large displacements and rotations.

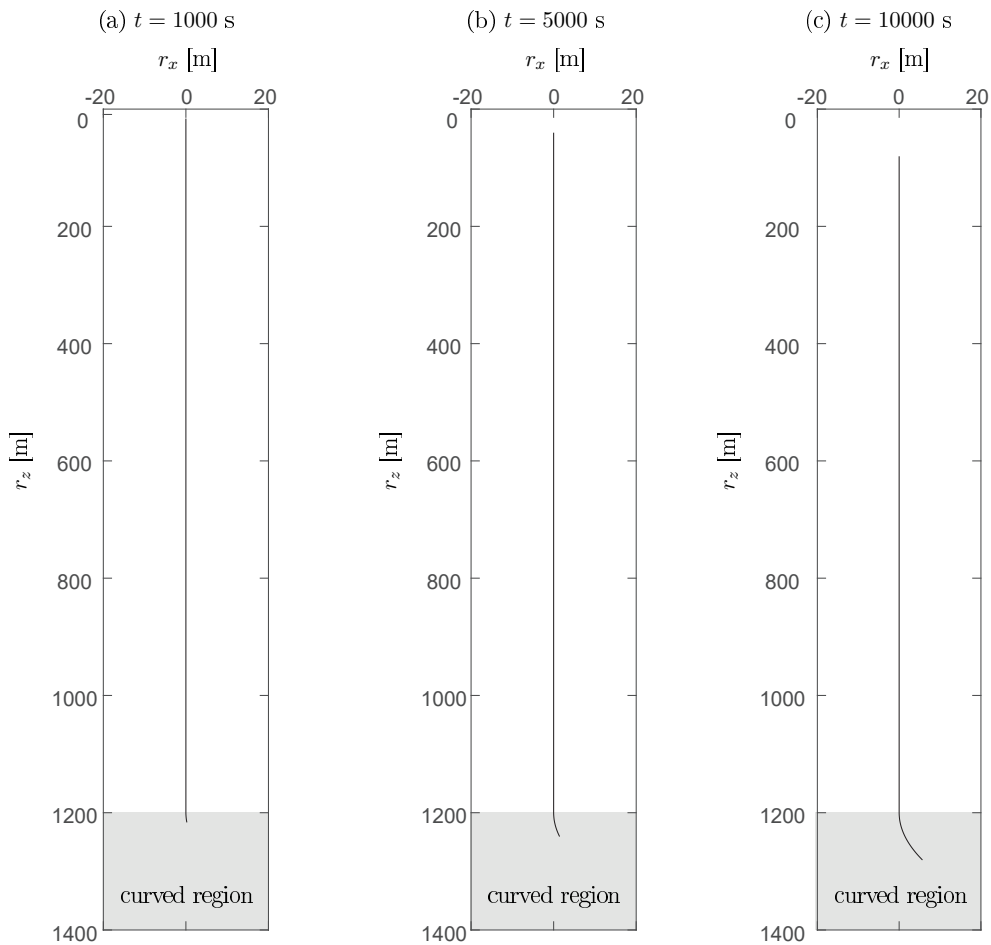


Figure 6.16: Position of the centreline of the string in the xz plane at (a) $t = 1000$ s; (b) $t = 5000$ s; $t = 10000$ s.

The torsional speed of the bit is shown in 6.15(a) and the axial one in 6.15(b). Also, in (a), some areas of the plot are zoomed in that illustration. The simulations show vanishing low-frequency oscillations. This behaviour is

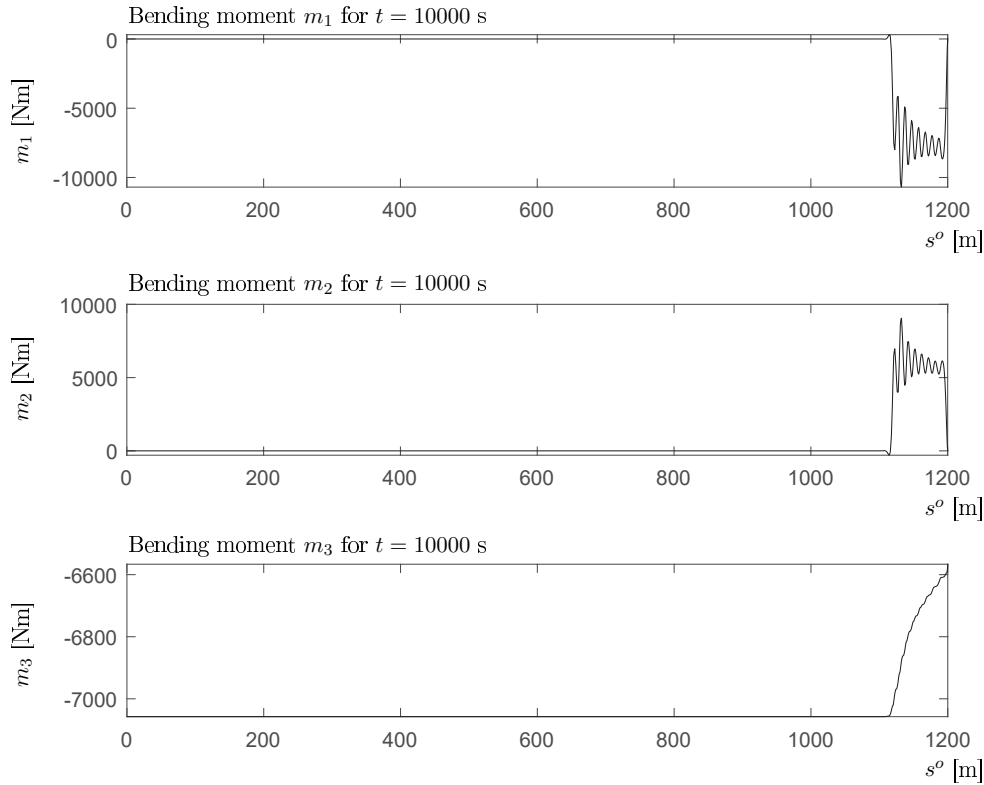


Figure 6.17: Well geometry considered in simulation C2.

similar to that observed for the same level of damping in a straight well, in the simulations C1 of Section 6.3.4. On top of that, a small variation is observed in 6.15(b) that the authors assume it could be linked to the lateral effects present in the simulations. It is important to recall that the spirit of this simulation is not to perform a deep analysis of the dynamics of the case, but rather to show some of the differences that justify the use of a more refined model such as M3.

The results, in terms of the angular speed and position, are not very different from those of the straight configuration in the highly damped system. This is due to two aspects: the lateral vibrations damp fast enough and do not present great amplitude due to the lateral wall distance being small; and the speed at the top is constant, which means that the power done by the top drive to the system will accommodate to assure the constant angular speed at the top, thus the forces are able to overcome the extra friction that is being added. Another graph is included in Fig. 6.19 to show how the power changes over time as the drilling takes place and the bit is deeper into the well. This is linked to the increment of the contact region as the string enters the curved path.

With regards to the performance, the drilling advanced 80.468 m, mea-

sured in the direction of the arc length of the curve that defines the well. The true vertical depth (max. r_z) that was achieved is 1280.62 m.

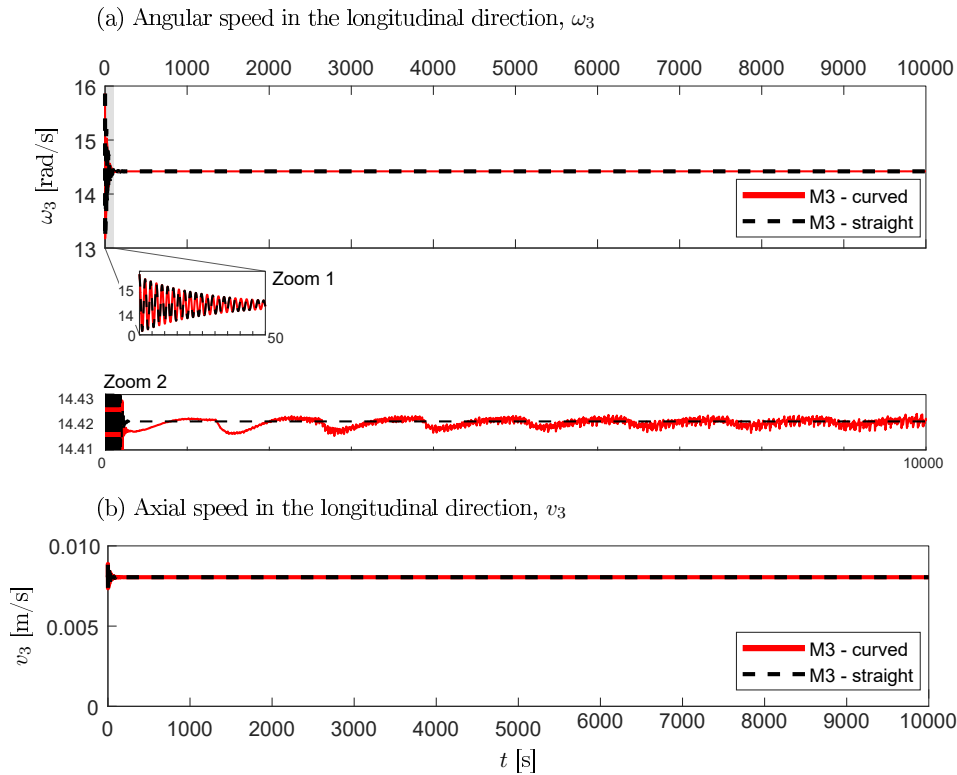


Figure 6.18: Comparison of the dynamics of the curved and straight boreholes. a) shows angular speed in the longitudinal direction; and b) the axial speed in the longitudinal direction.

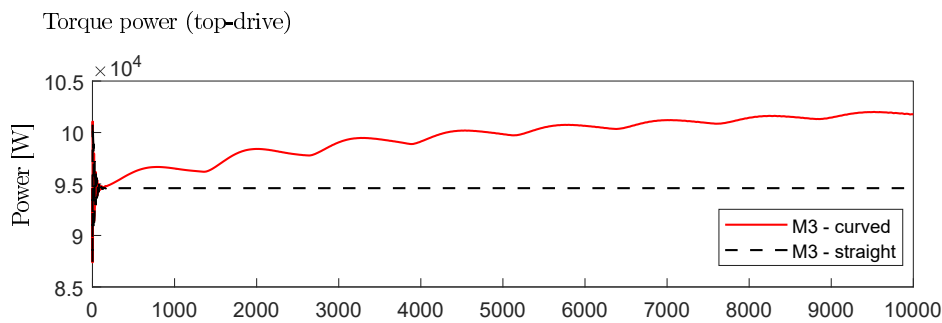


Figure 6.19: Mechanical power produced by the top-drive rotary system.

To sum up, with this application case, it was shown that the dynamics of the drill string comprise other aspects than those associated with the torsional and axial behaviour of the system. Some of those aspects can only be captured with a model that considers the lateral dynamics of the system. Although it

was not shown in the present application case, model M3 can be useful to study other phenomena that may occur, such as buckling. Also, the more information provided can be of use for a deeper understanding of the stresses that affect the mechanical system during the drilling process.

6.4

Final comments of this chapter.

In this Chapter, the dynamics of a drill-string were studied with a model that uses a Cosserat rod approach. The model, referred to as M3, considers a Kelvin-Voigt material; it includes lateral contact; and it takes into account the cutting dynamics of the bit, which allows defining the advancing of the column as a consequence of the bit-rock drilling dynamics.

The objective of the study was threefold: 1) to consider a comprehensive model that includes the 3-D motion of the structure, including the lateral dynamics, included in the other models that were compared, as well as the axial-torsional behaviour.; 2) to understand how the behaviour of the continuous model M3 changed for different values of the friction coefficient c_d , associated with internal structural damping, considering a Kelvin-Voigt material; and 3), to compare the results with those obtained with other models from the literature: a discrete model, M1, and semi-discrete one, M2.

The consideration of a Kelvin-Voigt material makes the model more general than that obtained by using a linear elastic constitutive relation given that the latter is contained in the Kelvin-Voigt approach if the damping coefficient were taken as zero.

With regard to the simulations, first, a verification of the Cosserat model M3 was conducted, showing that it can reproduce the results of M1. The verification relied on the addition of a parameter α in the equations, used to control whether the formulation behaves as a fully distributed approach or, in the limit where $\alpha \rightarrow 0$, as a quasi-static problem. The latter leads to mathematical expressions that coincide with those of M1. In a previous paper, a similar procedure had been used to verify that M1 is also contained in M2.

The Cosserat model M3 was used to study a 1,200 m column in two simulation scenarios. The simulations associated to the first scenario, C1, involved a column that moves within a straight vertical borehole. In this context, four simulations were carried out, each considering a different value for the damping coefficient. A comparison of the simulations of M3 obtained with different amounts of damping was conducted, both in the time and the frequency domain. In that analysis special attention was given to the axial and torsional speeds at the bit.

The graphs concerning the responses obtained with M3, in the time domain, showed a variation in the qualitative response of the mechanical system. For the highest levels of damping, the oscillations vanished; for intermediate damping, self-excited axial oscillations arose; and for the smaller one, self-excited oscillations that led to torsional and axial stick-slip were found.

When the previous results were compared against those obtained with the other models, M1 and M2, it was observed that the predictions also differed. For the higher values of damping, the results with all models were similar in terms of frequencies. The torsional fundamental frequency was dominant, but different qualitative behaviour was observed. However, the new Cosserat model produced vanishing torsional oscillations, while the discrete model and the semi-discrete models, M1 and M2, showed self-excited torsional stick-slip.

When lower values of damping were used, the simulations with M3 contained other frequencies than the fundamental ones, which were not excited in the simulations with M1 or M2. This was expected given the nature of the lumped axial representation used for the discrete and the semi-discrete models, which impedes the excitation or resonance with higher frequencies. However, from a qualitative point of view, all models predicted self-excited torsional stick-slip oscillations. Thus, for the lower dampings, the predictions were more similar in terms of qualitative behaviour.

Evaluations of the behaviour of the system in the frequency domain were performed, considering different time windows within a simulation. These evaluations allowed to assess the energy exchange between the axial and torsional modes that occur in a simulation as vibrations fully develop. The results showed that this exchange cannot be captured with a low-dimensional lumped model that uses for the axial response a 1-DOF formulation consisting of a rigid mass, such as the one used in M1 and M2. As a matter of fact, the model M3, with a continuous mathematical description, captured aspects that were not present in M1: those related to frequencies different than the fundamental one in the torsional response, and those related to the vibrations in the axial direction which cannot be captured with the 1-DOF rigid representation. The simulations, and particularly those with $c_d = 10^{-4}$, showed clearly that the axial dynamics are responsible for the higher frequencies observed in the torsional response, due to their coupling through the bit-rock interaction relations.

The analysis of the simulations in terms of the performance of the drilling process, taken as the maximum depth achieved, led to another interesting result. It was found that the drilling performance is higher for an intermediate amount of damping, what suggests that an operating point of maximum

efficiency exists, were the damping variable controllable. Also, it implied that axial vibrations could be not as detrimental to the drilling performance, as it is often presented in the literature.

Additionally, a second simulation scenario C2 was also conducted where the dynamics of the 1,200 m column entering into a curved well were studied. With this simulation, it was shown that the Cosserat model M3 has other advantages over the previous models. For instance, M3 is capable of simulating the lateral dynamics of the well, and it could also reproduce effects such as the buckling of the structure, should they occur. On top of that, the extra information that is obtained with the model can be of use to other studies that can help understand how the stress distribution changes over time.

With all the previous results, the most important findings in this study confirmed that a low-dimensional lumped representation can be insufficient to capture all the aspects involved in the dynamics of a drill-string, when a comprehensive representation of the column, that is, capable of describing the behaviour at the bit as well as the drill-pipes and the BHA, is sought.

The contributions of this study were: 1) the development of a drill-string model based on the theory of Cosserat rods where the dynamics of the cutting were also taken into account; 2) the inclusion of a strategy to account for the lateral contact along the string, if needed; 3) the consideration of internal damping by considering a Kelvin-Voigt material, recalling that the constitutive also contains the elastic model if damping is taken as zero; 4) the inclusion of the discrete model M1 as a limiting case of the new Cosserat model, M3, through a controllable parameter α ; 5) a comparison between the three models, M1, M2, M3, showing that the predictions obtained differ and that M3 captures aspects of the dynamics that are not present in discrete or semi-discrete low-dimensional lumped models, confirming the initial hypothesis that continuous models should be used instead; 7) the simulation of a curved borehole to illustrate the potential of the model to tackle 3-D drill-string dynamics.

This chapter presents a brief introduction to another important aspect to consider in the dynamics of a drill-string that has not been yet dealt with in this thesis: the uncertainties present in the elements that compose or interact with the system. For instance, randomness is an inherent attribute of the soil. For this reason, the problem dealt in [28] is revisited. The presentation of this problem does not pretend to be a comprehensive treatment of the variability affecting drill-strings. It just aims at presenting the reader with the problem of variability that is an inherent characteristic of these type of problems. In what follows, the axial dynamics of a drill-string moving within a horizontal section of the well are analysed with a Cosserat rod model. Analogously to [28], the torsional dynamics are not taken into account in this study.

The objective of the study is to compare the results of two different application cases, simulated with each model. One that considers the full lateral-axial dynamics, and a simpler one where the static solution is used for the lateral behaviour. In the first application case, the friction force is deterministic, taking a fixed value for the friction coefficient. In the second case, the friction coefficient is modelled as a random field.

Some of the novelties in this study lie in the combination of: 1) a stochastic approach to the modelling of the lateral friction forces, taking into account the randomness of the material to generate a random field; 2) the combination of the previous with a Cosserat model; 3) the evaluation of the effect of taking some simplification in the contact assumptions, this way disregarding the flexural dynamics, against a model where the flexural dynamics are taken into account and influence the contact forces.

The contents of this analysis have been published in [78].

7.1

Description of the problem

In [28], a bar model, described by a longitudinal wave equation, was employed to analyse the dynamics of a drill-string during the penetration process. This means that the formulation only accounts for longitudinal displacements and that no lateral and torsional motions are allowed. The model

also includes the bit-rock interaction force between the bit and the borehole wall by using a Coulomb model.

As already stated, the present study is a continuation of the work carried out in [28]. This time, the same problem is studied by means of a Cosserat rod. This approach is an improvement over the original proposal, as it allows studying the effects of the lateral dynamics in the axial predictions.

First, a comparison between the approach in [28] and the current model is made with a deterministic problem. The comparisons are used to evaluate the influence of the lateral displacements in the predictions. In particular, [28] considers a normal force that is the solution of the static problem, while the new model takes into account the whole dynamics of the structural system.

After that, a stochastic problem considering a random field for the friction coefficient is studied. The random field is constructed by using an approximation based on the Karhunen-Loève expansion.

7.2

The deterministic model

The dynamics of a horizontal drill-string considering contact at the bit as well as friction and contact within the drill-string length are studied in [28], where the authors employed a bar model given by a longitudinal wave equation. It was assumed that contact occurs along the whole length of the drill-string under static conditions, that is, the normal force equals the self-weight of the structure. Also, the frictional force was considered to be proportional to the self-weight.

In the new model, a Cosserat rod is employed to simulate the dynamics of a horizontal drill-string, considering the forces depicted in Fig. 7.1. Although the Cosserat rod can describe longitudinal, lateral, and torsional dynamics, as opposed to the original model where only longitudinal effects were considered, the torsional dynamics are not important for the present study. The focus is given to the lateral-flexural motion. The equations of motion are those given in (2-26), (2-51), and (2-61) of Chapter 2.

Three distributed forces are considered in the previous equations, being the total distributed force $\mathbf{f}_n^R = \mathbf{f}_s + \mathbf{f}_{fr} + \mathbf{f}_g$ with: \mathbf{f}_s being the normal force, \mathbf{f}_{fr} the friction force and \mathbf{f}_g the self-weight. The self-weight is taken into account in the dynamics of the drill-string, and in the calculation of the frictional force, which is proportional to the normal force. The geometric and material properties used in the simulations are shown in Table 7.1.

The expression for the distributed self-weight is given by

$$\mathbf{f}_g = -\rho A g \hat{\mathbf{k}}, \quad g = 9.81 \text{ m/s}^2 \quad (7-1)$$

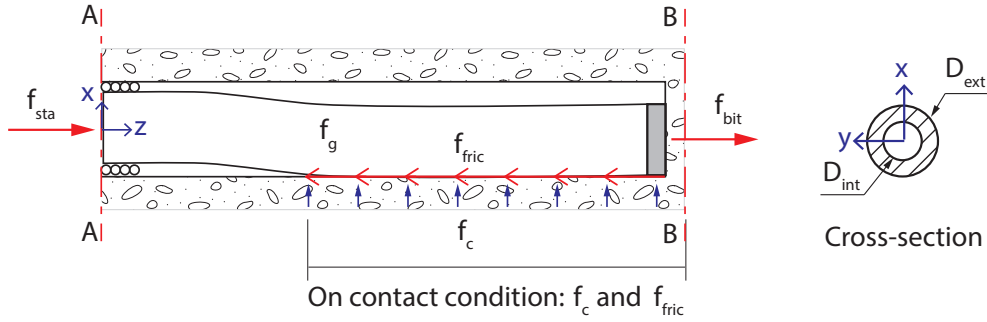


Figure 7.1: Sketch of the drill-string model employed. In the graphic, \mathbf{f}_{sta} stands for the force transmitted by the pipes before the simulated segment of drill-string, \mathbf{f}_c is the normal force, the friction force is given by \mathbf{f}_{fric} , and the self-weight is \mathbf{f}_g . D_{ext} and D_{int} are the internal and external diameters of the cross-section.

Property	Value	Description
L	60 m	Length of the drill-string
D_{ext}	0.15 m	Cross-section external diameter
D_{int}	0.10 m	Cross-section internal diameter
ρ	7850 kg/m ³	Material density
E	210 GPa	Young modulus
m_{bit}	20 kg	Mass at the bit
k_s	$1 \cdot 10^6 \text{ N/m}^2$	Soil constant
c_1	$1.4 \cdot 10^3 \text{ N}$	Coefficient of the bit-rock interaction model
c_2	400	Coefficient of the bit-rock interaction model
b	10	Bit-rock cross-correlation decay length
ω_f	$100 \cdot 2\pi/60 \text{ rad/s}$	Frequency of harmonic excitation
t	$\in [0, 10] \text{ s}$	Simulation time
f_{sta}	5500 N	Transmitted force
f_0	500 N	Mean magnitude of the oscillatory force
μ	—	Mean value of the friction coefficient
σ	—	Standard deviation for the friction coefficient

Table 7.1: Material and geometric properties used in the modelling of the horizontal drill-string.

The normal force \mathbf{f}_s is modelled with the penalty method, as explained in [40]. The force is supposed to be proportional to a penetration constant k_s , and it can be written as

$$\mathbf{f}_s = -k_s f_{sp} \hat{\mathbf{r}}_r \quad (7-2)$$

In the previous expression, $\mathbf{r}(x, t)$ is the current position vector of the centreline of the drill-string; $\mathbf{r}_p(s)$ is position vector of the centreline curve of the borehole; $\mathbf{r}_r = \mathbf{r} - \mathbf{r}_p$ is a relative position vector that describes the position of the centreline of the drill-string with respect to the borehole centreline; $\hat{\mathbf{r}}_r$ is a unitary vector in the same direction; and f_{sp} is a penetration function defined by

$$f_{sp} = \begin{cases} |\mathbf{r}_r| - c_{gap}, & \text{if } |\mathbf{r}_r| - c_{gap} \geq 0. \\ 0, & \text{otherwise.} \end{cases} \quad (7-3)$$

with c_{gap} being the radius of the borehole.

The friction force is given by the expression hereunder, where $\hat{\mathbf{v}}_c$ denotes a unitary vector in the direction of the velocity at the contact point. It is assumed that contact occurs only at one point of the cross-section.

$$\mathbf{f}_{fr} = -k_{fr}|f_s|\hat{\mathbf{v}}_c \quad (7-4)$$

The boundary conditions for this problem are: at the points lying in section A-A of Fig. 7.1, the rotation of the section in any direction is restricted, and no movement around the x-axis and y-axis is allowed, while in the z-axis direction a load $\mathbf{f}_{sta} = f_{sta}\hat{\mathbf{k}}$ is applied.

On the other hand, at the points within section B-B, a free-end condition with an applied load \mathbf{f}_{bit} is considered. The force applied to the bit actually describes the following three effects: a contact force with the wall (f_{wall}), a harmonic force (f_{har}) due to the mud motor, and the inertial effect of the mass of the bit (f_m), which is modelled as a lumped mass.

$$\mathbf{f}_{bit} = \mathbf{f}_{har} - \mathbf{f}_{wall} - \mathbf{f}_m \quad (7-5)$$

The contact force at the bit f_{wall} is expressed as in [28]. The constants c_1 and c_2 are two constants related to the bit-rock interaction.

$$\mathbf{f}_{wall} = \begin{cases} (c_1 e^{-c_2 \dot{u}(L, t)} - c_1)\hat{\mathbf{k}}, & \text{if } \dot{u}(L, t) > 0 \\ \mathbf{0}, & \text{otherwise} \end{cases} \quad (7-6)$$

A harmonic force applied at the bit is also imposed on the system, as the driving source of the horizontal drilling is the mud motor, which rotates about a given nominal rotational speed (in steady operation).

$$\mathbf{f}_{har}(x, t) = F_0 \sin(\omega_f t)\hat{\mathbf{k}} \quad (7-7)$$

Finally, the initial conditions are such that the structure is at rest at the initial time $t = 0$.

7.3

The stochastic model

The nature of the soil as a material is a source of uncertainties in any mechanical problem, given that properties such as the friction coefficient may vary greatly from one point to another. For this reason, following [28], the soil is simulated as a random force, by taking the friction coefficient k_{fr}^* as a random field.

It is assumed that k_{fr}^* follows a truncated gaussian field with support $[0, 0.6]$, and exponential autocorrelation given by

$$R(x_1, x_2) = \sigma^2 e^{-\frac{|x_2 - x_1|}{b}} \quad (7-8)$$

where b is the correlation length that measures the rate of decay of the autocorrelation function.

A Karhunen-Loève expansion is employed to approximate the friction field k_{fr}^* [41], by taking the first N terms of the series as follows:

$$k_{fr}^* \approx \mu(x) + \sum_{k=1}^N \sqrt{\lambda_k} Z_k(\zeta) \phi_k(x) \quad (7-9)$$

In the previous expression, μ is the mean value of the friction coefficient, λ_k and ϕ_k are the eigenvalues and eigenvectors of the autocorrelation function R . Z_k are independent standard Gaussian random variables.

7.4

Results

In this section, the results for the simulations are presented. Two different cases are considered. Firstly, a deterministic problem with the current approach is compared against a model where, like in [28], the normal force is the self-weight, which is the solution to the static problem. Secondly, a numerical approximation to the solution of the stochastic problem is shown.

7.4.1

The deterministic case

The Cosserat model is solved considering the parameters in Table 7.1. For the time being, the friction field is not considered stochastic.

For this problem, the friction coefficient k_{fr} takes the value $k_{fr} = 0.10$. All simulations use a Cosserat approach. Two different cases are considered. In case A the contact force is a direct consequence of the dynamics of the model. It is obtained by considering the penalty approach given as stated in (7-2), following the strategy presented in Section 4.2.2. Case B introduced

the normal contact force as a constant whose magnitude is the distributed self-weight of the rod along its whole length. The latter coincides with the hypothesis provided in [28]. The solution is shown in Fig. 7.2 and compared against that of [28].

The results show how a different contact model can drastically change the dynamics obtained for the system and in particular the displacement at the bit which is one of the possible measures of the performance of the driller.

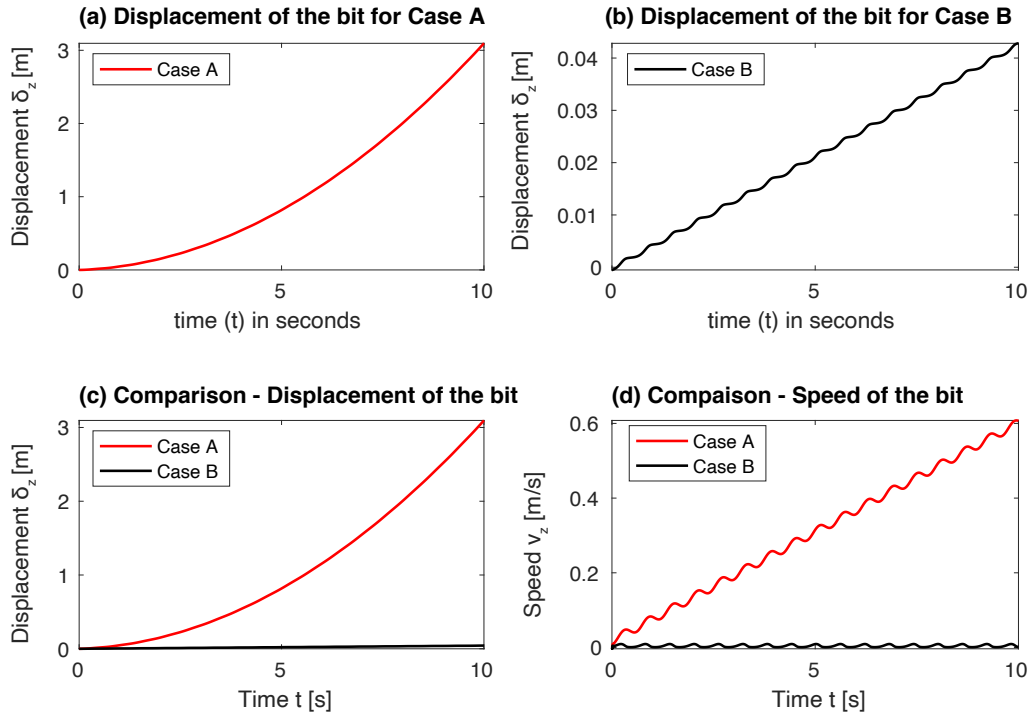
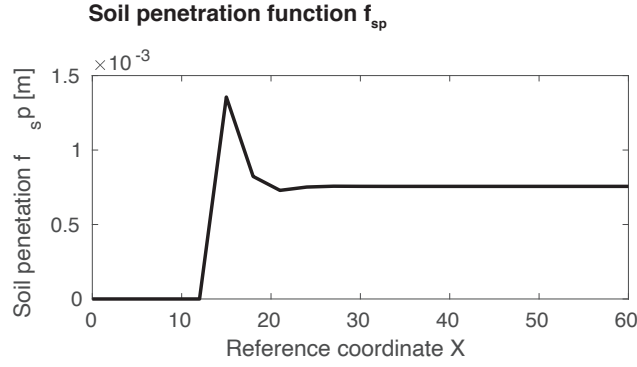


Figure 7.2: Results for the deterministic problem. Comparison of the displacements and velocities at the bit, which are directly linked to the performance of the drilling process. Case A corresponds to the hypothesis that contact occurs due to the deflection and contact of the beam. Case B considers contact on the whole length of the beam, with the hypothesis that the distributed normal force equals the self-weight of the structure. (a), (b) and (c) show the displacement of the bit in the direction of the z-axis δ_z , while (d) shows the velocity v_z at the bit.

A stick-slip motion in a mechanical system implies that two very distinct phases can be appreciated in the dynamics. Namely, the stick and the slip phases. On the one hand, the stick is characterized for presenting zero relative velocities between the two surfaces in contact for a given period (not just an instant). On the other hand, the slip phase is defined for those instants that do not comply with the previous conditions.

In a qualitative comparison between the solutions, it is observed that Case A and B differ greatly. Due to the use of a numerical model, the system

Figure 7.3: Soil penetration function f_{sp} [m].

exhibits vibrations in which the velocities go to almost zero, but not exactly zero, as observed in Case B from Fig. 7.2. For this reason, the motion is said to be pseudo stick-slip. In case A contact acts only on a section of the structure, as shown in Fig. 7.3. Therefore, the friction force varies in such way that case A does not exhibit any stick-slip-like behaviour, while case B exhibits pseudo-stick-slip motion. This implies that, under certain conditions, it is important to consider the lateral dynamics of the structure. Moreover, case A shows a penetration δ_z that is 100 times higher in order than that of case B.

7.4.2

Stochastic results

In this section, a stochastic problem considering friction as a random field (see Section 7.3) is presented. The parameters employed are those provided in Table 7.1 are employed in the simulations, with $\mu = 0.12$, $\sigma = 0.1\mu$, and $N = 100$ terms in the Karhunen-Loève expansion. The problem is treated in an analogue manner to previous case A in all simulations, that is, contact is obtained with the strategy presented in Section 4.2.2, and it is a consequence of the drillers' dynamics.

The power ratio $p_r = p_{out}/p_{in}$ is used as a measurement of the efficiency of the system. It is defined as the ratio between the input power (p_{in}) and the output power (p_{out}), given by the following expressions:

$$p_{in} = \frac{1}{t_1 - t_0} \int_{t_0}^{t_1} (f_{sta} \dot{r}_z(0, t)) + f_{har} \dot{r}_z(L, t) dt \quad (7-10)$$

$$p_{out} = \frac{1}{t_1 - t_0} \int_{t_0}^{t_1} f_{bit} \dot{r}_z(L, t) dt \quad (7-11)$$

The probability density function (PDF) of the power ratio is shown in Fig. 7.5, as well as a convergence graph for the standard deviation of the

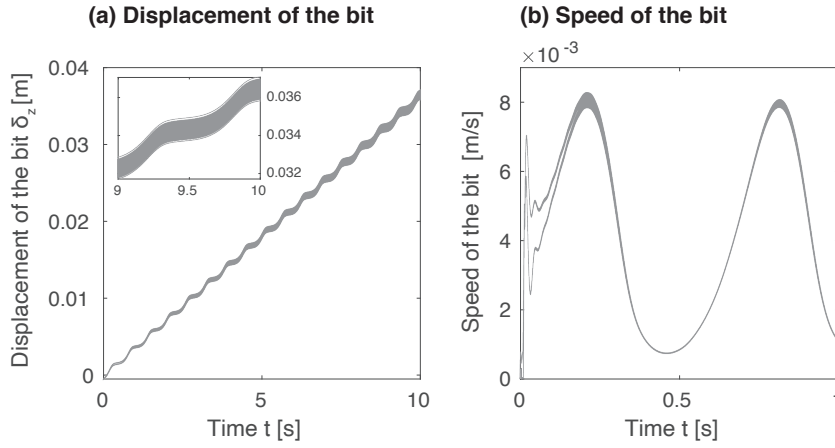


Figure 7.4: Some realisations from the Monte-Carlo simulations. (a) Displacement of the bit. (b) Speed of the bit.

response. The PDF obtained is very different from those presented in [28], showing a better performance for the analysed case. This result is expected. The contact forces produced are smaller in magnitude, thus less energy is dissipated and the driller's performance in terms of the power ratio is improved.

7.5

Final comments concerning this chapter

In this chapter, a model capable of capturing the longitudinal, lateral and torsional dynamics of a drill-string has been employed. The Cosserat rod model has been compared with a bar model to show the importance of considering lateral displacements in the calculation of the contact and friction forces involved. Firstly, it is observed that the mechanical system changes its behaviour depending on the value of the friction coefficient. In fact, under some conditions, stick-slip motion is shown, which greatly affects the rate of penetration. Moreover, when the contact and friction forces are obtained as a result of the dynamics of the system, the solution can be different than that obtained by considering contact to be equal to the self-weight (at an equilibrium state). Secondly, the stochastic problem is solved by employing the current Cosserat rod model, and the PDF of the power ratio is obtained, which is one possible measure of the performance of the drilling process.

To conclude, although the objective of this chapter is not to present an extensive study in relation to the techniques involving stochastic simulations, some interesting publications worth reading, regarding techniques to perform uncertainty propagation can be found in [93–96].

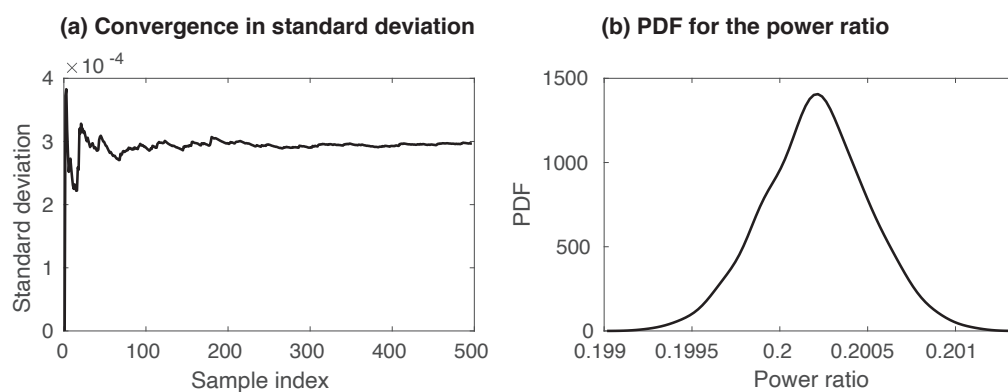


Figure 7.5: Results for the stochastic problem with the stochastic approach. (a) Convergence graph for the standard deviation of the power ratio. (b) PDF for the power ratio.

8

Final considerations

8.1

Summary

In this thesis, the study of the dynamics of drill-strings was tackled through a formulation based on the theory of Cosserat rods. The literature related to the modelling of drill-strings is vast and many different approaches can be found, from low-dimensional lumped models to continuous ones. For this reason, to the author of this thesis, it was not entirely clear to what extent the low-dimensional formulations found in other studies had the ability to reproduce the dynamics of a real-scale column. The main objective of the thesis was to show that a Cosserat rod approach can successfully account for the many different phenomena that affect such structures, particularly when drill-strings move within curved boreholes. On top of that, it was desired to provide answers as to how a Cosserat rod performed at representing long drill-strings in comparison with the low-dimensional approaches found in the literature. Also, it was desired to investigate the advantages that the continuous model herein presented could have over the low dimensional models and other continuous formulations where contact is treated via simplifying assumptions, for example by considering the lateral response in the static case, thus simplifying the complexity of the problem.

For this quest, first, the foundations for the Cosserat theory of rods were revisited. After that, through an application example consisting of an off-bottom drill-string, the formulation was used to study the dynamics of a string within a curved borehole. In particular, a strategy involving a parametrisation of the borehole was developed, to relate the position of the string with the position where contact occurs in the borehole. This was calculated by adding an extra algebraic equation to be solved along with the equations of motion. On top of that, a comparison between the dynamics obtained with a Cosserat rod model and those with a straight shaft that used an ad-hoc hypothesis to account for the curvature of a well was made. The simulations provided similar results in terms of the torsional oscillations. However, the Cosserat model showed differences in the distribution of the contact forces (normal and

friction) in the region where the well bends. These differences justify the use of the newly developed approach, particularly if interest is paid to this region of the string.

Next, a study including the dynamics of the cutting was carried out. The objective of this study was two-fold. To compare the predictions of one low-dimensional model from the literature, with those given by a continuous approach, and to include the dynamics of the cutting in the bit-rock interaction model. The model of [14] concerning the bit-rock interaction relations was extended to account for other operation regimes, where now backward rotation and bit-bounce can occur. As already stated, in this study two different approaches to modelling the structure were used. One of them considered a 2-DOF discrete formulation, and the other a semi-discrete formulation, where the torsional dynamics were given by a wave-equation and the axial with a 1-DOF equation. In these models, the forces and torques associated with the bit-rock interaction were calculated through a depth-of-cut that depends on the dynamics of the cutting. For this purpose, an advection equation was also solved together with the equations of motion. An interpretation of the behaviour given by the equation and a geometrical interpretation of the boundary conditions was provided. At this stage, the predictions of 2-DOF model (one axial, one torsional) were compared with those of a semi-discrete model that employed a wave equation for the torsional dynamics. Among the main results of this study, it was shown that some aspects of the dynamics could be neglected by using low-dimensional models, which was in line with the main assumption presented in this thesis. In particular, it was observed that the semi-discrete model could capture higher frequencies than those present in the low-dimensional one. Nevertheless, the formulations used so far were conservative, with the exception of the forces associated with the bit-rock interaction. This implies that other possible sources of damping were not been included in the study. For this reason, it was deemed of interest to assess what role introducing some level of damping would play in mitigating the higher frequencies, as well as what would be the effect of this damping in the general qualitative behaviour of the dynamics. Additionally, it is important to reinforce that, up to here, the two models contained a 1-DOF axial formulation, which was an arbitrary choice.

Following the previous analysis, a new model, based on the Cosserat rod formulation was utilised to continue the study. The dynamics were described through a continuous formulation, thus eliminating the previously mentioned arbitrary selection of a lumped axial formulation. With this model, the effects of introducing internal damping were analysed through the consideration of

a Kelvin-Voigt material constitutive. The results obtained with the Cosserat approach for different values of the damping coefficient were compared against each other, and against the predictions obtained for the discrete and semi-discrete approaches used in the previous study. The analysis showed that low-dimensional lumped models cannot reproduce the behaviour obtained with continuous approaches. This was tested by analysing the predictions considering different values of the damping coefficients. It was found that, with the higher values, the predictions led to responses where low frequencies were present in both approaches, but with different amplitudes, and that the general behaviour of the solution changed. For instance, while the Cosserat approach showed vanishing oscillations in some scenarios, the discrete and semi-discrete models showed non-vanishing stick-slip vibrations. Additionally, when the level of damping was low enough, all models experienced stick-slip vibrations, but the predictions with the Cosserat model and the semi-discrete one contained higher frequencies than those captured by the discrete low-dimensional formulation. Also, with the latter low-damping cases, it was possible to evaluate how the signals change their frequency content as the vibrations develop. By doing so, and combining the results with the previous observations, it is clear that the low-dimensional models are not able to predict nor capture the general behaviour of the dynamics of a real-size drill-string.

Finally, there are many elements involved in drill-string dynamics that show some source of variability. Particularly those associated with the soil, which is inherently heterogeneous. Including the stochastic aspects of the problem was an idea originally contemplated in the work plan of the Ph.D. For this reason, it was decided to include a brief study concerning stochastic simulations in this thesis, just as a mean to grasp the complexities involved and future lines of research to continue all the work that has been presented so far. To this purpose, a problem from the literature was revisited. The Cosserat approach was used to evaluate the difference in the results between this model, and another simpler model where the normal contact force is considered constant along the length, instead as a result of the dynamics and the boundary conditions.

8.2

Contributions

With regards to the structural model:

- A complete and accessible description of the Cosserat rod formulation was provided. This can be of use for didactic purposes too, and for those interested in continuing this line of research;

- the rotations were parametrised by utilising a quaternion approach. This approach is not often studied in a general engineering course. Thus, the importance of explaining the details of the formulation also has some didactic implications too. This was combined with the findings of [53], who developed a formulation to perform the time integration of quaternions in the context of the dynamics of a rigid body without enforcing the unitary quaternion constraint, a constraint that would be required in a more classical approach involving quaternions;
- a procedure to derive the constitutive relations from a known 3-D constitutive was presented. This procedure was used to state the constitutive relations of the linear material in this thesis. In addition, although it was not included in this text, because it is not the focus of the study, this procedure was originally used to find the constitutive relations for a piezoelectric material, which up to the author's knowledge, was also a novelty;
- the utilisation of a Kelvin-Voigt material model in the Cosserat formulation that for zero damping coincides with that of an isotropic elastic material. For other values it can be used to assess the effect of considering internal damping;
- the inclusion of an algorithm for the Cosserat model to detect when and where contact and friction occur along the drill-string, as well as the magnitudes of the forces and torques involved. In this approach, the friction depends upon some parameters which were unknown. These parameters were calibrated with the results of [29]

With regard to the bit-rock interaction at the bit:

- The definition of a new bit-rock interaction relation that does not restrict backward rotation of the bit nor bit-bounce, and that is dependent on the dynamics of the cutting blade, such as the depth-of-cut;
- the implementation of an advection equation to avoid dealing with a system of delay-differential equations in the simulation of the cutting process;
- the extension of the advection approach treated in the previous works of [14, 73] to allow rotation in both directions;
- the inclusion of the 2-DOF model as a limiting case of the continuous models M2 and M3. For this purpose, a strategy considering an extra parameter α is developed.

With the results:

- it is shown the Cosserat model can successfully deal with contact and friction in inclined and curved boreholes;
- a comparison between the three models, M1, M2 and M3, shows that there are conditions where the continuous approaches provide different predictions than those obtained with the simpler discrete model M1. Thus, the findings are an important step into showing that the continuous Cosserat model can capture aspects of the dynamics that cannot be reproduced by the low-dimensional models.

8.3

Future work

Future lines of work include

- Further explore the dynamics of a drill-string considering cutting in curved boreholes, such as the one used in the chapter related to the lateral contact formulation;
- The implementation of reduced-order techniques to reduce the simulation time of the current models;
- The stochastic treatment of the problem, where the soil is treated as a stochastic field, and other sources of uncertainty are considered;
- A study considering the variable mass problem, as pipes are added as the drilling advances, which is also related to the free boundary problem concerning the cutting of the soil;
- An analysis focusing on other phenomena such as buckling, helical buckling, and whirling, that can be reproduced with the theory of Cosserat rods.

Bibliography

- [1] SPEIGHT, J. G.. **An introduction to petroleum technology, economics, and politics.** Wiley-Scrivener, Jan. 2011.
- [2] KESHAVARZIAN, M.; KAMALI ANARAKI, S.; ZAMANI, M. ; ERFANIFARD, A.. **Projections of oil demand in road transportation sector on the basis of vehicle ownership projections, worldwide: 1972-2020.** *Economic Modelling*, 29(5):1979–1985, 2012.
- [3] PLC, B.. **Oil demand dataset from the Statistical Review of World Energy.** Technical Report 71, BP, Dec. 2022.
- [4] MA, T.; CHEN, P. ; ZHAO, J.. **Overview on vertical and directional drilling technologies for the exploration and exploitation of deep petroleum resources.** *Geomechanics and Geophysics for Geo-Energy and Geo-Resources*, 2(4):365–395, 2016.
- [5] GUPTA, V. P.; SANFORD, S. R.; MATHIS, R. S.; DIPIPO, E. K. ; EGAN, M. J.. **Case history of a challenging thin oil column extended reach drilling (ERD) development at Sakhalin.** *SPE/IADC Drilling Conference, Proceedings*, 2(October 2012):929–950, 2013.
- [6] SILVEIRA, M.. **A comprehensive model of drill-string dynamics using Cosserat rod theory.** PhD thesis, University of Aberdeen, 2011.
- [7] GHASEMLOONIA, A.; GEOFF RIDEOUT, D. ; BUTT, S. D.. **A review of drillstring vibration modeling and suppression methods.** *Journal of Petroleum Science and Engineering*, 131:150–164, 2015.
- [8] YIGIT, A. S.; CHRISTOFOROU, A. P.. **Coupled torsional and bending vibrations of actively controlled drillstrings.** *Journal of Sound and Vibration*, 234(1):67–83, 2000.
- [9] NAVARRO-LÓPEZ, E. M.; CORTÉS, D.. **Avoiding harmful oscillations in a drillstring through dynamical analysis.** *Journal of Sound and Vibration*, 307(1-2):152–171, 2007.

- [10] CHRISTOFOROU, A. P.; YIGIT, A. S.. **Fully coupled vibrations of actively controlled drillstrings.** *Journal of Sound and Vibration*, 267(5):1029–1045, 2003.
- [11] DIVENYI, S.; SAVI, M. A.; WIERCIGROCH, M. ; PAVLOVSKAIA, E.. **Drill-string vibration analysis using non-smooth dynamics approach.** *Nonlinear Dynamics*, 70(2):1017–1035, 2012.
- [12] RITTO, T. G.; GHANDCHI-TEHRANI, M.. **Active control of stick-slip torsional vibrations in drill-strings.** *Journal of Vibration and Control*, 25(1):194–202, 2019.
- [13] HOVDA, S.. **Semi-analytical model of the axial movements of an oil-well drillstring in deviated wellbores.** *Journal of Sound and Vibration*, 433:287–298, 2018.
- [14] RICHARD, T.; GERMAY, C. ; DETOURNAY, E.. **A simplified model to explore the root cause of stick-slip vibrations in drilling systems with drag bits.** *Journal of Sound and Vibration*, 305(3):432–456, 2007.
- [15] GUPTA, S. K.; WAHL, P.. **Global axial-torsional dynamics during rotary drilling.** *Journal of Sound and Vibration*, 375:332–352, 2016.
- [16] NANDAKUMAR, K.; WIERCIGROCH, M.. **Galerkin projections for state-dependent delay differential equations with applications to drilling.** *Applied Mathematical Modelling*, 37(4):1705–1722, 2013.
- [17] YAN, Y.; WIERCIGROCH, M.. **Dynamics of rotary drilling with non-uniformly distributed blades.** *International Journal of Mechanical Sciences*, 160(May):270–281, 2019.
- [18] XIE, D.; HUANG, Z.; MA, Y.; VAZIRI, V.; KAPITANIAK, M. ; WIERCIGROCH, M.. **Nonlinear dynamics of lump mass model of drill-string in horizontal well.** *International Journal of Mechanical Sciences*, 174, 2020.
- [19] TIAN, K.; DETOURNAY, E.. **Influence of PDC bit cutter layout on stick-slip vibrations of deep drilling systems.** *Journal of Petroleum Science and Engineering*, 206(February):109005, 2021.
- [20] TRINDADE, M. A.; SAMPAIO, R.. **Modeling of axial-torsional coupled vibrations of drill-strings.** 13th international workshop on dynamics and control, 2005.

- [21] SAMPAIO, R.; PIOVAN, M. T. ; VENERO LOZANO, G.. **Coupled axial/torsional vibrations of drill-strings by means of non-linear model.** *Mechanics Research Communications*, 34(5-6):497–502, 2007.
- [22] GERMAY, C.; VAN DE WOUW, N.; NIJMEIJER, H. ; SEPULCHRE, R.. **Nonlinear drillstring dynamics analysis.** *SIAM Journal on Applied Dynamical Systems*, 8(2):527–553, 2009.
- [23] RITTO, T. G.; SOIZE, C. ; SAMPAIO, R.. **Robust optimization of the rate of penetration of a drill-string using a stochastic nonlinear dynamical model.** *Computational Mechanics*, 45(5):415–427, 2010.
- [24] AARSNES, U. J. F.; VAN DE WOUW, N.. **Dynamics of a distributed drill string system: Characteristic parameters and stability maps.** *Journal of Sound and Vibration*, 417:376–412, 2018.
- [25] PIOVAN, M. T.; SAMPAIO, R.. **Modelos continuos de sondas de perforación para la industria petrolera: Análisis de enfoques y su discretización [continuum drill-string models for the oil industry: analysis of different approaches and their discretization].** *Revista Internacional de Metodos Numericos para Calculo y Diseno en Ingenieria*, 25(3):259–277, 2009.
- [26] AARSNES, U. J. F.; VAN DE WOUW, N.. **Axial and torsional self-excited vibrations of a distributed drill-string.** *Journal of Sound and Vibration*, 444:127–151, 2019.
- [27] DONG, G.; CHEN, P.. **A review of the evaluation, control, and application technologies for drill string vibrations and shocks in oil and gas well.** *Shock and Vibration*, 2016:1–34, 2016.
- [28] RITTO, T. G.; ESCALANTE, M. R.; SAMPAIO, R. ; ROSALES, M. B.. **Drill-string horizontal dynamics with uncertainty on the frictional force.** *Journal of Sound and Vibration*, 332(1):145–153, 2013.
- [29] AARSNES, U. J. F.; SHOR, R. J.. **Torsional vibrations with bit off bottom: Modeling, characterization and field data validation.** *Journal of Petroleum Science and Engineering*, 163:712–721, 2018.
- [30] AURIOL, J.; AARSNES, U. J. F. ; SHOR, R.. **Self-tuning torsional drilling model for real-time applications.** In: *2020 American Control Conference (ACC)*, p. 3091–3096, Denver, CO, USA, USA, July 2020. IEEE.

- [31] NGUYEN, K.-L.; TRAN, Q.-T.; ANDRIANOELY, M.-A.; MANIN, L.; MENAND, S. ; DUFOUR, R.. **A rotordynamics model for rotary drill-string with nonlinear interactions in a 3D well.** In: Proceedings of the 10th international conference on rotor dynamics – IFToMM, volume 62, p. 325–339. Springer International Publishing, Cham, 2019.
- [32] BELYAEV, A. K.; ELISEEV, V. V.. **Flexible rod model for the rotation of a drill string in an arbitrary borehole.** *Acta Mechanica*, 229(2):841–848, 2018.
- [33] LIU, D.; CAO, D. Q.; ROSING, R.; WANG, C. H. T. ; RICHARDSON, A.. **Finite element formulation of slender structures with shear deformation based on the Cosserat theory.** *International Journal of Solids and Structures*, 44(24):7785–7802, 2007.
- [34] CAO, D. Q.; LIU, D. ; WANG, C. H. T.. **Three-dimensional nonlinear dynamics of slender structures: Cosserat rod element approach.** *International Journal of Solids and Structures*, 43(3-4):760–783, 2006.
- [35] KAPITANIAK, M.; VAZIRI HAMANEH, V.; CHÁVEZ, J. P.; NANDAKUMAR, K. ; WIERCIGROCH, M.. **Unveiling complexity of drill-string vibrations: Experiments and modelling.** *International Journal of Mechanical Sciences*, 101-102:324–337, 2015.
- [36] COSSERAT, E.; COSSERAT, F.. **Théorie des corps déformables.** *Nature*, 81(2072):67–67, 1909.
- [37] ANTMAN, S. S.. **Nonlinear Problems of Elasticity**, volume 107. Springer, 2005.
- [38] MUNICH, F. P.; WIEN, F. G. R. ; PALAISEAU, J. S.. **Generalised Continua from the theory to engineering applications.** Springer Science & Business Media, 2013.
- [39] GOICOECHEA, H.; LIMA, R.; SAMPAIO, R.; BUEZAS, F. ; ROSALES, M.. **Derivation of different constitutive laws for the Cosserat medium.** In: *Mecánica computacional*, volume XXXVII, p. 5–7, 2019.
- [40] GOICOECHEA, H. E.; BUEZAS, F. S. ; ROSALES, M. B.. **A non-linear Cosserat rod model for drill-string dynamics in arbitrary borehole geometries with contact and friction.** *International Journal of Mechanical Sciences*, 157-158(March):98–110, 2019.

- [41] TRINDADE, M. A.; WOLTER, C. ; SAMPAIO, R.. **Karhunen-Loève decomposition of coupled axial/bending vibrations of beams subject to impacts.** *Journal of Sound and Vibration*, 279(3-5):1015–1036, 2005.
- [42] BUEZAS, F. S.; SAMPAIO, R.; ROSALES, M. B. ; FILIPICH, C. P.. **Three different guises for the dynamics of a rotating beam.** *Journal of Sound and Vibration*, 330(22):5345–5362, 2011.
- [43] GOICOECHEA, H. E.; FILIPICH, C. P. ; ROSALES, M. B.. **Natural vibrations of plane frames under compression through a power series solution.** In: *Mecánica computacional*, volume 32, p. 3433–3448. Asociación Argentina de Mecánica Computacional, 2013.
- [44] GOICOECHEA, H. E.; BUEZAS, F. S. ; ROSALES, M. B.. **Bayesian inference applied to crack detection in beam-like structures.** In: *Mecánica computacional*, p. 3321–3334. Asociación Argentina de Mecánica Computacional, 2016.
- [45] GARCÍA, D. A.; SAMPAIO, R. ; ROSALES, M. B.. **Eigenproblems in timber structural elements with uncertain properties.** *Wood Science and Technology*, 50(4):807–832, 2016.
- [46] BALLABEN, J. S.; SAMPAIO, R. ; ROSALES, M. B.. **Uncertainty quantification in the dynamics of a guyed mast subjected to wind load.** *Engineering Structures*, 132:456–470, 2017.
- [47] RANGO, B. J.; SERRALUNGA, F. J.; PIOVAN, M. T.; BALLABEN, J. S. ; ROSALES, M. B.. **Identification of the tension force in cables with insulators.** *Meccanica*, 54(1-2):33–46, 2019.
- [48] DE PAZ, L. V. G.; ORTEGA, N. F. ; ROSALES, M. B.. **Assessment of wood utility poles' deterioration through natural frequency measurements.** *Journal of Civil Structural Health Monitoring*, 9(1):53–61, Feb. 2019.
- [49] SPILLMANN, J.; TESCHNER, M.. **CORDE: Cosserat rod elements for the dynamic simulation of one-dimensional elastic objects.** *Symposium on Computer Animation 2007 - ACM SIGGRAPH / Eurographics Symposium Proceedings, SCA 2007*, p. 63–72, 2007.
- [50] MOAKHER, M.; MADDOCKS, J. H.. **A double-strand elastic rod theory.** *Archive for Rational Mechanics and Analysis*, 177(1):53–91, 2005.

- [51] RYU, H.-T.; KANG, L. ; YI, B.-J.. **Application of Cosserat rod theory to configuration estimation of coionoscope.** In: 2018 15TH international conference ON ubiquitous robots (UR), p. 11–13, Honolulu, HI, June 2018. IEEE.
- [52] LEVINSON, M.. **A new rectangular beam theory.** Journal of Sound and Vibration, 74(1):81–87, 1981.
- [53] RUCKER, C.. **Integrating rotations ssing nonunit quaternions.** IEEE Robotics and Automation Letters, 3(4):2979–2986, 2018.
- [54] GURTIN, M. E.; FRIED, E. ; ANAND, L.. **The mechanics and thermodynamics of continua.** Cambridge University Press, Cambridge, 2010.
- [55] KUIPERS, J. B.. **Quaternions and rotation sequences: a primer with applications to orbits, aerospace, and virtual reality,** volume 37. Princeton University Press, 1999.
- [56] HERBERT GOLDSTEIN; POOLE, C. P. ; SAFKO, J. L.. **Classical Mechanics.** Addison-Wesley, 2001.
- [57] HAMILTON, W. R.. **On quaternions; or on a new system of imaginaries in algebra.** The London, Edinburgh, and Dublin Philosophical Magazine and Journal of Science, 31(208):278–293, Oct. 1847.
- [58] LINN, J.; LANG, H. ; TUGANOV, A.. **Geometrically exact Cosserat rods with Kelvin–Voigt type viscous damping.** Mechanical Sciences, 4(1):79–96, Feb. 2013.
- [59] DUCARNE, J.. **Modélisation et optimisation de dispositifs non-linéaires d’amortissement de structures par systèmes piézoélectriques commutés.** PhD thesis, Conservatoire national des arts et metier, 2009.
- [60] GÉRADIN, M.; CARDONA, A.. **Flexible multibody dynamics: a finite element approach.** Wiley, Chichester, 2001.
- [61] CAO, D. Q.; TUCKER, R. W.. **Nonlinear dynamics of elastic rods using the Cosserat theory: Modelling and simulation.** International Journal of Solids and Structures, 45(2):460–477, 2008.
- [62] ATTENBOROUGH, M.. **Differential equations and difference equations.** In: Mathematics for electrical engineering and computing, p. 346–381. Elsevier, 2003.

- [63] GOICOECHEA MANUEL, H. E.; LIMA, R. ; SAMPAIO, R.. **A Cosserat rod model for a cantilever beam that exhibits large displacements.** In: ABCM, Uberlandia, 2019. Springer.
- [64] GOICOECHEA, H. E.; LIMA, R.; SAMPAIO, R. ; BUEZAS, F. S.. **A verification of the Cosserat rod implementation for drill-string dynamics under large displacement conditions.** In: Proceeding series of the brazilian society of computational and applied mathematics. SBMAC, 2020.
- [65] HAKIMI, H.; MORADI, S.. **Drillstring vibration analysis using differential quadrature method.** Journal of Petroleum Science and Engineering, 70(3-4):235–242, 2010.
- [66] SHEPPARD, M. C.; WICK, C. ; BURGESS, T.. **Designing well paths to reduce drag and torque.** SPE Drilling Engineering, 2(4):344–350, 1987.
- [67] TIKHONOV, V.; VALIULLIN, K.; NURGALEEV, A.; RING, L.; GANDIKOTA, R.; CHAGUINE, P. ; CHEATHAM, C.. **Dynamic model for stiff-string torque and drag.** SPE Drilling & Completion, 29(03):279–294, 2014.
- [68] COMSOL AB. **COMSOL Multiphysics® v. 5.4**, 2018.
- [69] TUCKER, R. W. R.; WANG, C.. **Torsional vibration control and cosserat dynamics of a drill-rig assembly.** Meccanica, 38(1):143–159, 2003.
- [70] JEAN, M.. **The non-smooth contact dynamics method.** Computer Methods in Applied Mechanics and Engineering, 177(3-4):235–257, 1999.
- [71] BUEZAS, F. S.; ROSALES, M. B. ; FILIPICH, C. P.. **Collisions between two nonlinear deformable bodies stated within Continuum Mechanics.** International Journal of Mechanical Sciences, 52(6):777–783, 2010.
- [72] VIGUÉ, P.; VERGEZ, C.; KARKAR, S. ; COCHELIN, B.. **Regularized friction and continuation: Comparison with Coulomb’s law.** Journal of Sound and Vibration, 389:350–363, 2017.
- [73] WAHI, P.; CHATTERJEE, A.. **Self-interrupted regenerative metal cutting in turning.** International Journal of Non-Linear Mechanics, 43(2):111–123, 2008.
- [74] GOICOECHEA, H.; LIMA, R.; BUEZAS, F. ; SAMPAIO, R.. **Drill-string with cutting dynamics: A mathematical assessment of two models.** Journal of Sound and Vibration, 544:117364, Feb. 2023.

- [75] PATIL, P. A.; TEODORIU, C.. **A comparative review of modelling and controlling torsional vibrations and experimentation using laboratory setups.** Journal of Petroleum Science and Engineering, 112:227–238, Dec. 2013.
- [76] REAL, F. F.; LOBO, D. M.; RITTO, T. G. ; PINTO, F. A.. **Experimental analysis of stick-slip in drilling dynamics in a laboratory test-rig.** Journal of Petroleum Science and Engineering, 170:755–762, 2018.
- [77] GOICOECHEA, H. E.; BUEZAS, F. S. ; ROSALES, M. B.. **Stochastic drill-string dynamics via Cosserat rod models.** In: Mecánica Computacional, volume 36, p. 703–712, Santa Fe, 2018. Asociación Argentina de Mecánica Computacional.
- [78] GOICOECHEA, H. E.; LIMA, R.; SAMPAIO, R.; ROSALES, M. B. ; BUEZAS, F. S.. **A stochastic approach for a Cosserat rod drill-string model with stick-slip Motion.** In: 5th international symposium on uncertainty quantification and stochastic modelling, p. 103–110. Springer, Rouen, 2021.
- [79] ROBNETT, E. W.; HOOD, J. A.; HEISIG, G. ; MACPHERSON, J. D.. **Analysis of the stick-slip phenomenon using downhole drillstring rotation data.** Proceedings of the IADC/SPE Asia Pacific Drilling Technology Conference, APDT, 2:33–44, 1999.
- [80] GERMAY, C.; DENOËL, V. ; DETOURNAY, E.. **Multiple mode analysis of the self-excited vibrations of rotary drilling systems.** Journal of Sound and Vibration, 325(1-2):362–381, 2009.
- [81] GERE, J. M.; TIMOSHENKO, S.. **Mechanics of materials.** PWS Pub Co, Boston, 4th ed edition, 1997.
- [82] KREYSZIG, E.. **Advanced engineering mathematics.** WILEY, S.I., 2020.
- [83] BLACK, A. D.; WALKER, B. H.; TIBBITTS, G. A. ; SANDSTROM, J. L.. **Pdc bit performance for rotary, mud motor, and turbine drilling applications.** SPE Drilling Engineering, 1(6):409–416, 1986.
- [84] TEALE, R.. **The concept of specific energy in rock drilling.** International Journal of Rock Mechanics and Mining Sciences & Geomechanics Abstracts, 2(1):57–73, Mar. 1965.
- [85] GOICOECHEA, H. E.; LIMA, R.; BUEZAS, F. S. ; SAMPAIO, R.. **Avoiding formulations with delays to simulate cutting in drill-string**

- operations. In: *Mecánica Computacional*, volume 39, Bahía Blanca, 2022. Asociación Argentina de Mecánica Computacional.
- [86] WIERCIGROCH, M.. **Modelling of dynamical systems with motion dependent discontinuities**. 11:2429–2442, 2000.
- [87] WIERCIGROCH, M.; BUDAK, E.. **Sources of nonlinearities, chatter generation and suppression in metal cutting**. *Philosophical Transactions of the Royal Society A: Mathematical, Physical and Engineering Sciences*, 359(1781):663–693, 2001.
- [88] BESSELINK, B.; VAN DE WOUW, N. ; NIJMEIJER, H.. **A semi-analytical study of stick-slip oscillations in drilling systems**. *Journal of Computational and Nonlinear Dynamics*, 6(2):1–9, 2011.
- [89] SAMUEL, G. R.. **Percussion drilling... is it a lost technique? A review**. In: *Society of Petroleum Engineers - Permian basin oil and gas recovery conference*, OGR 1996, p. 741–747, Richardson, Mar. 1996. SPE.
- [90] FRANCA, L. F.. **A bit-rock interaction model for rotary-percussive drilling**. *International Journal of Rock Mechanics and Mining Sciences*, 48(5):827–835, 2011.
- [91] PAVLOVSKAIA, E.; HENDRY, D. C. ; WIERCIGROCH, M.. **Modelling of high frequency vibro-impact drilling**. *International Journal of Mechanical Sciences*, 91:110–119, 2015.
- [92] LIMA, R.; SAMPAIO, R.. **Stick-mode duration of a dry-friction oscillator with an uncertain model**. *Journal of Sound and Vibration*, 353:259–271, 2015.
- [93] JORGE S. BALLABEN; HECTOR E. GOICOECHEA ; MARTA B. ROSALES. **An alternative to Monte Carlo**. In: *Mecánica Computacional*, volume 36, p. 631–640, San Miguel de Tucuman, 2018. Asociación Argentina de Mecánica Computacional.
- [94] SOUZA DE CURSI, J. E.; SAMPAIO, R.. **Uncertainty quantification and stochastic modeling with Matlab**. Elsevier, 2015.
- [95] LIMA, R.; SAMPAIO, R.. **What is uncertainty quantification?** *Journal of the Brazilian Society of Mechanical Sciences and Engineering*, 40(3), 2018.
- [96] LIMA, R.; SAMPAIO, R.. **Uncertainty quantification and cumulative distribution function: how are they Related?**, volume 239. Springer International Publishing, 2018.

- [97] SIMO, J. C.; VU-QUOC, L.. **On the dynamics of flexible beams under large overall motions-the plane case: Part II.** Journal of Applied Mechanics, Transactions ASME, 53(4):855–863, 1986.
- [98] KANE, T. R.; RYAN, R. R. ; BANERJEE, A. K.. **Dynamics of a cantilever beam attached to a moving base.** Journal of Guidance, Control, and Dynamics, 10(2):139–151, 1987.
- [99] AMBRÓSIO, J. A. C.; EBERHARD, P.. **Advanced design of mechanical systems: from analysis to optimization**, volume 511. CISM International Centre for Mechanical Sciences, 2009.

A

Appendix to Chapter 2

A quick introduction of some mathematical concepts that are required for the current implementation of the theory of Cosserat rods is presented. In particular, the formulation that is adopted in Chapter 2 uses quaternions, a mathematical tool the reader might not be familiar with, to parametrise rotations.

The aim of is to present the mathematical tools without going into very complex demonstrations. To do such thing, an intuitive idea for the development of quaternions is provided: first, a brief discussion about rotations in \mathbb{R}^2 by employing complex numbers is shown. Next, the previous notion is extended to define quaternions, which are hyper-complex numbers of rank 4, and to provide an elegant means to treat rotations in \mathbb{R}^3 .

A.1

Quaternions as a tool to parametrise rotations in space

It is known that the components of a vector that rotates rigidly with a given frame of reference can be expressed as a linear transformation $\mathbf{p}_\theta = \mathbf{Q}\mathbf{p}$. Here, \mathbf{Q} is some rotation matrix with its columns formed by the directors of the rotated frame with respect to the original frame of reference (see Fig. A.1), \mathbf{p} is the vector to rotate in the original frame, and \mathbf{p}_θ the resulting rotated vector.

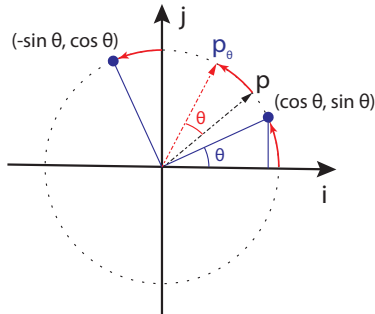


Figure A.1: A representation of the directors of the rotating frame with respect a the fixed frame of reference, employed to form the rotation matrix \mathbf{Q} .

Let \mathbf{v} be any vector such that $\mathbf{v} \in \mathbb{R}^2$, and θ be a rotation angle, as in Fig. A.1, then

$$\mathbf{p}_\theta = \mathbf{Q}\mathbf{p} = \begin{bmatrix} \cos \theta & -\sin \theta \\ \sin \theta & \cos \theta \end{bmatrix} \begin{bmatrix} x \\ y \end{bmatrix} = \begin{bmatrix} x \cos \theta - y \sin \theta \\ x \sin \theta + y \cos \theta \end{bmatrix}. \quad (\text{A-1})$$

It is also known that complex numbers can be employed to describe rotations in \mathbb{R}^2 . The mathematical aspects of this affirmation are simple. Let $\{p, z_\theta\} \in \mathbb{C}$, $\{x, y\} \in \mathbb{R}$, and consider a vector $\mathbf{v} = (x, y)$ to rotate. Then, some complex numbers $p = x + iy$, $z_\theta = e^{i\theta} = \cos \theta + i \sin \theta$ can be defined such that the multiplication $p_\theta = z_\theta p$ results in a rotation from the origin of \mathbf{p} in an angle θ in the complex plane. Moreover, the real and imaginary parts of the product are the components of the rotated vector.

$$\begin{aligned} z_\theta(x + iy) &= (\cos \theta + i \sin \theta)(x + iy) \\ &= x \cos \theta - y \sin \theta + i(x \sin \theta + y \cos \theta) \end{aligned} \quad (\text{A-2})$$

Note that the real and imaginary parts of (A-2) coincide with the components of the rotated vector in (A-1), as expected.

Second, any complex number $\{z \in \mathbb{C}, \{a, b\} \in \mathbb{R} : z = a + bi\}$ can be represented in matrix form so that the operations between complex numbers become simple matrix operations:

$$z = a\mathbf{I} + b\mathbf{i}_q = a \begin{bmatrix} 1 & 0 \\ 0 & 1 \end{bmatrix} + b \begin{bmatrix} 0 & -1 \\ 1 & 0 \end{bmatrix} = \begin{bmatrix} a & -b \\ b & a \end{bmatrix}. \quad (\text{A-3})$$

Here the matrix \mathbf{i}_q satisfies the condition $\mathbf{i}_q^2 = -\mathbf{I}$. Therefore, it behaves like the imaginary unit.

In a few words, a multiplication of complex numbers can be used to define a rotation in \mathbb{R}^2 , and that operation can be expressed by means of matrix multiplications. With this idea in mind, it seems natural to extend the use of complex numbers to represent rotations in \mathbb{R}^3 . It was Hamilton who, in 1843, developed the tool for such calculation: the so-called hyper-complex number of rank 4, namely a quaternion [55].

Let \mathbf{q} be a quaternion, an object defined by considering a 4-tuple $\mathbf{q} = \{q_a, q_b, q_c, q_d\}$, such that

$$\mathbf{q} = q_a\mathbf{I} + q_b\mathbf{i}_q + q_c\mathbf{j}_q + q_d\mathbf{k}_q, \quad (\text{A-4})$$

with

$$\mathbf{I} = \begin{bmatrix} 1 & 0 \\ 0 & 1 \end{bmatrix}, \quad \mathbf{i}_q = \begin{bmatrix} 0 & -1 \\ 1 & 0 \end{bmatrix}, \quad \mathbf{j}_q = \begin{bmatrix} 0 & -i \\ -i & 0 \end{bmatrix}, \quad \mathbf{k}_q = \begin{bmatrix} i & 0 \\ 0 & -i \end{bmatrix}, \quad (\text{A-5})$$

or expressed in matrix form as

$$\mathbf{q} = \begin{bmatrix} q_a + iq_d & -q_b - iq_c \\ q_b - iq_c & q_a - iq_d \end{bmatrix}. \quad (\text{A-6})$$

Also, let \mathbf{q}^* be the quaternion conjugate defined as

$$\mathbf{q}^* = q_a - q_b\mathbf{i}_q - q_c\mathbf{j}_q - q_d\mathbf{k}_q. \quad (\text{A-7})$$

With the previous definitions, a relation between vectors in \mathbb{R}^3 and quaternions can be stated. Consider a vector in \mathbb{R}^3 such that $\mathbf{p} = p_1\mathbf{i} + p_2\mathbf{j} + p_3\mathbf{k}$, where $\{\mathbf{i}, \mathbf{j}, \mathbf{k}\}$ is some base on \mathbb{R}^3 . The same vector can be represented in quaternion form as $\mathbf{p}_q = 0 + p_1\mathbf{i}_q + p_2\mathbf{j}_q + p_3\mathbf{k}_q$. This means that a correspondence between vector in \mathbb{R}^3 and quaternions can be established, as illustrated in Fig.A.2.

$$\begin{array}{ccc} \mathbf{g} = b\mathbf{i} + c\mathbf{j} + d\mathbf{k} & \longleftrightarrow & \mathbf{g}_q = 0\mathbf{I} + b\mathbf{i}_q + c\mathbf{j}_q + d\mathbf{k}_q \\ \text{Vectors in } \mathbb{R}^3 & & \text{Pure imaginary} \\ & & \text{quaternion} \end{array}$$

Figure A.2: Correspondence vector - quaternion, and vice versa.

The matrixes $\mathbf{i}_q, \mathbf{j}_q, \mathbf{k}_q$ behave similarly to the imaginary unit: $\mathbf{i}_q^2 = \mathbf{j}_q^2 = \mathbf{k}_q^2 = \mathbf{i}_q\mathbf{j}_q\mathbf{k}_q = -\mathbf{I}$. Moreover, some analogy can be established between the product of those matrixes and the vectorial product of elements that form an orthonormal base. For example, as illustrated in Fig. A.3, $\mathbf{i}_q\mathbf{j}_q = \mathbf{k}_q$ if multiplied in the clockwise sense, or $\mathbf{j}_q\mathbf{i}_q = -\mathbf{k}_q$ if multiplied counter-clockwise.

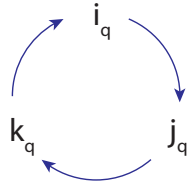


Figure A.3: Multiplication diagram.

Now, let a pure real quaternion be of the form $\{q_a, 0, 0, 0\}$, a pure imaginary quaternion be of the form $\{0, q_b, q_c, q_d\}$, and let the norm of a quaternion be $|\mathbf{q}| = \sqrt{q_a^2 + q_b^2 + q_c^2 + q_d^2}$. In what follows, consider \mathbf{q} and \mathbf{e}_q to be unitary ($|\mathbf{q}| = |\mathbf{e}_q| = 1$), with $\mathbf{e}_q = \{0, e_{q1}, e_{q2}, e_{q3}\}$.

Then,

$$L_q(\mathbf{p}_q) = \mathbf{q}\mathbf{p}_q\mathbf{q}^*, \quad \mathbf{q} = \cos\left(\frac{\theta}{2}\right)\mathbf{I} + \mathbf{e}_q \sin\left(\frac{\theta}{2}\right) \quad (\text{A-8})$$

defines an operator $L_q(\mathbf{p}_q)$ applied to some pure imaginary quaternion $\mathbf{p}_q = \{0, p_{q1}, p_{q2}, p_{q3}\}$ that results in a rotation of vector \mathbf{p} in a angle θ over the axis defined by $\{e_1, e_2, e_3\}$. In fact, $L_q(\mathbf{p}_q)$ gives another imaginary quaternion, whose imaginary parts coincide with the rotated vector.

Also, the transformation can be expressed in terms of a rotation matrix \mathbf{Q} as $L_q(\mathbf{p}_q) = \mathbf{Q}\mathbf{p}$ such that

$$L_q(\mathbf{p}_q) = \begin{bmatrix} q_a^2 + q_b^2 - q_c^2 - q_d^2 & 2(q_b q_c - q_a q_d) & 2(q_a q_c + q_b q_d) \\ 2(q_a q_d + q_b q_c) & q_a^2 - q_b^2 + q_c^2 - q_d^2 & 2(q_c q_d - q_a q_b) \\ 2(q_b q_d - q_a q_c) & 2(q_a q_b + q_c q_d) & q_a^2 - q_b^2 - q_c^2 + q_d^2 \end{bmatrix} \begin{pmatrix} p_1 \\ p_2 \\ p_3 \end{pmatrix}, \quad (\text{A-9})$$

with

$$q_a^2 + q_b^2 + q_c^2 + q_d^2 = 1. \quad (\text{A-10})$$

A.1.1 Demonstration

In order to prove that the product in (A-8) is in fact a rotation, the following strategy will be used: first, any vector (\bullet) can be written as a pure imaginary quaternion. The subscript $(\bullet)_q$ will be used to denote explicitly the quaternion representation. With this in mind, let \mathbf{q} be a quaternion with imaginary part \mathbf{e}_q . Let $\mathbf{p} = \mathbf{p}_t + \mathbf{p}_n$ be an arbitrary vector resolved into two orthogonal components: the component along \mathbf{e} , $\mathbf{p}_t = \alpha \mathbf{e}$, and its normal component \mathbf{p}_n . Then, it is shown that under the quaternion rotation operator, the first component is invariant, and the second is rotated about \mathbf{e} through an angle θ .

As stated above, \mathbf{e} and \mathbf{p} are some vectors in \mathbb{R}^3 , and can be written as purely imaginary quaternions

$$\mathbf{e}_q = e_1 \mathbf{i}_q + e_2 \mathbf{j}_q + e_3 \mathbf{k}_q, \quad (\text{A-11})$$

$$\mathbf{p}_q = p_1 \mathbf{i}_q + p_2 \mathbf{j}_q + p_3 \mathbf{k}_q. \quad (\text{A-12})$$

It is evident that the sum of pure imaginary quaternions still belongs to \mathbb{R}^3 . This reasoning does not apply to multiplication of pure imaginary quaternions, a calculation which can be written in terms of the usual scalar and vectorial products of vectors, as follows:

$$\mathbf{e}_q \mathbf{p}_q = -\mathbf{e} \cdot \mathbf{p} + \mathbf{e} \times \mathbf{p} \quad (\text{A-13})$$

Immediately, some comments can be made from the analysis of the previous equation: given that the scalar product is always a real number,

$\mathbf{e} \cdot \mathbf{p} = 0$ if $\mathbf{e}_q \mathbf{p}_q$ is also a pure imaginary quaternion. On the other hand, $\mathbf{e}_q \mathbf{p}_q$ is a pure real quaternion only if the vector product $\mathbf{e} \times \mathbf{p} = 0$, which means that \mathbf{e} and \mathbf{p} are on the same direction.

Now, let \mathbf{e}_q and \mathbf{q} be unitary quaternions, then it is shown that the operators

$$L_q(\mathbf{p}_q) = \mathbf{q} \mathbf{p}_q \mathbf{q}^*, \quad \mathbf{q} = \cos\left(\frac{\theta}{2}\right) \mathbf{I} + \mathbf{e}_q \sin\left(\frac{\theta}{2}\right) \quad (\text{A-14})$$

$$L_q^*(\mathbf{p}_q) = \mathbf{q}^* \mathbf{p}_q \mathbf{q}, \quad \mathbf{q} = \cos\left(\frac{\theta}{2}\right) \mathbf{I} + \mathbf{e}_q \sin\left(\frac{\theta}{2}\right) \quad (\text{A-15})$$

produce rotations of \mathbf{p} .

The conjugate of a complex number is such that the imaginary part has a sign change. In the case of quaternions, it is defined analogously: let \mathbf{q}^* be the conjugate of \mathbf{q} , then the conjugate is obtained by multiplying by -1 the imaginary part

$$\mathbf{q}^* = \cos\left(\frac{\theta}{2}\right) \mathbf{I} - \mathbf{e}_q \sin\left(\frac{\theta}{2}\right), \quad (\text{A-16})$$

and the inverse is defined as

$$\mathbf{q}^{-1} = \frac{\mathbf{q}^*}{|\mathbf{q}|^2}. \quad (\text{A-17})$$

Given that \mathbf{q} is unitary, $\mathbf{q}^{-1} = \mathbf{q}^*$. The existence of an inverse implies that the multiplication to the left or to the right by \mathbf{q} and \mathbf{q}^* is also invertible.

To show that $L_q(\mathbf{p}_q)$ defines rotations, two properties need to be satisfied: first, there has to exist a set of points within an axis that, after the application of the rotation operator, remain unchanged. That axis is the axis of rotation itself. Second, it needs to be shown that distances are preserved and angles are preserved.

To prove the first affirmation, $L_q(\mathbf{p}_q)$ will be applied to any linear combination of \mathbf{e}_q , which represent all the vectors in the direction of \mathbf{e} in \mathbb{R}^3 .

$$\begin{aligned} L_q(\mathbf{e}_q) &= \mathbf{q} \alpha \mathbf{e}_q \bar{\mathbf{q}} \\ &= \alpha \left(\cos\left(\frac{\theta}{2}\right) \mathbf{I} + \mathbf{e}_q \sin\left(\frac{\theta}{2}\right) \right) \mathbf{e}_q \left(\cos\left(\frac{\theta}{2}\right) \mathbf{I} - \mathbf{e}_q \sin\left(\frac{\theta}{2}\right) \right) \\ &= \alpha \left(\mathbf{e}_q \cos\left(\frac{\theta}{2}\right) \mathbf{I} + \mathbf{e}_q^2 \sin\left(\frac{\theta}{2}\right) \right) \left(\cos\left(\frac{\theta}{2}\right) \mathbf{I} - \mathbf{e}_q \sin\left(\frac{\theta}{2}\right) \right), \\ &= \alpha \left(\mathbf{e}_q \cos^2\left(\frac{\theta}{2}\right) - \mathbf{e}_q^2 \sin\left(\frac{\theta}{2}\right) \cos\left(\frac{\theta}{2}\right) + \mathbf{e}_q^2 \sin\left(\frac{\theta}{2}\right) \cos\left(\frac{\theta}{2}\right) + \mathbf{e}_q \sin^2\left(\frac{\theta}{2}\right) \right) \\ &= \alpha \left(\mathbf{e}_q \cos^2\left(\frac{\theta}{2}\right) + \mathbf{e}_q \sin^2\left(\frac{\theta}{2}\right) \right) \\ &= \alpha \mathbf{e}_q \end{aligned} \quad (\text{A-18})$$

The previous equation shows that $L_q(\alpha \mathbf{e}_q) = \alpha \mathbf{e}_q$, which means that \mathbf{e} defines an axis that is left unchanged under the transformation. Namely, the rotation axis.

Second, if \mathbf{w}_q is a pure imaginary quaternion, it is shown that $L_q(\mathbf{p}_q - \mathbf{w}_q)$ is an isometry, meaning that distances are preserved. To do so, the following properties will be used: the norm of a quaternion is given by $|\mathbf{q}| = \sqrt{\mathbf{q}\mathbf{q}^*} = \sqrt{\mathbf{q}^*\mathbf{q}}$, and $(\mathbf{q}\mathbf{b})^* = \mathbf{b}^*\mathbf{q}^*$, where \mathbf{b} is another quaternion.

$$\begin{aligned}
 |L_q(\mathbf{p}_q - \mathbf{w}_q)| &= |\mathbf{q}(\mathbf{p}_q - \mathbf{w}_q)\mathbf{q}^*| \\
 &= \sqrt{\mathbf{q}(\mathbf{p}_q - \mathbf{w}_q)\mathbf{q}^*\mathbf{q}(\mathbf{p}_q - \mathbf{w}_q)^*\mathbf{q}^*} \\
 &= \sqrt{\mathbf{q}|\mathbf{p}_q - \mathbf{w}_q|\mathbf{q}^*} \\
 &= \sqrt{|\mathbf{p}_q - \mathbf{w}_q|^2\mathbf{q}\mathbf{q}^*} \\
 &= |\mathbf{p}_q - \mathbf{w}_q|
 \end{aligned} \tag{A-19}$$

This shows that distances are preserved, and if $\mathbf{w}_q = 0$, it shows that norms are also maintained during the transformation.

Finally, let $\mathbf{p} = \mathbf{p}_t + \mathbf{p}_n$, where \mathbf{p}_n be orthogonal to \mathbf{e} in \mathbb{R}^3 . Then $\mathbf{e} \cdot \mathbf{p}_t = 0$, and \mathbf{p}_t is unchanged by L_q .

$$\begin{aligned}
 \mathbf{e}_q \mathbf{p}_{qn} &= \mathbf{e} \times \mathbf{p}_n = \mathbf{w}_q \\
 \mathbf{p}_{qn} \mathbf{w}_q &= \mathbf{e}_q \\
 \mathbf{w}_q \mathbf{e}_q &= \mathbf{p}_{qn}
 \end{aligned} \tag{A-20}$$

Remembering that quaternion multiplication is non commutative,

$$\begin{aligned}
 \mathbf{q}\mathbf{p}_{qn}\mathbf{q}^* &= \left(\cos\left(\frac{\theta}{2}\right)\mathbf{I} + \mathbf{e}_q \sin\left(\frac{\theta}{2}\right) \right) \mathbf{p}_{qn} \left(\cos\left(\frac{\theta}{2}\right)\mathbf{I} - \mathbf{e}_q \sin\left(\frac{\theta}{2}\right) \right) \\
 &= \mathbf{p}_n \cos^2\left(\frac{\theta}{2}\right) + 2\mathbf{e}_q \mathbf{p}_{qn} \sin\left(\frac{\theta}{2}\right) \cos\left(\frac{\theta}{2}\right) - \mathbf{e}_q \mathbf{p}_{qn} \mathbf{e} \sin^2\left(\frac{\theta}{2}\right) \\
 &= \mathbf{p}_n \cos^2\left(\frac{\theta}{2}\right) + \mathbf{p}_{qn} \mathbf{e}_q \mathbf{e}_q \sin^2\left(\frac{\theta}{2}\right) + 2\mathbf{e}_q \mathbf{p}_{qn} \sin\left(\frac{\theta}{2}\right) \cos\left(\frac{\theta}{2}\right) \\
 &= \mathbf{p}_{qn} \cos(\theta) + \mathbf{w}_q \sin(\theta)
 \end{aligned} \tag{A-21}$$

and

$$\mathbf{q}\mathbf{p}_q\mathbf{q}^* = \mathbf{p}_{qt} + \mathbf{p}_{qn} \cos \theta + \mathbf{w}_q \sin \theta \tag{A-22}$$

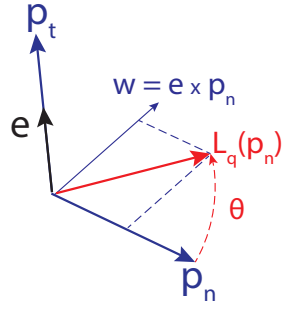


Figure A.4: Representation of the effect of the application of the operator L_q to some vector \mathbf{v} .

Eq. (A-22) shows that the vector in the direction of \mathbf{e} remain unchanged; that normal vectors \mathbf{n} to \mathbf{e} rotate in an angle θ on a plane that is perpendicular to \mathbf{e} ; and that distances are preserved, which demonstrate that the operator actually defines a rotation.

B

Appendix to Chapter 4

B.1

Benchmarks and model verifications

The objective of this section is to present set of verifications that were performed to verify the implementation of the Cosserat formulation in COMSOL [68]. The solution for the Cosserat rod (CR) model are compared against known solutions for non-linear problems reported in the literature.

B.1.1

A pendulum under the action of gravity

In this test, the dynamics of a pendulum are analysed. The pendulum consists of a straight beam pinned at one end, and free on the other. Only the effect of gravity is considered, with no friction at the hinge. In its initial position, the pendulum is horizontal and at-rest, as in Fig. B.1. The geometrical and material properties of the structural element are presented in the aforementioned figure.

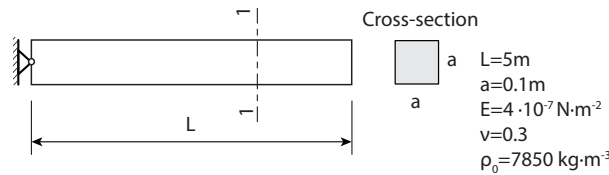


Figure B.1: Example B.1.1. Initial configuration for the pendulum, with its respective geometrical and material properties.

The time response for the centreline of the pendulum is depicted in Fig. B.2, along with the results from [42]. In the latter, two models are compared: Model SM1 where the motion described by a small displacement theory is composed with a rigid motion; Model SM2 where a 2D non-linear theory of elasticity (NLTE) accounting for finite displacements is considered. Then, the shapes of the solution presented herein coincide with the results for model SM2, that is, a plane stress model that accounts for large displacements.

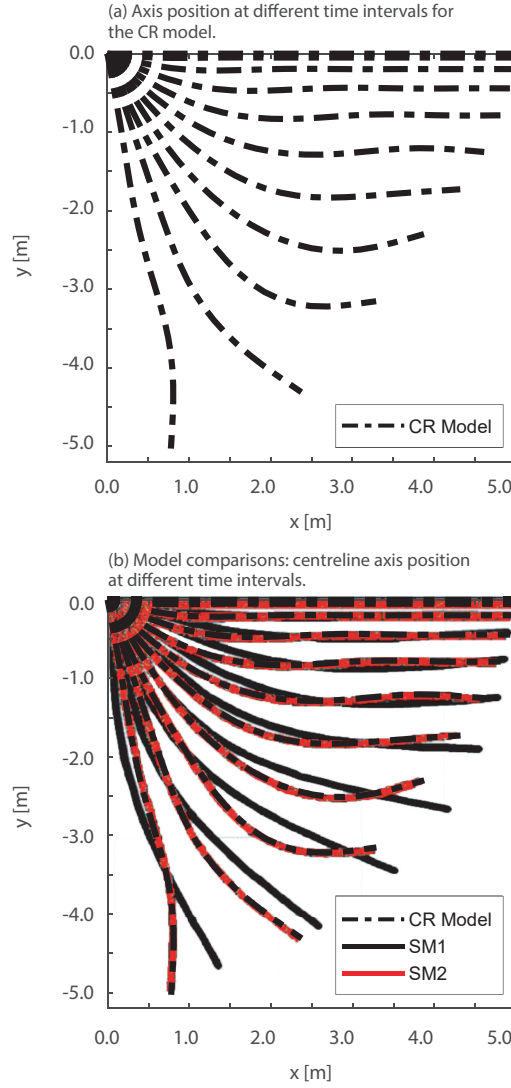


Figure B.2: Example B.1.1. (a) Cosserat rod (CR) model centerline position at different times. Intervals $\Delta t = 0.1s$ are considered. (b) Model comparison. The results obtained with the models SM1 and SM2 from Reference [42] vs the CR model are shown.

B.1.2

A spin-Up manoeuvre

This problem was proposed in [97] in an attempt to demonstrate that solutions obtained for linearised models could completely differ from non-linear models and from real observed phenomena. The problem has been employed by many authors, such as [42, 98, 99], to verify results for non-linear theories. A cantilever beam under the influence of a spin-up manoeuvre is analysed. A rotation is forced from one of its end, accelerating from at-rest position to a constant angular speed as described by the function $\Psi(t)$.

The geometrical and material aspects of the beam are shown in Fig. B.3. The rotation is applied at point P .

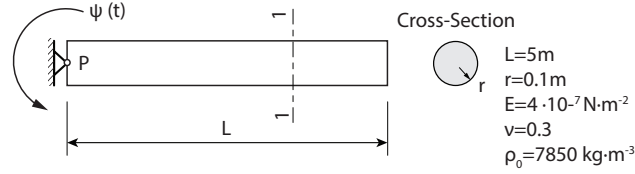


Figure B.3: Example B.1.2. Initial configuration for the cantilever beam with its respective geometrical and material properties.

$$\Psi(t) = \begin{cases} \frac{6}{15} \left[\frac{t^2}{2} + \left(\frac{15}{2\pi} \right)^2 \left(\cos\left(\frac{2\pi t}{15}\right) - 1 \right) \right] & \text{if } t \leq 15 \\ 6t - 45 & \text{if } t > 15 \end{cases}$$

Considering a perfectly rigid beam as reference, the difference between positions for the non-linear model and the rigid beam are evaluated at the free-end. Its longitudinal component δ in the direction of the rigid-beam axis is plotted against time in Fig. B.4. The authors of [42] present a solution based on a plain stress non-linear theory, while a solution based on a rod theory is shown in [97].

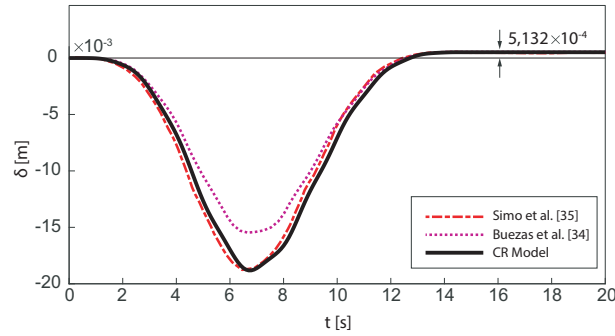


Figure B.4: Example B.1.2. Spin-up manoeuvre. Comparison of the δ values obtained by the Cosserat rod (CR) model and the works of [42] and [97]. The model from S is that of Reference [97], model B is that of [42], and the CR model stands for the Cosserat approach herein presented.

B.1.3

A beam under pure bending

The problem of a cantilever beam with an applied moment at its free end is presented in [42]. A bending moment is applied at the free-end of the beam and its magnitude is varied until the beam axis turns into a perfect circumference where its ends meet. The CR model solution is compared to that reported in [42], which is based on a non-linear plain stress elasticity theory.

The geometrical and material aspects of the beam are shown in Figure B.5.

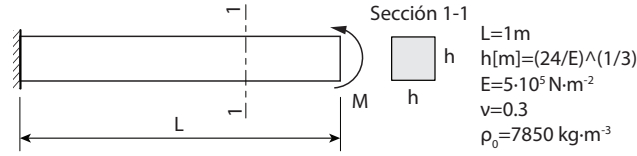


Figure B.5: Example B.1.3. Sketch of the bending beam problem with its geometrical and material properties.

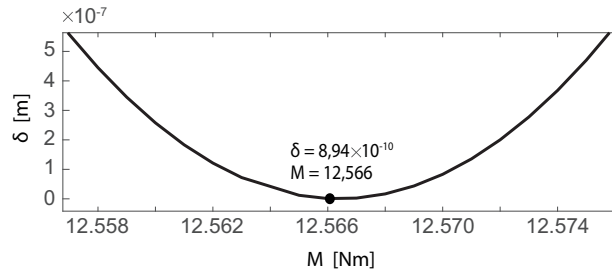


Figure B.6: Example B.1.3. Distance between the beam ends (δ) vs. applied bending moment (M).

The results are shown in Fig. B.6. The bending moment required to close the beam into a perfect circumference is $M = 4\pi \approx 12.566$ Nm, which coincides with the value reported in the literature.

B.1.4

A drill-string model for a straight vertical borehole

The kinematics of a drill-string for the friction model proposed by [20] are analysed. The original problem consists of a straight beam under axial-torsional effects, with a friction law acting at the bit of the drill-string. The authors solve the axial and torsional wave equation. Concentrated masses at both ends of the rod representing the top-drive and the BHA-bit, respectively, are considered.

B.1.4.1

Rotary speed control

An optimal drilling operation implies that the drill-string angular speed ω matches the target speed Ω . With this aim, a control strategy is implemented via a proportional-integral controller (PI-Controller) at the top drive.

Following [20], the response of the PI controller in terms of torque at the top of the drill-string is introduced as a boundary condition at the upper end.

$$T_{top} = k_p(\Omega - \omega) + k_i((\Omega \cdot t - \phi)) \quad (\text{B-1})$$

Table B.1: Adopted parameter values for the PI controller, based on the values presented in [20].

Variable	Symbol	Value	Units
Target Speed	Ω	100	rpm
Proportional constant	k_p	200	N m s rad ⁻¹
Integral constant 1	k_i	100	N m rad ⁻¹

B.1.4.2

Contact model

The original model only considers axial and torsional effects. The CR model can also account for lateral displacements. A simple contact model for the borehole wall and bit is proposed, with a penalisation method to the Signorini problem. The soil is assumed to be fully elastic, and the contact force is considered linearly proportional to the penetration on the borehole wall, with k_s the proportionality constant. For this reason, Hooke's law is adopted to represent soil behaviour. To avoid any possible lateral deflection, e.g. product of the buckling of the drill-string due to the WOB magnitude, a value k_s is chosen so that the drill-string remains bounded within the specified clearance $c_{gap} = 1 \cdot 10^{-4}$ m. As already stated, the clearance is considered sufficiently small in order to guarantee that the solution cannot differ greatly from the straight configuration of the original model.

B.1.4.3

Friction model

The friction model was obtained from drilling measurements under stable drilling conditions by [20], for constant drill-bit angular speed ($\Omega \approx 100$ rpm). It correlates the frictional torque-on-bit (TOB), weight-on-bit (WOB), depth-of-cut (DOC), angular speed, and rate-of-penetration (ROP), through the following expressions.

$$ROP = -a_1 + a_2 WOB + a_3 \Omega \quad (\text{B-2})$$

$$DOC = \frac{ROP}{\Omega} \quad (\text{B-3})$$

$$TOB = a_4 DOC + a_5 \quad (\text{B-4})$$

Table B.2 depicts the set of chosen parameters for the friction model.

Table B.2: Parameters for the friction model presented in [20].

Variable	Symbol	Value	Units
Weight on bit	WOB	100	kN
Model parameter 1	a_1	$3.429 \cdot 10^{-3}$	$m \, s^{-1}$
Model parameter 1	a_2	$5.672 \cdot 10^{-8}$	$m \, N^{-1} \, s^{-1}$
Model parameter 2	a_3	$1.374 \cdot 10^{-4}$	$m \, rad^{-1}$
Model parameter 4	a_4	$9.537 \cdot 10^6$	$N \, rad$
Model parameter 5	a_5	$1.475 \cdot 10^3$	$N \, m$

As stated by the authors, in order to model Coulomb frictional effects, it is necessary to regularise the frictional torque and rate-of-penetration so that they vanish as the drill-bit angular speed tends to zero [69]. Therefore, the following expression is considered, with a regularisation factor $\epsilon = 2 \, rad \, s^{-1}$ and a varying angular speed ω .

$$TOB = (-a_1 + a_2 F_{bit}) a_4 \frac{\omega_L^3}{(\omega_L^2 + \epsilon^2)^2} + a_3 a_4 \frac{\omega_L^3}{(\omega_L^2 + \epsilon^2)^{3/2}} + a_5 \frac{\omega_L}{(\omega_L^2 + \epsilon^2)^{1/2}} \quad (B-5)$$

B.1.5

Initial Conditions

At $t = 0$, the drill-string is supposed to be rotating at a uniform speed of 70 RPMs.

B.1.5.1

Solution

The responses of the drill-string for times $t = 0 \, s$ to $t = 100 \, s$, at the top and the bit, are shown in Fig. B.7 and Fig. B.8 respectively. The solution matches that presented by [20].

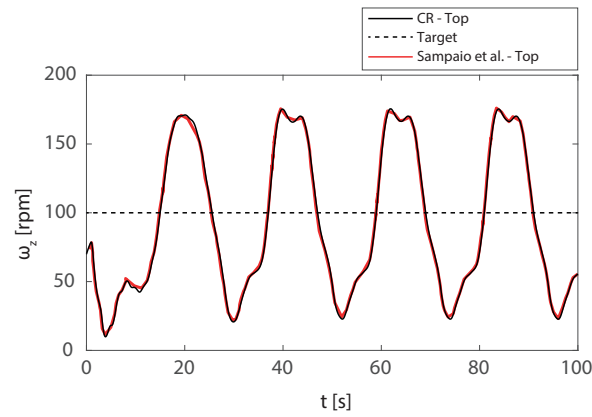


Figure B.7: Comparison between the Cosserat rod (CR) model and that presented in [20]. Angular speed ω_z at the top vs time. The target speed for the PI-controller is represented by a dashed line. The model used by Sampaio et al. is that of [21].

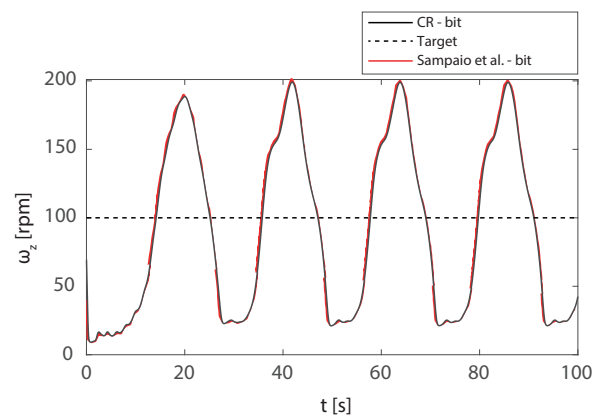


Figure B.8: Comparison between the Cosserat rod (CR) model and that presented in [20]. Angular speed ω_z at the bit vs time. The target speed for the PI-controller is represented by a dashed line. The model used by Sampaio et al. is that of [21].

C

Appendix to Chapter 6

C.1

Geometrical interpretation of the equation for the cutting process

A geometrical interpretation for the equation (5-21) and boundary conditions (5-22) and (5-23) is given through Fig. C.1.

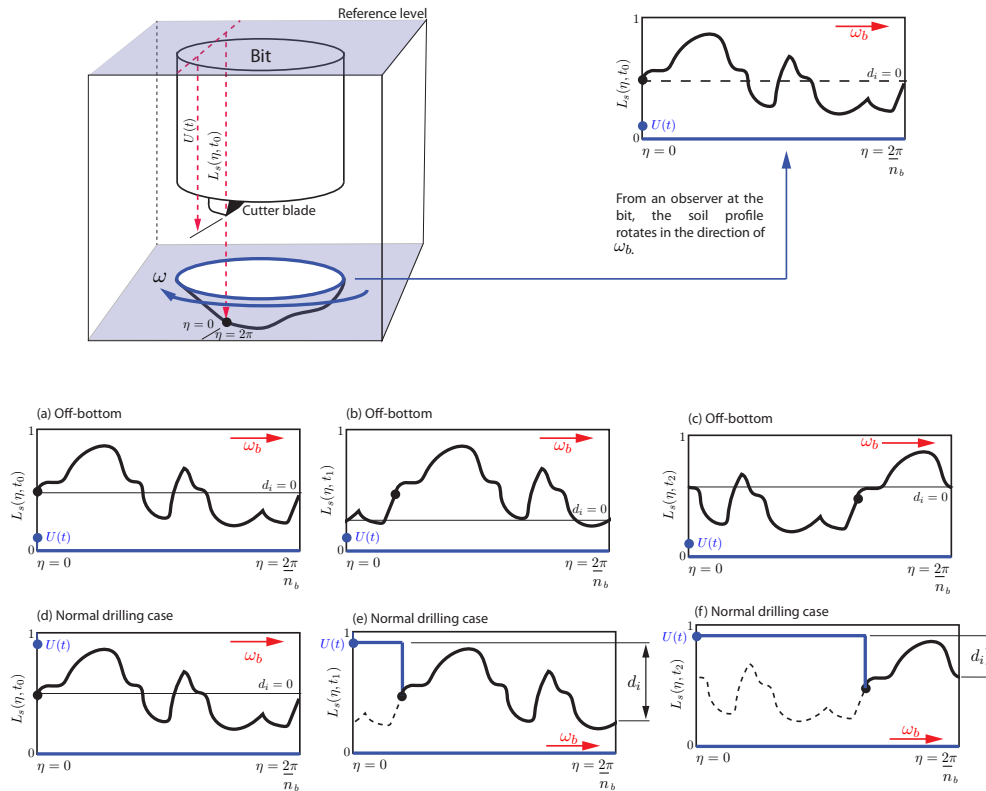


Figure C.1: Schematic example of the behaviour of the advection equation to model the cutting process. (a-c) depict an off-bottom case, at times t_0 , $t_1 > t_0$, and $t_2 > t_1$, respectively. (d-e) show an example of a normal drilling condition. The red arrow depicts the direction in which the advection equation translates the soil profile with a speed ω .

The Fig. C.1 (a-c) exemplifies the behaviour of (5-21) for an off-bottom case, i.e. when the bit is rotating without contact with the soil. Meanwhile, Fig. C.1 (d-f) shows an example of a normal cutting condition.

To better understand the behaviour of the equation, consider a frame that is fixed at the cutting blade, so that the blade is always at angle $\eta = 0$.

During the drilling process, the cutter will move following a circular path over the soil. The equation and the boundary conditions are devised so that the endpoints $\eta = 0$ and $\eta = \frac{2\pi}{n_b}$ represent the soil profile immediately after and before the cutting blade.

Let (a) define the soil profile for the off-bottom case $L_s(\eta, t = t_0)$, (b) and (c) be a snapshot of the soil profile at times $t_1 > t_0$ and $t_2 > t_1$, respectively. In the off-bottom case, the solution of the advection equation in conjunction with a periodic boundary condition give a response that is a spatial translation of the solution at time t_0 (there is no change in the shape of the profile). The speed at which the soil profile moves spatially is given by ω , thus it is coupled with the torsional equation of motion. Moreover, it is observed that the endpoints $\eta = 0$ and $\eta = \frac{2\pi}{n_b}$ coincide, which means that the instantaneous depth of cut is exactly $d_i = 0$.

Now, Fig. C.1 (d-f) depict an example of a normal drilling condition. Let (d) show an initial state of the soil profile $L_s(\eta, t = t_0)$. Also, let the position of the bit $U(t = t_0)$ be given by the blue dot, and for the illustrative purpose of this example only, it is assumed that the axial position $U(t)$ remains constant in time. The fact that $U(t) > L_s(\eta = 0, t)$ means that cutting is taking place. Then, (b) and (c) show the evolution of the soil profile at times $t_1 > t_0$ and $t_2 > t_1$. As depicted in the sketch. Now there is a difference between the values of $L_s(\eta = 0, t)$, the soil height after cutting has taken place, and $L_s(\eta = \frac{2\pi}{n_b}, t)$, the soil height before cutting. This difference is the so-called instantaneous depth of cut given by (5-24). Finally, the recently removed soil depth is depicted by a dashed line.

C.2

Non-dimensional parameters

The problems studied throughout this work are defined in terms of parameters with direct physical interpretations, such as a length or an elasticity modulus. Therefore, the equations of motion are not required in their non-dimensional form, as employed in [14]. Nonetheless, for the sake of completion and to ease comparison with their results, the definitions of the non-dimensional parameters in terms of the dimensional ones are stated below.

$$\hat{u} = \frac{U - U_0}{L^*}, \quad \hat{v} = \frac{Vt^*}{L^*} \quad (\text{C-1})$$

$$\hat{\omega} = \Omega t^*, \quad \omega_0 = \Omega_0 t^*. \quad (\text{C-2})$$

$$t^* = \sqrt{I/C}, \quad L^* = \frac{2C}{\epsilon_1 a^2} \quad (\text{C-3})$$

$$d = \sum_i d_i, \quad \delta = \frac{d}{L^*}, \quad \tau = \frac{t}{t^*} \quad (\text{C-4})$$

$$\mathcal{W} = \frac{W}{\zeta \epsilon_1 a L^*}, \quad \mathcal{W}_0 = \frac{W_0}{\zeta \epsilon_1 a L^*} \quad (\text{C-5})$$

$$\mathcal{T} = \frac{T}{C}, \quad \mathcal{T}_0 = \frac{T_0}{C} \quad (\text{C-6})$$

$$\beta = \mu \gamma \zeta, \quad \lambda = \frac{\sigma_1 l}{\zeta \epsilon_1 L^*}, \quad \psi = \frac{\zeta \epsilon_1 a I}{MC} \quad (\text{C-7})$$

In the previous equations, the quantities \hat{u} , \hat{v} , $\hat{\omega}$ represent the non-dimensional axial position, axial speed, and angular speed, respectively. They are calculated in terms of the dimensional magnitudes U and U_0 , the position of the bit and the nominal position of the bit; V , the axial speed; t^* , a time parameter; and L^* , a length parameter. d stands for the instantaneous depth of cut. All other parameters are defined in Table 6.1.

D

The weak form

In what follows the expression for the weak form associated to some equations that will be used in the simulations is given. The general form is given by

$$\Xi_{1,i} + \Xi_{2,i} + \Xi_{3,j} + \Xi_4 + \Xi_5 = 0, \quad (\text{D-1})$$

where

- $\Xi_{1,i}$ and $\Xi_{2,i}$ are the terms associated to the weak formulation of the Cosserat theory of rods given by (2-51) and (2-61). In this case, $i = \{1, 2, 3\}$, and the test functions $\Lambda_{1,i}$ and $\Lambda_{2,i}$ are used.
- $\Xi_{3,j}$ is linked to the integration of the quaternion components in (2-26), with $j = \{1, 2, 3, 4\}$. In its expression, the test functions $\Lambda_{3,j}$ are used.
- Ξ_4 is related to the integration of the advection equation. The test function Λ_4 is used.
- Ξ_5 is an algebraic equation linked to the detection of the lateral contact. The test function Λ_5 is used.

Each of the expressions can be written as

$$\begin{aligned} \Xi_{1,i} = & -\Lambda_{1,i} n_i^R \Big|_{s^o=0}^{s^o=L} + \int_{s^o=0}^{s^o=L} \left(n_i^R \frac{d}{ds^o} (\Lambda_{1,i}) - f_{n,i}^R \Lambda_{1,i} \right) ds^o + \\ & \int_{s^o=0}^{s^o=L} \left(\Lambda_{1,i} \frac{d}{dt} (\rho^R A^R \dot{r}_i^R) \right) ds^o, \end{aligned} \quad (\text{D-2})$$

$$\begin{aligned} \Xi_{2,i} = & -\Lambda_{2,i} m_i^R \Big|_{s^o=0}^{s^o=L} + \int_{s^o=0}^{s^o=L} \left(m_i^R \frac{d}{ds^o} (\Lambda_{2,i}) - f_{m,i}^R \Lambda_{2,i} \right) ds^o + \\ & \int_{s^o=0}^{s^o=L} \left(-\Lambda_{2,i} \zeta_i + \Lambda_{2,i} \frac{d}{dt} (I_{ii}^R \omega_i^R) \right) ds^o \text{ with } \eta_i = \left(\frac{d}{ds^o} (\mathbf{r}^R) \times \mathbf{n}^R \right)_i, \end{aligned} \quad (\text{D-3})$$

$$\Xi_{3,j} = \int_{s^o=0}^{s^o=L} \Lambda_3 \left(-\frac{1}{2} \psi_j - cq_m + \frac{d}{dt} q_j \right) ds^o, \text{ with } \psi_j = (\boldsymbol{\Omega} \mathbf{q})_j, \quad (\text{D-4})$$

$$\Xi_4 = \int_{s^o=0}^{s^o=L} \Lambda_4 \left(\frac{\partial L_s}{\partial t} + \omega \frac{\partial L_s}{\partial \eta} \right) ds^o, \quad (\text{D-5})$$

$$\Xi_5 = \int_{s^o=0}^{s^o=L} \Lambda_5 \left(\mathbf{r}_r \cdot \mathbf{t}_p \right) ds^o. \quad (\text{D-6})$$

In the previous expressions, $(\cdot)_i$ and $(\cdot)_j$ represent the components of some vector (\cdot) .